Controls on the REE patterns in sodic pyroxenes in Green Foyaite from the Pilanesberg Complex, South Africa

Marie Foldøy Solem

Thesis submitted for the degree of
Master in Geology
(Mineralogy, petrology and geochemistry)
60 credits

Department of Geosciences
Faculty of mathematics and natural sciences

UNIVERSITY OF OSLO

Spring 2019

Controls on the REE patterns in sodic pyroxenes in Green Foyaite from the Pilanesberg Complex, South Africa

Marie Foldøy Solem
Supervised by Tom Andersen (UiO), Marlina Elburg (UJ)
and Muriel Erambert (UiO)

June, 2019

Supervisor(s): Tom Andersen (UiO), Marlina Elburg (UJ) and Muriel Erambert (UiO)

Controls on the REE patterns in sodic pyroxenes in Green Foyaite from the Pilanesberg Complex, South Africa

http://www.duo.uio.no/

Printed: Reprosentralen, University of Oslo
Front page photo: Photo taken by the author of the Pilanesberg national park.

Abstract

Intrusive rocks of the Green Foyaite Suite make up a substantial fraction of the southern part of the Pilanesberg Complex. The rocks range from fine-grained foliated foyaites (nepheline syenites) with clinopyroxenes (cpx;<0.25 mm) as the main mafic mineral, to coarse-grained heterogeneous and unfoliated foyaites with variations of astrophyllite, cpx, and amphibole as the main constituents. The cpx in the fine-grained foyaites display a shape-preferred orientation. Both varieties contain a range of rare Zr-minerals as well as other accessory minerals identified by SEM-EDS analyses. The petrology and whole rock compositions place the Green Foyaites in two distinct groups which correlate with the two locations where the samples were collected. Clinopyroxene in the Green Foyaite is aegirine, ranging from a more magnesian ($Aeg_{58}Hd_{25}Di_{16}$) to close to pure aegirine ($Aeg_{99}Hd_0Di_1$). Clinopyroxenes are both early and late magmatic, where the early magmatic clinopyroxene is often zoned and has lower aegirine component than the acicular late magmatic pyroxenes with no observed color differences. The aegirine in the Green Foyaites has a high concentration of titanium. In the unfoliated foyaites, the titanium content in aegirine exceeds >0.1 apfu, which suggest that it can be classified as titanian-aegirine. Amphibole is a blue-green pleochroic amphibole intergrown with the aegirine. The amphibole ranges from magnesio-arfvedsonite to arfvedsonite with $Fe_{tot}/(Fe_{tot} + Mg)$ ranging from 0.48 to 0.83.

Chondrite-normalized REE patterns in pyroxenes from the Green Foyaite ranges from LREE-enriched, relatively straight patterns to distinctly MREE depleted, trough-shaped patterns. The aegirine component can be correlated with the REE-patterns, where low-aegirine samples have a high La/Lu and low Lu/Ho ratio, while the high-aegirine pyroxenes have La/Lu ratios close to 1 and high Lu/Ho ratios. This results in the high-aegirine samples to be more MREE depleted relative to LREE and HREE than the low-aegirine crystals. Amphibole mimics the REE-pattern of the pyroxenes. Because aegirine formed early in the crystallization sequence of the Green Foyaite magma, MREE depletion in the Green Foyaite cannot be explained by in-situ processes and is more likely to be a result of a complex fractionation removing the middle REEs from the melt forming the agpaitic Green Foyaite prior to the final emplacement of the magma. A more primitive amphibole fractionation has previously been suggested, however, fractional crystallization of clinopyroxene is in this thesis the proposed mechanism removing the MREE.

Acknowledgements

I hope you, the reader, will enjoy this paper and appreciate the labor that has gone into it. This thesis probably would not be here if it were not for copious amounts of tea, coffee, the occasional snus and an endless loop of upbeat music to keep me going in the face of tired shoulders from the continuous physical process of writing this. If you have ever undertaken a project like this or are in the middle of one, just know I am rooting for you!

I also want to thank all of those who knowingly and unknowingly supported me through this process, you made all the difference. Thank you to my supervisor, Professor Tom Andersen, for the guidance throughout this thesis, for always having an open door and answering all my questions. Thank you, Professor Marlina Elburg at the University of Johannesburg, for the fantastic field trips in South Africa, and for giving me thorough feedback. Thank you, Muriel Erambert for the many hours you helped me with the electron microprobe, the methodology and help with identifying the rare minerals in these rocks. Thank you to Magnus Kristoffersen for all the help with the ICP-MS and answering all the questions I had along the way. Thank you, Siri Simonsen, for the many hours helping me with the scanning electron microprobe, and thank you Salahalldin Akhavan for making the thin sections. I would especially like to thank Kristine Giles for sharing her data from her thesis about the White Foyaite, as well as sharing her knowledge about the subject. It has all been greatly appreciated.

Special thanks to my loving friends and family, my personal cheerleaders, and moral support. Finally, I would like to thank all my fellow students of Geology at the University of Oslo. Without all the breaks, jokes, laughs and the camaraderie, these years would not have been the same. You kept me sane throughout this process.

Glossary

- **Foyaite:** Historical term for nepheline syenite that remains in use in certain complexes.
- **Peralkaline:** Chemical term for rocks that are oversaturated with alkalis and undersaturated with aluminum. The chemical definition of a peralkaline rock on a molar basis is thus: $(Na + K)/Al > 1$.
- **Miaskitic:** The term "miaskite" is defined as *"a leucocratic variety of biotite nepheline monzosyenite with oligoclase and perthitic oligoclase"*, while "miaskitic" is *"a general term for nepheline syenites in which the molecular ratio of* $(Na_2O + K_2O)/Al_2O_3 < 1$" (Le Maitre *et al.*, 2002). The term has also been extended to cover peralkaline nepheline syenites that do not show the typical mineralogical characteristics of agpaitic rocks (Marks & Markl, 2017).
- **Agpaitic:** Peralkaline nepheline syenite with $(Na + K)/Al \geq 1.2$ (Ussing, 1912) and/or characterized by complex Zr- and Ti-minerals, such as eudialyte and mosandrite, rather than simple minerals such as zircon and ilmenite (Marks & Markl, 2017).
- **REE:** Rare earth elements.
- **LREE:** Light rare earth elements: La-Nd.
- **MREE:** Middle rare earth elements: Sm-Ho.
- **HREE:** Heavy rare earth elements: Er-Lu.
- **PPL:** Plane polarized light.
- **XPL:** Plane polarized light, observed with crossed polars.

Table 1: *Abbreviations and theoretical mineral formulas for the minerals found in the Green Foyaite. Formulas from mindat.org*

Mineral	Abbreviations	Formula
Aegirine	Aeg	$NaFe^{3+}Si_2O_6$
Arfvedsonite	Arf	$[Na][Na_2][Fe_4^{2+}Fe^{3+}]Si_8O_{22}(OH)_2$
Ancylite-(Ce)	Anc	$CeSr(CO_3)_2(OH) \cdot H_2O$
Apatite	Ap	$Ca_5(PO_4)_3(OH, F, Cl)$
Astrophyllite	Ast	$K_2NaFe_7^{2+}Ti_2Si_8O_{28}(OH)_4F$
Britholite gr.[1*]	Bth	$(REE, Ca)_5[(Si, P)O_4]_3X$
Burbankite gr.	Bur	$(Na, Ca)_3(Sr, Ba, Ce)_3(CO_3)_5$
Celestine	Cel	$SrSO_4$
Diaspore	Dia	$AlO(OH)$
Eudialyte	Eud	$Na_{15}Ca_6(Fe^{2+}, Mn^{2+})_3Zr_3[Si_{25}O_{73}](O, OH, H_2O)_3(OH, Cl)_2$
Fluorite	Fl	CaF_2
Hilairite/Catapleiite	Hil/Cat	$Na_2Zr[SiO_3]_3 \cdot 3H_2O$ $Na_2Zr(Si_3O_9) \cdot 2H_2O$
Jinshajiangite	Jin	$BaNaFe_4^{2+}Ti_2(Si_2O_7)_2O_2(OH)_2F$
Lorenzenite	Lor	$Na_2Ti_2(Si_2O_6)O_3$
Mn-oxide	MnO	MnO
Monazite-(Ce)	Mnz	$(Ce, La, Nd)PO_4$
Parisite-(Ce)	Par	$CaCe_2(CO_3)_3F_2$
Pectolite gr.	Pec	$NaCa_2Si_3O_8(OH)$
Phyrophanite	Phy	$Mn^{2+}TiO_3$
Pyrochlor gr.[2*]	Pyr	$A_2Nb_2(O, OH)_6Z$
Pyrrhotite	Pyt	Fe_7S_8
REE-carbonate	REE-C	$REECO_3$
Rinkite-(Ce)	Rin	$(Ca, Ce)_4Na(Na, Ca)_2Ti(Si_2O_7)_2F_2(O, F)_2$
Rosenbuschite	Ros	$(Ca, Na)_3(Zr, Ti)Si_2O_7(O, F)_2$
Sodalite	Sod	$Na_8(Al_6Si_6O_{24})Cl_2$
Sphalerite	Sph	ZnS
Strontium apatite	Sr-ap	$SrCaSr_3(PO_4)_3F$
Strontium carbonate	Sr-C	$SrCO_3$
Thorite	Th	$Th(SiO_4)$
Titanite	Ttn	$CaTi(SiO_4)O$
Tritomite-(Y)	Trt	$Y_5(SiO_4, BO_4)_3(O, OH, F)$
Wöhlerite gr.	Wöh	$NaCa_2(Zr, Nb)Si_2O_7(O, OH, F)_2$
Zircon	Zrn	$ZrSiO_4$

[1*] REE includes Y. X = F^-, $(OH)^-$, Cl^-

[2*] A is Na, Ca, Sn^{2+}, Sr, Pb^{2+}, Sb^{3+}, Y, U^{4+}, H_2O. Z is OH, F, O, H_2O

Contents

List of Figures

Introduction

1.1 Why do we study peralkaline rocks?

Alkaline rocks are interesting rocks to study as these rocks have unique mineral assemblages and petrology. The processes which form these rocks are highly unusual and, therefore, by studying these rocks, these processes which ultimately form peralkaline rocks are better understood. Furthermore, alkaline rocks have high concentrations of incompatible elements such as the rare-earth elements (REE) and the high field strength elements (HFSE) which have a range of applications within clean energy, technology as well as medical and military sectors (Beard, 2018).

1.2 The objective of this study

Most of the Pilanesberg Complex is today within a popular national park. The park offers safari opportunities and wild animals such as elephants, lions, and zebras roam the area freely. The samples from this thesis are collected from outside the borders of the national park.

This study focuses on the agpaitic Green Foyaite Suite, collected from two localities from the southern part of the complex, close to the small town Ledig. The first locality was chosen as it was close to a riverbed, which made the rocks easily accessible. These rocks have a clear laminar foliation and are petrologically very different from the rocks from the other locality. The second locality was chosen as boulders of rocks were dumped due to the construction of a new road and were therefore easily accessible. These rocks have no laminar foliation.

The target of this thesis is to understand the processes which lead to this suite of rocks. In order to understand these processes, a thorough mineralogical and petrological analysis has to be conducted. Furthermore, this thesis will analyze the trace and major elements in these rocks and compare these rock types to previously described and analyzed rocks from the Pilanesberg Complex. The trace elements REE-distribution patterns of pyroxenes and amphiboles will be achieved, and the cause of this distribution will be discussed.

Classification and formation of peralkaline rocks

"Peralkaline" is a term for igneous rocks that are oversaturated with alkalis, and thus undersaturated with aluminum (Le Maitre *et al.*, 2002). The chemical definition of a peralkaline rock on a molar basis is thus:

$$(Na + K)/Al > 1 \tag{2.1}$$

Therefore, the magma contains more alkalis than can be accommodated in the feldspars, and for this reason other alkali-bearing minerals are formed such as aegirine ($NaFe^{3+}Si_2O_6$), riebeckite ($Na_2Fe_2^{2+}Fe^{3+}Si_8O_{22}(OH)_2$), arfvedsonite ($Na_3Fe_4^{2+}(Al, Fe^{3+})Si_8O_{22}(OH)_2$) and/or aenigmatite ($Na_2Fe_5^{2+}TiO_2Si_6O_{18}$). Peralkaline rocks are in general rich in otherwise incompatible elements such as the large ion lithophile elements (LILE), halogens, the rare earth elements (REEs), the high field strength elements (HFSEs) as well as otherwise relatively rare elements such as Be, Sn, Zn, and Ga (Marks & Markl, 2017). Peralkaline rocks are subdivided into miaskitic and agpaitic varieties based on their mineralogy and peralkalinity:

2.1 Miaskitic rocks

The term "miaskite" is defined as *"a leucocratic variety of biotite nepheline monzosyenite with oligoclase and perthitic oligoclase"*, while "miaskitic" is *"a general term for nepheline syenites in which the molecular ratio of* $(Na_2O + K_2O)/Al_2O_3 <$ 1" (Le Maitre *et al.*, 2002). Whereas this is the use recommended by Le Maitre *et al.* (2002), the usage has been extended to also cover peralkaline nepheline syenites that do not show the typical mineralogical characteristics of agpaitic rocks (see section 2.2) (Marks & Markl, 2017). With the latter definition, miaskitic rocks are the more common peralkaline variety with several thousand reported occurrences worldwide. In peralkaline miaskitic rocks, their high field strength elements and rare earth elements are stored in more common minerals such as titanite and zircon (Marks & Markl, 2017).

2.2 Agpaitic rocks

The original definition of agpaitic rocks was a pure geochemical definition where the whole rock composition on a molar basis exceeded $(Na+K)/Al \geq 1.2$ (Ussing, 1912). The currently accepted definition is based on their HFSE mineralogy (Sørensen, 1960). Le Maitre *et al.* (2002) defines "agpaite" and "agpaitic" as being *"restricted to peralkaline nepheline syenites characterized by complex Zr- and Ti-minerals, such as eudialyte and mosandrite, rather than simple minerals such as zircon and ilmenite."*

Agpaitic rocks are very rare and are only found at about a hundred occurrences worldwide. The extreme enrichment of alkalis, halogens, HFSEs and REEs during differentiation of peralkaline agpaitic magmas can lead to crystallization of a wealth of rare minerals not found elsewhere. The most common minerals that store HFSE and REE in agpaitic rocks are members of the eudialyte, rinkite and wöhlerite mineral groups. Other minerals that commonly occur in agpaitic rocks are sodic minerals such as sodalite, sodic amphibole, sodic pyroxenes, aenigmatite as well as volatile-bearing HFSE-silicates. The most common type of agpaitic rock is a nepheline syenite with eudialyte-group minerals.

Agpaitic nepheline syenites are often medium- and coarse-grained, but fine-grained and porphyritic varieties also exist. Agpaitic mineral assemblages can be early magmatic, late magmatic or hydrothermal. It has therefore been suggested that the best way to characterize agpaitic rocks is by careful textural studies to distinguish the stage of evolution at which agpaitic minerals were stabilized, as this is the only way to understand the various physiochemical parameters during different evolutionary stages of these mineralogically and texturally diverse rocks (Marks & Markl, 2017).

2.2.1 Varieties of agpaitic mineral assemblages

Even though the classical case of an agpaitic rock is a nepheline syenite, containing eudialyte-group minerals (EGM), similar assemblages, partly lacking EGMs, but comprising of halogen-free, Na-rich Zr-Ti-silicates, fluorine-rich Zr-Ti-silicates or a combination of both have also been reported in, eg. Pilanesberg and in the Langesundfjord (Marks & Markl, 2017). Fluorine rich Zr-Ti-silicates may form if a_{HF} in a magma increases above a critical minimum level. As a result, the stable assemblage zircon + fluorite shifts to assemblages with wøhlerite and rinkite group minerals + fluorite (Andersen *et al.*, 2010).

Rocks containing primary F-rich Zr-Ti-silicates (with or without associated EGMs) do not reach as high peralkalinity indices (PI) as rocks containing pure EGM-sodalite

assemblages. Pure F-rich Zr-Ti silicates assemblages and mixed assemblages with additional EGMs have been known to also occur in metaluminous compositions. These findings are, however, ambiguous as it is not clear if these mineral assemblages crystallized in metaluminous conditions (Marks & Markl, 2017). Pure EGM-sodalite assemblages lacking F-rich Zr-Ti silicates are, however, primarily restricted to rocks with a peralkalinity index (PI) >1.2. Hydrothermal alteration and autometasomatism in already peralkaline rocks can also produce secondary agpaitic mineral assemblages (Marks & Markl, 2017).

2.2.2 Formation of agpaitic rocks

The rarity of the mineral assemblages in agpaitic rocks and their high concentration of otherwise incompatible elements indicate that their formation requires conditions that generally are not met during crystallization of peralkaline rocks. As the agpaitic rocks are extremely enriched in incompatible elements, it is generally believed that the mantle source from which peralkaline melts are generated, has had to be metasomatically pre-enriched in halogens, HFSEs, REEs, and other incompatible elements to explain the unusual enrichment of these elements. Melting of such altered mantle could produce alkaline melts that are enriched in incompatible elements if the degree of melting is low enough. The higher the degree of melting, the less alkaline the resulting melt would be. Other factors which are important for generating alkaline melts are subsequent differentiation at low oxygen fugacity, low water activity as well as low pressure. A combination of these factors will enrich the magma in iron, increase the peralkalinity and retain the incompatible elements such as the HFSE and REE (see below) (Marks & Markl, 2017).

2.2.3 The role of oxygen fugacity

Oxygen fugacity represents the oxidation state of a system. There are several reactions that can be used to monitor the the oxygen fugacity. For example, the iron- wüstite equation describes the coexistence of metallic iron FeO and Fe^{2+} in extremely reducing environments:

$$O_2 + 2Fe = 2FeO \tag{2.2}$$

For this equation the oxygen fugacity is defind as:

$$fO_2 = aFeO^2/aFe^2 \tag{2.3}$$

where a is the activity, which is the effective concentration in the mixture. How oxidized the environment in which the magma evolves has crucial consequences for its composition. High oxygen fugacity will lead to precipitation of magnetite, leading to FeO depletion, and enrichment of silica in the remaining melt. In reduced conditions, however, the suppression of magnetite crystallization leads to the enrichment of iron and a lack of silica enrichment in more evolved magma compositions. If such a system is further differentiated, the presence of minerals that are typical for peralkaline and agpaitic rocks such as aegirine, arfvedsonite, and aenigmatite can appear (Marks & Markl, 2017).

2.2.4 The importance of fluids for agpaitic rocks

Several agpaitic minerals contain halogens, alkalis, and other fluid-mobile components. The retention and release of fluids containing these fluid-mobile components are therefore necessary during the evolution of peralkaline magmas. Whether these fluids are retained or exolved comes down to the magmatic fluid composition and the oxygen fugacity.

Magmatic fluids can either be methane-rich or they can be a mixture of carbon dioxide and water:

$$CH_4 + 2O_2 = CO_2 + 2H_2O \tag{2.4}$$

The magmatic fluids largely depend on the availability of elements in the system. What further controls the magmatic fluids is the redox conditions. Generally, at low oxygen fugacity, the magmatic fluids will be methane-dominated, and at higher oxygen fugacities, the fluids would be more water-rich. This is apparent in eq. 2.4. Agpaitic rocks are formed under reduced conditions, and their magmatic fluids are dominated by CH_4-rich fluids with high salinity (Konnerup-Madsen & Rose-Hansen, 1982). Miaskitic rocks, on the other hand, evolve under more oxygenated conditions and their magmatic fluids tend to be more water-rich. The oxidizing conditions will cause early exsolution of water-dominated fluids and deplete the remaining melt in the water-soluble species. The agpaitic rocks will, on the other hand, retain the water-soluble species which are then enriched during further evolution. The halogen- and alkali-rich melt compositions will, in turn, have high solubilities for HFSEs and will be capable of crystallizing typical agpaitic minerals such as the eudialyte group minerals, as soon as the required enrichment level for Zr is reached in the magma (Marks & Markl, 2017).

Volatile components in the magma

In addition to water, the activity of volatile components like HF and HCl have an impact on the stabilization of the halogen-bearing HFSE-mineral phases (Andersen *et al.*, 2010). By increasing the a_{HF} in the magma, the mineral assemblage can transition from a stable miaskitic assemblage with zircon to an agpaitic assemblage with wöhlerite- and rinkite-group minerals + fluorite. Peralkaline nepheline syenite magmas crystallizing these mineral assemblages can also eventually crystallize eudialyte if the a_{HCl} together with the required Zr level is high enough (Andersen *et al.*, 2010; Marks & Markl, 2017).

2.2.5 The impact of pressure

The pressure estimates performed on agpaitic rocks indicate, for the most part, shallow level emplacement of 1 kbar or less. The pressure influences the composition of late-stage and hydrothermal fluids. At low pressure, the salinity of evolving fluids will increase with progressive crystallization. At higher pressures, their salinity will, however, be lower than of early magmatic fluids. This is because the partitioning behavior of Cl between silicate melt and coexisting fluid is pressure dependent, and the proportion of chlorine partitioning into the aqueous fluids is higher at lower pressures (Cline & Bodnar, 1991). The high salinity fluids have high solubilities for HFSE and can, therefore, produce the mineral assemblages that are defined as agpaitic. Magmatic rocks emplaced on deep crustal levels might, therefore, end up miaskitic even though their geochemical composition would allow for an agpaitic mineral assemblage (Marks & Markl, 2017).

2.2.6 Suggested magma sources of agpaitic rocks

Agpaitic rocks represent the most evolved stages of the peralkaline system, and radiogenic isotope studies suggest that the magma that eventually forms agpaitic rocks are mantle-derived (Kramm & Kogarko, 1994). The two suggestions for the primary magmas that can ultimately give rise to agpaitic magmas are either plagioclase bearing with alkali basaltic to basanitic compositions or feldspar free with mostly nephelinitic compositions. These might evolve towards peralkaline compositions by crystal fractionation. Plagioclase can incorporate Sr^{2+} and Eu^{2+} in its structure, making magmas that derivate from plagioclase bearing compositions low in strontium. Hence, EGMs from rocks that were derived from alkali basaltic magmas usually have low Sr levels and show pronounced negative Eu anomalies.

Nephelinitic magmas, on the other hand, do not fractionate plagioclase, and the EGMs will not show these prominent Eu and Sr anomalies (Marks & Markl, 2017).

Agpaitic rocks from the Ilímaussaq Complex are highly evolved products of an alkali basaltic magma. These rocks have low Sr-concentrations and show pronounced negative Eu anomalies (Sørensen, 1992). The presence of anorthositic xenoliths in Gardar intrusive rocks also points towards the presence of plagioclase-rich cumulates at depth (Upton, 2013; Bridgwater & Harry, 1968). Rocks from Khibina, Lovoozero, and Pilanesberg, on the other hand, have high Sr content and precipitate Sr-rich minerals such as lamprophyllite which are absent or insignificant in the Ilímaussaq Complex. This suggests a nephelinitic parental magma compositions (Kramm & Kogarko, 1994).

2.3 Nepheline syenite (Foyaite)

Syenite is a plutonic rock that consists mainly of alkali feldspar with sodic plagioclase, biotite, pyroxene, amphibole, and occasional fayalite. Nepheline syenite is now defined in field 11 in the modal QAPF diagram (figure 2.1) as a variety of foid syenite in which nepheline is the most abundant foid (Le Maitre *et al.*, 2002). As shown in figure 2.1, 10 percent of the feldspar can be plagioclase, and 10-60 % has to be foids, with nepheline being the most abundant foid (Le Maitre *et al.*, 2002).

For historical reasons, nepheline syenite is sometimes referred to as "foyaite" in the Pilanesberg Complex (Elburg & Cawthorn, 2017). According to Le Maitre *et al.* (2002), the term foyaite should now be restricted to nepheline syenites having trachytic texture caused by the alignment of alkali feldspar crystals, although they do note that foyaite is sometimes used as a group name for nepheline syenites. For our purposes, the latter definition will be used to maintain consistency with traditional usage in the region.

2.3.1 Lujavrite

Lujavrites are rare meso- to melanocratic agpaitic nepheline syenites that are rich in eudialyte, arfvedsonite, and aegirine characterized by perthitic alkali feldspar or separate microcline and albite. Lujavrite shows a clear igneous lamination and is rich in incompatible elements such as REE, Zr, Li, Nb, Th, and U (Sørensen *et al.*, 2006; Le Maitre *et al.*, 2002).

2.3.2 Tinguaite

Tinguaite is a fine-grained rock of nepheline syenite composition with a special texture of aegirine needles (Le Maitre et al., 2002).

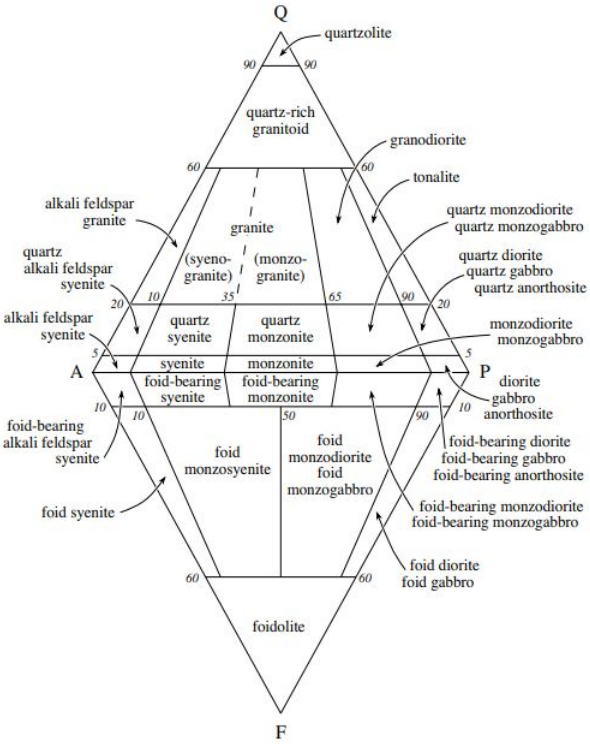

Figure 2.1: *QAPF classification diagram. Figure from Le Maitre* et al. *(2002)*

Geological setting

3.1 Previous work

The first description of nepheline syenites (foyaites) in Pilanesberg was a short two page preliminarily note written by Molengraaff (1905). The Pilanesberg Complex (PC) was then further described by Brouwer (1911) and mapped by Humphrey (1912). Shand (1928) made a major contribution by further producing a geological map and continue the petrographic descriptions of Brouwer (1911). Shand (1928) introduced the terminology of Red Syenite, and Red, White, and Green Foyaite. He was also the first to distinguish between 'inner' and 'outer' varieties based on their geographical location in the complex (Elburg & Cawthorn, 2017).

An unpublished Ph.D. thesis by Retief (1963), at the University of Oxford, introduced the terms Ledig Foyaite and lujavrite. A small patch of arfvedsonite granite in the center of the complex was mentioned by Lurie in his unpublished Ph.D. thesis from 1973 at Rhodes University. Lurie later published an extended version of his Ph.D. thesis on the University of Johannesburg library website in 2004. Lurie (2004) and Retief (1963) have been the main workers on the intrusive rocks of the complex, however, summaries of their work have been presented by Mathias (1974), Wolley (2002) and Verwoerd (2006).

Recent studies from the area include Elburg & Cawthorn (2017), Mitchell & Liferovich (2006), Andersen *et al.* (2017), Andersen *et al.* (2018) and Cawthorn (2015) which offers new insight, and includes trace, major, whole rock analysis and mineral chemistry of the various rock types in the complex. Excluding these studies, minimal further work has been published on the complex due to inadequate exposure, therefore making it difficult to interpret field relations. In addition to poor exposure, extreme auto-metasomatism of the rocks can make different rock types challenging to distinguish in the field (Cawthorn, 2015).

3.2 Regional Geology

The Kaapvaal craton is located north-east in South Africa (figure 3.1). The craton covers an area of around $1.6 \cdot 10^2$ km^2 and has rocks in the age interval 3.7–2.6 Ga (Verwoerd, 2006). The craton consists of greenstone belts and tonalite-trondhjemite-

granodiorite (TTG) with a transition to granite-monzogranite-syenogranite (GMS). This progression is interpreted to reflect progressive reworking and differentiation of the crust (Agangi *et al.*, 2018). Overlying the craton are several kilometers of sedimentary sequences.

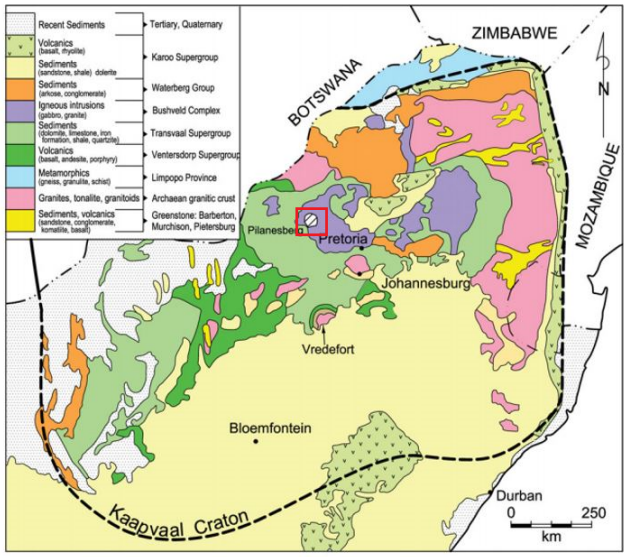

Kaapvaal Craton, Southern Africa

Age (Ma)	Formation*	Group	Supergroup	
≈ 1800		Soutpansberg Waterberg		
U				
2200 - 2400	Silverton Strubenkop Timeball Hill	Pretoria	Up	Transvaal
A/P Boundary		Chuniespoort		
2600	Black Reef Selati	Wolkberg	Lo	
U				
2700	Bothavill		Ventersdorp	
2800 - 2850	K8 Booysens	Central Rand	Witwatersrand	
2900 - 2950	Roodepoort Promise Brixton Parktown Orange Grove	West Rand		
3070		Dominion		
Relation Unknown				
2920 - 2940		Mozaan Nsuze	Pongola	
U				
3300 3400		Moodies Fig Tree	Swaziland	
3450		Onverwacht Scharpenberg		

* Not all formations are listed
U = major unconformities.

Figure 3.1: *Geological map over the Kaapvaal Craton with the overlying sedimentary and volcanic supergroups, and a stratigraphic column. Figures from Cawthorn (2015) and Jahn & Condie (1995). The red box represents the Pilanesberg Complex.*

The Swaziland Supergroup is the oldest sequence in the Kaapvaal Craton. The supergroup contains some of the oldest-known, metamorphosed sedimentary as well as volcanic rocks on earth and ranges in age between 3.45 – 3.0 Ga (Knauth & Lowe, 2003). Younger units include the Pongola, Witwatersrand, Ventersdorp, and Transvaal supergroups (figure 3.1). The Ventersdorp Supergroup is composed dominantly of volcanic successions, ranging in composition from basaltic komatiite to rhyodacite, and minor clastic and chemical sediments. The Transvaal Supergroup is predominantly sedimentary and contains dolomites, limestones, iron formations, shales, and quartzites, with limited volcanic intervals. The Soutpansberg and Waterberg groups are sedimentary covers of mostly shale and quartzite and are believed to have been deposited between 1850 and 1750 Ma. The latest sedimentation covering large areas of South Africa was from the Karoo Supergroup. These sedimentary rocks are prominent in the southern part of the Kaapvaal Craton and were deposited between late Carboniferous and Early Jurassic (Chima *et al.*, 2018).

The Bushveld Complex (BC) was emplaced into the Kaapvaal Craton at ca. 2055 Ma (Zeh *et al.*, 2015), more precisely it intruded into the Transvaal Supergroup. The BC consists of both felsic and mafic intrusions (Cawthorn & Walraven, 1998). The

Pilanesberg Complex is a composite intrusion which is cross-cutting the Paleoproterozoic Bushveld Complex. The intrusion was emplaced at a shallow crustal level, intruding into its cogenetic volcanic rocks (Shand, 1928).

3.3 The Pilanesberg Complex

The Pilanesberg Complex (PC) in South Africa is one of the largest alkaline complexes in the world. The PC is located within the Northwest Province of South Africa, and is emplaced into the Kaapvaal Cration. The complex has a circular shape with a diameter of ca. 30 km and includes trachytes, phonolites, syenites, and nepheline syenites (Lurie, 2004). It consists of intrusive and extrusive units that range from metaluminous through peralkaline, miaskitic to strongly agpaitic, and possibly hyperagpaitic compositions (Mitchell & Liferovich, 2006). The existence of hyperagpaitic residual liquids in Pilanesberg is, however, entirely speculative and lacking real supporting evidence. One unique feature is the preservation of the volcanic carapace, that is generally not found in other larger alkaline complexes. The PC is Mesoproterozoic, and the most recent dating of the complex is an U-Pb age of 1395 +10/-11 Ma (Elburg & Cawthorn, 2017).

The PC has intrusive contact to the rocks of the Bushveld Complex with mafic units on the western side and felsic units on the northeastern side of the Pilanesberg Complex. The PC is a part of the widespread igneous event referred to as the Pilanesberg Alkaline Province, consisting of dikes, central volcanoes, and circular intrusions (Verwoerd, 2006; Cawthorn, 2015). The pattern of the intrusive rocks demonstrates a concentric nature throughout the entire complex.

Verwoerd (2006) summarized the order of events from oldest to youngest:

1. Explosive volcanism resulting in trachyte and phonolite.
2. Red syenites
3. More lavas and pyroclastic deposits
4. Red Foyaite
5. Further volcanic activity
6. White Foyaites
7. Green Foyaite and tinguaite
8. Ledig Foyaite
9. Alkali granite

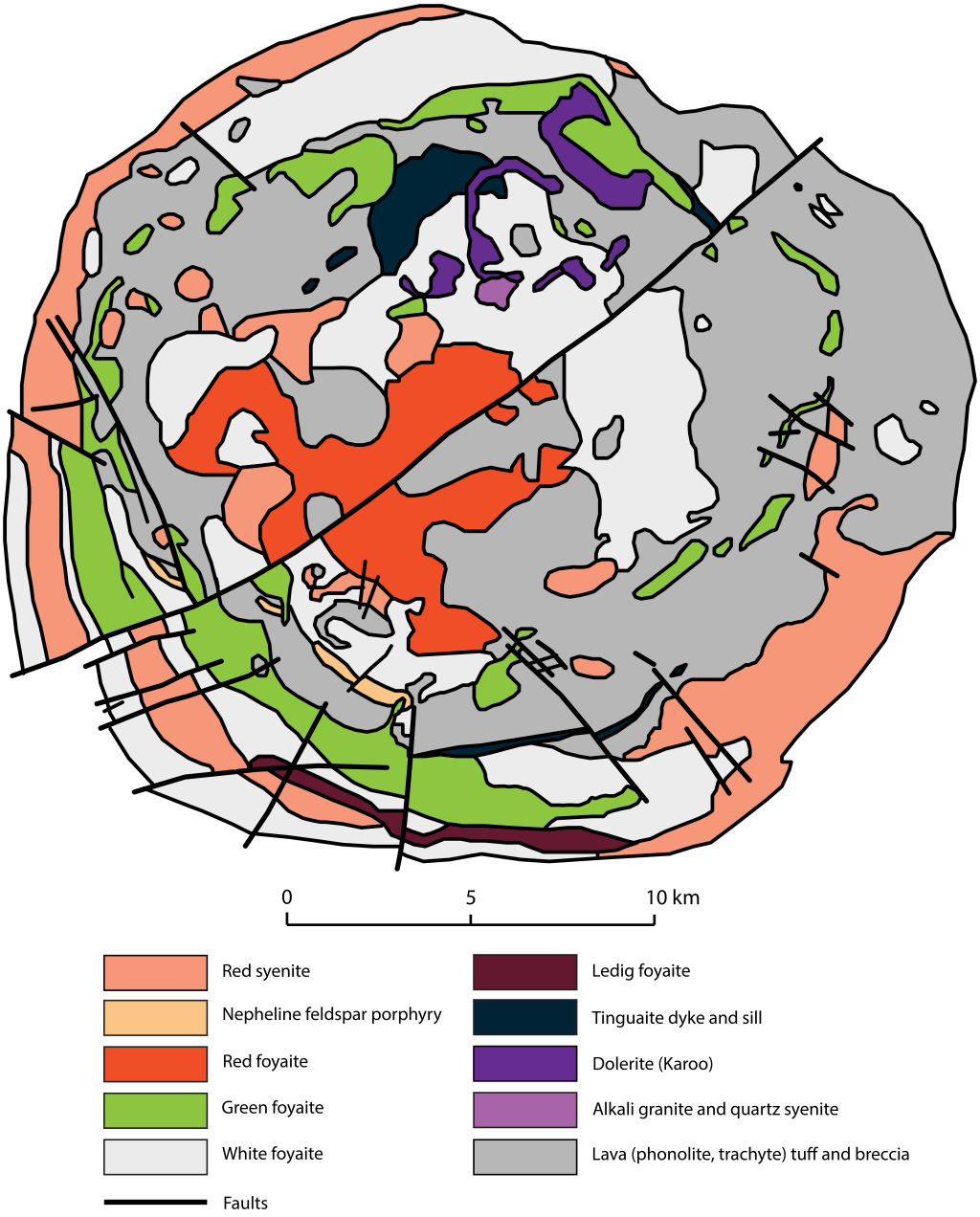

Figure 3.2: *Geological map over the Pilanesberg Complex displaying the intrusive rocks and dikes. Map modified by Giles (2018) after Lurie (2004) The location of the complex on a regional scale can be seen in fig. 3.1.*

The distribution of rock types in the Pilanesberg Complex are pictured in figure 3.2. The intrusive rock types range from early, metaluminous Red syenite through increasingly peralkaline nepheline syenite intrusions, reaching an agpaitic stage in residual liquids forming interstitial mineral assemblages in the White Foyaite and the whole-rocks of the Green Foyaite Suite (Giles, 2018; Andersen *et al.*, 2017; Elburg & Cawthorn, 2017; Andersen *et al.*, 2018). Tinguaite dikes are rare but have been found to cut the volcanic succession and the Green Foyaite. It has been suggested by Lurie

(2004) that these tinguaite dikes are related to the Green Foyaite Suite, and if so, the Green Foyaite Suite can be considered to have post-dated some of the volcanic rocks as the tinguaite dikes are supposed to be feeders to lavas. For the coarse-grained intrusive rock, no exposed cross-cutting relationship exists. The different intrusive members are orientated conformably to each other. Gradual contacts between the different rock types is observed, but the extensive coverage of vegetation and lack of good outcrops makes field relations difficult to determine (Cawthorn, 2015).

3.3.1 The structure of the Pilanesberg Complex

The structure of the Pilanesberg Complex has long been debated. Shand (1928) first described the complex as a laccolith body, whereas Lurie (2004) described the structure as a sequence of concentric cone sheets. Cawthorn (2015) went back and modified Shands's (1928) original model and described is as a composite layered intrusion influenced by repeated cauldron subsidence events. Cawthorn (2015) argues that the three-dimensional shape of concentric cone sheets is based on insufficient field evidence: The cross-section produced by Lurie (2004) (figure 3.3 a) shows steep sides to the north, and given the 30 km diameter size, the extrapolation of this proposed geometrical shape downwards would reach unrealistic depths. He further argues that Lurie's (2004) interpretation of tilting is not consistent with certain observations: if southward tilting had occurred, the volcanic succession forming the upper part of this complex would be more likely to be preserved in the south than in the north, whereas the exact reverse is the case. He also argues that dips would be steeper in the northeast, and gentler in the southwest, which is not observed.

Cawthorn (2015) based his model on an interpretation of a regional Bouguer gravity map, where he interprets the data as a relatively flat sheet rather than steep-sided. His conclusion was a lopolithic structure with possibly multiple magmas feeding into the center of a still partially liquid sheet, rather than into solidified, steeply dipping earlier intrusive phases (figure 3.3 b). The shape in three dimensions is, however, purely speculative because there is no systematic modal layering, and orientations of contacts between the intrusive rocks cannot be identified in the field (Cawthorn, 2015).

3.4 Green Foyaites in the Pilanesberg Complex

Intrusive rocks of the Green Foyaite Suite makes up a substantial fraction of the southern part of the Pilanesberg Complex. The Green Foyaite Suite is both mineralogically and texturally diverse, and comprises a group of meso-to melanocratic

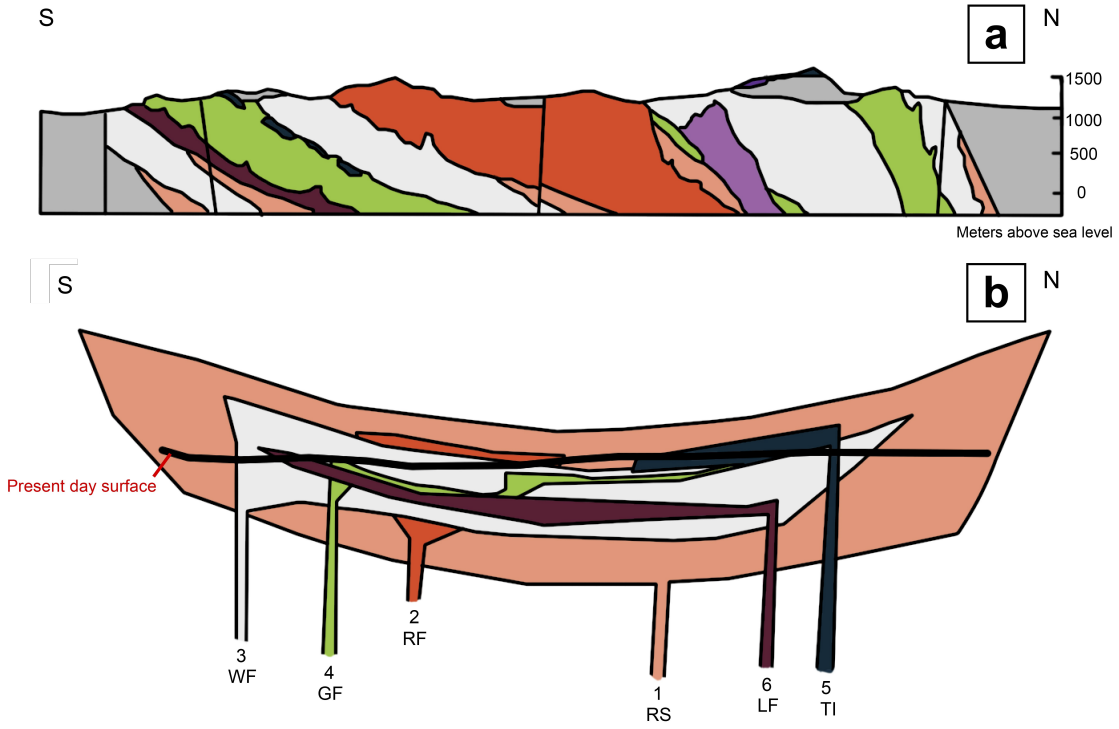

Figure 3.3: *Geological cross section of the Pilanesberg Complex showing the two theories of a) concentric cones and b) layered intrusions. The cross sections are reproduced by Giles (2018), after Lurie (2004) and Cawthorn (2015).*

nepheline syenites with variable modal mineralogy and structure (Lurie, 2004; Retief, 1963). The Green Foyaite includes unfoliated as well as flow-foliated varieties. A variety of the unfoliated Green Foyaite Suite shows a distinct texture of radiating aegirine rosettes. This variety has been referred to as the Ledig Foyaite in previous literature (Retief, 1963).

Mitchell & Liferovich (2006) incorrectly used lujavrite as a general term for the entire Green Foyaite Suite. There is overall some confusion of how to define the Green Foyaite Suite, and some argue that the Green Foyaite, Ledig Foyaite, and lujavrite may be part of the same suite of rocks or that the Ledig Foyaite is closer to the White Foyaite (Elburg & Cawthorn, 2017; Retief, 1963). In the Pilanesberg Complex, the lujavrite has been mapped as a part of the Green Foyaite Suite (figure 3.2). Based on field relationships and similar mineral content, the Green Foyaite, Ledig Foyaite, and lujavrite may be part of the same suite of rocks that are the youngest, excluding the dikes.

The Ledig Foyaite is a possible member of the Green Foyaite Suite, and in Pilanesberg, the actual difference between the Ledig Foyaite and the Green Foyaite Suite is not clear. It is supposed to be the final endmember of the Green Foyaite to intrude into the Pilanesberg Complex based on its overall highest content of trace elements (Verwoerd, 2006; Lurie, 2004). Retief (1963) defined the Ledig Foyaite as an unfoliated variety that forms aegirine-rosette structures. It has as also been noted that Ledig Foyaite can be difficult to distinguish from the White Foyaite in both thin section and field observations (Retief, 1963).

The Ledig Foyaite, lujavrite and tinguaite may all be variations within the 'Green Foyaite Suite.' They can all contain minerals such as eudialyte, aenigmatite, lamprophyllite, and astrophyllite, which are typical for agpaitic rocks (Elburg & Cawthorn, 2017).

3.5 Sampling localities

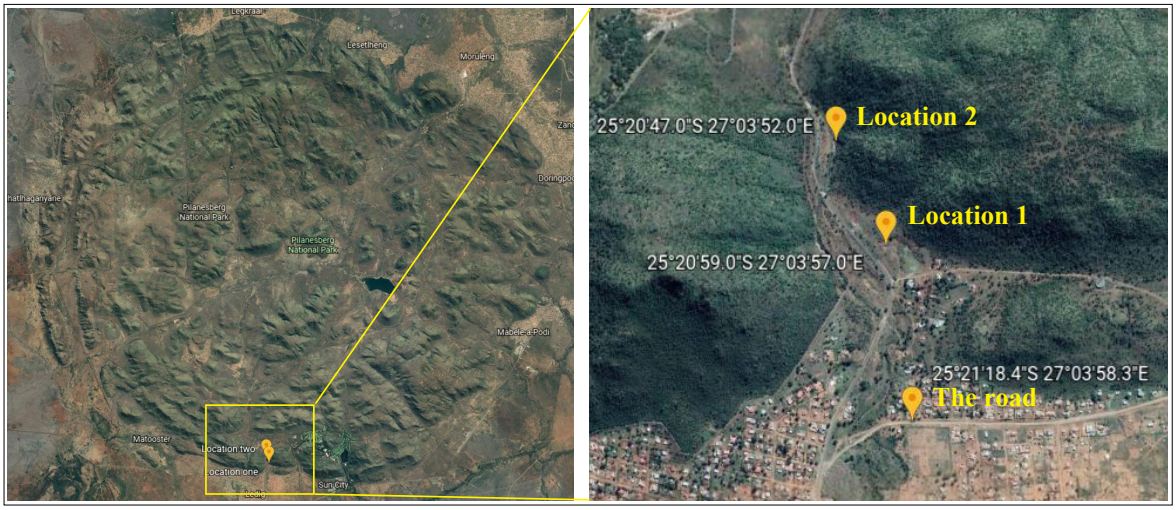

Figure 3.4: *Overview over the sampling localities. The images are collected from Google Earth, and reworked by author*

Seventeen rocks samples (MEPB60-76) have been collected for this study by T. Andersen and M. A Elburg on 14.05.2017. MEPB60-68 were collected from location 2, and MEPB69-76 from location 1. The author went back with Elburg in January 2019 to visit the sampling locations, taking coordinates, and the pictures presented in this thesis. The sampling localities lie outside the Pilanesberg national park, close to the small town Ledig, which makes sampling more accessible. This area is where the Ledig Foyaite first was described by Retief (1963). The samples have been collected from two locations close to each other, with locality one having coordinates: 25.353°S, 27.06654°E and locality two is located at 25.3463°S, 27.06583°E (figure 3.4).

Location 1 consist of boulders of rocks that were not in situ but had been moved there during the construction of a new road a few hundred meters away from the locality. The road can be seen in figure 3.4. These blocks were of Green Foyaite and had insignificant surface weathering as they were blasted for the road construction a short time before sample collection. The rock is coarse-grained, with heterogeneous distribution of pyroxene, astrophyllite, nepheline, and feldspar crystals (figure 3.5 a). The feldspar crystals have a greenish color, which is characteristic for the Green Foyaite compared to the White Foyaite. These blocks gave a unique opportunity to see structures and local inhomogeneities that otherwise would be difficult to observe on weathered surfaces in the field. Examples of this were aegirine rosettes (figure 3.5 b) and thick (∼6 cm) pegmatite veins with large crystals of aegirine,

astrophyllite, and feldspars (figure 3.5 c). The aegirine rosettes observed close to the pegmatite vein were bright green, while the rosettes elsewhere were black, suggesting compositional differences.

Location two is a pavement in a riverbed. At this location, the rock has a prominent flow foliation with mostly elongated phenocrysts of feldspar (figure 3.5 d and e) and a fine-grained matrix with pyroxene needles. The rocks have a weathered surface making further identification in hand specimen more difficult. A thin (< 1 mm) fine-grained vein was observed, with clearly altered feldspars approximately 1 cm in each direction from the vein center (figure 3.5 f).

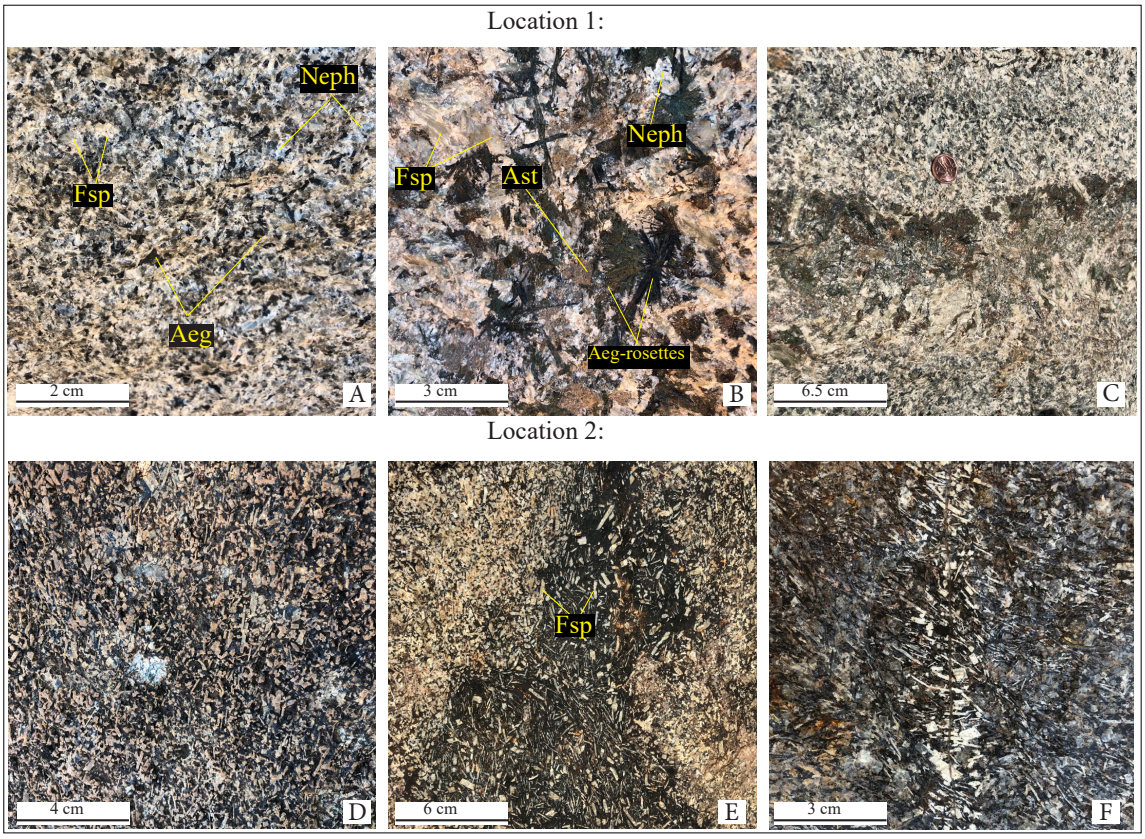

Figure 3.5: *Field appearance of the rocks at location one (A-C) and location two (D-F). Image A-C are the unfoliated Green Foyaite varieties. D-F show the flow-foliated varieties.*

Geochemical concepts

4.1 Trace elements

Trace elements constitute a small fraction (< 0.1 wt.%) in minerals and do not affect the chemical or physical properties of the system as a whole in any significant way (White, 2013). Variations in the concentration of many trace elements are more significant than variations in major elements. There are also more trace elements than major elements within a system, and trace elements are sensitive to processes that major elements may be insensitive to. The trace element distribution can, therefore, give information about the system of interest (White, 2013). In agpaitic rocks and peralkaline rocks in general, the element groups of interest are the high field strength elements (HFSEs), the large ion lithophile elements (LILEs) and the rare earth elements (REEs). In this study, the REE distribution will be of particular interest.

4.1.1 High field strength elements

Field strength is defined as charge/radius. The HFSEs have high ionic charge and relatively small cations, resulting in high field strength. The high field strength elements group consist of zirconium (Zr^{4+}), hafnium (Hf^{4+}), niobium (Nb^{5+}) and tantalum (Ta^{5+}). Uranium (U) and thorium (Th) are sometimes considered to be in this group. Their high charge makes substitutions highly unfavorable, thus making them incompatible elements most environments (White, 2013). They are, however, compatible in agpaitic rocks and form their own minerals. HFSEs can, therefore, be considered major elements in agpaitic rocks.

4.1.2 Light ion lithophile elements

K, Rb, Cs, Sr, and Ba are often called the light ion lithophile elements (LILEs). The elements in this group have large ion radii and therefore tend to not fit into the crystal lattice in minerals. The LILEs, therefore, concentrates into the melt phase rather than into the mineral structure, and therefore are incompatible in many systems (White, 2013). Strontium is highly compatible in agpaitic rocks, and form own minerals such as celestine, ancylite, and sr-apatite.

4.1.3 The rare earth elements

The rare earth elements begin with lanthanum (La-57) and end with lutetium (Lu-71) in the periodic table, and they are together known as the lanthanides. The light rare earth elements (LREE) are the larger, low atomic numbered elements, and the heavy rare earth elements (HREE) are the high atomic numbered varieties that end with Lu. The middle rare earth elements (MREE) are the elements between, from samarium (Sm) to holmium (Ho). Yttrium (Y) is often mentioned in relation to the REEs as it has similar ionic radii and charge as the HREE and therefore behaves much like them. The REE +Y are in the 3+ state over a wide range of oxygen fugacities. Cerium (Ce) can, however, be in the 4+ state at the oxygen fugacity of the earth surface, and Eu in the 2+ state in reduced conditions. The REEs have medium ionic radii and high charge, which usually makes them incompatible elements (White, 2013). The ionic radius decreases progressively from La (103.2 pm) to Lu (86.1 pm), making HREEs more compatible than the LREE in mafic minerals such as garnet and hornblende (Janoušek *et al.*, 2015). The ion radii used are the effective ionic radii by Shannon (1976).

4.2 Partition coefficient

The partition coefficient is a measure of the distribution of an element between crystals and the coexisting melt. The partition coefficient K_D is defined as:

$$K_D = (C_{Min})/(C_L) \tag{4.1}$$

A compatible element ($K_D > 1$) concentrates into the crystal rather than in the liquid, while an incompatible element ($K_D < 1$) will prefer the liquid phase. In addition to melt composition, the presence of volatiles, temperature, pressure, and the redox state of the system influence the K_D values (Janoušek *et al.*, 2015).

Analytical Methods

For the production of thin sections, rectangular rock pieces of ca. 4 x 2.5 x 1 cm were cut from hand specimen using a diamond saw. Polished thin sections (30 μm) were made by Salahalldin Akhavan in the thin section laboratory at the Geology Department at the University of Oslo, using an automatic Thorlag grinding and polishing machine with diamond as the polishing medium.

5.1 X-ray fluorescence

The whole-rock major element analysis was performed by x-ray fluorescence (XRF) using a Panalytical Axios Fast 1 MagiX PRO X-Ray Fluorescence Spectrometer at the University of Johannesburg by Ph.D. student Juliet Akoh and Professor Marlina Elburg. The precision and reproductivity of XRF produce accurate results.

The calibration curve for the XRF is obtained from a wide range of synthetic and natural reference materials, of which ten are routinely measured during the analytical runs. This is in order to perform drift corrections off-line. The natural reference materials include BE-N, JSy-1, SARM2, SARM16 and SARM 32, plus several synthetic mixtures of Al, Ti, K, Si and Ca. The unknown samples were dried at 105 °C, and loss on ignition (LOI) comes after 30 minutes at 930 °C in air.

In XRF, an x-ray irradiates the sample, and the elements present emit fluorescent x-ray radiation, which is characteristic for each element. A quantitative analysis is possible by measuring the intensities of the emitted energies (Brouwer, 2006). The whole rock results have been plotted in an A/CNK – A/NK plot after Shand (1943) and a TAS diagram after Cox et al. 1979 using GCDkit 5.0 in R 3.4.3 (Janoušek *et al.*, 2015). The whole rock result can be found in table B.1.

5.2 Scanning electron microscope

Energy Dispersive X-ray Spectroscopy (EDS) was conducted at the Department of Geosciences at the University of Oslo with the scanning electron microscope (SEM) using a Hitachi SU5000 Scanning Electron Microscope, equipped with a Bruker XFlash 630 detector. The instrument was used to qualitatively identify accessory mineral phases with EDS spectra as well as taking back-scattered electron (BSE)

images used in this thesis. An acceleration voltage of 15 kV and a spot intensity of 50 was set before analysis.

5.3 Electron microprobe analysis

The electron microprobe (EMP) is used for chemical analysis of solids materials at small scales. The schematic cross section of the electron microprobe is shown in figure 5.1. The electron source consists of a tungsten filament which is heated to the point where it starts to emit electrons. The electrons then pass through the electromagnetic lenses, which focuses the electrons to the sample. The electron beam interacts with the sample and has enough energy to excite electrons in an atom within the sample, resulting in both electrons reflected from the incident electron beam and ejected from the sample as well as characteristic x- rays from each element (Reed, 2005). The electron beam will, in principle not damage the sample, making it possible to reanalyze the same materials.

X-rays are generated when an inner-shell electron is ejected from its orbit, leaving a vacancy. A higher-shell electron falls into the vacancy with lower energy and sheds the energy difference. This energy is the quantized x-rays and is characteristic of the element, making identification possible. (Reed, 2005). The backscattered electron (BSE) image represents the average atomic number within the samples where lighter areas have a higher atomic number and higher back scatting power. Dark spots have lower atomic numbers and do not reflect as many electrons.

In the electron microprobe, a variety of detectors are used to collect the x-rays and electrons emitted from the sample. The microprobe used in this study is equipped with a wavelength dispersive spectroscopy (WDS) and an energy dispersive spectroscopy (EDS). WDS is used for quantitative analysis, giving the wt.% of each element in the sample. EDS is set up for semi-quantitative analysis, however, the EDS was only used qualitatively to produce EDS spectra for the minerals of interest. WDS and EDS are complementary to each other. However, WDS has significantly higher spectral resolution and quantitative potential.

The electron microprobe analysis was performed at the Department of Geoscience at the University of Oslo, using a Camera SX100 instrument fitted with 5 WDS spectrometers and an SSD EDS detector from Bruker.

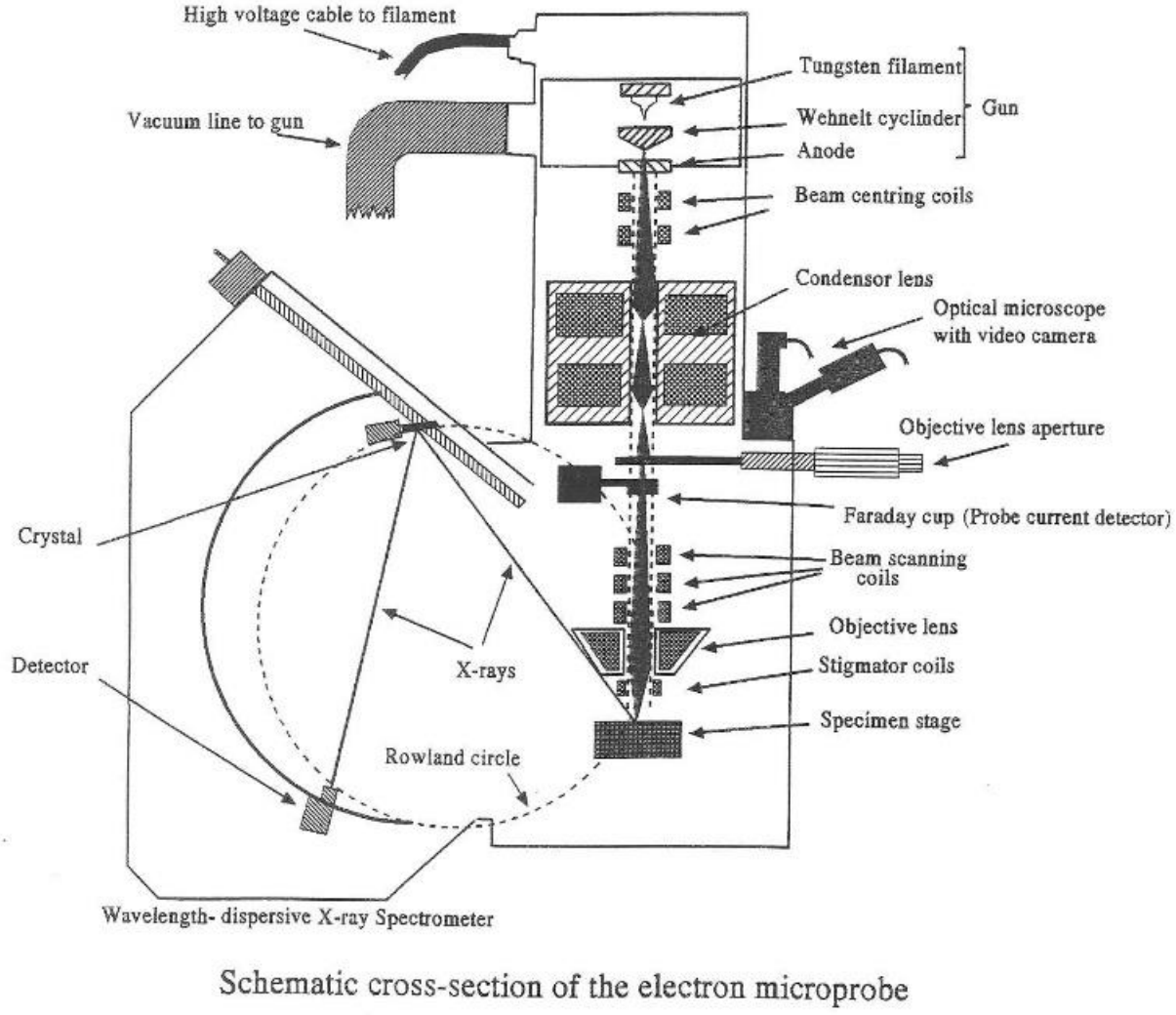

Figure 5.1: *The internal structure of an electron microprobe instrument. Figure from Reed (2005)*

The thin sections were coated with a carbon film before analysis to avoid charging of the sample surface. An accelerating voltage of 15 kV and a beam current of 15 nA were set before the analysis. An electron beam focus of 0.1 μm diameter was set, giving an excitation volume of 1-2 μm^3. Counting time was 10s on peak and 5s on each of the two background positions. WDS analysis was used to analyze major element concentrations in individual phases such as pyroxenes and amphiboles. EDS-spectra has also been acquired using the EMP to qualitatively identify the elements present in accessory minerals. The optical system of the microprobe was used to identify areas of interest within the thin section sample before the BSE images were acquired to precisely determine the best points for analysis. Zonation of pyroxenes was of particular interest in this study, which was best identified using

BSE images.

The calibration standards and x-ray lines used used were wollastonite (Si Kα, Ca Kα), Al_2O_3 (Al Kα) , pyrophanite (Ti Kα ,Mn Kα), Fe metal (Fe Kα), MgO (Mg Kα) orthoclase (K Kα), albite (Na Kα), Monastery Mine zircon (Zr Lα), Nb metal (Nb Lα), Cr_2O_3 (Cr Kα) $BaSO_4$(Ba Lβ). $SrSiO_3$ glass (Sr Lα) was used as a calibration standard. Matrix corrections were according to the PAP procedure (Pouchou & Pichoir, 1984). Na and K were analyzed first. This is important as the minerals in the sample are high Na-minerals, and the lighter elements like Na can easily migrate away from the beam, giving incorrect Na values. Relative uncertainties (2σ) for major elements (concentration$\geq$ 5 wt%) were 0.5–2% for Si, Ti, Al, Ca, Na, K, 1–3% for Fe, Mn and 2–10% for Zr (Andersen *et al.*, 2018). The disadvantage of the EMP is that it cannot detect hydrogen (H), Helium (He) and lithium (Li), and quantitative analysis if the lightest elements Be to O and in part F, is quite challenging. This means that OH groups and H_2O within minerals are not detected, so water-rich minerals will not sum up to 100 wt.% (Reed, 2005).

5.4 Quadrupole laser ablation inductively coupled plasma mass spectrometry

The trace element analysis was performed by quadrupole laser ablation inductively coupled plasma mass spectrometry (QLA-ICP-MS) at the Department of Geoscience, University of Oslo. The Bruker Aurora M90 Elite quadruple mass spectrometer is equipped with a CETAC LSX-213 G2 +Nd:YAG laser microprobe. The laser is controlled in the program DigiLaz G2. Glitter (Griffin, 2008) is used for selection of integration and background intervals as well as chondrite normalization and element quantification. The chondrite normalization values in Glitter are from Barrat *et al.* (2012). This thesis, however, uses the un-normalized ppm results from the Bruker Aurora and is plotted in GCDkit (Janoušek *et al.*, 2015) which uses the chondrite normalization after Anders & Grevesse (1989).

The QLA-ICPMS irradiates the sample surface with a focused laser beam to generate aerosols, which are further transported into the plasma chamber by helium gas. The plasma is argon gas which is heated to 6000-7000K. At this temperature, there is sufficient energy to remove electrons, which generates ions. After the sample has been ionized, it is transported through the interface region to the mass spectrometer. The interface transports the ions efficiently, consistently and with electrical integrity from the plasma. From the interface region, the electrons are transported to the ion optics. The function of the ion optics system is to bring ions

from the hostile environment of the plasma to the mass separation device (Thomas, 2001). The ions are further focused into the mass analyzer by an ion mirror. The ion mirror is a special feature of the Bruker Aurora and the ion mirror has a 90° deflection of the beam to prevent photons from the plasma from entering the mass analyzer, as well as neutral atoms and molecules which would result in background noise. The 90 ° deflection also keeps a maximum of positive ions. Other instruments do not focus the ions with this technology, and thus loose sensitivity.

The mass separation device uses a quadrupole mass filter technology to separate the ions of interest. The mass analyzer is maintained at vacuum at approximately 10^{-6} Torr by a turbomolecular pump. The ions are separated by their mass to charge ratio. The quadrupole consists of four cylindrical metallic rods of the same length and diameter. Two pairs of rods are kept at opposite high voltage and superpowered by oscillating radiofrequency potential on each pair. Ions of selected mass can pass through the rods to the detector, while others are ejected from the quadrupole mass analyzer. The scanning process is then repeated for another analyte at an entirely different mass to charge ratio until all the analytes in a multielement analyte have been measured (Thomas, 2001).

The ions emerging from the mass analyzer are detected by an all-digital electron multiplier. In the Bruker aurora M90 ICP-MS instrument, the detector is an all digital, discrete dynode electron multiplier (DDEM). The Bruker aurora M90 has a selective attenuation factor. Attenuation makes the detector less sensitive so that higher count rates can be measured and enables count rates of 10^9. The auto attenuation has a wide calibration range with the lowest possible detection limit. When the detector signal is low, the attenuation will automatically be turned off by the software. This results in the highest possible sensitivities for analyses at a low concentration level which results in the lowest detection limit.

Results

6.1 Petrography and SEM results

6.1.1 Introduction: definition of groups

The thin section samples have been subdivided into seven groups for the petrological descriptions (table 6.1), where group 1-4 are samples collected from the riverbed and group 5-7 are from the boulders. The grouping is based on their petrological similarities in thin section and hand specimen. The results from the major and rare earth element analyses contribute to this grouping of the samples. Scanned images of the seventeen thin sections for further overview can be found in appendix C. The mineral abundance in percent in the petrographic descriptions are estimated values. The scanning electron microscope (SEM) has been used to identify accessory mineral phases, and the occurrences of these minerals are presented in table 6.2 and their EDS-spectra of the identified accessory minerals are presented in appendix A.

Table 6.1: *Individual groups with short petrological descriptions.*

Group	Groupe name	Description	Compaired to Lurie's definitions
1: MEPB60, 61 and 63	Tinguaite	Fine grained flow-foliated tinguaite	Tinguaite
2: MEPB62 and 64	Foyaite -I	Coarse grained unfoliated nepheline syenites.	Possibly resemble the Ledig Foyaite.
3: MEPB65 and 68	Foayite-II	Medium grained foliated nepheline syenite.	Lujavrite subgroup
4: MEPB66 and 67	Foyaite-III	Sodalite free, foliated nepheline syenites	Lujavrite subgroup
5: MEPB70 and 71	Foyaite-IV	Unfoliated nepheline syenite dominated by perthitic feldspar aligning in two directions with an angle to each other	Normal Green Foyaite
6: MEPB72 and 73	Foyaite-V	Coarse grained unfoliated nepheline syenites with high content of astrophyllite	Normal Green Foyaite
7: MEPB69 and 74-76	Foyaite-VI	Coarse grained unfoliated nepheline syenites with low content of astrophyllite. MEPB75 is included in this group but has high astrophyllite content.	Normal Green Foyaite

6.1.2 The individual minerals

The rocks in the Pilanesberg Complex in part contain some relatively unusual minerals. It is, therefore, necessary first to explain these features of the common and not-so-common minerals before going into the features of the rock groups.

Nepheline

Nepheline is the predominant feldspathoid in all samples. However, the crystal size and content vary significantly between the samples. The Green Foyaites collected

from the boulders (group 5-7) generally have higher nepheline content as well as larger (up to 5 mm in diameter) grain size than the samples collected from the riverbed. Primary nepheline is early crystalized and mostly euhedral. The crystal form can be limited to subhedral due to earlier formed feldspar (figure 6.1 C). Secondary nepheline is smaller ($< 1mm$) and subhedral with its shape controlled by the available space. Secondary nepheline, sodalite, and zeolite group minerals can together partially-or-completely replace primary nepheline grains (figure 6.1 F). These observations are based on the SEM analysis of the smaller secondary grains at the grain boundaries. Sodalite and nepheline occur as inclusions in unaltered poikilitic clinopyroxene-I crystals. In PPL nepheline are colorless/cloudy, with negative-to-low-positive relief. In XPL, the nephelines show first order gray interference color (δ=0.005) and the extinction angle is parallel to the one visible cleavage in {001}-axis. The interference figure of nepheline is uniaxial negative, and nepheline has a positive sign of elongation on the {001} cleavage.

Sodalite

Sodalite occurs as a primary mineral and as a replacement after nepheline. Sodalite never makes up more than a few percents in the samples. Primary sodalite is mostly subhedral, and their shape is controlled by the interstitial space available. As with the nepheline, the Green Foyaites collected from the boulders have higher sodalite content and larger grain size (up to 5 mm in diameter) than in the samples from the riverbed. Sodalite also occurs as a secondary replacement product after nepheline (figure 6.1 F). Sodalite is colorless in PPL and is isotropic in XPL (figure 6.1 C). Sodalite is fluorescent and displays a bright orange color when subjected to long-wave ultraviolet light. Sodalite is present in variable amounts in all groups except for group 4 samples where sodalite is absent. Sodalite has moderate negative relief and has lower relief than nepheline.

Feldspars

The feldspars are mostly perthitic with varying albite (Ab) and orthoclase (Or) composition. Albite (Ab) has a higher refractive index (RI) than orthoclase (Or), which is used to estimate the average relative abundance of the two exsolved endmember components Or/Ab in the feldspars in each sample. The exsolved feldspars generally have higher orthoclase composition, however, single grains of anti-perthite are found (figure 6.1) The orthoclase is colorless in PPL with occurring cloudy light-brown patches. The perthitic feldspars are colorless. The feldspars have moderate positive relief with an euhedral columnar shape. Carlsbad twinning is common amongst the

orthoclase grains in group one samples. The feldspars have a perfect cleavage along the c-axis and one good cleavage perpendicular to this. The grains have a biaxial interference figure, however fuzzy isogyres makes it difficult to estimate a 2V angle.

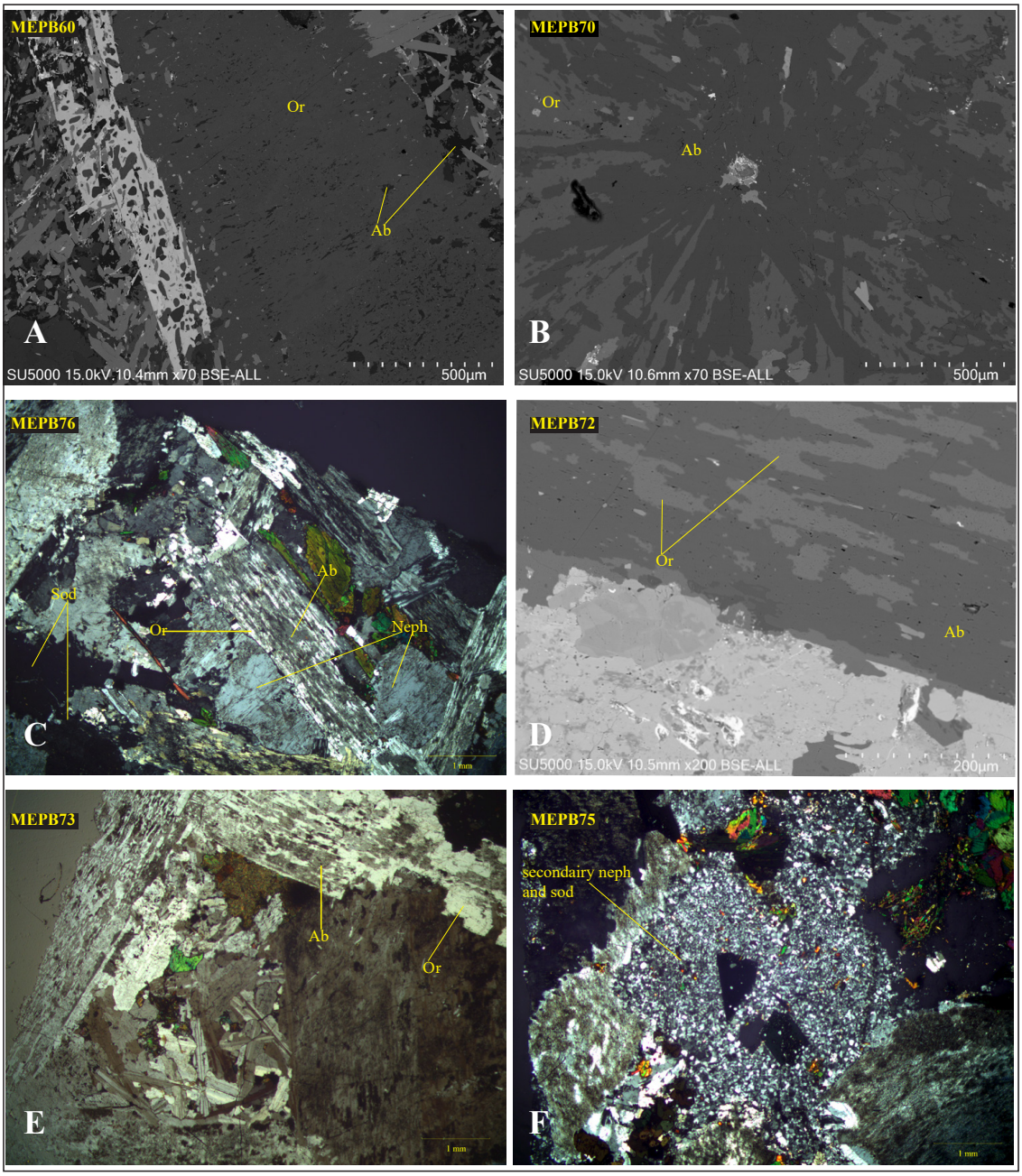

Figure 6.1: *A) orthoclase grain in the flow-foliated MEPB60 sample, containing small amounts of albite. Albite also occurs in between the orthoclase and clinopyroxenes. B) Radiating perthitic feldspar in MEPB70. C) Sample MEPB76 with primary nepheline and sodalite amongst perthitic feldspar. D) Anti-perthite ($Or_{40}Ab_{60}$). E) Secondary radiating feldspar cluster surrounded by perthitic feldspar. F) Full replacement of primary nepheline to secondary sodalite and nepheline.*

Clinopyroxene

Clinopyroxene is the main mafic mineral and occurs as four distinct textural generations. Clinopyroxene-I occurs as green euhedral prisms that poikilitically encloses nepheline and sodalite (figure 6.2 A). Later generations of acicular clinopyroxene (cpx-III) replace Clinopyroxene-I. Cpx-I have the largest grain size of the clinopyroxene-generations and can be up to 5 mm along the c-axis. Clinopyroxene-II have a slender prismatic habit. Cpx-III occurs as smaller acicular crystals and are primarily restricted to the samples collected from the riverbed (figure 6.2 D). The samples from the boulders, however, have clinopyroxenes which begin to display the characteristics of cpx-III. Cpx-IV occurs as small inclusions with an acicular habit in feldspathoids and feldspars.

Judging by the textural relationships, cpx-I, cpx-II and cpx-IV are considered as primary magmatic pyroxenes, while cpx-III are late to post-magmatic. Cpx-II frequently displays zonation, from a deep-moss green core to a lighter rim (figure 6.2 C). The post-magmatic varieties have no observed color differences. All clinopyroxene generations have two distinct cleavages with 90° angle to each other. The clinopyroxenes have moderate to high positive relief and are pleochroic from light yellowish-green in {001} to forest green in {010}. In XPL the clinopyroxenes have nearly straight extinction in their longest direction, with a positive sign of elongation. The interference figure is biaxial positive with high 2V angle suggesting aegirine composition. Birefringence is variable, but usually within second-order interference color.

Amphibole

The amphiboles are identified in both the samples collected from the riverbed and those collected from the boulders. The amphiboles are, however, far more common in the boulder-samples. The amphiboles in the samples from the riverbed have a sea-green color (figure 6.2 D), while the amphibole in the boulder-samples is dark brownish-green. Both amphiboles have moderate to high relief in PPL and are highly pleochroic. The amphibole in the samples from the riverbed is pleochroic from seaweed-green in {001} to sea-green in {010}, while the amphibole from the boulder-samples varies between brown in {001} to brownish-green in {010}. Two prominent cleavages can be observed 120/60° to each other in both varieties. The grains have variations in birefringence but are generally within the second order interference color.

Biotite

The biotite has a deep brown color, with moderate relief in PPL. The biotite is subhedral with tabular crystal shape with one distinct cleavage along the c-axis. The grains are deeply pleochroic, from dark brown in {010} to light yellow/brown in {001}. The interference figure is pseudo-uniaxial, and the interference color is within the fourth order.

Sphalerite

Sphalerite is a common accessory mineral in both the foliated and unfoliated samples. They are reddish-brown with high positive relief (figure 6.2 D). Sphalerite is isotropic.

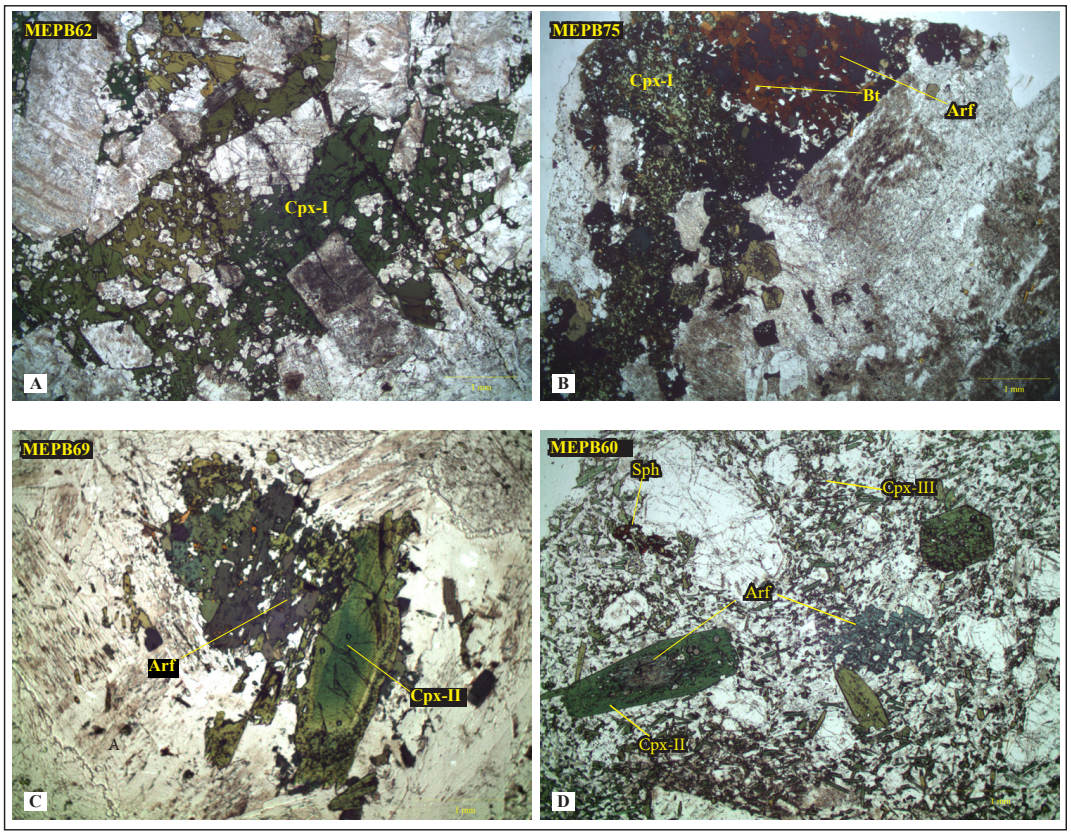

Figure 6.2: *A) Poikilitic clinopyroxene-I in MEPB62 enclosing nepheline and sodalite. B) Clinopyroxene-I which is extensively replaced by amphibole. The amphibole is overgrown by laths of biotite. C) Zoned clinopyroxene-II in MEPB69, with arfvedsonite overgrowing clinopyroxene. D) Clinopyroxene-II and III in a flow-foliated tinguaite vein. Amphibole occurs as a relict phase within cpx-II and as a primary phase interstellar cpx-III in the fine-grained matrix. Sphalerite occurs amongst the cpx-III.*

Astrophyllite

Astrophyllite has a deep honey-yellow color in PPL with high positive relief (figure 6.3 A and B). The crystals are mostly stubby prisms which are elongated along the c-axis with one clear cleavage along this axis. The astrophyllite is highly pleochroic from honey yellow in {001} to light yellow in {010}. The extinction in XPL is parallel to the cleavage and astrophyllite has second order interference colors (δ=0.030). The interference figure shows that the crystals are biaxial positive.

Lorenzenite

The lorenzenite occurs as poikilitic euhedral grains or as clusters of secondary acicular needles after rinkite (figure 6.3 C-F). The larger lorenzenite is weakly-yellow with weak pleochroism and have one good cleavage in {010}. The needle-like crystals are almost colorless and display no pleochroism. The lorenzenite has very high surface relief, and the interference figure shows that they are biaxial negative, with the 2V angle around 40°.

Rinkite

The rinkite is orange-yellow and is strongly pleochroic. The interference figure of rinkite is biaxial negative, and rinkite has birefringence within the second order.

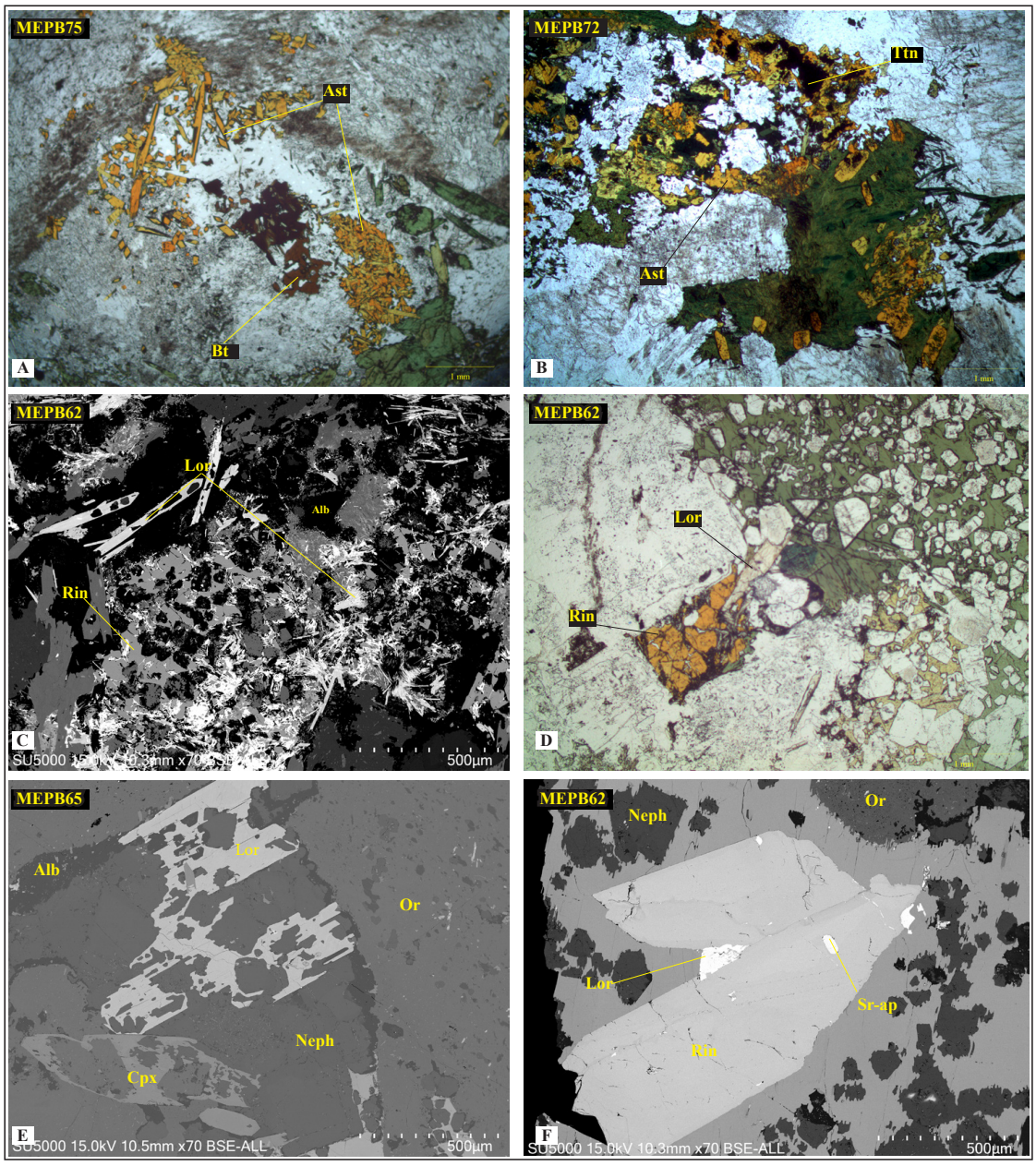

Figure 6.3: *A) Columnar astrophyllites with biotite laths interstitial to nephelines and feldspars. B) Astrophyllite epitaxially overgrowing clinopyroxenes, with titanite overgrowing the astrophyllite. C) BSE image of poikilitic rinkite and acicular lorenzenite crystals. D) Image of fractured rinkite with associated lorenzenite. E) BSE image of poikilitic euhedral lorenzenite with primary nepheline, orthoclase and albite. F) BSE image of rinkite crystals within poikilitic clinopyroxene-I, with an inclusion of strontium-apatite. A small lorenzenite crystal lies between the two rinkite crystals.*

Wöhlerite

Wöhlerite group minerals are a common accessory mineral and are found as euhedral prismatic to columnar crystals. They have high relief and are nearly colorless to weakly-yellow (figure 6.4 A). They are within the second order interference color and have high relief.

Fluorite

Fluorite is a common accessory mineral and occurs as anhedral to subhedral crystals with an undefined "smeared" grain boundary (figure 6.4 A). The fluorite is violet in PPL, with moderate negative relief and is isotropic.

Apatite

Apatite group minerals are common accessory phases which shows a wide variation between primary fluorapatite through strontium apatite and ultimately to britholite-(Ce) identified by SEM-spectra (figure 6.4 B and C). The apatite is colorless in PPL with high positive relief. The crystals have low first order interference color (δ=0.005)

Eudialyte

Eudialyte is severely altered and range between bright pink to almost colorless (figure 6.4 C). The pink samples have moderate relief and are strongly pleochroic. Birefringence ranges within the first order interference color.

Pectolite

Pectolite group minerals can be up to 0.25 mm. They are colorless with moderate to high relief. They are distinctive due to their bright third order interference color (δ=0.037) (figure 6.4 D).

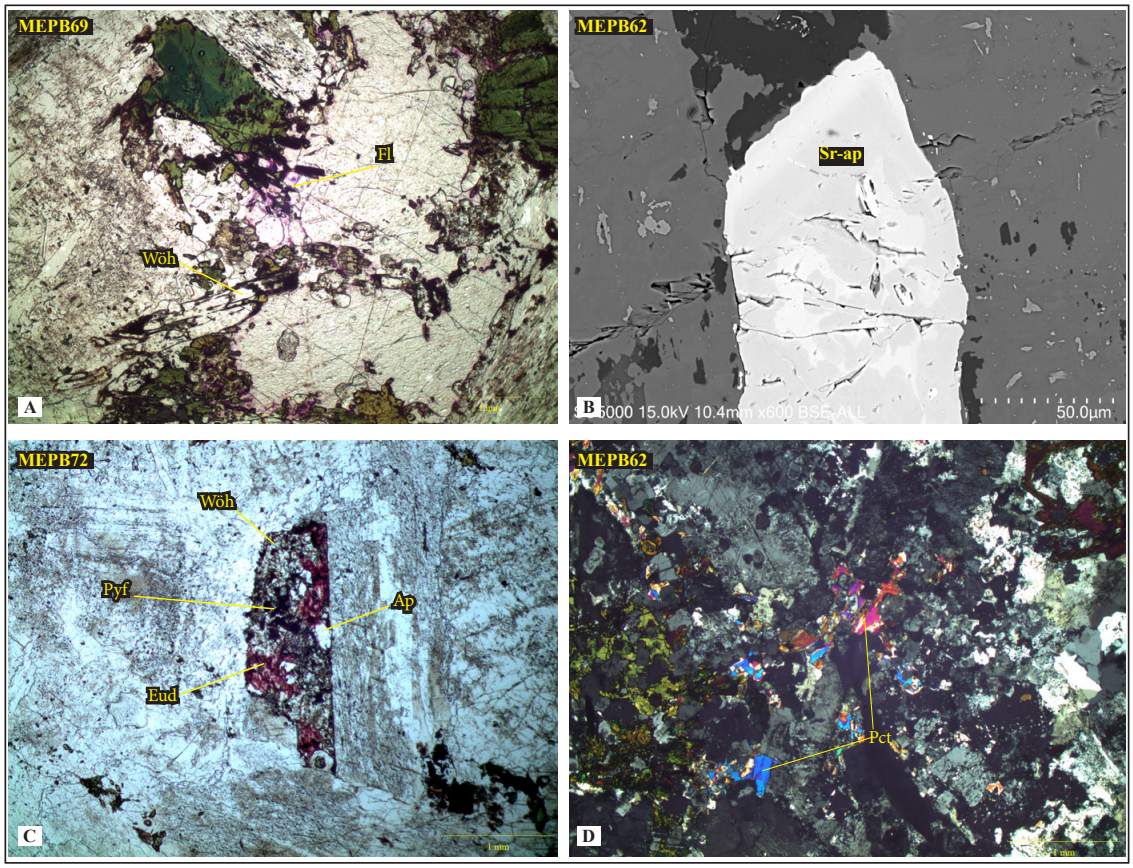

Figure 6.4: *A) Euhedral wöhlerite crystals with high relief with violet fluorite. B) BSE image of strontium-apatite C) Altered eudialyte crystal replaced by wöhlerite group minerals and pyrrhotite, with fluorapatite lying suboffitically in the altered eudialyte. D) XPL image of pectolite group minerals.*

Other minerals

Numerous less-common minerals occur at <1% and were only identified using the SEM. EDS spectra of these minerals can be seen in appendix A. The occurrence of the less common minerals within the samples are presented in table 6.2 and their theoretical formulas are shown in table 1 in the glossary.

Table 6.2: *Comprehensive table of minerals observed from each analysed sample.*

	MEPB60	MEPB61	MEPB62	MEPB63	MEPB64	MEPB65	MEPB66	MEPB67	MEPB68	MEPB69	MEPB70	MEPB71	MEPB72	MEPB73	MEPB74	MEPB75	MEPB76
Ancylite-(Ce)	x			x		x											x
Apatite											x	x	x	x	x	x	x
Astrophyllite										x	x	x	x	x	x	x	x
Burbankite gr.				x													
Celestine													x				
Diaspore																x	
Eudialyte	x	x		x		x				x	x	x	x				x
Fluorite	x	x		x		x		x	x		x				x		
Hilairite/ Catapleiite	x	x		x	x	x		x			x						
Jinshajiangite	x							x	x		x						
Lorenzenite	x	x	x	x	x	x	x	x	x								
Mn-oxide								x									
Monazite																x	
Parisite-(Ce)								x						x			
Pectolite gr.	x	x		x	x	x			x								
Phyrophanite													x			x	x
Pyrochlor gr.											x					x	
Pyrrhotite					x												
REE-carbonate																x	
Rinkite-(Ce)	x	x	x	x	x	x	x		x	x		x	x		x	x	x
Rosenbuschite	x				x							x	x				
Sphalerite		x	x						x		x	x	x				
Strontium apatite			x		x		x		x								
Strontium carbonate							x										
Thorite											x		x	x		x	
Titanite								x					x				x
Tritomite-(Y)						x										x	
Wöhlerite gr.					x	x			x	x					x	x	x
Zircon											x			x		x	
Unknown 1																x	
Unknown 2																x	
Unknown 3																x	

6.1.3 The samples

The samples have been subdivided into 7 groups based on their petrographic similarities in thin section, such as texture and mineral occurrence (See table 6.1). These groups have further been related to previous descriptions of the Green Foyaites types by Lurie (2004) and Retief (1963).

Group 1: Tinguaite (MEPB60, 61 and 63)

Tinguaite is a fine-grained rock of nepheline syenite composition with a distinctive texture of aegirine needles (Le Maitre *et al.*, 2002). In the Pilanesberg Complex, the term is used as a general term for fine-grained nepheline syenite sheets, dikes, and veins. The samples in group 1 are very similar both in thin section and in hand specimen, and they are collected from the same tinguaite vein.

The texture is dominated by euhedral crystals of clinopyroxene-III (50%), arranged as flow-aligned aggregates. These crystals are no longer than 0.25 mm and make up the fine grained-matrix together with sub-microscopic nepheline and sodalite. Eudialyte is occasionally found as cement between cpx-III and subhedral orthoclase crystals in the matrix (figure 6.5 A). A lesser amount (ca. 5%) of the pyroxenes are cpx-II. Nepheline is not abundant and makes up <5%. Early crystallized nepheline phenocrysts is rare but is euhedral crystals but can reach up to 4.5 mm in diameter. Late magmatic nepheline and sodalite are subhedral and are distributed throughout the samples, and can partially replace primary nepheline grains at the rim of the crystal. Early magmatic phenocrysts of orthoclase (20%) occur as long tabular grains up to 6 mm in length, which are primarily aligned with the flow direction (figure 6.5 B). The orthoclase contains minor amounts (<5%) of exsolved albite, orientated perpendicular to the cleavage. Pure albite is found to fill interstitial space between the minerals present. Poikilitic subhedral magnesio-arfvedsonite (1%) is extensively replaced by secondary cpx-III. The amphibole is also found as a relict phase within cpx-II.

During SEM-EDS analysis, the samples MEPB60 and MEPB63 were found to contain a large portion of accessory minerals which occur together in clusters. The clusters contain minerals such as pectolite group minerals, hilairite, burbankite group minerals, jinshajiangite, ancylite-(Ce), fluorite, rosenbuschite, rinkite and lorenzenite (figure 6.5 C and D). The clusters are most likely pseudomorphs, however, it is difficult to determine what mineral they replace.

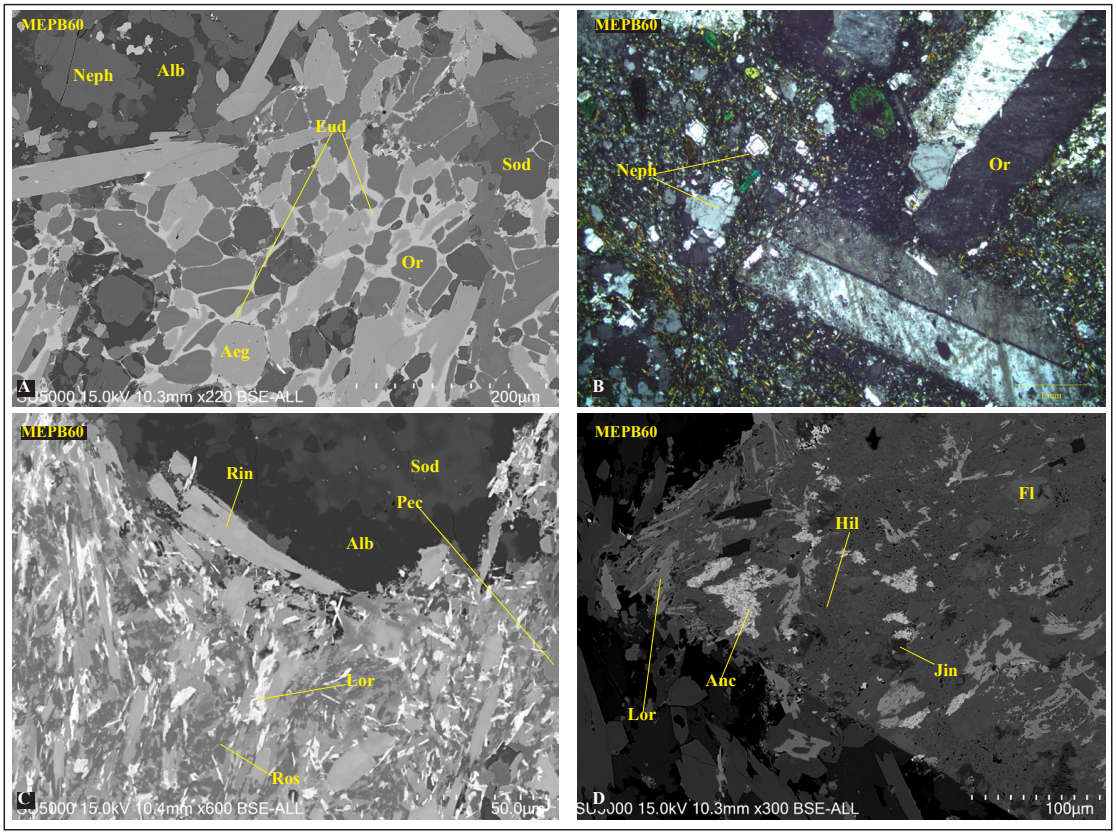

Figure 6.5: *A) Eudialyte occuring as cement between aegirine and orthoclase. B) Secondary nepheline in the fine-grained flow-foliated matrix. C and D) Mineral clusters of accessory minerals.*

Group 2: Foyaite-I (MEPB62 and 64)

This group contains medium-to-coarse grained unfoliated nepheline syenites, which are the only samples that have the most typical and easily recognizable poikilitic clinopyroxene-I. MEPB62 is coarser grained than MEPB64, with euhedral clinopyroxene-I up to 5 mm in length. Cpx-I is the main mafic constituent (50%) which poikilitically encloses nepheline and sodalite (see mineral description). Minor amounts (5%) of the clinopyroxene in MEPB62 are late-magmatic acicular shaped cpx-III crystals without inclusions. Primary nepheline makes up 15% of the sample and is commonly fractured. The nepheline is equidimensional with a slight elongation and is up to 4.5 mm long. The feldspars (15%) are mostly pure orthoclase and have a euhedral columnar crystal habit and are up to 6 mm along the c-axis. The vast majority is however 4 mm long. Rinkite (10%) is the second most abundant colored mineral and shares grain boundaries with clinopyroxene-I or lies interstitially between feldspar crystals. The rinkite is commonly fractured with lorenzenite filling the spacing. Acicular lorenzenite replaces the larger rinkite epitaxially.

MEPB64 has a similar mineral assemblage to MEPB62 but is medium grained. The size of the clinopyroxenes are smaller and makes up less of the sample than in MEMPB62 (<2.5 mm; 30%) and about half of the clinopyroxene crystals have acicular habit (cpx-III), while the rest are poikilitic clinopyroxene-I. The acicular clinopyroxene-III form radial structures suggesting that the rock matches the description of Ledig Foyaite by Lurie (2004). Late magmatic to secondary sodalite and nepheline are heterogeneously distributed in the sample and makes up a large portion of the colorless phases (15%). Primary nephelines (<3%) are no larger than 3 mm while late magmatic to secondary sodalite and nepheline are <0.1 mm. The feldspar (40%) ranges from pure orthoclase to perthitic feldspar ($Or_{90}Ab_{10}$). The feldspars display simple twinning. Rinkite and lorenzenite (5%) are primarily restricted to two clusters and occur together with cpx-I.

Group 3: Foyaite-II (MEPB65 and 68)

This group is dominated by columnar clinopyroxene-II up to 4 mm along the c-axis. MEPB65 generally has larger grain sizes, and large Carlsbad-twinned feldspar laths can be up to 9 mm (20%). The cpx-II makes up about 30% of the sample and has a definitive weak flow-foliated trend. The feldspars are oriented with this foliation. Primary euhedral phenocryst of nepheline makes up less than 5% of the sample. Late-magmatic nepheline and sodalite (<0.1 mm) are distributed heterogeneously interstitially to the cpx and feldspars. The clinopyroxene replaces arfvedsonite (<1%). Sample MEPB65 has one circular aggregate consisting of submicroscopic ancylite-(Ce), pectolite group minerals, lorenzenite, and whölerite group minerals. A rim of sodalite surrounds this circular cluster of minerals. The cluster in XPL has bright second-order birefringence colors, most likely due to the pectolite group minerals, zeolites and ancylite-(Ce) (figure 6.6). This cluster is likely another pseudomorph.

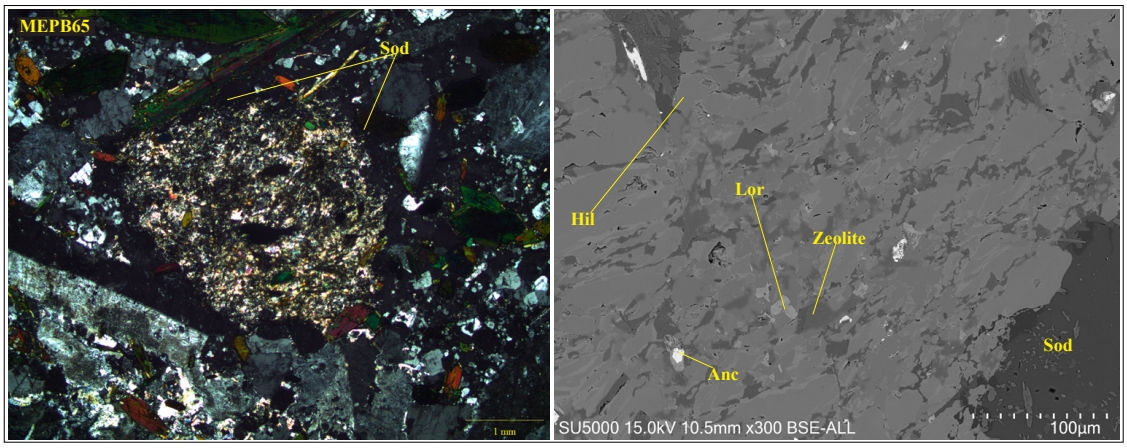

Figure 6.6: *XPL and BSE images of circular mineral cluster containing accessory minerals*

The clinopyroxenes-II crystals in MEPB68 are smaller. Clinopyroxene dominates the sample (50%), with a clearer flow-foliation than MEPB65. Sodalite and nepheline content matches sample MEPB65. The orthoclase crystals are no longer than 5 mm. MEPB68 has fewer arfvedsonite grains as the clinopyroxene replaces the amphibole. Rinkite, wöhlerite, and pectolite occur as small sub-microscopic accessory minerals throughout the sample, and were identified using SEM. Lorenzenite (<1%) is found as a 1 mm long euhedral crystal.

Group 4: Foyaite-III (MEPB66 and 67)

This group differs from the rest of the samples in the sense that no sodalite was found in microscope or when the samples were subjected to long-wave ultraviolet light. This group has similarities to group 3 as they are dominated by flow-foliated cpx-II aggregates. The cpx-II make up between 50-60% of the samples. Large euhedral (7.5 mm) orthoclase crystals follow the flow-foliation. Primary nepheline makes up less than 5% of the samples, and no replacement of nepheline occurs. The interstices between the orthoclase and the cpx-II are filled by pure subhedral albite. In both samples, feldspar grains have been partially-to-completely replaced by zeolite group minerals, identified by SEM-EDS analyses.

Le Maitre *et al.* (2002) defines lujavrite as a term for a melanocratic agpaitic variety of nepheline syenite rich in eudialyte, arfvedsonite, and aegirine with perthitic alkali feldspar or separate microcline and albite with a characteristic igneous lamination. Lurie (2004) further described the lujavrite as a coarse-grained nepheline syenite with a trachyoid texture. Aegirine-augite is the main constituent and occurs in dense aggregates of prismatic crystals oriented their long axis parallel to the plane of orientation, with tablets of feldspar following the orientation. This description is

consistent with foyaite-II and foyaite-III and these groups are therefore interpreted members the lujavrite subgroup within the Green Foyaite Suite.

Group 5: Foyaite-IV (MEPB70 and 71)

This group is unfoliated and dominated by euhedral perthitic feldspar aligning in two directions to each other. The angles are, however, variable. The perthitic feldspar in MEPB70 is up to 2 mm making up 60% of the sample. Perthitic feldspar also occurs as a rosette of smaller (ca 1 mm) feldspars radiating from a nucleus with thorite, fluorite, and clinopyroxene (figure 6.7). Primary subhedral nepheline and sodalite fill the space between the perthitic feldspar.

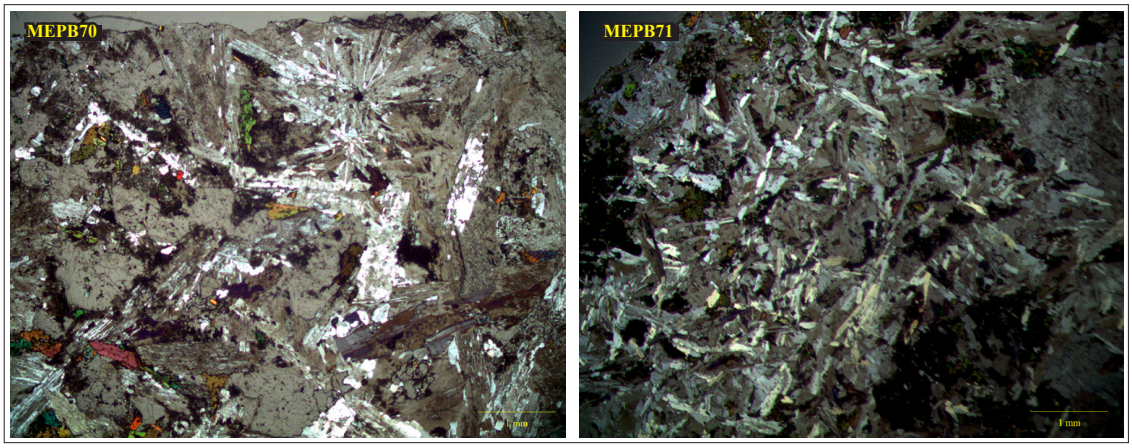

Figure 6.7: *XPL images of perthitic feldspar aligning in two directions.*

The feldspathoids (5%) are no larger than 5 mm and enclose cpx-IV. Minor (<3%) replacement of nepheline to secondary sodalite are observed at grain boundaries. The secondary replacement is subhedral and are <0.1 mm.

Zoned clinopyroxene-II is the dominant colored phase in PPL (20%) and is up to 2 mm in length. Astrophyllite (10%) and clinopyroxene cross-cut each other and appear to have crystallized simultaneously. Titanite occurs as inclusions within both the clinopyroxene and astrophyllite. The perthitic feldspar (70%) in MEPB71 is smaller than in the previous sample and averages at ca. 0.5 mm along the c-axis. One large (4 mm) euhedral perthitic feldspar (<5%: $Or_{80}Ab_{20}$) is observed in thin section. Subhedral primary nepheline and sodalite (2 mm, 3%) fill the space between the feldspars. Minor secondary replacement of nephelines occurs along grain boundaries. Arfvedsonite extensively replaces cpx-II. Titanite typically overgrows the clinopyroxene. Subhedral astrophyllite often shares grain boundaries with the clinopyroxene.

Retief (1963) described the normal Green Foyaite type as fully crystalline without igneous lamination. He further wrote that as a rule, the feldspars show no definite orientation whereas the feldspars in group 5 from this thesis have feldspars aligning in two orientations. Retief (1963) did not describe a type of Green Foyaite with feldspars in a definitive orientation, but as this group is similar in other respects to the unfoliated Green Foyaites, they will be assigned to be a part of a subgroup within the normal type Green Foyaite.

Group 6: Foyaite-V (MEPB72 and 73)

This group is unfoliated and coarse-grained. The dominant mineral is euhedral columnar (up to 9 mm) perthitic feldspar. Subhedral nepheline and sodalite (5 mm, 20%) fill the space between the feldspars. Complete replacement of nepheline grains to secondary sodalite and nepheline occurs in 10% of the nepheline crystals. In addition, most of the nepheline crystals have partial replacement to secondary sodalites and nephelines at the rim of the crystal. The primary feldspathoids contain inclusions of small (0.1 mm) cpx-IV crystals.

Arfvedsonite extensively replaces primary clinopyroxene, with the arfvedsonite crystals having inclusions of small laths of biotite and later generations of cpx-III crystals. The primary cpx-II display zonation, while the acicular cpx-III have a homogeneous composition. Clinopyroxenes together make up 20% of the sample. Astrophyllite (10%) crystallized simultaneously with the primary clinopyroxene and the astrophyllite is found by SEM-EDS analysis to be overgrown by pyrophanite. Altered eudialyte makes up 1% of the sample. The eudialyte crystals vary from colorless to bright pink. The perthitic feldspar ($Or_{60}Ab_{40}$ to $Or_{40}Ab_{60}$) in MEPB73 is generally larger than in MEPB72 and make up 60% of the sample. Clusters of secondary nepheline and sodalite replace the majority of primary nepheline. Secondary albite fills the space between the perthitic feldspars.

Group 7: Foyaite-VI (MEPB69 and 74-76)

These samples are unfoliated with perthitic feldspars as the dominant mineral phase. The perthitic feldspar range from $Or_{80}Ab_{20}$ to $Or_{60}Ab_{40}$ and can be up to 13 mm. The feldspars and feldspathoids contain numerous inclusions of small (<0.2mm) acicular pyroxene (cpx-IV). The nepheline and sodalite (ca. 20%) grains are subhedral and can reach up to 5 mm. They also fill the space between the large feldspar grains, and their crystal shape is restricted by the earlier formed feldspar. The primary nephelines are partially-to-entirely replaced by secondary nepheline and sodalite in this group of samples. The samples contain both primary cpx-II crystals

and to a lesser degree secondary cpx-III, where the primary clinopyroxenes begin to be replaced by later generations of acicular cpx-III and can be overgrown by opaque phases. The clinopyroxene is extensively replaced by poikilitic arfvedsonite which contains laths of biotite. The samples generally have <1% astrophyllite grains and are generally restricted to inclusions in the arfvedsonites. In MEPB76, pink eudialyte is a common accessory mineral (5%).

Sample MEBP75 has large orthoclase as the main feldspar with only minor amounts of perthitic feldspar ($Or_{60}Ab_{40}$). Secondary clusters of twinned plagioclase (1-2mm) are also common. This sample contains astrophyllite (10%) as euhedral tabular-to-bladed crystals with cleavage in the long direction. The astrophyllite occurs mainly in assemblages interstitial to the feldspars which is not found in the other samples. The majority of nephelines are entirely replaced by secondary sodalite and nepheline, while the other crystals only show partial replacement. A halo of high-birefringence minerals with high REE occurs around the magnesio-arfvedsonite. EDS analysis determined these minerals to be monazite, REE-carbonate, thorite, tritomite-(Y) and the three unknown minerals (table 6.2).

Group 6 and 7 contain rare Zr-bearing accessory minerals such as eudialyte and astrophyllite and have K-feldspars and albite in roughly equal amounts. According to Retief (1963), these are characteristics of the Ledig Foyaite. These samples do not have, however, radiating aegirine which the Ledig Foyaite should contain. In other respects, these groups are similar to what Retief (1963) described as the normal type Green Foyaite: *"without igneous lamination where the aegirine a have prismatic habit and are commonly zoned"*. Furthermore, Retief (1963) described the normal Green Foyaite to commonly show partial replacement of nepheline. On the basis of lacking radiating pyroxene, these groups will be categorized as a part of the subgroup within the normal Green Foyaite described by Retief (1963).

6.2 Major element geochemistry

Whole-rock major element analyses of selected Green Foyaite samples (table B.1) plot in the nepheline syenite field in the TAS classification diagram of Cox et al. (1979) (figure 6.8 B).

The samples are highly peralkaline with (Na+K)/Al between 1.11 and 1.47 (Figure 6.8 A and table B.1). SiO_2 contents vary between 49.29 and 56.97 wt.%. The peralkalinity of the samples is reflected by Na_2O content of around 9 wt.% and K_2O content of approximately 6 wt.%. The average Al_2O_3 lies around 17 wt.%, and the total iron content (Fe_2O_3) are around 5 wt.%. Sample MEPB66 (foyaite-III) has anomalous Fe_2O_3 and Al_2O_3 content, compared with the other samples, of 11 and 13 wt.% respectively. The low Al_2O_3 content in sample MEPB66 yielded the highest (Na+K)/Al value of 1.47. (Table B.1). MgO, MnO, TiO_2 and P_2O_5 contents are less than 2.17 wt.% and CaO values are <3.19 wt.%.

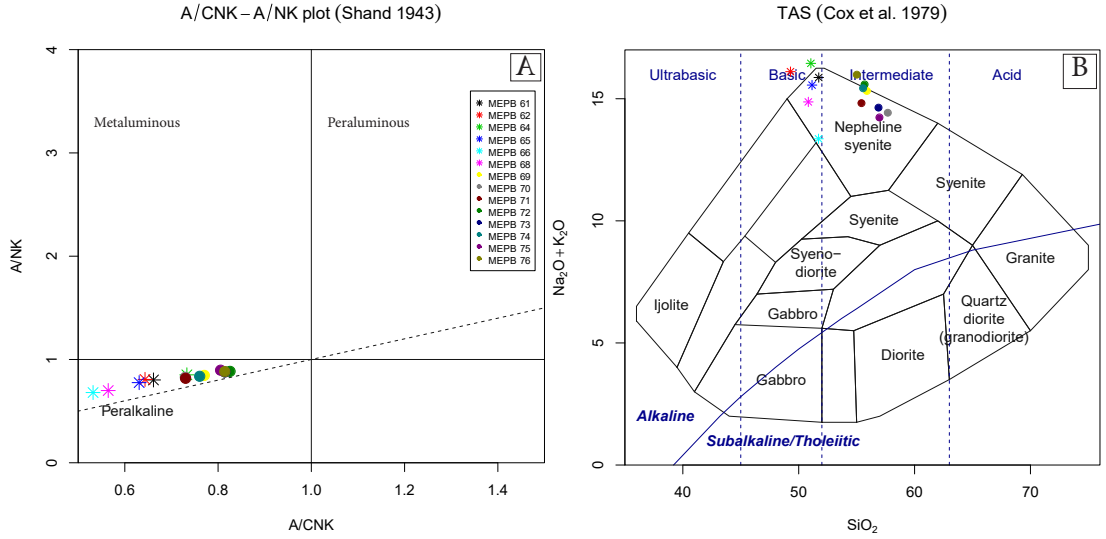

Figure 6.8: *A) peralkalinity diagram of the whole rock analyses where A/NK= $Al_2O_3/(Na_2O + K_2O)$ and A/CNK=$Al_2O_3/(CaO + Na_2O + K_2O)$ after Shand (1943). B) Total Alkali Silica (TAS) classification diagram after Cox* et al. *(1979). The stars represent the samples collected from the riverbed, and circles are samples collected from the boulders. Data plotted in GCDkit.*

The whole rock chemistry correlates with the petrographic groups, where the groups 1-4 collected by the riverbed (the tinguaites, foyaite-I to foyaite-III) have the highest (Na+K)/Al ratios between 1.24 to 1.47, while the boulder samples (group 5-7; foyaite-IV to foyaite-VI) have lower ratios between 1.11 to 1.22 (riverbed samples represented by stars and boulder samples with circles in figure 6.8 A). The boulder samples have overall higher Na_2O content, but lower K_2O and Al_2O_3, resulting

in the differences in the ratios. Furthermore, the riverbed samples plot within the basic nepheline syenite field in the TAS classification diagram after Cox *et al.* (1979), while the boulder samples are intermediate nepheline syenites (figure 6.8 B). This is matched by the riverbed samples have lower SiO_2 content between 49.29-51.71 wt.% while the boulder samples have SiO_2 content ranging from 55.02 to 57.69 wt.% (table B.1).

6.2.1 Normative mineral content

The normative mineral content (ICPW norm) of minerals were calculated in GCDkit based on the whole rock analyses with a Fe_2O_3/FeO ratio of 0.4 (table B.2). The 0.4 Fe_2O_3/FeO ratio is based on Rollinson (2014). The nepheline, orthoclase, and albite normative content have been plotted in figure 6.9 and define two groups which correlate with the locations where the samples are collected. The samples from the riverbed (the foliated samples + MEPB62 and 64) have a higher normative content of orthoclase. This correlates with the petrographic groups where the main feldspar in groups 1 to 4 (The tinguaites, foyaite-I to foyaite-III) was described to be orthoclase. Albite only occurs as small anhedral crystals which fill the space between nepheline and orthoclase. The main feldspar in the samples collected from the boulders (group 5-7; foyaite-IV to foyaite-VI) is perthitic with Or/Ab content averaging between $Or_{60}Ab_{40}$ to $Or_{40}Ab_{60}$.

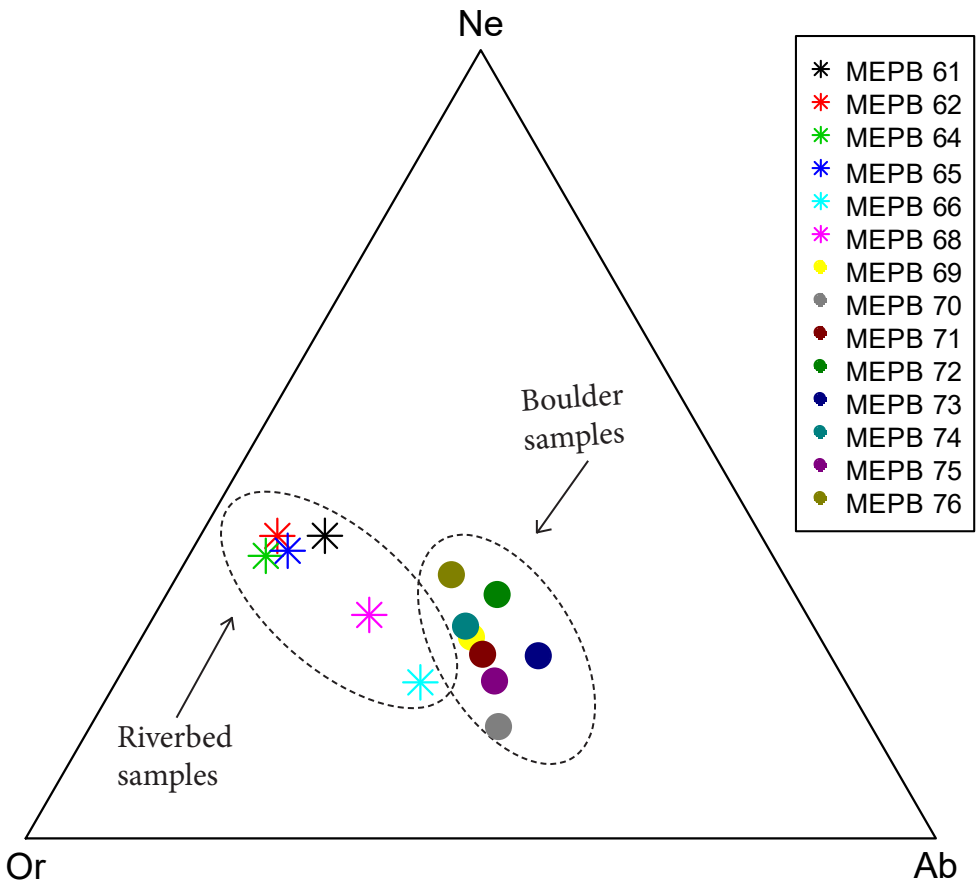

Figure 6.9: *Normative content of nepheline, orthoclase and albite in a ternary diagram. The samples define two groups: the samples collected from the riverbed represented by stars and the samples from the boulders in circles.*

6.2.2 Comparison to previous whole rock analyses of Green Foyaites

Whole-rock analyses of samples from the Pilanesberg Complex have previously been published by Andersen *et al.* (2018) and Elburg & Cawthorn (2017). Figure 6.10 is a published figure from Andersen *et al.* (2018) with added data from this thesis.

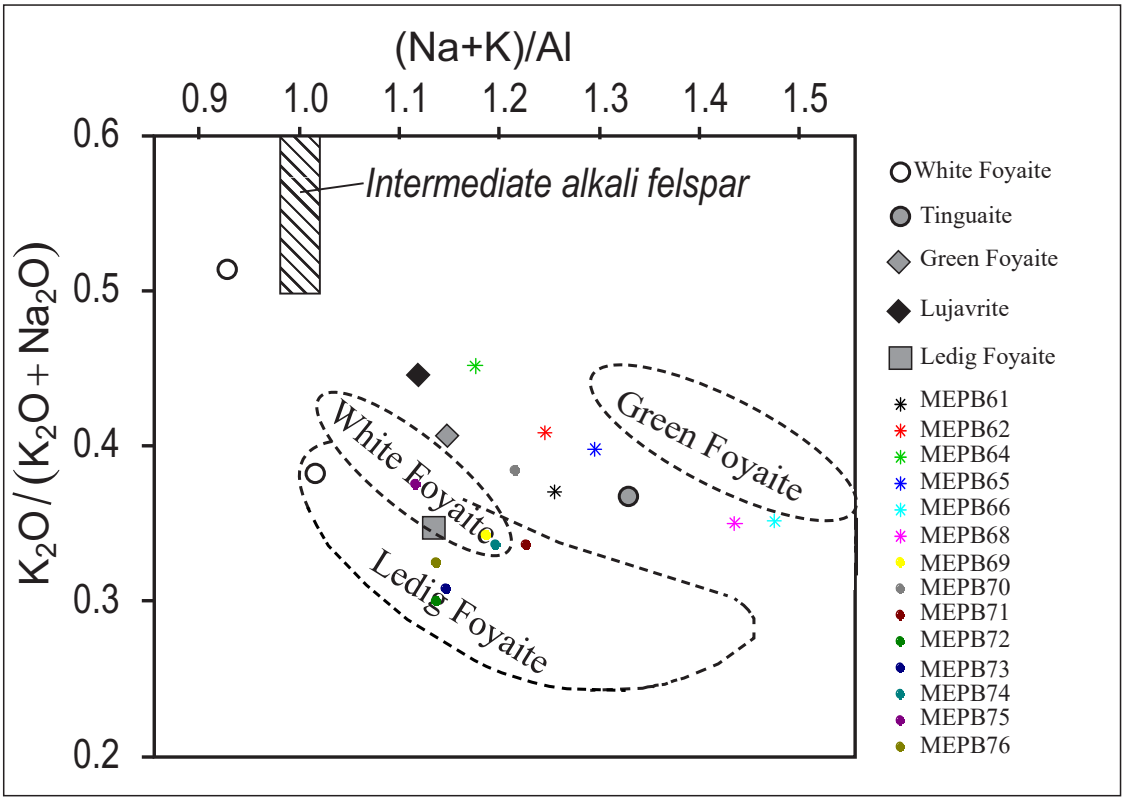

Figure 6.10: *Earlier published whole rock major element variations of White Foyaite, Green Foyaite, Ledig Foyaite, lujavrite and tinguaite from Andersen* et al. *(2018) and Elburg & Cawthorn (2017) compared to whole rock major element results produced in this thesis. The stars represent the samples collected from the riverbed, while the circles are collected from the boulders.*

The published White Foyaite, Green Foyaite, tinguaite, lujavrite and Ledig Foyaite points in figure 6.10 are plotted based on whole-rock analyses from table 1 in Elburg & Cawthorn (2017) and represent average values for the different rock types. All samples are characterized by low MgO content ranging from 0.51 and 0.87 wt.% , but relatively high total iron content between ca. 6 and 9 wt.%. The inner White Foyaite has a peralkalinity index of 0.93, whereas the outer White Foyaite, lujavrite, Ledig Foyaite, and Green Foyaite have peralkalinity idices increasing from 1.07 to

1.14. The Green Foyaite, White Foyaite, and Ledig Foyaite fields are based on data from Andersen *et al.* (2018).

The Green Foyaite samples analysed by Andersen *et al.* (2018) has high peralkalinity indices between 1.35-1.51 and $K_2O/(K_2O + Na_2O)$ between 0.35 and 0.45. The unfoliated Green Foyaites (MEPB69-76) have lower $K_2O/(K_2O + Na_2O)$ ratios and lower peralkalinity than the Green Foyaite field, which results in these samples to plot within the Ledig Foyaite and White Foyaite fields. The exception is sample MEPB70 which plot slightly higher than the other unfoliated samples. The difference in peralkalinity in these samples is reflected by lower K_2O content which averages around 5 wt.% for the unfoliated Green Foyaites versus 6 wt.% in Green Foyaites analyzed by Andersen *et al.* (2018). Furthermore, the Na_2O in the Green Foyaite averages ca. 10 wt.% in this thesis, while the Green Foyaites from Andersen *et al.* (2018) have average Na_2O values of 9.5 wt.%. The lujavrites (MEPB65-68) and tinguaite (MEPB61), on the other hand, plot close to the Green Foyaite field and the average tinguaite from Elburg & Cawthorn (2017).

6.3 Mineral chemistry: Major elements

The mineral formula of pyroxene were calculated based on four cations in the clinopyroxene formulae and the analyses vary between Aeg_{56} to Aeg_{99} (figure 6.11 and table B.3). The major element analyses of pyroxene have been plotted with respect to the pyroxene endmember compositions hedenbergite ($Hd : CaFe^{2+}Si_2O_6$), aegirine ($Aeg : NaFe^{3+}Si_2O_6$) and diopside ($Di : CaMgSi_2O_6$). The method used for endmember calculations is described in appendix D, which also include the endmembers AlTsch, Jd and ZrTiAeg. Figure 6.11 is therefore a projection from a multidimensional space into the Aeg-Hd-Di plane, which results in higher aegirine component in the plot for the analyses with a high ZrTiAeg component. All groups of pyroxenes plot within the upper triangle at approximately $< 40\%$ Hd, and for this reason, only this upper segment is shown in the figures.

6.3.1 The major elements in pyroxene of the samples collected from the riverbed

Group 1

In group one, only MEPB61 was analyzed. As described in the petrological descriptions, this sample contains cpx-II (primary) and cpx-III (secondary or late-magmatic) type pyroxenes. The analysis of cpx-II yielded values between

$Aeg_{58}Hd_{18}Di_{24}$ and $Aeg_{65}Hd_{15}Di_{20}$. Cpx-III have a higher aegirine component, from $Aeg_{68}Hd_{18}Di_{13}$ to $Aeg_{87}Hd_3Di_{10}$ (table 6.3). Furthermore, cpx-III has significantly higher titanium content. The average titanium content lies around 2 wt.% in cpx-III while the cpx-II titanium values averages 1 wt.%. This is matched by drastically lower calcium values in cpx-III, down to 3 wt.%, versus up to 10 wt.% in cpx-II. The Fe^{2+}/ Fe^{3+} ratio is higher in cpx-II than in cpx-III. Zr values are generally low, between 0.12 and 0.44 wt.%.

Group 2

The analyses of pyroxenes in this group generally plot on a linear trend and have aegirine component from $Aeg_{67}Hd_{25}Di_9$ to $Aeg_{86}Hd_7Di_6$ (figure 6.11 and table 6.3). Cpx-I (primary) generally has lower aegirine component than the acicular late magmatic clinopyroxene (cpx-III). The major element composition represents a gradual transition between the two pyroxene types. The titanium contents range between 6 wt.% and 2 wt.%. There is, however, no clear distinction between the pyroxene varieties, although the most typical cpx-I have the lowest titanium concentration.

Group 3

The variations in aegirine content are largely reflected by the zonation displayed in the cpx-II grains. Examples of this are analyses 25/1-29/1 in MEPB68 which range between Aeg_{70} and Aeg_{87} (figure 6.11). As for the previous groups, higher sodium content is correlated with higher titanium values and lower calcium (table 6.3)

Group 4

This group contains cpx-II in a flow-foliated pattern. The compositional variations in MEPB66 reflect zonation from the core to rim. The rim of the clinopyroxenes have higher sodium content and vary between Aeg_{81} to Aeg_{90} while the core ranges from Aeg_{73} to Aeg_{79} (figure 6.11). The analyses in MEPB67 have a larger range of aegirine component, between Aeg_{67} and Aeg_{95}. The titanium concentration reaches 3.5 wt.% in the rim and up to 2 wt.% in the cores. The titanium concentration in aegirine in MEPB67 follows the same trend but is generally lower. The analysis with the highest aegirine component has the lowest Ti value of 0.69 wt.%.

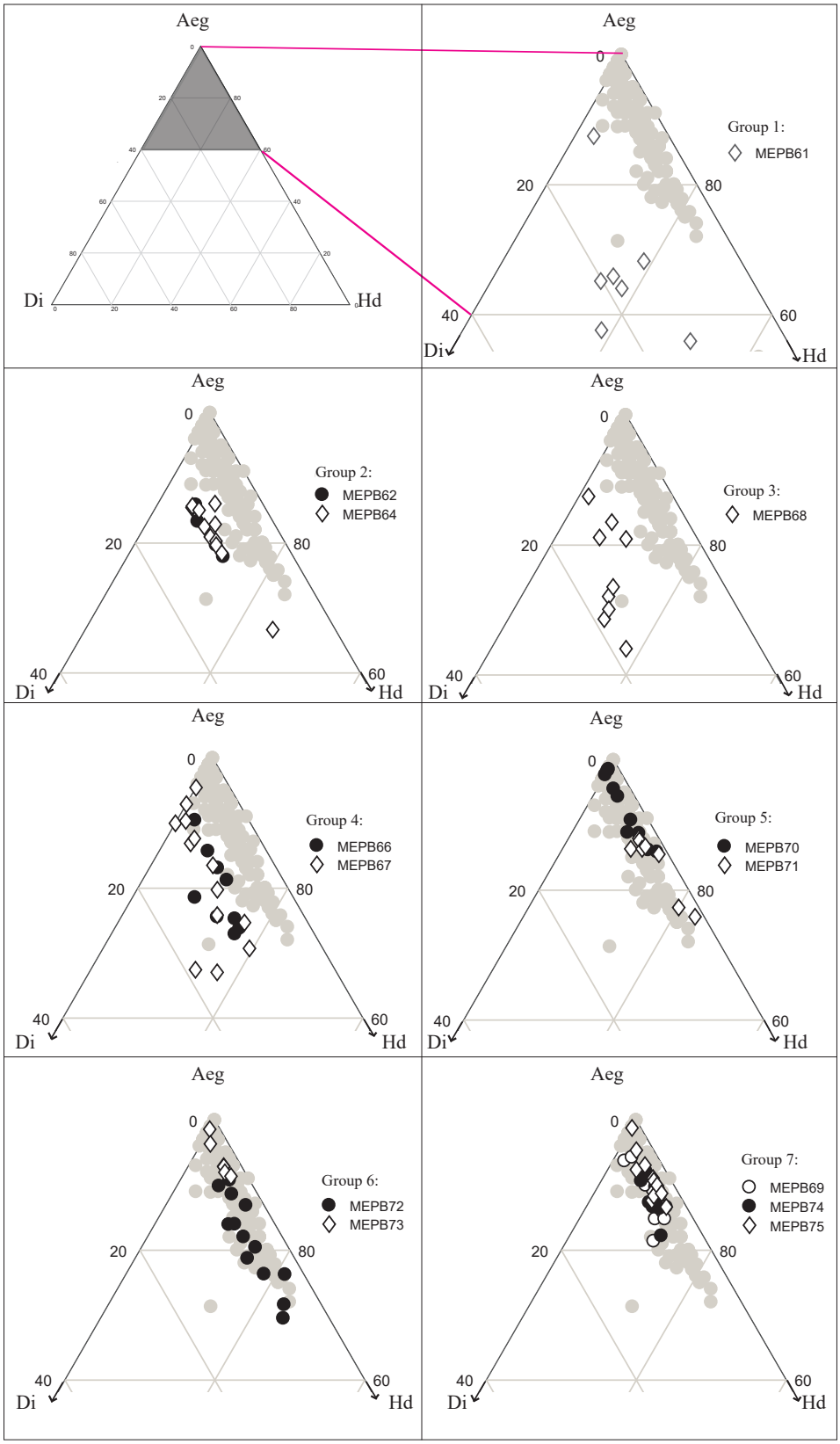

Figure 6.11: *Clinopyroxene plotted in the Na rich part of the Di-Hd-Aeg triangle. The gray background is made up by analyses of aegirine in White and Green Foyaite from Andersen* et al. *(2018).*

Table 6.3: *Selected EMP pyroxene analysis data. (R/OR/MR= Rim/outer rim/middle rim, C=core)*

Type	cpx-II	cpx-II	cpx-III	cpx-III	cpx-I	cpx-III	cpx-III	cpx-II	cpx-II	cpx-II	cpx-II (R)	cpx-II (R)	cpx-II (C)	cpx-II (C)	cpx-II (C)
Sample	MEPB61	MEPB61	MEPB61	MEPB61	MEPB64	MEPB64	MEPB62	MEPB68	MEPB68	MEPB68	MEPB66	MEPB66	MEPB66	MEPB66	MEPB67
Point	28/1.	30/1.	36/1.	37/1.	5/1.	4/1.	16/1.	25/1.	27/1.	29/1.	46/1.	47/1.	45/1.	50/1.	9/1.
Wt.%															
SiO_2	52.04	51.84	51.74	53.24	51.61	52.03	51.23	51.14	51.09	52.59	52.89	52.82	52.03	51.46	50.67
TiO_2	0.81	1.08	1.92	2.13	4.67	3.16	6.06	1.43	1.27	2.67	2.80	1.84	2.00	1.59	1.05
Al_2O_3	0.86	0.83	0.80	1.22	0.49	0.80	0.78	0.80	0.82	1.05	1.08	0.82	0.85	0.75	0.84
FeO	21.86	23.28	23.84	24.36	22.40	24.66	21.56	24.88	24.06	23.71	24.55	25.68	25.02	24.51	23.93
MnO	1.11	0.93	0.94	0.68	2.27	1.45	2.00	0.82	0.85	1.35	1.17	0.80	0.98	0.91	0.93
MgO	3.89	3.13	2.00	1.42	1.08	0.90	1.08	2.23	2.63	1.56	1.08	1.10	1.51	1.88	2.73
CaO	10.11	8.53	6.43	2.99	5.81	3.62	3.66	6.25	7.41	2.78	3.63	1.77	6.00	6.16	8.61
Na_2O	7.98	8.90	9.74	12.20	10.11	11.68	11.50	9.93	9.39	12.11	11.63	12.56	10.20	10.37	8.81
ZrO_2	0.31	0.42	0.21	0.26	0.13	0.00	0.02	0.37	0.45	0.19	0.03	0.14	0.31	0.59	0.39
Total	98.96	99.00	97.64	98.51	98.56	98.30	97.87	97.84	97.98	98.02	98.83	97.52	98.92	98.24	97.99
Apfu*															
Si	1.98	1.97	2.00	2.00	1.99	1.98	1.97	1.96	1.96	1.99	2.00	2.01	1.98	1.97	1.95
Ti	0.02	0.03	0.06	0.06	0.14	0.09	0.17	0.04	0.04	0.08	0.08	0.05	0.06	0.05	0.03
Al	0.04	0.04	0.04	0.05	0.02	0.04	0.04	0.04	0.04	0.05	0.05	0.04	0.04	0.03	0.04
Fe^{3+*}	0.53	0.60	0.58	0.70	0.48	0.68	0.54	0.68	0.65	0.70	0.65	0.76	0.62	0.69	0.64
Fe^{2+*}	0.16	0.14	0.19	0.07	0.24	0.10	0.15	0.12	0.13	0.05	0.13	0.05	0.18	0.10	0.13
Mn	0.04	0.03	0.03	0.02	0.07	0.05	0.06	0.03	0.03	0.04	0.04	0.03	0.03	0.03	0.03
Mg	0.22	0.18	0.11	0.08	0.06	0.05	0.06	0.13	0.15	0.09	0.06	0.06	0.09	0.11	0.16
Ca	0.41	0.35	0.27	0.12	0.24	0.15	0.15	0.26	0.30	0.11	0.15	0.07	0.25	0.25	0.36
Na	0.59	0.66	0.73	0.89	0.75	0.86	0.86	0.74	0.70	0.89	0.85	0.93	0.75	0.77	0.66
Zr	0.01	0.01	0.00	0.00	0.00	0.00	0.00	0.01	0.01	0.00	0.00	0.00	0.01	0.01	0.01
Endmember															
AlTsch	0.02	0.01	0.00	0.00	0.01	0.02	0.00	0.00	0.00	0.01	0.00	0.00	0.02	0.00	0.00
Jd	0.00	0.00	0.03	0.05	0.00	0.00	0.00	0.00	0.00	0.03	0.05	0.04	0.01	0.00	0.00
ZrTiAeg	0.06	0.08	0.12	0.13	0.28	0.18	0.35	0.10	0.09	0.16	0.16	0.11	0.13	0.11	0.08
Di	0.22	0.18	0.11	0.08	0.06	0.05	0.06	0.13	0.15	0.09	0.06	0.06	0.09	0.11	0.16
Hd	0.17	0.13	0.16	0.02	0.18	0.06	0.04	0.10	0.11	0.01	0.09	0.02	0.14	0.07	0.12
Aeg	0.53	0.58	0.58	0.70	0.48	0.68	0.50	0.64	0.61	0.70	0.65	0.76	0.62	0.66	0.58

*Atoms per formula unit (apfu) calculations based on four cations in formula. Fe^{3+} and Fe^{2+} proportions are calculated values.

Table 6.4: *(Continued)*

Type	cpx-II (R)	cpx-II (R)	cpx-II (C)	cpx-II (R)	cpx-II (C)	cpx-II (R)	cpx-II (R)	cpx-II (MR)	cpx-II (OR)	cpx-II (C)	cpx-II (R)	cpx-II (OR)	cpx-II (MR)	cpx-II (C)	cpx-III
Sample	MEPB67	MEPB66	MEPB71	MEPB70	MEPB70	MEPB71	MEPB71	MEPB72	MEPB72	MEPB72	MEPB73	MEPB75	MEPB75	MEPB75	MEPB69
Point	1/3.	49/1.	36/1.	26/1.	35/1.	37/1.	32/1.	27/1.	28/1.	29/1.	42/1.	19/1.	20/1.	21/1.	7/1.
Wt.%															
SiO_2	52.06	52.27	51.43	52.17	52.14	51.80	52.02	51.74	51.69	51.34	52.34	52.40	52.21	52.29	51.69
TiO_2	0.69	3.52	2.52	6.63	0.87	3.70	4.78	3.14	1.11	2.24	4.74	1.05	1.78	3.13	5.61
Al_2O_3	1.59	0.64	0.54	0.72	1.03	1.10	1.03	0.80	0.98	0.53	0.76	1.10	1.66	0.79	0.69
FeO	26.93	24.35	25.71	23.58	28.49	25.27	24.10	24.74	26.44	24.05	24.30	27.85	27.29	25.43	22.93
MnO	0.28	1.29	2.21	1.22	0.52	1.18	0.86	1.48	0.92	1.95	1.57	0.34	0.34	1.39	1.97
MgO	0.66	1.08	0.25	0.13	0.29	0.28	0.31	0.86	0.64	0.85	0.21	0.35	0.24	0.46	0.49
CaO	1.23	4.14	5.35	0.36	1.28	3.14	2.29	4.07	2.77	5.91	0.21	1.70	1.39	2.49	2.15
Na_2O	12.81	11.42	10.43	13.63	12.82	11.89	12.21	11.10	11.99	9.98	13.58	12.77	13.21	12.41	12.51
ZrO_2	0.15	0.00	0.15	0.00	0.14	0.14	0.97	0.12	0.16	1.01	0.00	0.58	0.11	0.17	0.11
Total	96.38	98.73	98.59	98.41	97.58	98.50	98.56	98.05	96.74	97.84	97.70	98.13	98.21	98.56	98.16
Apfu*															
Si	1.99	1.99	1.98	1.97	1.99	1.97	1.99	1.99	1.99	2.00	1.99	1.99	1.97	1.98	1.97
Ti	0.02	0.10	0.07	0.19	0.02	0.11	0.14	0.09	0.03	0.07	0.14	0.03	0.05	0.09	0.16
Al	0.07	0.03	0.02	0.03	0.05	0.05	0.05	0.04	0.04	0.02	0.03	0.05	0.07	0.04	0.03
Fe^{3+*}	0.85	0.64	0.64	0.64	0.87	0.66	0.57	0.63	0.80	0.57	0.72	0.83	0.85	0.73	0.63
Fe^{2+*}	0.02	0.13	0.19	0.10	0.03	0.14	0.19	0.16	0.05	0.22	0.05	0.05	0.01	0.08	0.10
Mn	0.01	0.04	0.07	0.04	0.02	0.04	0.03	0.05	0.03	0.06	0.05	0.01	0.01	0.04	0.06
Mg	0.04	0.06	0.01	0.01	0.02	0.02	0.02	0.05	0.04	0.05	0.01	0.02	0.01	0.03	0.03
Ca	0.05	0.17	0.22	0.01	0.05	0.13	0.09	0.17	0.11	0.25	0.01	0.07	0.06	0.10	0.09
Na	0.95	0.84	0.78	1.00	0.95	0.88	0.90	0.83	0.90	0.75	1.00	0.94	0.97	0.91	0.92
Zr	0.00	0.00	0.00	0.00	0.00	0.00	0.02	0.00	0.00	0.02	0.00	0.01	0.00	0.00	0.00
Endmember															
AlTsch	0.01	0.01	0.01	0.01	0.01	0.02	0.01	0.01	0.01	0.00	0.01	0.01	0.03	0.02	0.00
Jd	0.06	0.00	0.00	0.00	0.02	0.00	0.02	0.01	0.03	0.02	0.01	0.02	0.01	0.00	0.00
ZrTiAeg	0.05	0.20	0.15	0.38	0.06	0.22	0.31	0.19	0.07	0.17	0.27	0.08	0.10	0.18	0.33
Di	0.04	0.06	0.01	0.01	0.02	0.02	0.02	0.05	0.04	0.05	0.01	0.02	0.01	0.03	0.03
Hd	0.00	0.07	0.19	0.00	0.02	0.07	0.07	0.12	0.05	0.20	0.00	0.02	0.00	0.03	0.01
Aeg	0.85	0.64	0.63	0.62	0.87	0.66	0.57	0.63	0.80	0.57	0.72	0.83	0.85	0.73	0.60

*Atoms per formula unit (apfu) calcualations based on four cations in formula. Fe^{3+} and Fe^{2+} proportions are calculated values.

6.3.2 The major elements in pyroxene of the samples collected from the boulders

Group 5

The cpx-II in group 5 follow a linear trend in figure 6.11, with a high aegirine component between Aeg_{76} and up to Aeg_{99}, and a diopside component lower than Di_4. The analysis with Aeg_{99} in the Aeg-Hd-Di projection, in reality do not have sufficient Fe^{3+} to be classified as pure aegirine, but has a high ZrTiAeg component of 0.38 and Aeg-component of 0.62 (table 6.3). MEPB70 generally have higher aegirine component in the pyroxenes than MEPB71, and MEPB70 also have higher ZrTiAeg. As with previous samples, the cores have lower aegirine component. The lowest aegirine content observed in this sample is Aeg_{85}. Titanium content reaches a maximum of 6.6 wt.% in analysis 26/1, resulting in this analysis to have the highest ZrTiAeg component. The pyroxene composition in MEPB71 ranges between Aeg_{76} to Aeg_{88}. Titanium content is up to 4.8 wt.%.

Group 6

The cpx-II in group 6 have similar compositions as group 5. Points 27/-29/1 in MEPB72 represents the gradual compositional change between the core ($Aeg_{70}Hd_{24}Di_6$), the middle rim ($Aeg_{79}Hd_{16}Di_6$), to the outer rim ($Aeg_{90}Hd_6Di_4$) (table 6.3). Interestingly, the titanium concentration in the middle rim is higher (3.1 wt.%) than the outer rim (1.1 wt.%) and has higher sodium content. This is accompanied by the total iron content is 2 wt.% higher in the outer rim than in the middle rim. In MEPB73, the highest aegirine content in the Aeg-Hd-Di projection is point 42/1 (table 6.3) with Aeg_{98} and is obtained from the acicular cpx-III in the sample. This analysis has in reality a high ZrTiAeg component of 0.27.

Group 7

Cpx-II from this group generally have similar major element composition, as the other unfoliated groups 5 and 6, with the highest aegirine component in this group being in point 20/1 in MEPB75 ($Aeg_{98}Hd_1Di_1$). This value is taken from the middle rim of a zoned grain. The core (21/1) yields a value of ($Aeg_{93}Hd_4Di_3$), while the outer rim (19/1) has a composition in between these values (figure 6.11). The core has the highest titanium content of 3.1 wt.%, while inner and outer rim have 1.8 and 1 wt.% respectively. The core has the lowest total iron of 25.4 wt.%, while the rims have total iron of close to 28 wt.% (table 6.3)

In point 7/1 in MEPB69, the titanium value reaches 5.6 wt.%, and has the highest aegirine component in the sample. This matches its low total iron content of 22.9 wt.%. This point is from an acicular cluster of cpx-III (point 4/1-8/1 in table B.3). These points, as with the other cpx-III in the unfoliated samples, have in reality a higher ZrTiAeg component, rather than a high aegirine component.

6.3.3 Diopside trend in the samples

The normative mineral calculations from the whole rock analysis in section 6.2.1 defined two trends based on the orthoclase and albite content which is correlated with the sampling locations. The sampling localities further show two trends based on their clinopyroxene major element geochemistry. The clinopyroxenes in the samples from the riverbed show a linear decreasing trend towards lower diopside component and higher ZrTiAeg content. The clinopyroxenes from the boulders, on the other hand, overall have overall low diopside content, but variable ZrTiAeg (figure 6.12). Group 2 samples are collected close to the riverbed, however, most of the clinopyroxenes follow the trend of the boulder samples, while a minority of the clinopyroxenes follow the trend from the riverbed.

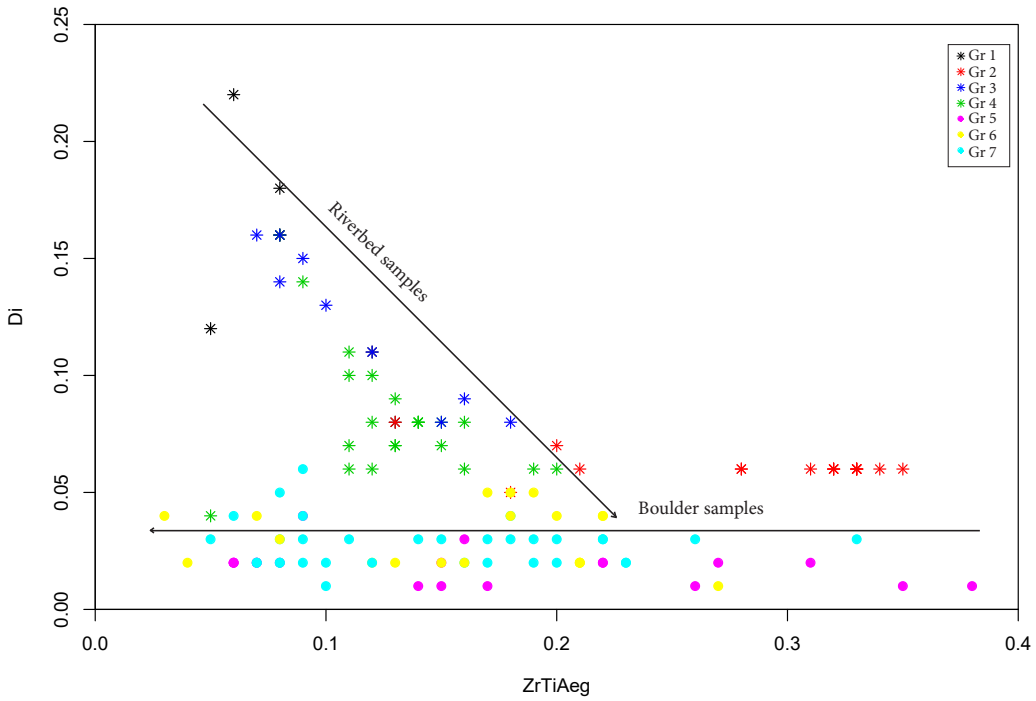

Figure 6.12: *Diopside plotted against ZrTiAeg showing two trends correlating with the sampling localities. Samples from the riverbed are represented by stars, and the boulder samples in circles.*

6.3.4 Major elements in amphibole

The amphibole formula calculation was based on 24 anions, and the major element analyses of amphibole (table B.4, and selected samples in table 6.5) have been plotted with respect to Na, Mg and total iron content. The stars in figure 6.13 represent the idealized amphibole endmembers. The amphiboles form two distinct groups. The amphiboles in the foliated nepheline syenites i.e. the samples from the riverbed, have higher magnesium and lower total iron content with $Fe_{tot}/(Fe_{tot} + Mg)$ ranging between 0.48 to 0.57. These amphiboles are relict magnesio-arfvedsonites which are found within cores in cpx-II, or extensively replaced by cpx-III. The amphiboles in the unfoliated varieties are found to replace primary cpx and have higher $Fe_{tot}/(Fe_{tot} + Mg)$ from 0.71 to 0.83.

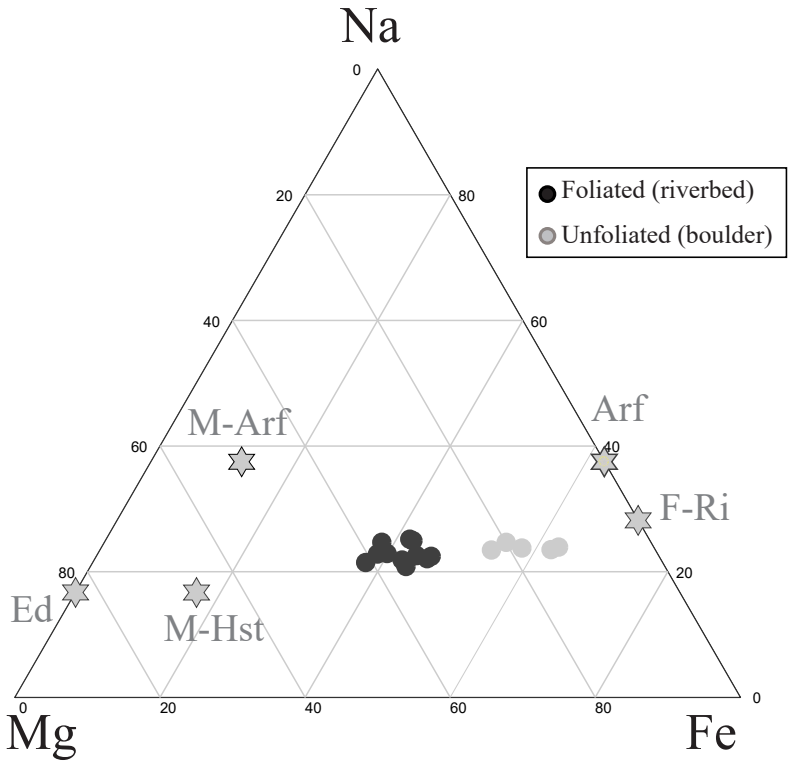

Figure 6.13: *Major element ananlyses of amphibole in ternary diagram with Mg, Fe (total) and Na (atomic percent). The stars are idealized amphibole endmembers: Ed= edenite, M-Hst= magnesio-hastingsite, F-Ri= ferro-richterite, M-arf= magnesio-arfvedsonite, Arf=arfvedsonite.*

The arfvedsonites have Si (apfu) concentration that ranges between 7.64 and 7.88, while the average Si content in the magnesio-arfvedsonites is 8.25. The lower Si content is accommodated by higher Al and Ti content. Zr is generally low, however, in the arfvedsonites the ZrO_2 can reach 0.3 wt.%, while the magnesio-arfvedsonites have no ZrO_2 content higher than 0.06 wt.%. The zirconium level in magnesio-arfvedsonite is under the detection limit. The arfvedsonites have lower MnO and K_2O concentrations than the magnesio-arfvedsonites, which correlates well with the whole rock compositions.

Table 6.5: *Selected EMP amphibole analysis data*

Point	35/1.	44/1.	4/1.	28/1.	30/1.	40/1.	41/1.	21/1.	22/1.
Sample	MEPB61	MEPB66	MEPB67	MEPB68	MEPB68	MEPB73	MEPB73	MEPB74	MEPB74
Type	M-arf	M-arf	M-arf	M-arf	M-arf	Arf	Arf	Arf	Arf
SiO_2	54.93	52.96	53.81	53.31	53.93	47.59	48.02	50.17	49.98
Al_2O_3	0.80	0.70	0.95	0.58	0.67	3.02	2.92	1.88	2.25
TiO_2	0.85	1.20	0.20	0.81	0.74	2.00	1.94	1.23	1.81
ZrO_2	0.02	0.00	0.01	0.05		0.27	0.28	0.18	0.15
FeO	16.29	18.12	16.18	17.05	17.70	25.70	25.44	22.91	23.05
MnO	2.80	3.73	1.47	3.53	3.53	3.14	2.74	3.05	2.88
MgO	8.83	7.66	9.84	8.91	7.62	2.98	3.28	5.36	4.64
CaO	1.18	0.76	0.48	1.36	0.66	1.14	1.26	1.20	1.00
Na_2O	9.02	7.94	7.91	8.39	8.92	8.37	8.26	8.54	8.81
K_2O	1.72	3.23	4.05	2.33	2.28	1.81	1.76	1.89	1.93
total	96.46	96.29	94.89	96.32	96.06	96.00	95.89	96.42	96.51
Apfu*									
Si	8.27	8.15	8.25	8.14	8.25	7.64	7.68	7.88	7.84
Al	0.10	0.14	0.02	0.09	0.09	0.24	0.23	0.15	0.21
Ti	0.14	0.13	0.17	0.10	0.12	0.57	0.55	0.35	0.42
Zr	2.05	2.33	2.08	2.18	2.27	3.45	3.40	3.01	3.02
Fe	0.36	0.49	0.19	0.46	0.46	0.43	0.37	0.41	0.38
Mn	1.98	1.76	2.25	2.03	1.74	0.71	0.78	1.25	1.09
Mg	0.19	0.13	0.08	0.22	0.11	0.20	0.22	0.20	0.17
Ca	2.63	2.37	2.35	2.48	2.65	2.61	2.56	2.60	2.68
Na	0.33	0.63	0.79	0.45	0.44	0.37	0.36	0.38	0.39
K	0.00	0.00	0.00	0.00	0.00	0.02	0.02	0.01	0.01
$Fe_{tot}/(Fe_{tot}+Mg)$	0.51	0.57	0.48	0.52	0.57	0.83	0.81	0.71	0.74

*Atoms per formula unit (apfu) calculations based on 24 anions.

6.4 Trace element composition of aegirine and amphibole

Trace element analysis by Q-LA-ICP-MS has been conducted on pyroxene and amphibole grains. Cpx-I, cpx-II and cpx-III have been analyzed, while the grain size of cpx-IV was to small to analyze. The results have been plotted in GCDkit which uses chondrite normalization after Anders & Grevesse (1989). The data results used in the normalised trace element diagrams can be found table B.6 for pyroxene and table B.7 for amphibole.

6.4.1 REE-distribution of the samples collected from the riverbed

The pyroxene analyses in the normalized trace element distributions collected from the riverbed are represeted with a diamond shape. Amphibole analyses are marked with an A in the legend and are represented by star in the plot.

Group 1

Q-LA-ICP-MS analyses of cpx-III were hard to obtain due to its small grain size. The vast majority of the analysis of MEPB61 was therefore on cpx-II. The only successful analysis of cpx-III is point 03.01, which shows a depletion from dysprosium to thulium relative to the other analyses. Primary cpx-II has relatively flat rare earth patterns, with high LREE concentrations (figure 6.14). The lanthanum concentrations in cpx-II range from ca. 160 to 2000 times chondrite and gradually decrease to lutetium concentrations between ca. 200 to 10 times chondrite. Point 01.02 and 07.01 have anomalously low rare earth element concentrations, relative to the other cpx-II analysis. Both analyses were taken close to the relict amphibole core, and could be a mix between amphibole and pyroxene analysis.

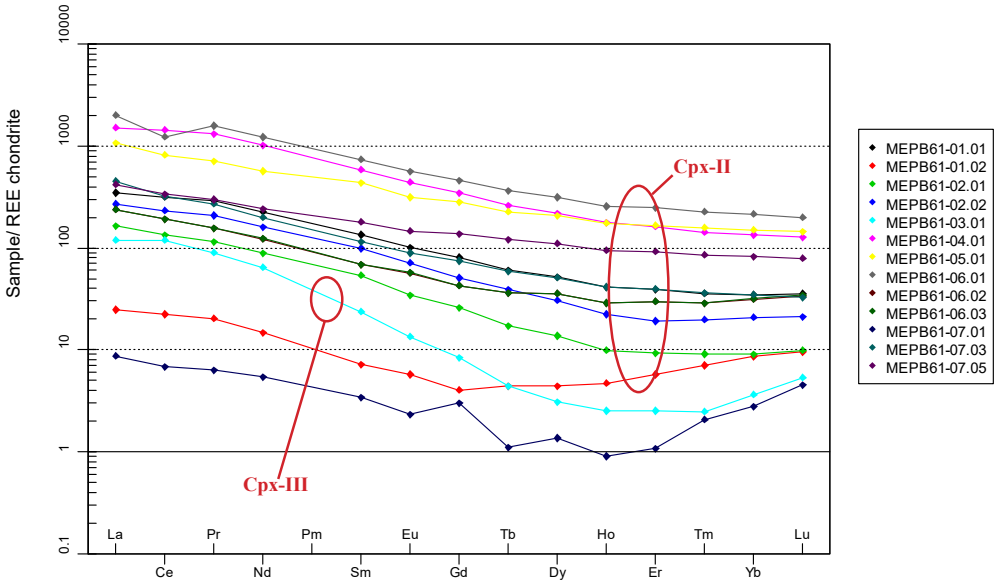

Figure 6.14: *REE distribution of pyroxene in MEPB61 from group 1, with cpx-II showing relatievely flat patterns, and cpx-III (03.01) having MREE/HREE depletion*

Group 2

Pyroxenes from MEPB62 have two distinct REE patterns (figure 6.15). The cpx-I have La concentrations from 85 to 50 times chondrite. This pattern has a strong MREE depletion relative to the LREE, with the lowest REE concentration being between 1- and 1.5-times chondrite at Ho. From Ho there is an increase to ca. 5 times chondrite at Lu. The fibrous to acicular clinopyroxene-III generally have lower LREE patterns, with an MREE depletion realtive to HREE and LREE. From Ho, there is a drastic increase in the HREE from Ho towards Lu, resulting in a La/Lu ratio close to 1. The HREE in the fibrous cpx-III are generally higher than in cpx-I, with the highest Lu concentration at 23 times chondrite.

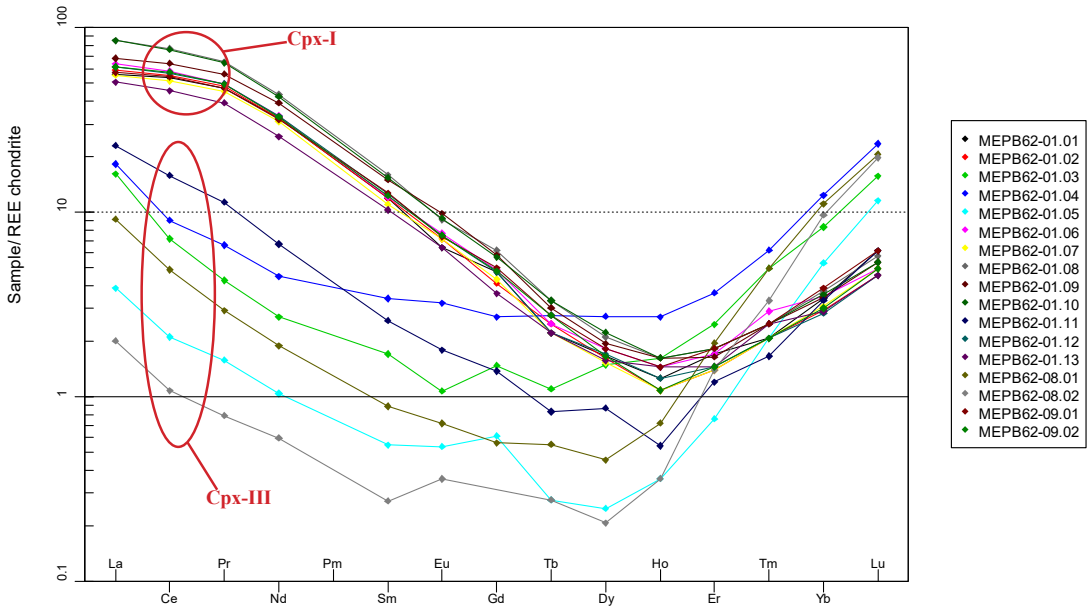

Figure 6.15: *REE distribution of pyroxene in MEPB62 from group 2, with two distinct REE patterns. Cpx-I is LREE enriched relative to MREE and HREE, while cpx-III is MREE depleted relative to LREE and HREE.*

The Q-LA-ICP-MS analysis from MEPB64 was taken on the acicular cpx-III. The pattern matches the cpx-III REE-pattern in MEPB62 with MREE depletion relative to LREE and HREE (figure 6.16). However, the LREE concentrations are generally higher in MEPB64. Point 02.03 has the highest La value of 57 times chondrite, but the lowest Lu value of 6 times chondrite. Point 02.01, on the other hand, have the lowest La value, but the highest Lu value.

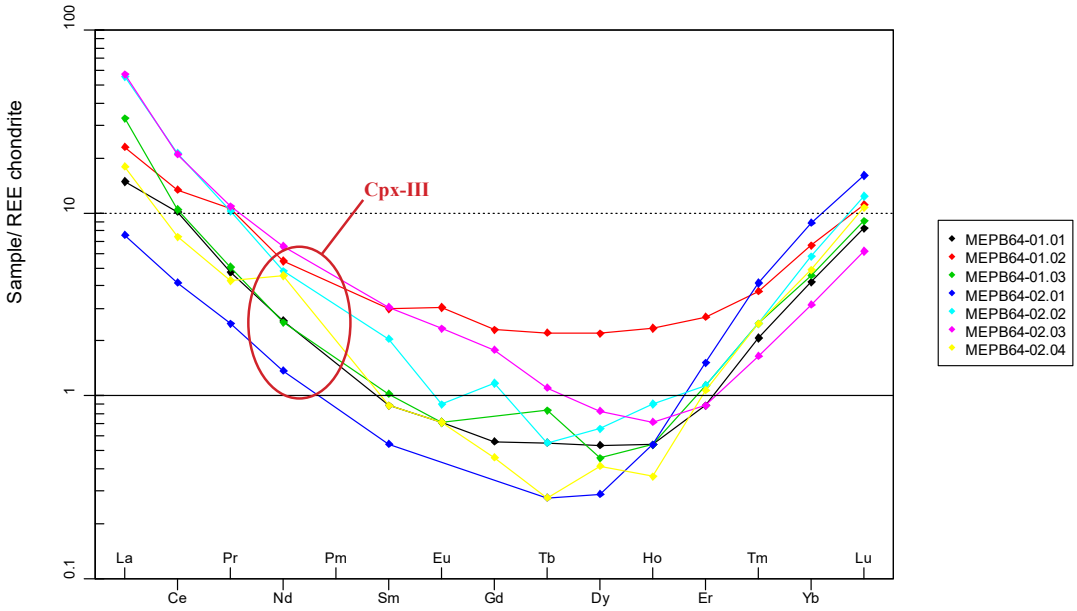

Figure 6.16: *REE distribution of pyroxene in MEPB64 from group 2, where cpx-III have MREE depletion relative to LREE and HREE.*

Group 3

In MEPB68, both pyroxenes and amphiboles were analyzed. Pyroxenes and amphibole analyses generallys follow the same REE trend, with MREE depletion relative to the LREE and HREE (figure 6.17). La concentrations ranges between ca. 10 and 100 times chondrite, while Lu has concentrations between ca. 4 and 10 times chondrite. The lowest concentration in pyroxene is Ho which is at ca. 1 times chondrite. Although pyroxenes and amphiboles follow the same REE trend, most of the amphibole analyses have lower total REE concentrations. Cpx-II analysis of point 01.02 and 01.03 show a flatter clinopyroxene REE pattern with a gradual decrease from the LREE to Ho, and a flat HREE pattern.

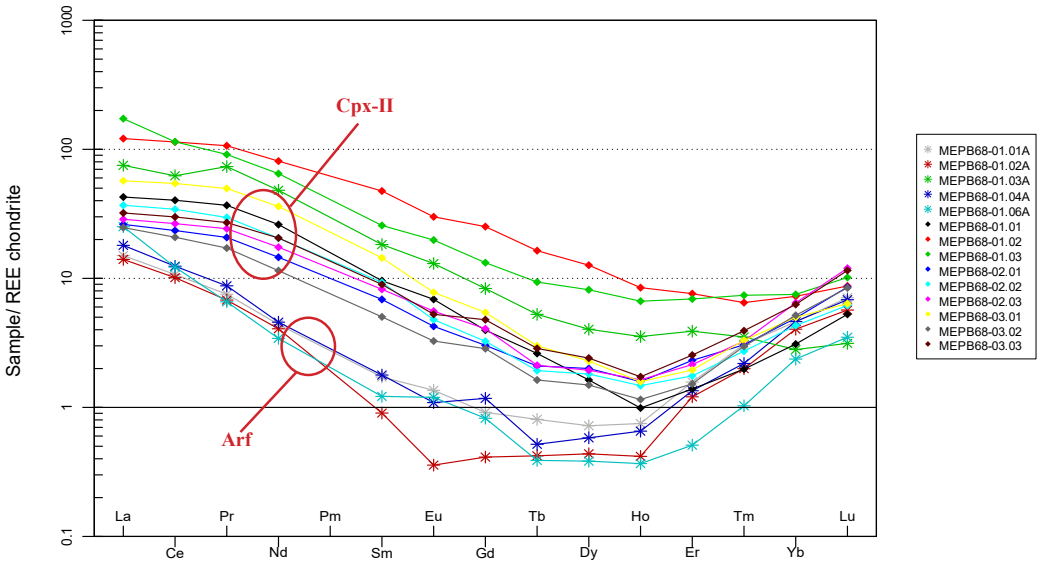

Figure 6.17: *REE distribution of cpx-II and amphibole in MEPB68 from group 3. Cpx-II shows MREE depletion relative to LREE and HREE. Amphibole is marked with an A in the legend and as stars in the plot. The amphibole generally follow the same REE-trend.*

Group 4

Cpx-II in group 4 have MREE depletion relative to LREE and HREE, with La chondrite normalized values between ca. 10 and 100 times chondrite. Ho has the lowest concentrations between 0.3 and 4 times chondrite, before increasing towards Lu at ca. 2 to 9 times chondrite (figure 6.18 and 6.19).

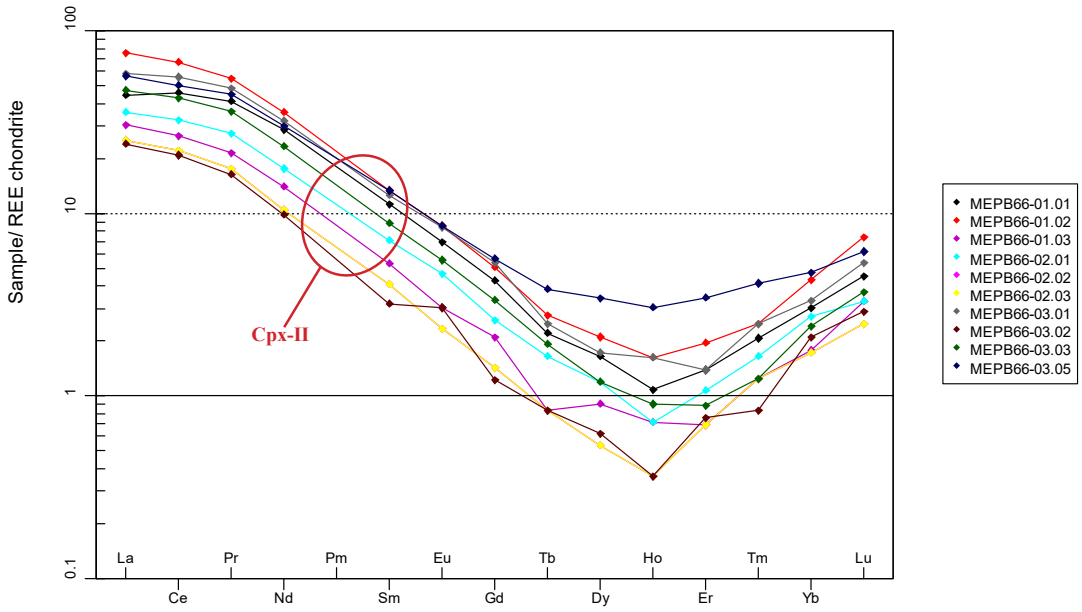

Figure 6.18: *REE distribution of cpx-II in MEPB66 from group 4, showing the typical cpx-II pattern with MREE depletion relative to HREE and MREE.*

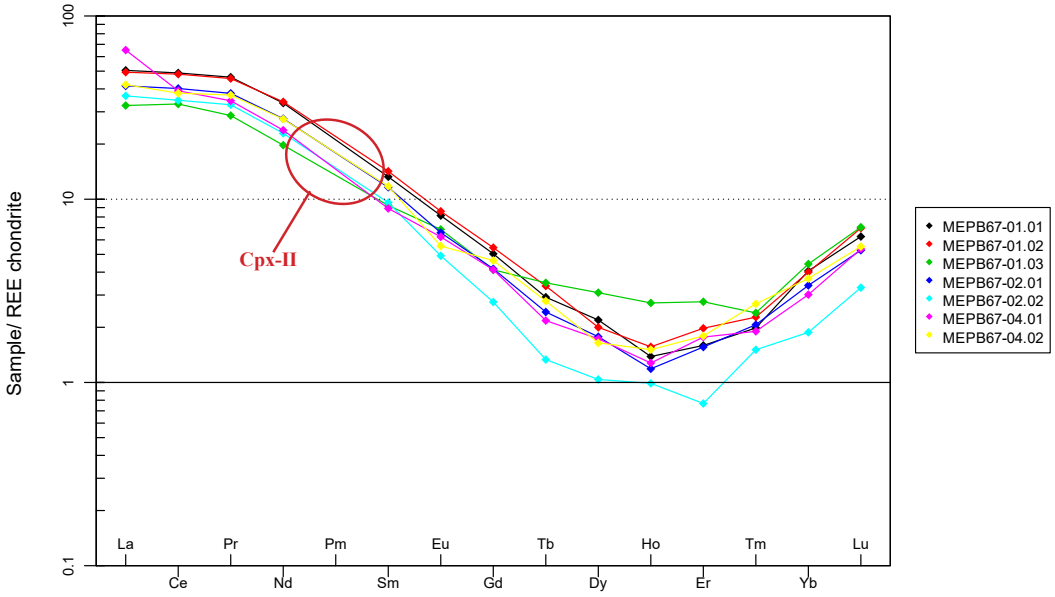

Figure 6.19: *REE distribution of cpx-II in MEPB67 from group 4, showing the typical cpx-II pattern.*

6.4.2 REE-distribution of the samples collected from the boulders

The pyroxene analyses in the normalized trace element distributions collected from the boulders are represeted with a square shape. Amphibole analyses are marked with an A in the legend and are represented by a circle with a cross in the plot.

Group 5

Cpx-II from MEPB70 have with an MREE depletion relative to the LREE and HREE (figure 6.20). The analyses in MEPB70 show a prominent negative cerium anomaly and an increase in praseodymium. The lowest REE normalized concentration in MEPB70 is Ho at ca. 4 times chondrite.

The pyroxenes in MEPB71 have a smoother LREE pattern than MEPB70. La concentrations are generally between 20-100 times chondrite, before decreasing towards Ho at ca. 1-10 times chondrite(figure 6.21). The HREE has similar concentrations as the LREE. In MEPB71, the amphiboles follow the REE pattern of cpx-II with MREE depletion relative to LREE and HREE.

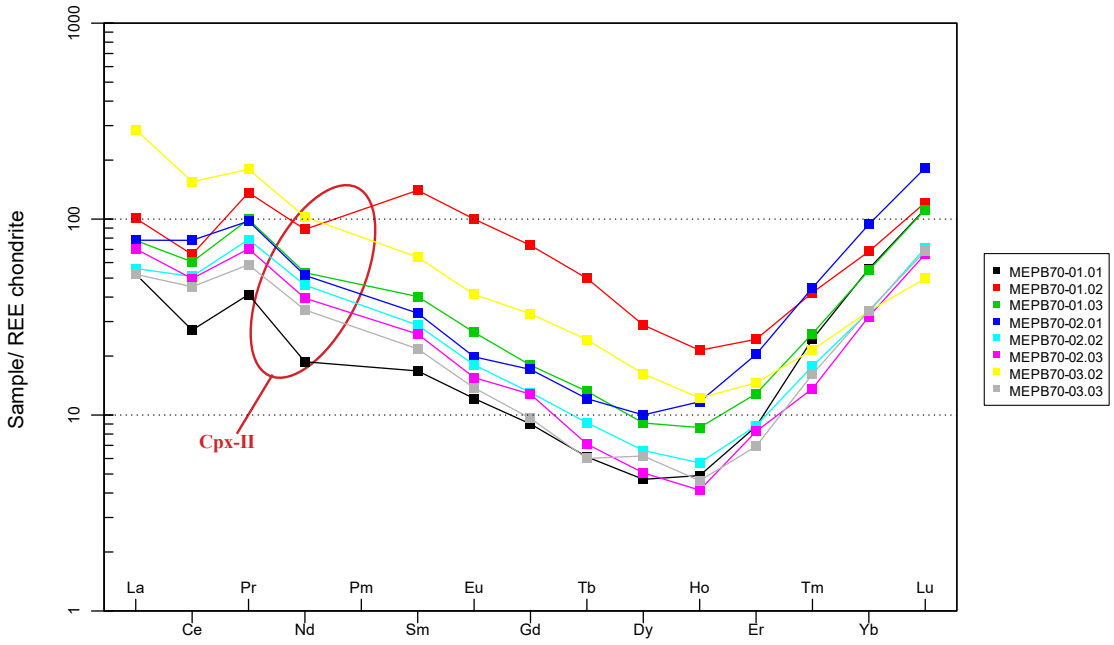

Figure 6.20: *REE distribution of cpx-II in MEPB70 from group 5 showing MREE depletion, relative to LREE and HREE.*

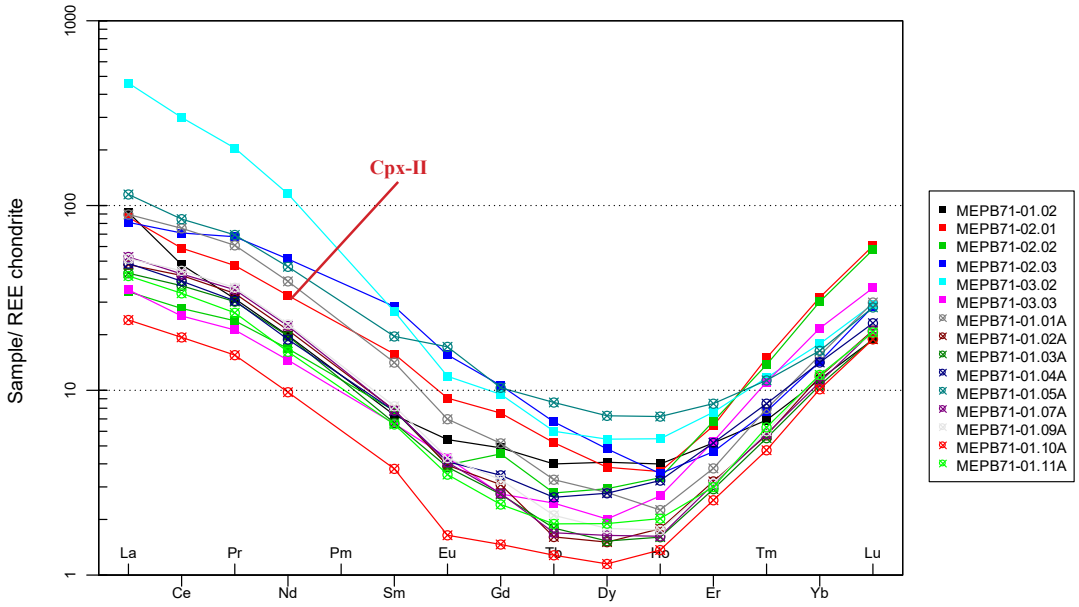

Figure 6.21: *REE distribution of cpx-II and amphibole in MEPB71 from group 5. The pattern is MREE depleted relative to LREE and HREE. Amphibole is marked with an A in the legend and as a circle with a cross in the plot. Cpx and amphibole follow the same REE trend with MREE depletion relative to LREE and HREE.*

Group 6

Cpx-II in group 6 have MREE depletion relative to the LREE and HREE, and a La/Lu ratio close to 1. Point 04.03 in MEPB72 has, however, a relatively flat HREE pattern from Er to Lu (figure 6.22). The amphiboles follow the cpx-II REE distribution. Point 04.02 and 03.01 in MEPB72 are cpx-III REE-pattern, with La between ca.10 and 40 times chondrite, with a severe MREE depletion relative to the LREE and HREE.

Cpx-II in MEPB73 have La concentrations between ca. 30-100 times chondrite. The pattern gradually decreases towards Ho at ca. 2-10 times chondrite. The HREE concentrations are generally match the LREE. Point 02.01-02.03 have a positive cerium anomaly (figure 6.23).

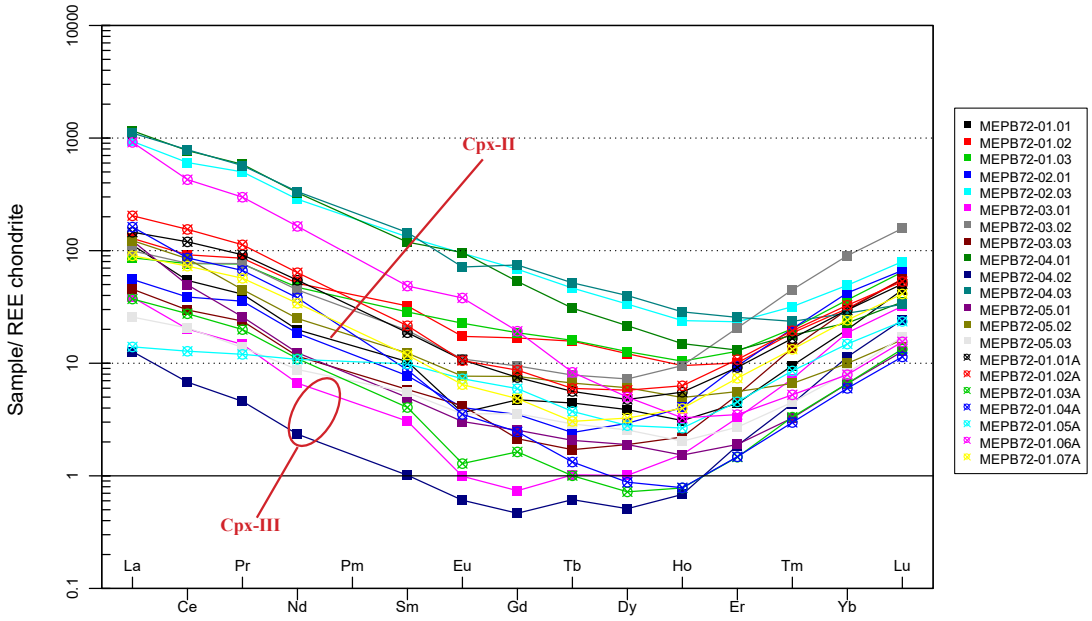

Figure 6.22: *REE distribution of cpx-II, cpx-III and amphibole in MEPB72 from group 6. The cpx has MREE depletion and La/ Lu ratio close to 1. Amphibole is marked with an A in the legend and as a circle with a cross in the plot.*

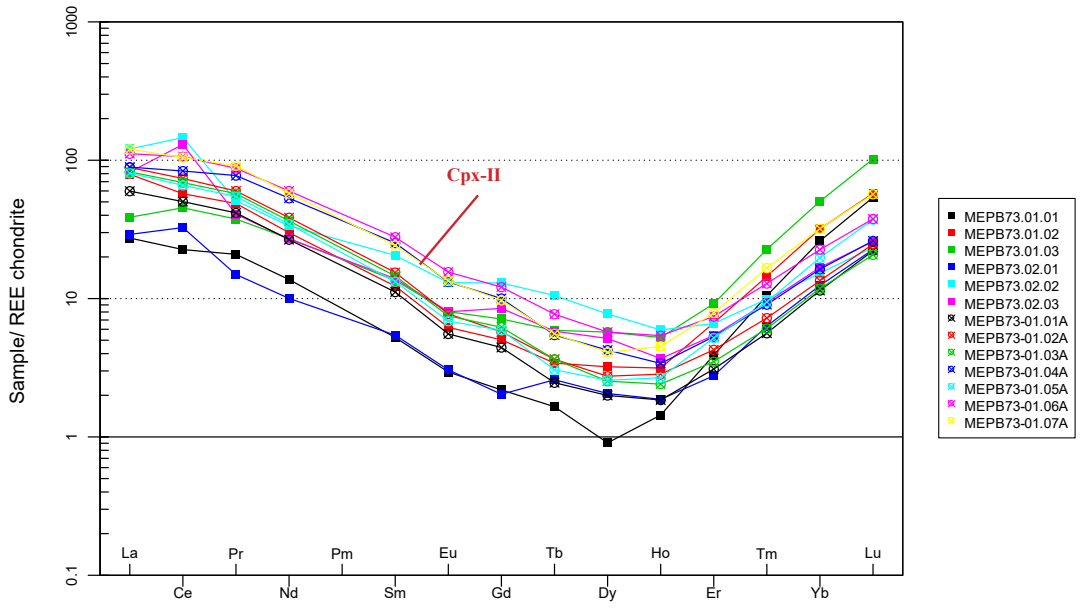

Figure 6.23: *REE distribution of cpx-II and amphibole in MEPB73 from group 6. The cpx has MREE depletion and La/ Lu ratio close to 1. Amphibole is marked with an A in the legend and as a circle with a cross in the plot.*

Group 7

Cpx-II in group 7 have LREE which matches the HREE concentrations. The MREE are depleted relative to LREE and HREE (figure 6.24 to 6.27). La and Lu concentrations range between 10- and 100-times chondrite with the lowest concentrations at Ho between ca 0.3 to 7 times chondrite.

In MEPB75, 03.01 and 05.01 are cpx-III with La and Lu at ca. 10 times chondrite, with a MREE depletion relative to HREE and MREE (figure 6.26). Point 01.01 in MEPB69 and points 02.03 and 03.02 in MEPB76 have relatively flat patterns without MREE depletion.

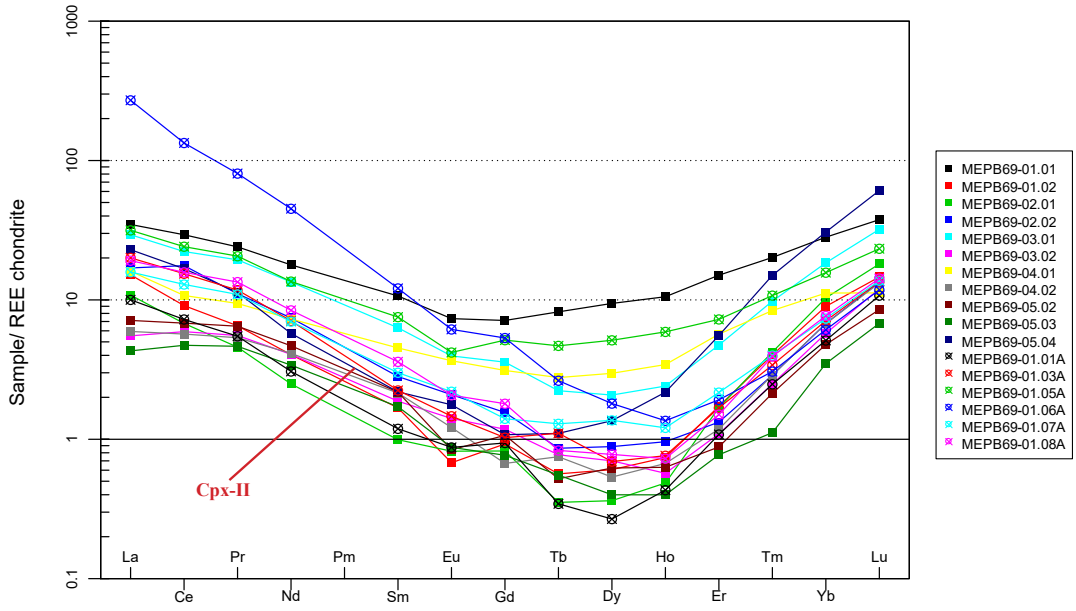

Figure 6.24: *REE distribution of cpx-II and amphibole in MEPB69 from group 7. The cpx has MREE depletion and La/ Lu ratio close to 1. Amphibole is marked with an A in the legend and as a circle with a cross in the plot.*

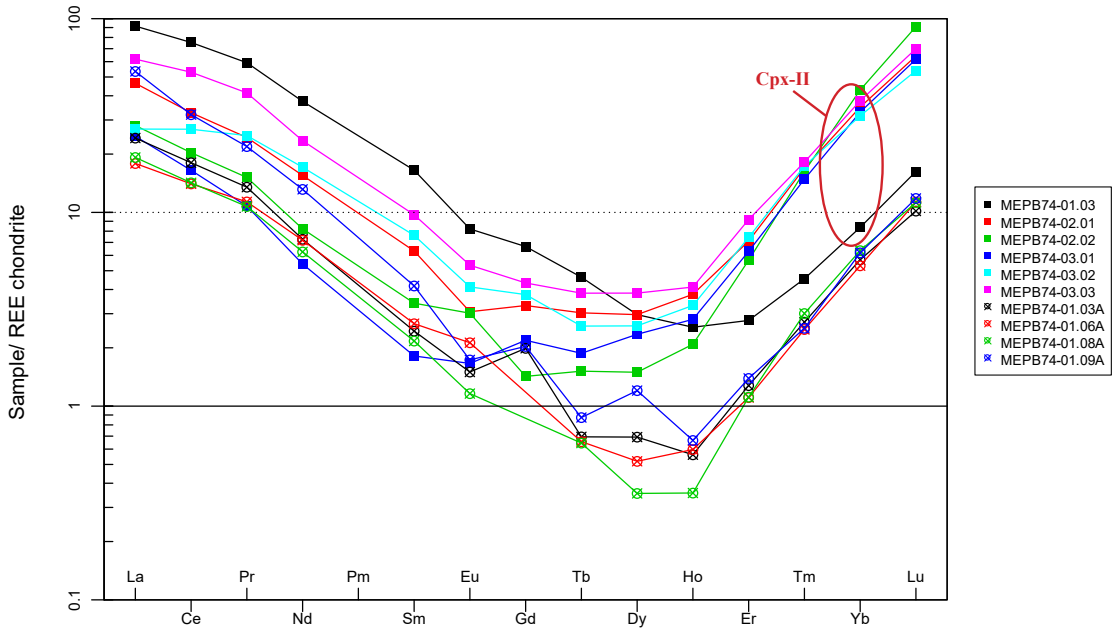

Figure 6.25: *REE distribution of cpx-II and amphibole in MEPB74 from group 7. The cpx has MREE depletion and La/ Lu ratio close to 1. Amphibole is marked with an A in the legend and as a circle with a cross in the plot.*

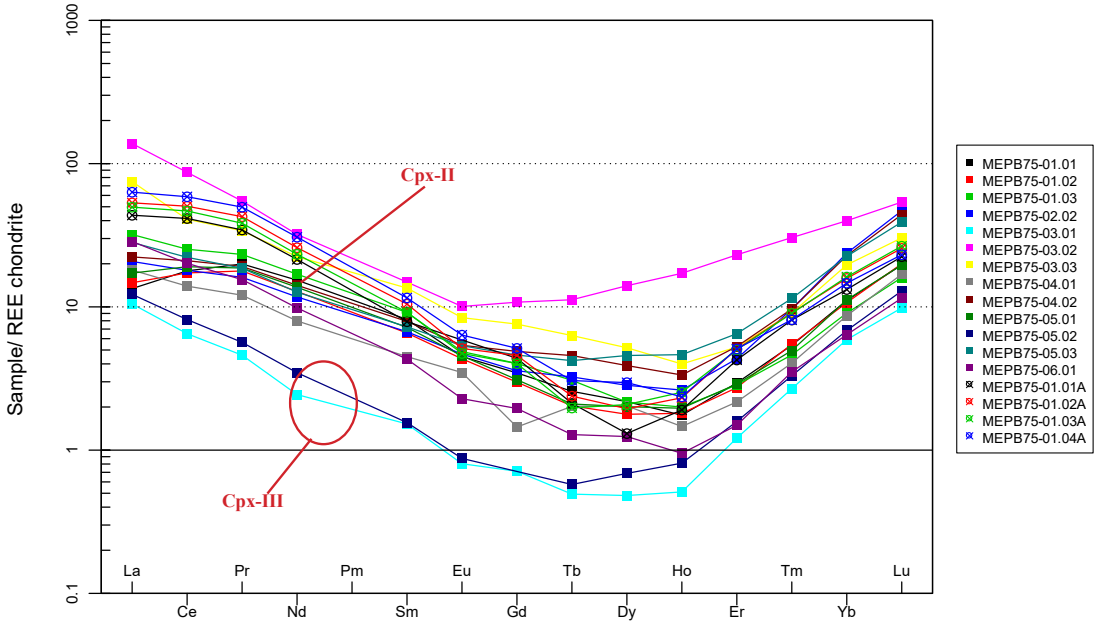

Figure 6.26: *REE distribution of cpx-II and amphibole in MEPB75 from group 7. The cpx has MREE depletion and La/ Lu ratio close to 1. Amphibole is marked with an A in the legend and as a circle with a cross in the plot.*

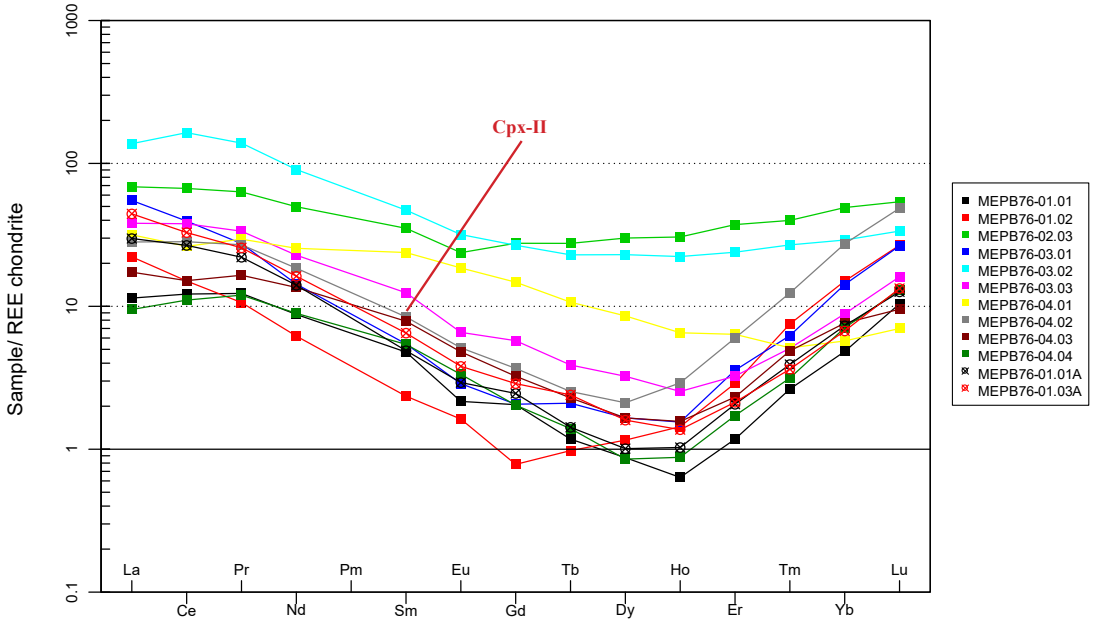

Figure 6.27: *REE distribution of pyroxene and amphibole in MEPB76 from group 7. The cpx has MREE depletion and La/ Lu ratio close to 1. Amphibole is marked with an A in the legend and as a circle with a cross in the plot.*

6.4.3 Average REE distributions of pyroxene and amphibole

The average REE-concentrations are calculated based on typical analyses in each group, for the different types of pyroxenes. The pyroxenes from the samples collected from the riverbed are marked with a diamond shape, while the pyroxenes from the boulders have a square shape. The amphiboles from the boulder samples are marked with a circle with a cross, and the amphiboles from the riverbed are stars. The values used in the plots can be found in table B.8.

Overall the cpx-II in the foliated and unfoliated samples have REE-patterns that are similar, with La ranging between ca. 40 to 100 times chondrite, with a gradual decrease towards Ho at ca. 1 to 10 times chondrite before increasing to between ca. 5 to 100 times chondrite. The cpx-II in the unfoliated samples collected from the boulders have, however, higher HREE than the cpx-II collected from the riverbed (figure 6.28). The samples from the riverbed therefore have a higher La/Lu ratio. Cpx-III in MEPB61 has similar LREE and MREE trends as the cpx-II in the foliated samples but have generally higher total REE concentrations. Cpx-III have the lowest REE/chondrite values and a higher degree of MREE depletion at 1 times chondrite, relative to the LREE and HREE, with La and Lu values at ca. 11 times chondrite.

The cpx-II in the tinguaite in group 1 have the overall highest REE concentrations, with a relatively flat pattern. The LREE in the tinguaite is higher than the HREE but has a lower La/Lu ratio than the other samples.

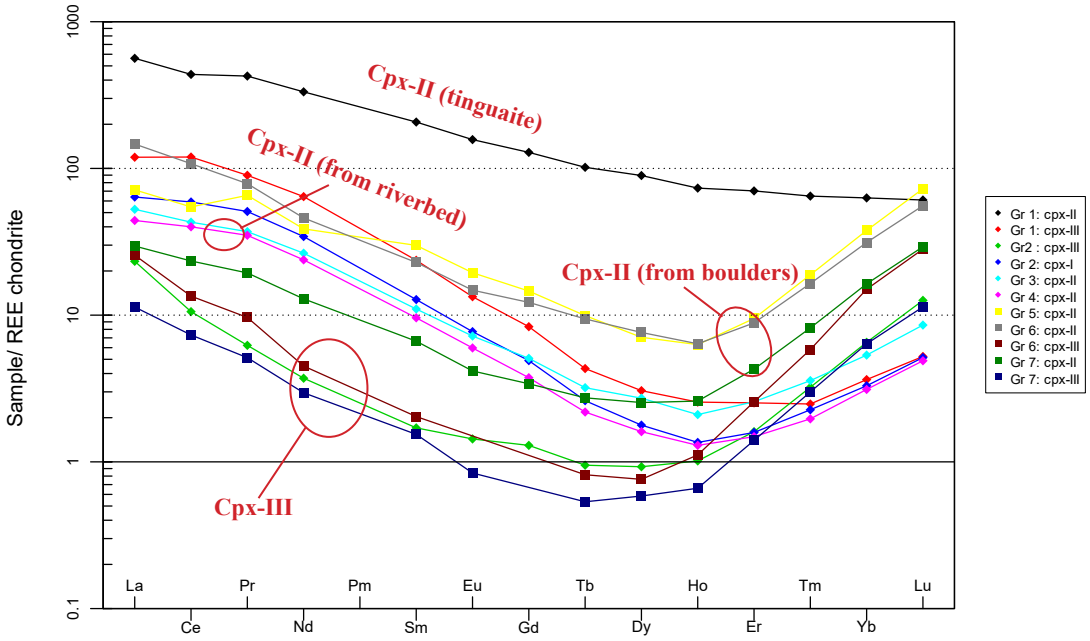

Figure 6.28: *Average REE distributions of pyroxene. Cpx-II shows to patterns, with cpx-II in from the boulders having higher HREE than the cpx-II from the riverbed. Cpx-I in group 2 have REE patterns similar to cpx-II from the riverbed. Cpx-III have the lowest total REE, and the most drastic MREE depletion.*

The average amphiboles in figure 6.29 follow the same depletion trend, with La values between 20-110 times chondrite, and the lowest point at Ho between 1-4 times chondrite, before a gentle increase towards Lu. The magnesio-arfvedsonite in group 3 have the lowest overall REE concentrations, and a larger difference between the LREE and HREE than the arfvedsonites from the boulder samples.

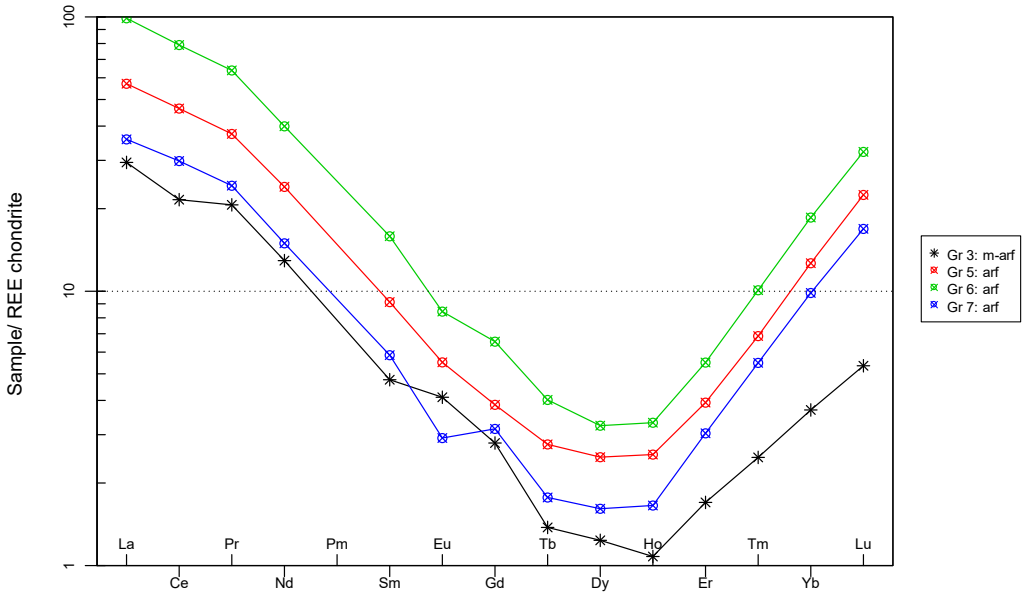

Figure 6.29: *Average REE distributions of amphibole by groups. The stars represent the average magnesio-arfvedsonite in group 3 collected from the riverbed. The circles with a cross represent the average arfvedsonites in each group collected from the boulders.*

Average amphibole divided by average cpx-II

To compare the REE-pattern of amphibole and pyroxenes, the average amphibole from each group has been divided by the average cpx-II from each group. The groups from the boulders are represented by a square, while the group from the riverbed is a diamond (figure 6.30).

Overall, the average amphiboles have lower REE-concentrations than the average cpx-II. The amphiboles in group 7, however, have higher average LREE than the pyroxenes, and lower MREE and HREE. The pattern for group 5 follow the same trend, as the pattern from group 7, with a higher LREE and a flatter MREE than HREE. The patterns from group 3 and group 6 have relatively flatt patterns, compared to the patterns of group 5 and 7. All patterns are relatively flat from the MREE to HREE indicating that the amphiboles follow the pyroxene pattern.

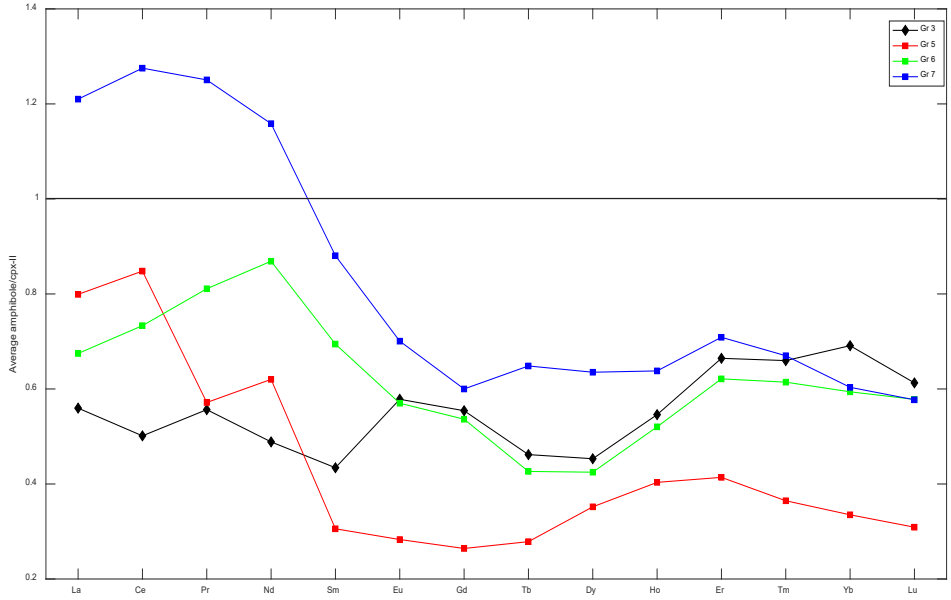

Figure 6.30: *Average amphibole divided by average cpx-II from each group. Group 3 collected from the riverbed is marked with a diamond, and groups 5-7 from the boulders are marked with a square.*

6.4.4 Correlation between major and trace elements

There appears to be a correlation between aegirine component and REE-concentration, with the samples with high aegirine component, generally having the lowest LREE concentrations, and higher HREE. For example, the average cpx-II in MEPB75 have an average aegirine component of Aeg_{90}, and La and Lu at 30 times chondrite, while cpx-II in MEPB68 have an average Aeg_{74} and La at 60 times chondrite, and Lu at 10 times chondrite (figure 6.31).

Figure 6.31 is based on average REE, Aeg, and Di values for the samples and the different cpx types. This plot will, therefore, show the general trend for each sample. The general trend in figure 6.31 shows that the samples collected from the boulders in general have higher aegirine component and have the highest Lu/Ho, and lower La/Lu ratios. The only exception is cpx-III from MEPB62 and 64 (collected from the riverbed), which have the most severe MREE depletion trends. These samples also have La/Lu ratios close to 1, showing that they are LREE and HREE enriched relative to the MREE. The samples from the riverbed, on the other hand, have lower aegirine component and relatively flat HREE pattern, as shown in their Lu/Ho ratio. The samples from the riverbed have the highest La/Lu ratios, meaning they are enriched in LREE relative to MREE and HREE. Higher diopside component (and

lower aegirine component) can be correlated with lower Lu/Ho, indicating that the samples with lower aegirine/higher diopside component have flatter HREE, and are less MREE depleted.

Cpx-II in group 1, represented by MEPB61, are generally anomalous relative to the other samples, with the lowest aegirine and highest diopside component. This sample has a flat HREE pattern resulting in the lowest Lu/Ho ratio (figure 6.14 and 6.31). In MEPB61, a single cpx-III (Aeg_{87}) grain had a moderate MREE and HREE depletion relative to the LREE. This can be observed from the high La/Lu and La/Ho ratio (figure 6.31).

.

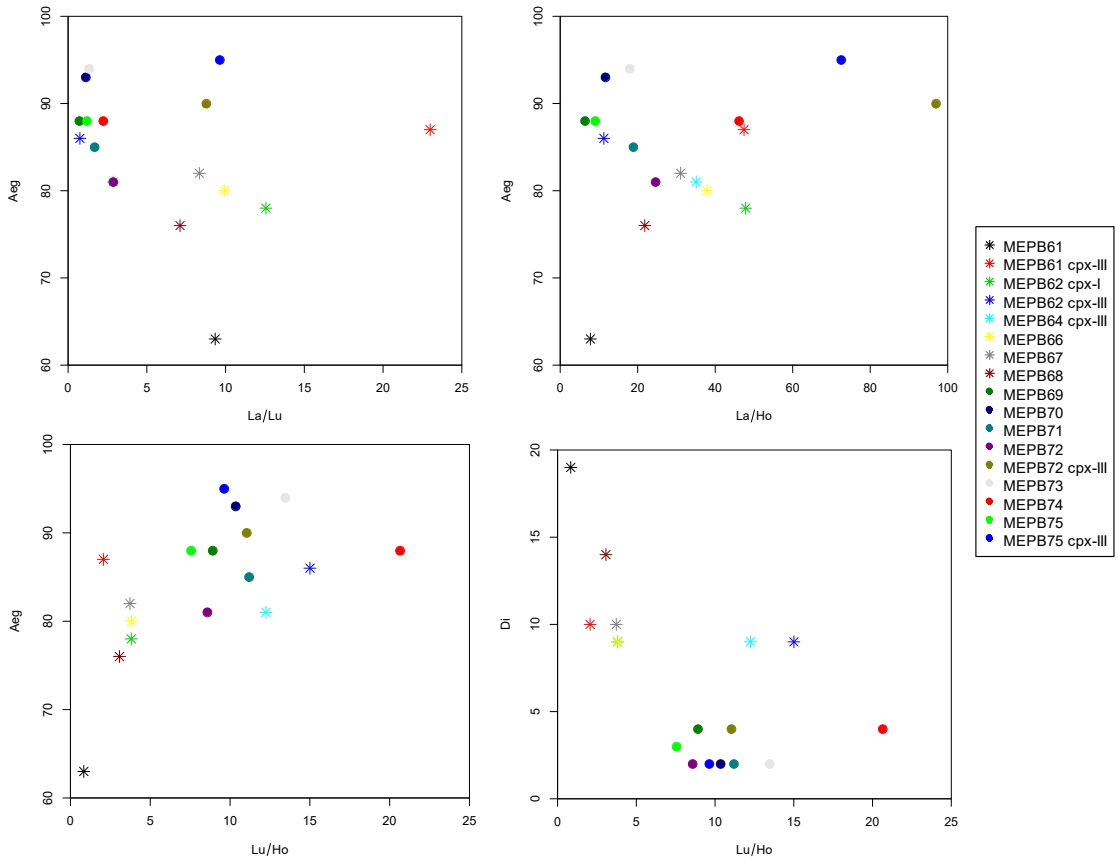

Figure 6.31: *Trace element ratios correlated with aegirine and diopside components. The results are based on average REE, Aeg and Di values. The plotted trace element values are un-normalized given in ppm. The pyroxene is cpx-II unless stated otherwise. Riverbed samples are represented by stars, and the boulder samples by circles.*

Discussion

7.1 Grouping of the samples

Overall the most substantial textural difference of the rock types observed in this study is whether the samples are foliated or unfoliated. This is consistent with Retief (1963) description of the Green Foyaite Suite where he describes the normal type with no igneous lamination, and the lujavrite type with a trachytic texture. The textural difference is further reflected in mineral composition. In foliated samples that contain amphibole, the amphibole is always magnesio-arfvedsonite while the amphibole in the unfoliated samples are exclusively arfvedsonites (figure 6.13). The foliated samples, as well as gorup 2 foyaites (from the riverbed) also have a higher modal percentage of orthoclase than the unfoliated samples (from the boulders) and have higher diopside component in their pyroxenes. Rinkite and eudialyte occur in both the unfoliated and the foliated varieties.

The foliated samples are subdivided into tinguaite and lujavrite. Group 1 defined in table 6.1 contains fine-grained flow-foliated tinguaite veins, while samples from group 3 and 4 can be classified as lujavrite based on their textural appearance, and their high alkalinity index. Lujavrite is the more evolved endmember of the Green Foyaite Suite, and the samples which have been defined as lujavrites have the highest whole rock (Na+K)/Al values. The tinguaites have lower (Na+K)/Al than the lujavrites and are closer in alkalinity to the unfoliated group 2 and 5 samples. These alkalinity values could indicate that the tinguaite veins are the dike equivalent of the unfoliated Green Foyaite, and not a dike equivalent to the more evolved lujavrite Green Foyaite endmember; alternatively the tinguaite could be unrelated from the Green Foyaite Suite altogether.

In the unfoliated Green Foyaite varieties, there are three subgroups based on their texture, REE patterns, and alkalinity. Group 6 and 7 samples are, based on Retief (1963) descriptions, part of the normal Green Foyaite type and this is the type which is petrographically most like the White Foyaite. Furthermore, this group has the lowest alkalinity values of the samples analyzed and these are comparable to the (Na+K)/Al and $K_2O/(K_2O + Na_2O)$ values of the White Foyaites and Ledig Foyaites (see figure 6.10). Even though they plot within to the Ledig Foyaite field, these samples do not display the typical pyroxene rosettes of the Ledig Foyaite.

The main difference between the White and the normal Green Foyaite is higher content of pyroxene in the Green Foyaites as well as higher modal percentage of agpaitic minerals, e.g. eudialyte and wöhlerite group minerals. As the unfoliated normal Green Foyaite share similarities in their major mineral assemblage as the White Foyaite, they could be two varieties crystalized from the same magma source. In the White Foyaite, the crystallization sequence is feldspar and nepheline followed by clinopyroxene, whereas in the Green Foyaite all three minerals were crystalizing simultaneously (Elburg & Cawthorn, 2017). It is difficult to determine if the White Foyaite is more closely related to the normal Green Foyaite or a total discrete intrusion or a combination of both.

Group 5 and group 2 of the unfoliated samples have different petrology and higher alkalinity than the normal Green Foyaite described above. The radiating plagioclase and plagioclase in a preferred orientation in group 5 samples has not been observed by Retief (1963), and he further described the normal Green Foyaite to not have feldspars in a preferred orientation. However, based on the major mineral chemistry and the accessory minerals found in the samples, group 5 is closest to the normal Green Foyaite with minerals such as astrophyllite and apatite. Therefore, the author proposes that these samples are a part of the normal Green Foyaite Suite.

Group 2 samples have a unique petrology compared to the other described samples. This group is the only group that contain poikilitic cpx-I as well as cpx-III in rosette-like structures. Furthermore, Group 2 samples have two distinct pyroxene REE-patterns, one that shows the MREE depletion in clinopyroxene (cpx-III) like the unfoliated samples and one clinopyroxene (cpx-I) REE-pattern that is more similar to the cpx-II in the foliated samples (figure 6.15). The sample with the highest content of rosette structures also has the highest alkalinity index of the unfoliated Green Foyaites. Ledig Foyaite is supposed to have radiating structures (Retief, 1963) and the highest alkalinity index (Lurie, 2004). As this applies to samples MEPB62 and MEPB64, they are compositionally close to the Ledig Foyaite. Retief (1963), however, described the Ledig Foyaite to have notable amounts of amphibole which is not observed in these samples. Furthermore, group 2 contains accessory minerals such as pectolite group minerals and lorenzenite, which are otherwise only identified in the foliated samples. The feldspar composition in group 2 samples is also similar to the foliated varieties as they are mainly pure orthoclase. It is important to note that group 2 samples are collected from the same area as the foliated samples. This, in addition to the alkalinity of the group 2 samples, can indicate that the group 2 samples are transitional between the foliated and unfoliated samples. They are, however, unique in their phosphorus content.

Based on the alkalinity of the samples, their textural relationship and accessory minerals, the proposed crystallization sequence is White Foyaites, the normal unfoliated Green Foyaite (group 6 and 7), group 5 Green Foyaites, Group 2 Green Foyaites, before the lujavrites (group 3 and 4). The tinguaites in group 1 are proposed to be the dike equivalent of the unfoliated Green Foyaites or could be unrelated to the Green Foyaite Suite all together based on their unique relatively flat REE-pattern and overall high REE content (figure 6.14).

7.1.1 The Ledig Foyaite

The Ledig Foyaite unit was first recognized by Retief (1963) in the field and was differentiated from the other units on the basis of characteristic radial clusters of pyroxene. The location of the unit can be seen in figure 3.2. Retief (1963) divided the Ledig Foyaite into type-I and type-II. In type-I, nepheline is fairly abundant and the feldspar is perthitic, and arfvedsonites are always present. Type-I, Ledig Foyaite is categorized by rare Zr-bearing accessory minerals such as eudialyte and astrophyllite. Zeolites, sodalite, and cancrinite are scarce. In type-II nepheline is absent, and the main feldspar is microcline. Arfvedsonites are present in small amounts while zeolites, cancrinite, and sodalite are abundant. Lurie (2004) further supported the existence of a separate Ledig Foyaite unit based on rare earth elements content and mineralogy, and argued that based on the mineralogy and rare earth element content that the Ledig Foyaite has a much closer resemblance to the Green Foyaite despite the resemblance to the White Foyaite in the field. Lurie (2004) contributed with geochemical analysis and found that the Ledig Foyaite as a whole contains the overall highest content of rare elements. Shand (1928) referred to the Ledig Foyaite suite as a transition between the White and Green Foyaite, as the Ledig Foyaite could resemble the White Foyaite on the southern side of the zone.

None of the samples studied in this thesis matches the exact descriptions of Retief (1963) and Lurie (2004), although some samples share similarities. Pyroxenes in MEPB64 (group 2) form radiating aegirine structures, where the primary feldspar is pure orthoclase with singe perthitic crystals. However, nepheline is relatively scarce, and no amphibole occurs in this sample, and the accessory minerals such as eudialyte, astrophyllite, and lamprophyllite, which are described as characteristic, are also absent. On the other hand, lorenzenite and rinkite occur in the sample and could be the yellow unknown accessory minerals that Retief (1963) described. Group 6 and 7 samples (from the boulders) described in this thesis do contain the characteristic mineral assemblage described for the Ledig Foyaite but do not have radiating aegirine structures in their cpx-III.

As argued in section 7.1, group 2 samples, which include MEPB64, have a unique petrology, with radiating cpx-III, but have mineral REE-patterns that are similar to the unfoliated samples and the foliated samples. The whole-rock analysis further have an alkalinity index that lies between the foliated and unfoliated samples. Therefore, the author believes that these samples are not the Ledig Foyaite, but a transitional phase between the foliated and unfoliated samples and therefore a subgroup of the Green Foyaites. It is, therefore, a possibility that the Ledig Foyaite is not a separate unit, but rather a variety within the Green Foyaite Suite.

7.1.2 Anomalous sample (MEPB75)

Compared to the other analyzed samples, one sample is anomalous. Sample MEPB75 (group 7) has the lowest whole rock (Na+K)/Al of 1.11, and plots very close to the White Foyaites in figure 6.10 A with a $K_2O/(K_2O + Na_2O)$ value of 0.37. Furthermore, it is the only sample which contains botn zircon and titanite, which by definition makes it miaskitic rather than agpaitic. This sample has by far the largest degree of replacement of early crystalized nepheline to secondary nepheline and sodalite and has the highest content of fluorite which is found together in a large cluster. The main feldspar is pure orthoclase, with only minor amounts of secondary perthitic feldspar, which is found in one large cluster, while the other samples in group 7 have mainly early crystallized perthitic feldspar.

Furthermore, this sample has large euhedral biotite crystals forming in one cluster interstitial to the feldspar and nepheline, while the other samples either have no biotite or the biotite is restricted to small laths within arfvedsonites. The clinopyroxene composition is similar to the other samples in the same group, except for one highly alkaline cpx analysis of Aeg_{98} which was obtained from a late formed rim of pyroxene. The REE-patterns are identical to the other samples in the same group. This sample also has a range of uncommon minerals with high REE-content such as the REE-carbonate and the three unknown minerals which have high concentrations of titanium, cerium, neodymium, and samarium. It is also the only sample where a secondary aluminum oxide (likely gibbsite, boehmite or diaspore) is found.

Based on the high degree of replacement of nepheline to sodalite and the high content of secondary REE minerals, this sample is likely to have gone through metasomatism with magmatic fluids with high activity of HF and HCl which also carry a large amount of incompatible elements, leading to the unusual mineral assemblage. This sample may therefore not be characterized as a normal Green Foyaite but as a profoundly altered sample with petrology and geochemical composition between the White and Green Foyaite.

7.2 Geochemistry

The whole rock major element chemistry shows that the samples MEPB60-76 are indeed peralkaline nepheline syenites. The foliated varieties and MEPB62 (from the riverbed) are more peralkaline than the unfoliated samples (from the boulders), and plot within the basic-nepheline syenite field, with basic meaning SiO_2 <52 wt.%. The boulder samples plot in the intermediate-nepheline syenites (figure 6.8). One can also include modal mineralogy to define the samples, as they all have typical agpaitic mineral assemblages with eudialyte and wöhlerite group minerals, which identifies them as agpaitic nepheline syenites. The elevated modal amount of clinopyroxene also show that they belong to the Green Foyaite Suite.

Compared to previous whole rock analysis of Andersen *et al.* (2018) and Elburg & Cawthorn (2017), the Green Foyaites overlap in peralkalinity with previously analyzed samples, however, the normal Green Foyaites from this thesis are mostly less peralkaline than the Green Foyaites from Andersen *et al.* (2018) and the unfoliated normal Green Foyaite has values that are more similar to the White Foyaite and the Ledig Foyaite. The peralkalinity of the average Green Foyaite from Elburg & Cawthorn (2017), however, matches the peralkalinity of the normal Green Foyaites in this thesis. These results indicate that the distinction between the Green and White Foyaites cannot only be made from peralkalinity.

The samples in this thesis are, however, do not overlap with the $K_2O/(K_2O + Na_2O)$ ratio of the previously analyzed Green Foyaites by Andersen *et al.* (2018), resulting in them plotting closer to the Ledig and White Foyaite field. As argued in section 7.1.1, the Ledig Foyaite might not be a separate suite in the Pilanesberg Complex, rather a subgroup of the Green Foyaites. Elburg & Cawthorn (2017) argued that the distinction between Na/K ratios between individual samples of the different units could point to the existence of different magmatic lineage or could be due to alteration. They further believe that the K_2O content of the samples with $>$ 10 wt.% has been modified by alteration process to some degree, as Na and K can be replaced on a 1:1 atomic basis. Na-K exchange has been described from similar rocks in Greenland (Elburg & Cawthorn, 2017). As the Na/K ratio differs greatly in the Green Foyaite samples from this thesis, and the Green Foyaites analyzed by Andersen *et al.* (2018), the explanation of the different $K_2O/(K_2O + Na_2O)$ ratio could be the result of a higher degree of fluid alteration in the unfoliated samples. There is, therefore, a possibility that the samples from this thesis are Green Foyaites which has been subjected to a higher degree of fluid alteration than the samples collected by Andersen *et al.* (2018), which were mainly derived from an area close

to Sun City.

7.2.1 Substitution mechanisms

The analyses of the aegirine crystals show high titanium concentrations up to 6.6 wt.%, where titanium enters certain coordination-polyhedra in the crystal lattice, not just as a trace element, but also as a major constituent. Titanium may enter into the aegirine crystal lattice in two ways:

The most common substitution mechanism is for the Ti^{4+} to substitute into the M1 position, which is compensated by one Al^{3+} to be incorporated into the tetrahedral (T) position: $NaTi^{4+}(SiAlO_6)$. The other substitution mechanism is less common but has been known to happen in highly alkaline environments. Here, instead of incorporating one Al in the T-position, the titanium enters the M1 position where Fe^{3+} will be replaced by 0.5 Ti and 0.5 Fe^{2+} resulting in: $Na_2Fe^{2+}Ti(Si_2O_6)_2$.

Figure 7.1 shows that when plotting Fe^{3+} against Ti+Zr, the analysis falls on a trend with a slope, suggesting that the $Fe^{3+}_{-1}(Ti, Zr)_{+0.5}Fe^{2+}_{+0.5}$ substitution mechanism is mainly responsible for Ti and Zr uptake in the pyroxenes. The high titanium content in aegirine suggests that it can be classified as titanian-aegirine only when Ti >0.1 apfu (Morimoto, 1989). Titanian-aegirine is found in the analysis of all the unfoliated Green Foyaite types, with the exception of MEPB74.

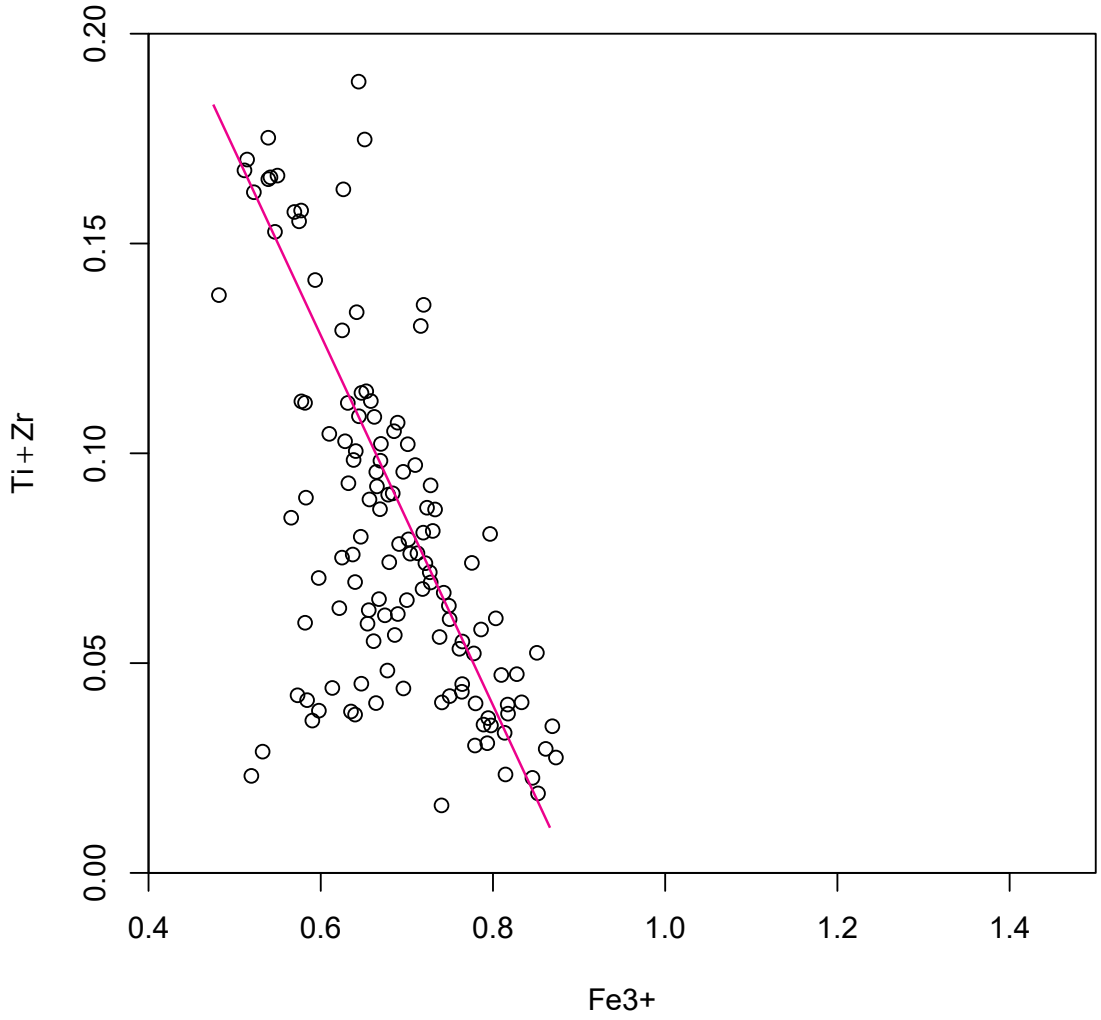

Figure 7.1: *Titanium substitution plot with the x-axis represents the cation (Fe^{3+}) which are substituted out of the crystals lattice of the pyroxene, while the y-axis represents the ions which are substituted into the crystals lattice (Zr and Ti). The data is plotted from the major element geochemistry in table B.3.*

7.2.2 Trace elements in clinopyroxene and amphibole

Clinopyroxene-II in the tinguaite (group 1), represented by sample MEPB61, have the highest chondrite-normalized REE values up to 2000 times chondrite at Lu. These analyses differ from the other samples in the fact that they have relatively flat patterns, with no MREE depletion. This can be observed in figure 6.31, where MEPB61 have the lowest Lu/Ho ratio and a relatively low La/Ho ratio. MEPB61 is LREE enriched relative to HREE, but less so than other samples. The average cpx-II in MEPB61 can also be seen in figure 7.2, which has a relatively flat pattern, and

significantly higher total REE than the other average clinopyroxenes. From these REE versus aegirine trends, it is not apparent that the tinguaite veins have evolved from the same magma as the other samples from the Green Foyaite Suite in this thesis. The closest chondrite-normalized values are one single grain from MEPB71, which reaches 1500 times chondrite at Lu. This grain was a euhedral, primary cpx-II, with low aegirine component. Other than the high Lu concentration in MEPB71, this sample shows no further similarities to cpx-II in MEPB61 in their REE pattern.

There appears to be a correlation between aegirine component and REE-concentration, with the samples with high aegirine component, generally having the lowest LREE concentrations, and higher HREE. For example, the average cpx-II in MEPB75 have an average aegirine component of Aeg_{90}, and La and Lu at 30 times chondrite, while cpx-II in MEPB68 have an average Aeg_{74} and La at 60 times chondrite, and Lu at 10 times chondrite (figure 6.28). Higher diopside component (and lower aegirine component) can be correlated with lower Lu/Ho, indicating that the samples with lower aegirine/higher diopside component have flatter HREE, and are less MREE depleted. The severe MREE depletion relative to the HREE and LREE suggests that cpx-III in MEPB62 and MEPB64 formed from a more evolved (because of the higher Aeg-content) and MREE-depleted magma. This is shown by these analyses having the highest Lu/Ho ratio, but the lowest La/Lu ratio (figure 6.31). These clinopyroxenes also display higher sodium content than the cpx-I from the same sample, also suggesting a more alkaline magma that has retained the more incompatible elements but has fractionated out the MREE. In MEPB62, the primary cpx-I have a much higher LREE content than Cpx-III and less MREE depletion, suggesting the primary clinopyroxenes formed from a less fractionated melt. This suggests that both LREE and MREE have been depleted in the more evolved melt.

Group 5, 6 and 7 samples (all collected from the boulders) together have similar cpx-II REE trends, with severe MREE depletion relative to LREE and HREE. The average cpx-II pattern for these unfoliated samples is plotted in figure 7.2. These samples, excluding cpx-III, have the highest Lu/Ho ratios and the highest aegirine components. The HREE and MREE in these samples have matching concentrations, resulting in La/Lu ratios close to 1. These samples have similar varieties of clinopyroxenes and amphiboles and the samples are collected from the same locality and are likely formed from the same magma. The amphiboles analyzed generally follow the same depletion trends as the pyroxenes in the same samples, indicating that in-situ amphibole fractionation is not the cause for the middle rare earth depletions. These samples also have La/Lu ratios close to 1, showing that the LREE

and HREE are enriched relative to the MREE, suggesting that LREE also has been depleted relative to the HREE.

Compared to the analysis from the White Foyaite in Giles (2018) master thesis, the overall REE-patterns of what she has described as the blue amphibole are similar to the REE-patterns of the arfvedsonite in the unfoliated Green Foyaite samples, with the average La values being between 10-100 times chondrite, with a decrease towards Ho at between 1-10 times chondrite and increase towards Lu at 20-30 times chondrite. The average arfvedsonite from this thesis and the average blue amphibole from the White Foyaite described by Giles (2018) have been plotted in figure 7.2, and show that these REE-patterns are almost identical. The unfoliated Green Foyaites are, however, only identical to the outer White Foyaite. MEPB42 is taken from the inner White Foyaite and displays a flatter REE-pattern which is more similar to the clinopyroxene in MEPB61 (figure 7.2). The inner variety (MEPB42) could be earlier crystallized than the outer White Foyaite, which has crystallized before the MREE has been depleted in the magma.

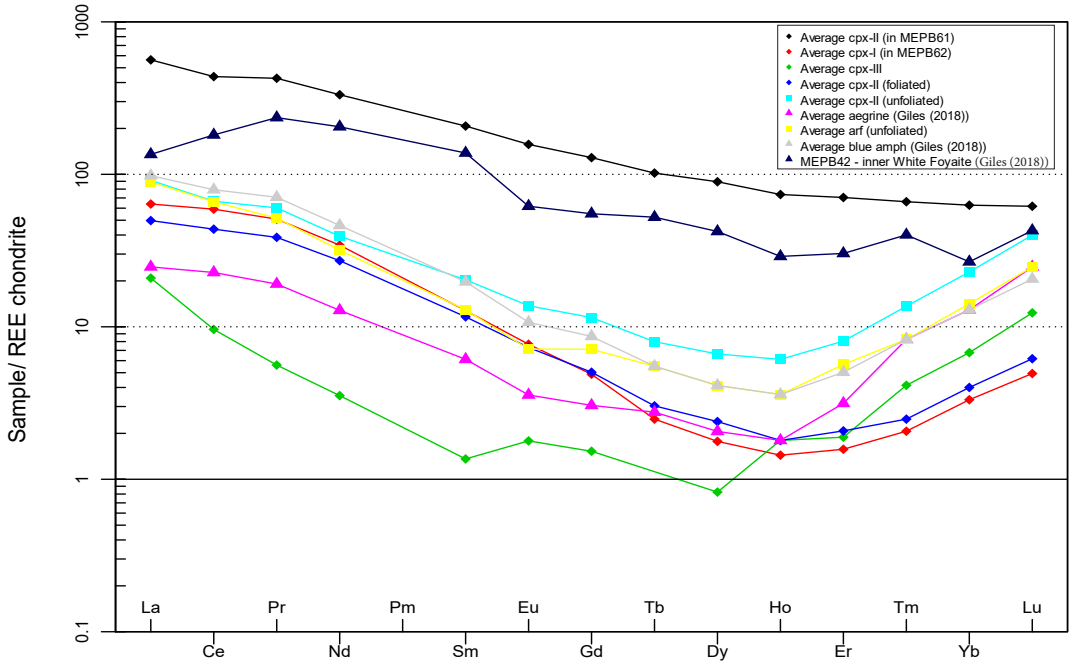

Figure 7.2: *Average cpx and arfvedsonite REE patterns in the Green Foyaite compared to the average REE pattern of the blue amphibole and pyroxene in the White Foyaite described by Giles (2018). The samples from the White Foyaite is marked with a triangle. The boulder samples are marked with a square, and the riverbed samples with a diamond shape. The data used in this plot is presented in table B.9.*

The average aegirine REE-patterns in the White Foyaite follow the same REE-patterns as the average cpx-II in the unfoliated Green Foyaite (figure 7.2). In general, the aegirines have La values between 6 and 80 times chondrite, with MREE depletion relative to the LREE and HREE. Positive Ce anosmalies can be found both in P9c in the White Foyaite and MEPB73 in the Green Foyaite. The average chondrite normalization values are, however, higher in the Green Foyaite.

The theory for the MREE depletion in Giles (2018) thesis was in-situ fractionation, with minerals such as apatite incorporating the MREE. Giles (2018), however, looked at pockets of residual melt on mm to cm scale. It is unlikely that such a model can be applicable for larger volumes of magma. A similar fractionation process operating at a much larger scale could possibly be an explanation in the unfoliated Green Foyaites as the SEM-EDS analyses of the unfoliated samples all contain apatite group minerals. This can, however not be the case in the more evolved foliated Green Foyaites, as they do not have apatite-group minerals, but this could be due to a deeper fractionation removing both P and the MREE. The question remains if there has been a more primitive amphibole fractionation. Based on experimental data, Bottazzi *et al.* (1999) suggested that MREE and HREE depletion could be due to early fractionation of amphibole, which is removed from the melt by sinking to the bottom of the magma chamber, thus removing the MREE and HREE from the liquid causing the depletion in the remaining magma. The experimentally derived distribution coefficients from Bottazzi *et al.* (1999) are not specifically for compositions similar to those observed in the Pilanesberg rocks.

7.3 Magma source

As mentioned in chapter 1, the suggested magma sources for agpaitic rocks are in general thought to be either plagioclase-bearing alkali basaltic to basanitic compositions or feldspar-free nephelinitic compositions. Plagioclase incorporates Sr and Eu, and fractionation of plagioclase will, therefore, deplete residual melt in these elements which will have negative Eu anomalies as a result. Further on, this will result in low Sr values in the resulting rock compositions. Samples of the Green Foyaite from Pilanesberg contain Sr-rich minerals such as strontium apatite, strontium carbonate, celestine, burbankite, and ancylite-(Ce), suggesting that strontium has not systematically been depleted in the residual magma, suggesting nephelinitic parent melt composition.

On the other hand, Elburg & Cawthorn (2017) argued that experimental studies indicate that high-pressure fractionation of alkali basaltic composition could yield

an evolved liquid with about 54 wt.% SiO_2 and 6 wt.% FeO*, which approximates the inferred Pilanesberg parental magma as represented by the dike compositions. These values are also close to the whole rock data of the Green Foyaites in this thesis. The observations from the experimental work suggest that fractionation assemblages of clinopyroxene and amphibole can produce evolved liquids without any plagioclase fractionation, which would keep the high Sr concentration observed in the Pilanesberg samples. A lower pressure fractionation event may separate plagioclase and lower pressure fractionation of alkali basaltic compositions thus could possibly explain the Eu anomaly in the amphiboles in the unfoliated Green Foyaites.

7.3.1 Late stage fluid interaction

One indication of shallow level emplacement is the high halogen content in the samples as the partitioning behavior of halogens are pressure dependent (see section 2.2.5). As previously mentioned, the rims of the pyroxenes in the unfoliated Green Foyaite have higher sodium content than the cores. These samples also showed a high degree of secondary sodalite replacement and high content of fluorite (and other F-bearing minerals) indicating formation from either late stage or hydrothermal fluids with high activity of HCl, HF and otherwise incompatible elements such as the alkali elements, HFSEs and REEs. Fluids with high salinity, therefore, have affected the mineralogy of the unfoliated Green Foyaites. One reaction which can produce sodalite from nepheline is:

$$KNa_3Al_4Si_4O_{16} + 2SiO_4 + NaCl \rightarrow Na_4Si_3Al_3O_{12}Cl + KAlSi_3O_8 \qquad (7.1)$$

In equation 7.1 additional silica as well as NaCl are required. To produce secondary sodalite, saline fluid interaction is the most likely cause.

Another evidence of fluid interaction was field evidence. A pegmatite vein at location 1 (figure 3.5) displayed bright green aegirine rosettes, while the aegirine elsewhere was black, suggesting compositional differences due to fluid interaction. There are no pegmatite samples in this thesis and these compositional differences could not be tested. However, based on the aegirine rims in this thesis, the aegirine rosettes in the pegmatites likely have a higher aegirine component than the black aegirine close to the pegmatite vein.

7.4 Estimate of the REE pattern of the least evolved melt

Analysis 01.02 of clinopyroxene-II in MEPB68 was determined to be the least evolved clinopyroxene in that its REE pattern is relatively flat with no MREE depletion and diopside component in this grain is Di_{15}. This analysis is plotted in figure 7.3. The sample overall does not appear to have been subjected to alteration as there is no replacement of nepheline to secondary sodalite, which makes this sample suitable to estimate the melt composition. The clinopyroxene in MEPB68 has euhedral shapes and are the earliest formed minerals in the sample together with the feldspars and nepheline. The REE distribution in the melt in equilibrium with the aegirine was determined using the partition coefficient (K_D) for the rare earth elements and the concentration of each REE in the clinopyroxene. Rearranging the definition of the partition coefficient described in eq. 4.1, one can attempt to determine the concentration of the melt in equilibrium with the clinopyroxene:

$$C_L = (C_{Min})/(K_D) \tag{7.2}$$

Estimations of the K_D values for a system can be challenging as in addition to melt composition, the presence of volatiles, the redox state of the system as well as pressure and temperature influence the K_D values (Janoušek *et al.*, 2015). Several attempts have, however, been made to use K_D values to estimate the melt in equilibrium with the mineral phase. The aim of this thesis is to estimate the shape of the REE-pattern in the liquid and not the absolute concentration.

In general, the REE partition coefficients range between 0.3-50, but are typically between 2-6, with a minimum for high aegirine pyroxenes. As pyroxenes become more Na- and less Ca-rich (Aeg_{25-50}), REE incorporation becomes less favorable, and both the M1 and M2 sites expand (to 0.79Å and 1.12Å) increasing D_{LREE}/D_{MREE}. Above Aeg_{50}, both M sites shrink slightly, and HREE partition strongly onto the M1 site, consistent with a reduced charge penalty for REE $\leftrightarrow$ Fe^{3+} substitution (Beard, 2018).

The Ph.D. thesis by Beard (2018) includes a model that predicts the trace-element partition coefficient between pyroxene and a silicate melt using only the mineral major element compositions, temperature, and pressure as input. The spreadsheet calculates the number of atoms in the T, M1 and M2 positions, where Si, Fe^{2+} and Al can be incorporated into the T position. In the M1, Al, Fe^{3+}, Fe^{2+}, Ti, Mg Mn and Ca can be incorporated, and the amount of each element in the M1

position are calculated. In M2, Mg, Fe^{2+}, Mn, Ca and Na can be incorporated and the spreadsheet calculates the amount of each in the M2 position. However, instead of calculating the T, M1 and M2 positions with the spreadsheet, these values were manually included as the amount of these elements in each sites were calculated during the apfu calculations of the pyroxene analyses, using the method in appendix D. For MEPB68, the K_D values calculated using this spreadsheet (named SD4) can be seen in table 7.1.

Table 7.1: *Data used in estimation of the REE pattern of the least evolved melt.*

Element	La	Ce	Pr	Nd	Sm	Eu	Gd	Tb	Dy	Ho	Er	Tm	Yb	Lu
MEPB-68-1.1	28.44	68.76	9.50	36.66	6.99	1.68	4.95	0.60	3.07	0.47	1.21	0.16	1.18	0.21
P4	315.51	480.66	36.93	82.05	6.01	1.51	4.24	0.63	3.27	0.74	2.58	0.26	3.21	0.33
K_D values:														
SD4	2.85	3.84	4.73	5.33	5.33	4.92	4.34	3.65	2.94	2.32	1.80	1.40	1.09	0.86
Marks max	0.99	2.06	-	3.56	7.29	9.39	-	9.74	-	-	-	2.00	2.10	2.83
Marks min	0.22	1.05	-	2.53	2.12	1.07	-	1.45	-	-	-	0.92	0.33	1.08
Botazzi	0.12	0.19	0.28	0.40	0.65	0.66	0.93	1.00	0.97	1.03	0.85	0.82	0.79	0.70
Calculated C_L:														
CL(SD4)	9.99	17.90	2.01	6.88	1.31	0.34	1.14	0.16	1.04	0.20	0.67	0.11	1.08	0.25
Cl(Marks max)	28.73	33.38	0.00	10.30	0.96	0.18	0.00	0.06	0.00	0.00	0.00	0.08	0.56	0.07
Cl(marks min)	129.27	65.49	0.00	14.49	3.30	1.57	0.00	0.41	0.00	0.00	0.00	0.17	3.58	0.20
Calculated C_0:														
C_0	8.20	14.92	1.71	6.01	1.21	0.32	1.12	0.16	1.04	0.20	0.65	0.11	1.03	0.23

Marks *et al.* (2011) published the maximum and minimum K_D values for aegirine in syenite. These values have, together with SD4, been used to calculate an attempt on the REE-melt-pattern (table 7.1). Using eq. 7.2 these K_D values were divided by the REE-concentrations in point 01.02 in MEPB68 (figure 7.3).

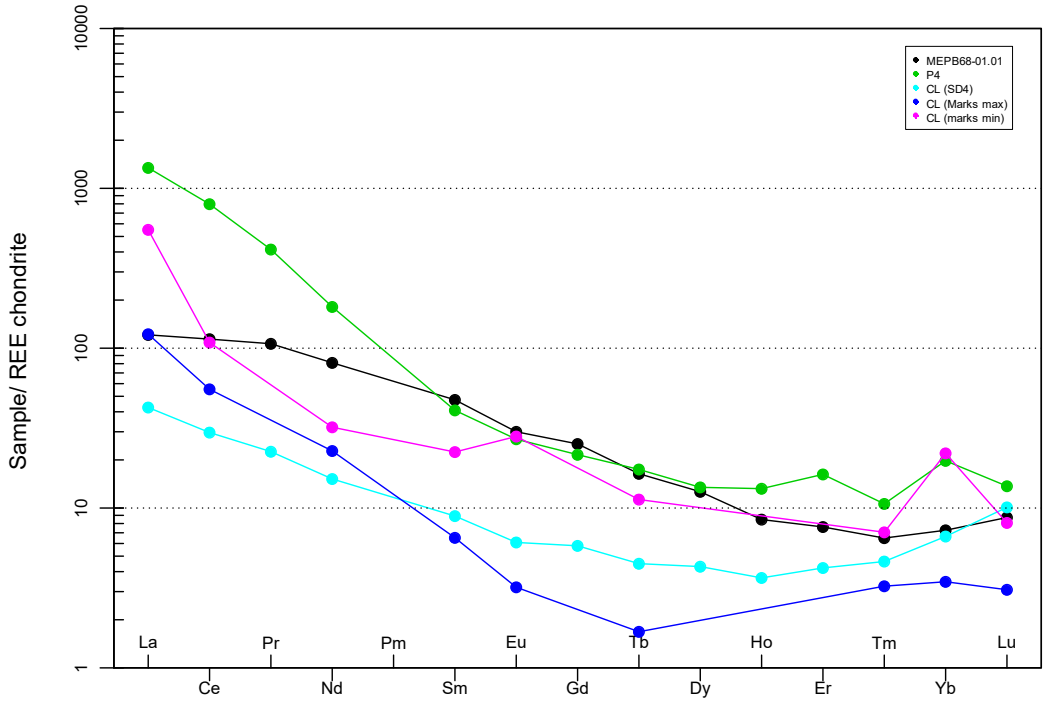

Figure 7.3: *Estimated liquid REE-compositions based on K_D values from Beard (2018) (SD4) and Marks* et al. *(2004) as well as the observed cpx analysis MEPB68-01.01 and the whole rock composition for a lujavrite from the Pilanesberg Complex (P4).*

The resulting patterns in figure 7.3 lie between 30 to ca. 1000 times chondrite at La and end at between 4 and 20 times chondrite at Lu. The pattern resulting from the calculated K_D values from Beard (2018) ($C_L(SD4)$) give a smooth pattern which gradually decreases towards Ho at 4 times chondrite, before a gentle increase towards Lu at 10 times chondrite.

The pattern based on K_D minimum values from Marks *et al.* (2011) gives a pattern that displays LREE depletion with Sm at 30 times chondrite, before gently increasing to Eu at 40 times chondrite. From Eu, the pattern has a gentle decrease towards Lu at 10 times chondrite except for a high Yb value of 40 times chondrite. There is a possibility that the Yb value is due to an analytical error. Using the maximal K_D values from Marks *et al.* (2011) gives a REE pattern which steeply decreases towards Tb, before showing a flat HREE pattern.

To determine whether these REE-patterns are realistic for a nepheline syenite liquid in equilibrium with aegirine, the patterns can be compared to other data from the Pilanesberg Complex. P4 is an unpublished whole rock analysis of a lujavrite, analyzed by M. Elburg in South Africa and has been plotted in figure

7.3 for comparison. The REE pattern of P4 shows a similar trend to $C_L(SD4)$, meaning these calculated REE trends could possibly represent the REE trend in the melt composition. The REE trend of P4 has, however, a different HREE pattern than $C_L(SD4)$. The negative spikes in the HREE for Tm and Lu for P4 are, however, likely analytical artifacts.

7.4.1 Estimation of the melt after amphibole fractionation

From the preferred estimated melt, which was chosen to be $C_L(SD4)$, one can further try to estimate the REE-content in the melt after 20 % amphibole fractionation. This is to determine if amphibole fractionation could be the cause for the observed MREE depletion. As argued in section 7.2.2, Bottazzi *et al.* (1999) suggested that MREE and HREE depletion could be due to early fractionation of amphibole. The amphbiole is removed from the melt by sinking to the bottom of the magma chamber and will therefore not re-equilibrate with any later melt, and thus causing depletion in the remaining magma. During fractional crystallization, the Rayleigh fractionation law can be used to describe the concentration of the given trace element in the melt (Luhr *et al.*, 1984; Janoušek *et al.*, 2015):

$$C_L/C_0 = F^{D-1} \tag{7.3}$$

Where C_0 is the parent relative to the residual melt C_L. F is the melt fraction, and D represent the distribution coefficient. The melt fraction, F, was set to 0.8 to represent 20% amphibole fractionation and the distribution coefficients used for amphibole were values from Bottazzi *et al.* (1999) (figure 7.4, and table 7.1). The distribution coefficients form Bottazzi *et al.* (1999) are based on experimental analysis on amphibole from alkali olivine basalt. By rearranging equation 7.3, one can attempt to estimate the melt after 20% amphibole fractionation:

$$C_L = C_0 * (F^{D-1}) \tag{7.4}$$

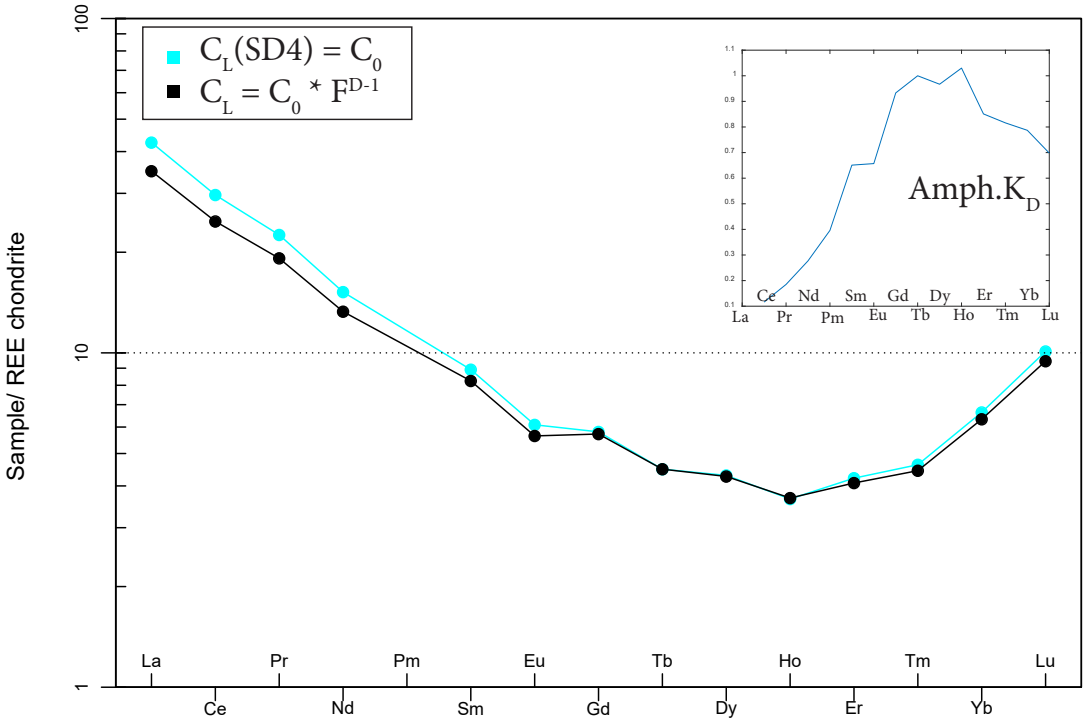

Figure 7.4: *REE-pattern of the estimated melt composition ($C_L(SD4)$), together with an estimated 20% amphibole fractionated melt (C_L). The figure in the right corner represent the amphibole K_D from Bottazzi* et al. *(1999).*

The resulting REE pattern (C_L figure 7.4) shows that the difference between the two patterns are minimal. The amphibole distribution coefficients do little to the patterns at 20% crystallization, and estimating amphibole fractionation using these values, therefore does not result in any significant results. To remove the MREE depletion with 20 % amphibole fractionation, one would need a system where the MREE are highly compatible, with distribution coefficients for the MREE ranging between 4 and 8.

7.4.2 The progressive crystallization theory

Another theory which could explain the MREE depletion is the different K_D values for the early magmatic cpx and the late magmatic cpx. The different types of pyroxenes are formed during different evolutionary stages of crystallization and the early magmatic and late magmatic pyroxene types have different major element compositions as together with temperature and pressure influence the K_D values of the pyroxene. Using the model by Beard (2018), that predicts the K_D values, shows that the early magmatic cpx-II has distribution coefficients for the LREE and

MREE that are compatible, which would result in the early magmatic pyroxenes to incorporate these elements (table 7.2). The residual magma could therefore be depleted in these elements before the late magmatic cpx-III are crystallized which could cause the drastic MREE depletion in cpx-III.

Table 7.2: *Calculated K_D values for the different types of pyroxene using the spredsheet by Beard (2018)*

	La	Ce	Pr	Nd	Sm	Eu	Gd	Tb	Dy	Ho	Er	Tm	Yb	Lu
Kd: cpx-I (Gr 2)	1.3	1.5	1.6	1.6	1.3	1.1	0.8	0.7	0.4	0.4	0.3	0.3	0.4	0.3
Kd: cpx-III (Gr 2)	3.4	3.6	3.6	3.5	2.8	2.5	2.1	1.8	1.3	1.2	1.0	0.8	0.7	0.5
Kd: cpx-II (Gr 6)	2.4	2.6	2.7	2.6	2.2	2.0	1.7	1.5	1.1	1.0	0.8	0.7	0.6	0.5
Kd: cpx-III (Gr 6)	2.0	2.1	2.1	2.0	1.6	1.4	1.2	1.0	0.7	0.7	0.5	0.4	0.3	0.3
Kd: cpx-II (Gr 7)	2.4	2.6	2.7	2.6	2.2	2.0	1.7	1.5	1.1	1.0	0.8	0.7	0.6	0.5
Kd: cpx-III (Gr 7)	2.0	2.1	2.1	2.0	1.6	1.4	1.2	1.0	0.7	0.7	0.5	0.4	0.3	0.3
Kd. Cpx-II (Gr 1)	1.0	1.3	1.5	1.6	1.3	1.1	0.9	0.7	0.4	0.4	0.5	0.6	0.6	0.7
Kd. Cpx-III (Gr 1)	1.3	1.5	1.6	1.5	1.1	0.9	0.7	0.5	0.3	0.2	0.2	0.2	0.2	0.2

By using eq. 7.2, one can estimate the REE-pattern in the melt using the K_D values and REE-concentrations in the mineral. When applying this to both the primary (type I and II) and secondary cpx (cpx-III) from the same sample, the resulting melt REE-patterns are similar (figure 7.5). This similarity can suggest that the primary and secondary cpx formed from the same magma, but as the primary cpx crystallized first, the LREE and MREE were incorporated in a higher degree in these primary pyroxenes.

To use the spreadsheet created by Beard (2018), one has to assume pressure and temperature conditions. As mentioned in section 2.2.5, the pressure estimates for agpaitic rocks are generally low, under 1 kbar. The pressure was set to 0.2 kbar and the temperature to 700°C. These conditions were also used by Beard (2018) for highly alkaline systems. The pressure and temperature conditions during crystallization of the different clinopyroxenes were likely within the same interval and the parameters chosen to be the same for both clinopyroxenes. However, by changing the pressure by 0.1 kbar and the temperature by 100°, either way, the K_D values changed <1%. Therefore, the eventual small change in pressure and temperature during crystallization of primary and secondary cpx, are deemed insignificant on the K_D values.

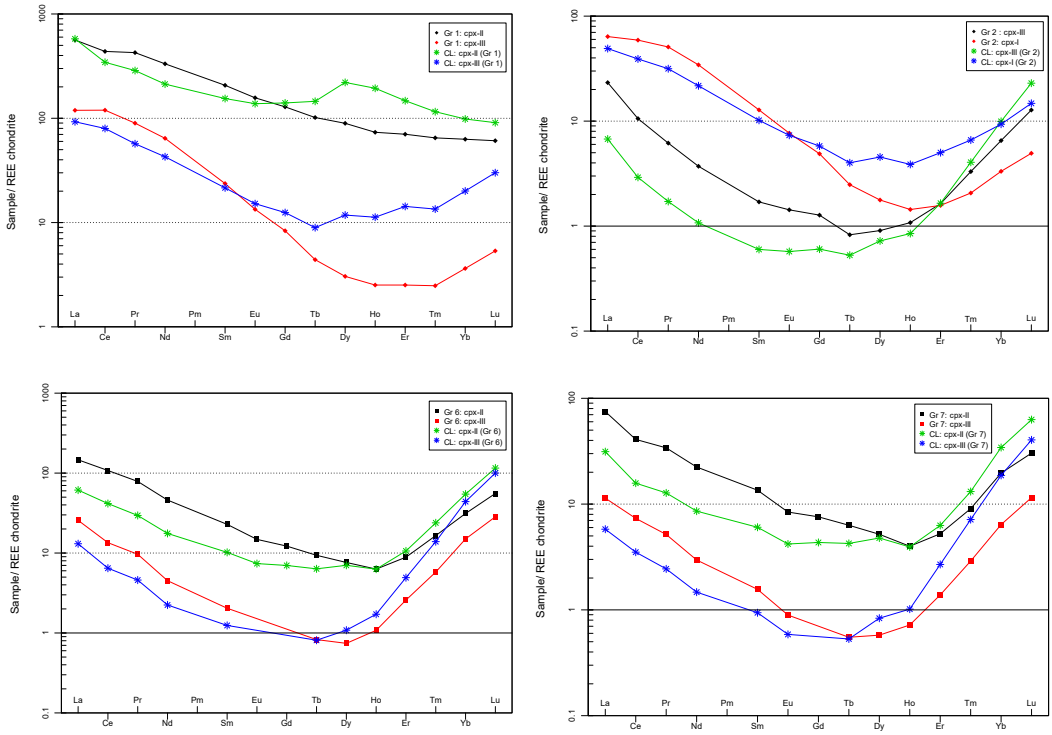

Figure 7.5: *REE melt compositions in equilibrium with the different pyroxene using unique K_D values for the different pyroxene types. Values used in this plot is presented in B.10*

7.4.3 Estimation of the melt after pyroxene fractionation

To test whether pyroxene fractionation could be the cause for the MREE depletion, one can estimate the REE-pattern in the liquid magma after 20% pyroxene fractionation. Furthermore, one can rearrange eq. 7.2 to calculate the REE-pattern for a clinopyroxene crystalizing from this fractionated residual magma:

$$C_{Min} = C_L * K_D \tag{7.5}$$

Using the REE-pattern of the inner White Foyaite (MEPB42), analyzed by Giles (2018), which is possibly a lesser evolved variety of the suite, one can first calculate the estimated melt pattern in equilibrium with the mineral using equation 7.2. The K_D values used was the calculated SD4 in table 7.1. These K_D values were chosen as they were calculated for a clinopyroxene without MREE depletion, and as the MEPB42 do not display MREE depletion this would be the best K_D estimations for this pattern. Major element analyses were not available for MEPB42, and therefore, K_D values for this exact analysis could not be calculated.

From the estimated REE-melt pattern in equilibrium with the clinopyroxene in MEPB42, one can further estimate the REE-pattern in the melt (C_L) after 20% pyroxene fractionation using eq. 7.4. The resulting fractionated melt pattern in figure 7.6 displays a moderate MREE depletion relative to LREE and HREE. From this fractionated liquid REE-pattern, one can use eq. 7.5 to calculate the REE concentrations in a clinopyroxene which crystalizes from the fractionated melt. The K_D values chosen for the estimated REE-pattern in a clinopyroxene crystalizing from the fractionated melt were the K_D values from cpx-II in group 6 (table 7.2). These K_D values were chosen as group 6 pyroxene were classified as the normal Green Foyaite, which is petrographically most similar to the White Foyaite. It is therefore most likely that the clinopyroxenes that crystallize from the fractionated melt from the White Foyaite are the primary clinopyroxenes in the samples which most resembles the White Foyaite.

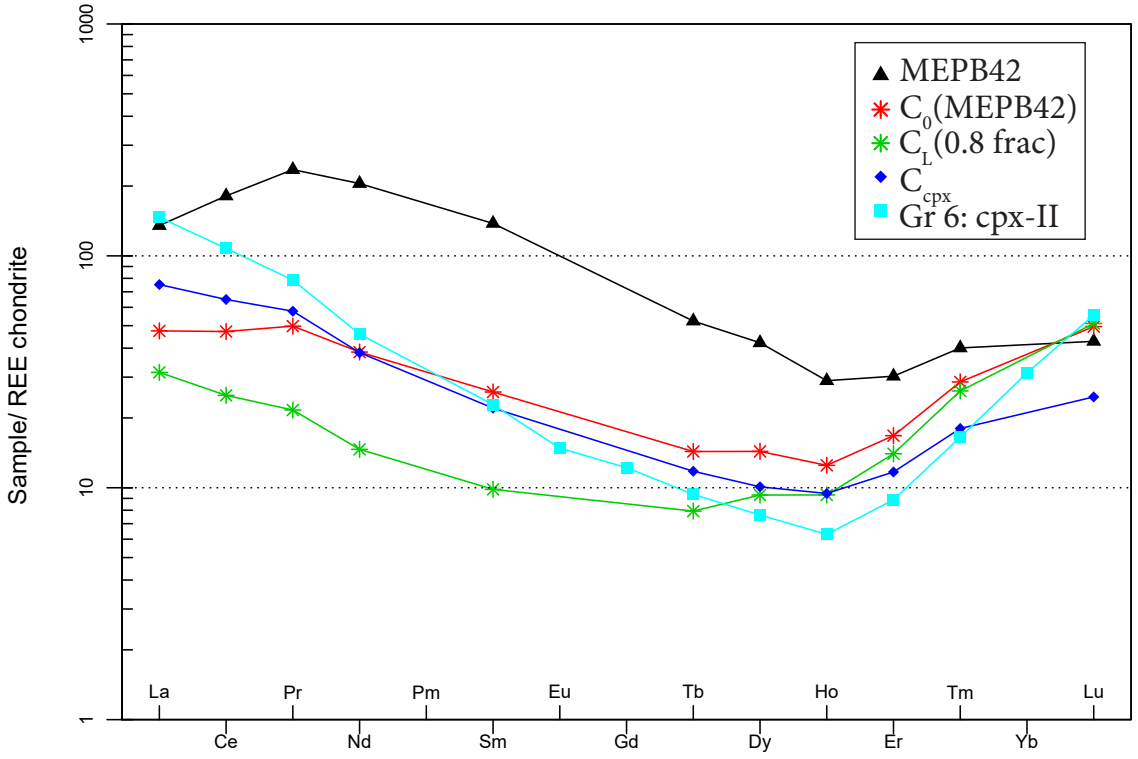

Figure 7.6: *Average pyroxene pattern from MEPB42 together with REE-pattern of the estimated melt composition in equilibrium with MEPB42 (C_0). The figure also includes the 20% pyroxene fractionated pattern which displays MREE depletion (C_L). Furthermore the figure includes the calculated REE-concentration of a cpx crystallizing from the fractionated melt (C_{cpx}). The average cpx-II from group 6 has been included for comparison. Values in this plot is presented in table B.11*

The resulting C_{cpx} pattern in figure 7.6 has chondrite normalized La values at

100 times chondrite, which gradually decrease towards Ho at ca. 10 times chondrite before an increase towards Lu at 30 times chondrite. When comparing this C_{cpx} pattern to the average cpx-II REE-pattern in group 6, the patterns are quite similar. This calculation can, therefore, suggest that fractionation of pyroxene could possibly cause the MREE depletion observed in the samples from this thesis, rather than fractionation of amphibole, which has previously been suggested.

7.5 Comparison to other alkaline complexes

The largest known agpaitic nepheline syenite intrusion is Khibina which is a part of the Kola alkaline province in Russia. Khibina has an exposed surface of 1327 km^2 and lies about 20 km south-east from the Lovozero intrusion which is also part of the Kola alkaline province (Kramm & Kogarko, 1994). Khibina is described as a laccolith type intrusion, much like the Cawthorn (2015) interpretation of the Pilanesberg Complex.

The Pilanesberg Complex and Ilìmaussaq are Proterozoic, however, relatively few other agpaitic rocks of this age are known. Most of the known agpaitic occurrences are in fact younger than 400 Ma, e.g. the nepheline syenites associated with the Kola province (Marks *et al.*, 2011). Agpaitic rocks most commonly occur as minor constituents in alkaline magmatic provinces, while agpaitic rocks in Pilanesberg, Ilímaussaq, Khibina, and Lovozero dominate the magmatic complex. However, in all the complexes mentioned above, miaskitic rocks still occur (Marks *et al.*, 2011). Further on, one can compare the Pilanesberg Complex to other alkaline complexes based on published whole rock data of major and trace element concentrations:

The samples from Pilanesberg are in general highly evolved with high Fe/(Fe+Mg) ratios, high peralkalinity, and enrichment of incompatible elements (Elburg & Cawthorn, 2017). The hyperagpaitic lujavrites from the Ilìmaussaq intrusion are more evolved than the Pilanesberg Complex has alkalinity indexes reaching over 2.3. Lujavrite from Lovozero has samples with alkalinity index of around 1.43 (Sørensen, 1997) which is comparable to the lujavrites studied in this thesis.

The Lovozero rocks have, however, a great variation of PI of the foyaites, from miaskitic to agpaitic with EGMs which reach PI of 1.75. In Khibina, there are no systematic chemical variations within the nepheline syenite intrusion, and the nepheline syenites have an alkalinity index of about 1.05 (Kramm & Kogarko, 1994). The nepheline syenites in Spitskop, South Afrika, are highly peralkaline with PI's generally between 1.1 and 1.3, which are comparable to the Green and White Foyaites in Pilanesberg (Elburg & Cawthorn, 2017; Harmer, 1999). Despite the high peralkalinity index of nepheline syenites in Spitskop, concentrations of Sr and Ba do not exceed 2250 ppm. Further on, both Nb and Y are low compared to other evolved alkaline rocks with average concentrations of only 19 ppm and 21 ppm respectively (Harmer, 1999).

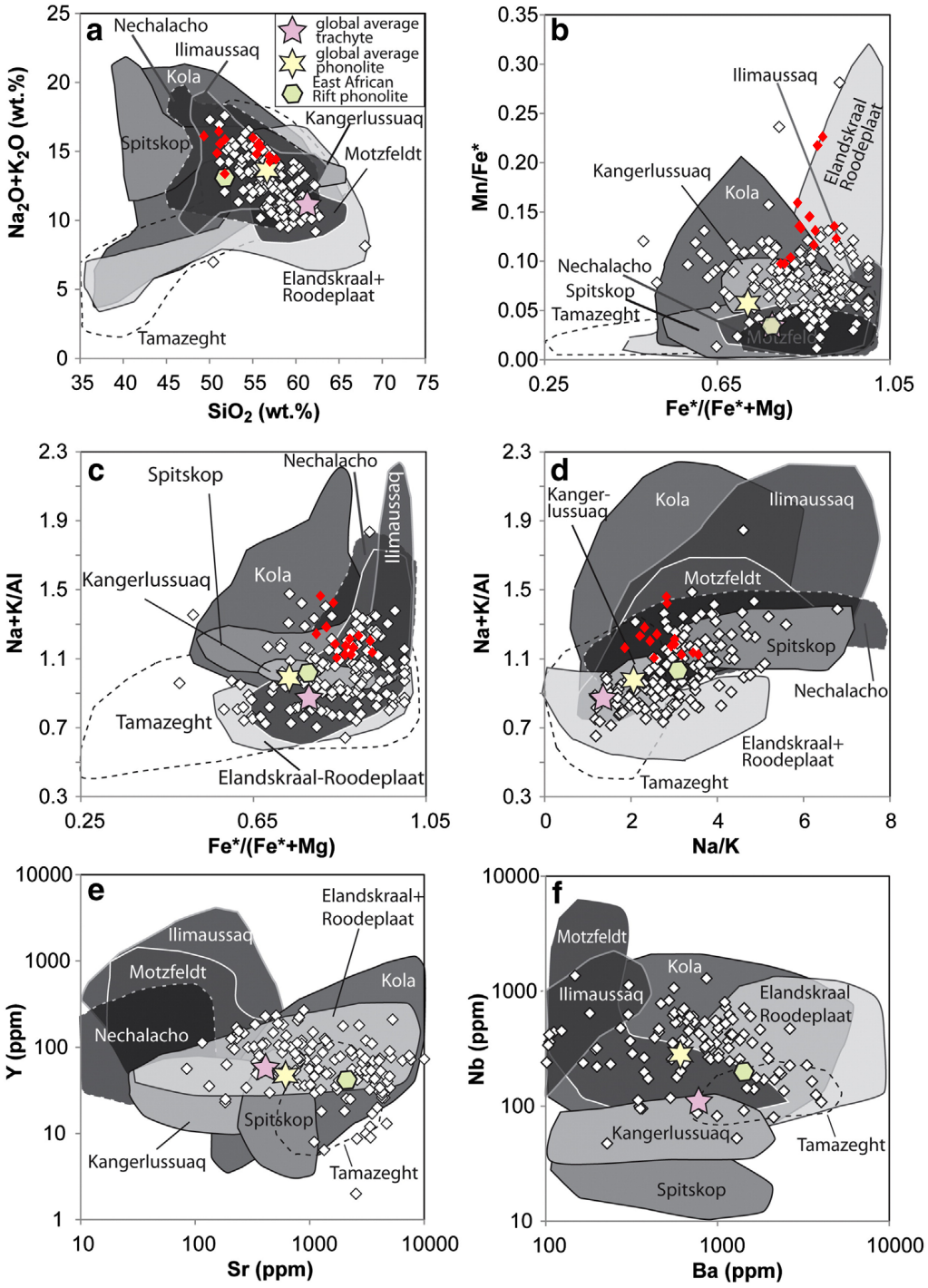

Figure 7.7: *Comparison of the Pilanesberg Complex data compared to whole rock data of other alkaline complexes. Figure from Elburg & Cawthorn (2017), and includes the whole rock data in this thesis in red.*

In terms of SiO_2 plotted against $Na_2O + K_2O$, the Pilanesberg samples are comparable most of the complexes in 7.7 a, but generally have higher SiO_2 concentrations than the nepheline syenites from the Spitskop Complex. Spitskop also differs from the Pilanesberg samples by having overall higher Na/K ratios, and the trace elements and other incompatible elements are significantly lower (Elburg & Cawthorn, 2017).

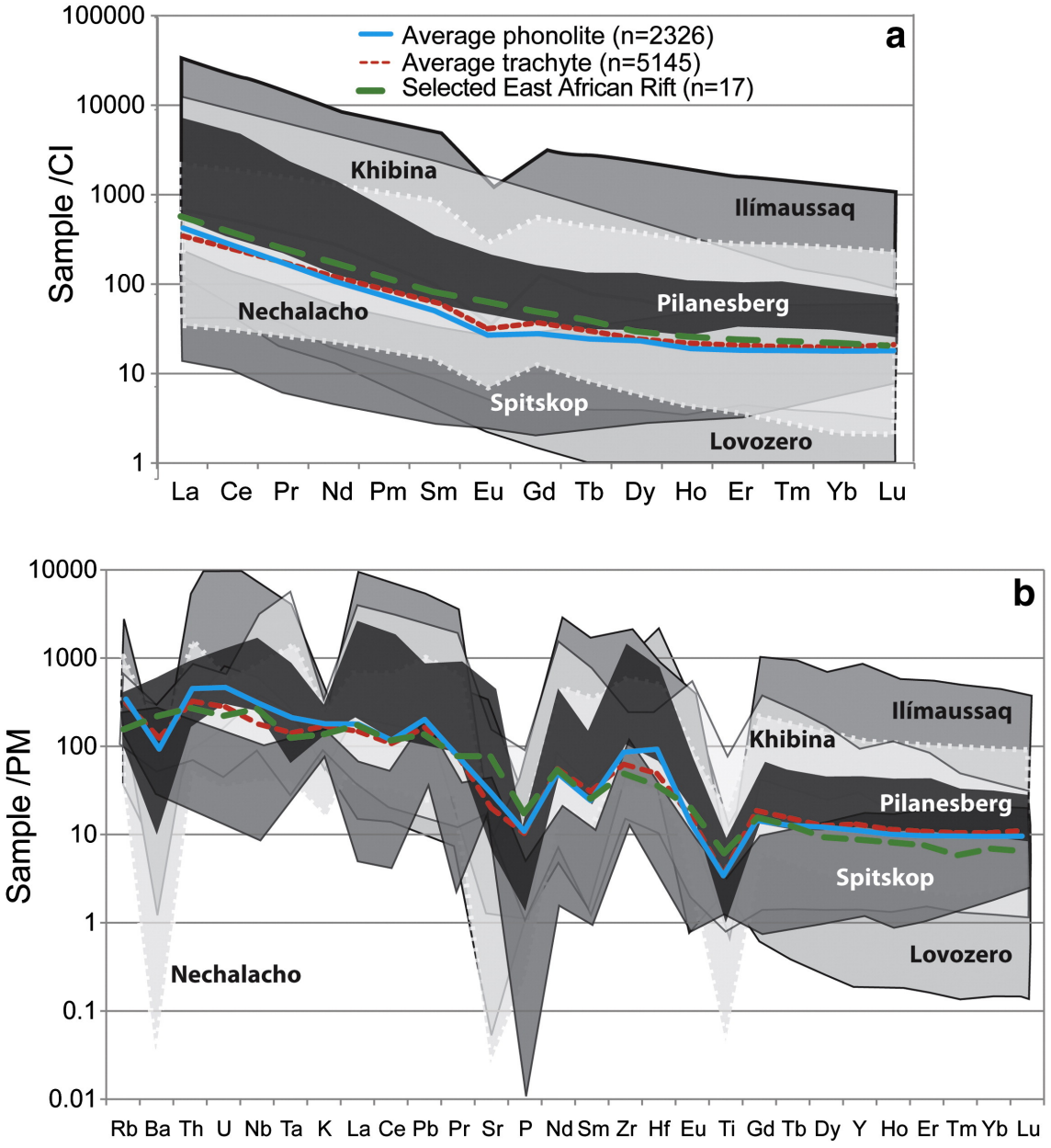

Figure 7.8: *Normalized trace element diagram for the Pilanesberg Complex compared to other complexes. Figure from Elburg & Cawthorn (2017).*

The nepheline syenites in Lovozero, as with Pilanesberg show a lack of significant Eu anomaly, which gives evidence that the agpaitic magma in the Kola region did

not form from basaltic liquids by fractional crystallization of plagioclase or anorthoclase at crustal level, but rather from a nephelinitic source (Kramm & Kogarko, 1994). Kogarko (1979) came to the same conclusion based on lower Sr/Ca ratios and more pronounced negative Eu anomalies in the REE patterns at Ilímaussaq compared to those at Lovozero. At Pilanesberg, the high Sr/Ca ratios and no Eu anomalies suggest that the nepheline syenites there were also derived from highly Si-undersaturated magmas. The Ilímaussaq system has in general high concentrations of REE with high LREE/HREE (Bailey *et al.*, 2001).

The Pilanesberg Complex is amongst the most Sr-rich complexes, together with the Kola and the East African rift, which suggest that plagioclase is not an important fractionation phase. The lower Sr content in Ilímaussaq together with negative Eu anomaly suggest plagioclase fractionation in these complexes.The presence of plagioclase megacysts and anorthositic xenoliths in intrusive rocks in the Gardar rift gives supporting evidence of plagioclase from magma that may have been parental to the Ilímaussaq Complex (Upton, 2013; Bridgwater & Harry, 1968). (Elburg & Cawthorn, 2017). In terms of Ba and Sr concentration, peralkalinity and Eu anomaly, the samples from the east African rift are the most comparable to the Pilanesberg Complex (figure 7.7 and 7.8).

Conclusion

Overall the most substantial textural difference of the rock types observed in this study is whether the samples are foliated or unfoliated. This is consistent with Retief (1963) description of the Green Foyaite Suite where he describes the normal type with no igneous lamination, and the lujavrite type with a trachytic texture. The textural difference is correlated with the sampling localities, where the samples from the riverbed are lujavrites, and the samples from the boulders have minerals heterogenous distributed and are categorized as a normal type Green Foyaite. The lujavrites have higher alkalinity indices than the normal Green Foyaites. The tinguaite, however, have PI's between the normal Green Foyaite and the lujavrite and could be the dike equivalent of the normal Green Foyaite or unrelated from the Green Foyaite altogether. The normal Green Foyaite is closest to the White Foyaite, and display similar REE-patterns with MREE depletion. The normal Green Foyaites have lower (Na+k)/Al and $K_2O/(K_2O + Na_2O)$ than the previously analyzed Green Foyaites collected from Sun City, resulting in them plotting within the White and Ledig Foyaite field. The normal Green Foyaites, however, do not display the petrology of the White or Ledig Foyaites, and have most likely been subjected to a higher degree of fluid alteration resulting in the different geochemical composition. The author also suggest that the Ledig Foyaite is not a separate unit, but rather a highly altered variety of the Green Foyaite Suite.

The aegirines analyzed in this thesis have high titanium concentrations, and several clinopyroxenes can be classified as titanian-aegirines. when plotting Fe^{3+} against Ti+Zr, the analysis falls on a trend with a slope, suggesting that the $Fe^{3+}_{-1}(Ti, Zr)_{+0.5}Fe^{2+}_{+0.5}$ substitution mechanism is mainly responsible for Ti and Zr uptake in the pyroxenes.

Trace element analysis shows that the clinopyroxenes in the foliated samples generally have higher total concentrations of rare-earth elements. The cpx-II in the foliated samples have, however, lower and straighter HREE concentrations than the unfoliated samples. The patters ranges from LREE-enriched, relatively straight patterns to distinctly MREE depleted through-shaped patterns. The later formed cpx-III in MEPB64 have the most drastic MREE depletion, suggesting that later formed clinopyroxenes have a higher degree of depletion of these elements. Amphibole in the samples they are analyzed, mimics the variations in the samples. This

shows that amphibole fractionation is not the cause of the depletion. The average cpx-II and arfvedsonites in this thesis show similar REE patterns as the average pyroxenes and blue amphiboles in the White Foyaite described by Giles (2018).

In the White Foyaite, the depletion of MREE in arfvedsonite and aegirine was most likely caused by in-situ apatite fractionation from a trapped, interstitial liquid in equilibrium with early amphibole. Because aegirine formed early in the crystallization sequence of the Green Foyaite magma, MREE depletion in the Green Foyaite cannot be explained by similar in-situ processes, and is more likely to be a result of a complex fractionation removing the middle REEs from the melt forming the agpaitic Green Foyaite prior to final emplacement of the magma. Fractional crystallization of clinopyroxene is a possible mechanism for progressively removing the MREE from the melt as shown by the calculations in this thesis.

8.1 Suggestions for further work

The pyroxene fractionation theory is only based on a few samples from this thesis. Therefore to further test this theory, analyses of the inner Green and White Foyaite could be correlated with the outer White and Green Foyaite to examine if the REE-patterns of the inner varieties could result in the REE-pattern of the outer varieties by fractional crystallization of pyroxene. Major and trace elements analysis of the inner varieties are therefore warranted to continue the calculations and comparison of the patterns.

References

Agangi, A., Hofmann, A., & Elburg, M. 2018. A review of Palaeoarchaean felsic volcanism in the eastern Kaapvaal craton: Linking plutonic and volcanic records. *Geoscience Frontiers*, **9**(3), 667–688.

Anders, E., & Grevesse, N. 1989. Abundances of the elements: Meteoritic and solar. *Geochimica et Cosmochimica acta*, **53**(1), 197–214.

Andersen, T., Erambert, M., Larsen, A.O., & Selbekk, R.S. 2010. Petrology of nepheline syenite pegmatites in the Oslo Rift, Norway: Zirconium silicate mineral assemblages as indicators of alkalinity and volatile fugacity in mildly agpaitic magma. *Journal of Petrology*, **51**(11), 2303–2325.

Andersen, T., Elburg, M., & Erambert, M. 2017. The miaskitic-to-agpaitic transition in peralkaline nepheline syenite (white foyaite) from the Pilanesberg Complex, South Africa. *Chemical Geology*, **455**, 166–181.

Andersen, T., Elburg, M., & Erambert, M. 2018. Contrasting trends of agpaitic crystallization in nepheline syenite in the Pilanesberg Alkaline Complex, South Africa. *Lithos*, **312**, 375–388.

Bailey, J.C., Gwozdz, R., Rose-Hansen, J., & Sørensen, H. 2001. Geochemical overview of the Ilímaussaq alkaline complex, South Greenland. *Geology of Greenland Survey Bulletin*, **190**(100), 35–53.

Barrat, J., Zanda, B., Moynier, F., Bollinger, C., Liorzou, C., & Bayon, G. 2012. Geochemistry of CI chondrites: Major and trace elements, and Cu and Zn isotopes. *Geochimica et Cosmochimica Acta*, **83**, 79–92.

Beard, C. 2018. *Mineral-melt Trace Element Partitioning in Alkaline Magmatic Systems*. Ph.D. thesis, McGill University Libraries.

Bottazzi, P., Tiepolo, M., Vannucci, R., Zanetti, A., Brumm, R., Foley, S.F., & Oberti, R. 1999. Distinct site preferences for heavy and light REE in amphibole and the prediction of Amph/L D REE. *Contributions to Mineralogy and Petrology*, **137**(1-2), 36–45.

Bridgwater, David, & Harry, William Trevelyan. 1968. *Anorthosite xenoliths and plagioclase megacrysts in Precambrian intrusions of South Greenland.* Vol. 185. CA Reitzel.

Brouwer, H.A. 1911. On peculiar sieve structures in igneous rocks, rich in alcalies. *Koninklijke Nederlandse Akademie van Wetenschappen Proceedings Series B Physical Sciences*, **14**, 383–387.

Brouwer, P. 2006. *Theory of XRF: Getting acquainted with the principles.* PANalytical BV.

Cawthorn, G.R. 2015. The geometry and emplacement of the Pilanesberg Complex, South Africa. *Geological Magazine*, **152**(5), 802–812.

Cawthorn, G.R., & Walraven, F. 1998. Emplacement and crystallization time for the Bushveld Complex. *Journal of Petrology*, **39**(9), 1669–1687.

Chima, P., Baiyegunhi, C., Liu, K., & Gwavava, O. 2018. Petrography, modal composition and tectonic provenance of some selected sandstones from the Molteno, Elliot and Clarens Formations, Karoo Supergroup, in the Eastern Cape Province, South Africa. *Open Geosciences*, **10**(1), 821–833.

Cline, J.S., & Bodnar, R.J. 1991. Can economic porphyry copper mineralization be generated by a typical calc-alkaline melt? *Journal of Geophysical Research: Solid Earth*, **96**(B5), 8113–8126.

Cox, K.G., Bell, J.D., & Pankhurst, R.J. 1979. The Interpretation of Igneous Rocks, 1979. *George Allen and Union. London*, **450**.

Elburg, M., & Cawthorn, G.R. 2017. Source and evolution of the alkaline Pilanesberg Complex, South Africa. *Chemical Geology*, **455**, 148–165.

Giles, K. 2018. *Distribution of trace elements among coexisting minerals in agpaitic nepheline syenites in the Pilanesberg Complex, South Africa.* M.Phil. thesis, University of Oslo.

Griffin, W.L., Powell W.J. Pearson N.J. O'Reilly S.Y. 2008. GLITTER: data reduction software for laser ablation ICP-MS. In: Sylvester, P. (Ed.), Laser Ablation–ICP–MS in the Earth Sciences. Mineralogical Association of Canada Short Course Series, **40**, 204-207.

Harmer, R.E. 1999. The petrogenetic association of carbonatite and alkaline magmatism: constraints from the Spitskop Complex, South Africa. *Journal of Petrology*, **40**(4), 525–548.

Humphrey, W. A. 1912. The volcanic rocks of the Pilandsberg. *Transactions of the Geological Society of South Africa 15, 100-106.*

Jahn, B.M., & Condie, K.C. 1995. Evolution of the Kaapvaal Craton as viewed from geochemical and Sm-Nd isotopic analyses of intracratonic pelites. *Geochimica et Cosmochimica Acta*, **59**(11), 2239–2258.

Janoušek, V., Moyen, J.F, Martin, H., Erban, V., & Farrow, C. 2015. *Geochemical Modelling of Igneous Processes: Principles and Recipes in R Language*. Springer. Chap. Dilute trace elements: Partition Coefficients, pages 101–104.

Jochum, K.P., Willbold, M., Raczek, I., Stoll, B., & Herwig, K. 2005. Chemical Characterisation of the USGS Reference Glasses GSA-1G, GSC-1G, GSD-1G, GSE-1G, BCR-2G, BHVO-2G and BIR-1G Using EPMA, ID-TIMS, ID-ICP-MS and LA-ICP-MS. *Geostandards and Geoanalytical Research*, **29**(3), 285–302.

Knauth, L.P., & Lowe, D.R. 2003. High Archean climatic temperature inferred from oxygen isotope geochemistry of cherts in the 3.5 Ga Swaziland Supergroup, South Africa. *Geological Society of America Bulletin*, **115**(5), 566–580.

Kogarko, L.N. 1979. Microcomponents as indicators of the differentiation of alkaline magmatic series. *Physics and Chemistry of the Earth*, **11**, 217–231.

Konnerup-Madsen, J., & Rose-Hansen, J. 1982. Volatiles associated with alkaline igneous rift activity: fluid inclusions in the Ilímaussaq intrusion and the Gardar granitic complexes (South Greenland). *Chemical Geology*, **37**(1-2), 79–93.

Kramm, U., & Kogarko, L.N. 1994. Nd and Sr isotope signatures of the Khibina and Lovozero agpaitic centres, Kola Alkaline Province, Russia. *Lithos*, **32**(3-4), 225–242.

Le Maitre, R. W., Streckeisen, A., Zanettin, B., Le Bas, M. J., Bonin, B., & Bateman, P. 2002. *Igneous Rocks : A Classification and Glossary of Terms*. Cambridge: Cambridge University Press.

Luhr, J.F., Carmichael, I.S.E., & Varekamp, J.C. 1984. The 1982 eruptions of El Chichón Volcano, Chiapas, Mexico: mineralogy and petrology of the anhydritebearing pumices. *Journal of Volcanology and Geothermal Research*, **23**(1-2), 69–108.

Lurie, J. 2004. *The Pilanesberg: geology, rare element geochemistry and economic potential (2nd edition).* Ph.D. thesis, UJ library.

Marks, M.A.W., & Markl, G. 2017. A global review on agpaitic rocks. *Earth-Science Reviews*, **173**, 229–258.

Marks, M.A.W., Hettmann, K., Schilling, J., Frost, B.R., & Markl, G. 2011. The mineralogical diversity of alkaline igneous rocks: critical factors for the transition from miaskitic to agpaitic phase assemblages. *Journal of Petrology*, **52**(3), 439–455.

Marks, M.and Halama, R., Wenzel, T., & Markl, G. 2004. Trace element variations in clinopyroxene and amphibole from alkaline to peralkaline syenites and granites: implications for mineral–melt trace-element partitioning. *Chemical geology*, **211**(3-4), 185–215.

Mathias, M. 1974. Alkaline rocks of southern Africa. *John Wiley London*, 189–202.

Mitchell, Roger H, & Liferovich, Ruslan P. 2006. Subsolidus deuteric/hydrothermal alteration of eudialyte in lujavrite from the Pilansberg alkaline complex, South Africa. *Lithos*, **91**(1-4), 352–372.

Molengraaff, G.A.F. 1905. Preliminary Note on the Geology of the Pilandsberg and a Portion of the Rustenburg District. *South African Journal of Geology*, **8**(Transactions 1905), 108–109.

Morimoto, N. 1989. Nomenclature of pyroxenes. *Mineralogical Journal*, **14**(5), 198–221.

Pouchou, J.L., & Pichoir, F. 1984. A new model for quantitative x-ray microanalysis. I.–application to the analysis of homogeneous samples. *Rech. Aerosp.*, 167–192.

Reed, S.J.B. 2005. *Electron microprobe analysis and scanning electron microscopy in geology.* Cambridge University Press.

Retief, E.A. 1963. *Petrological and mineralogical studies in the southern part of the Pilanesberg Alkaline Complex, Transvaal, South Africa.* Ph.D. thesis, Oxford University.

Rollinson, H.R. 2014. *Using geochemical data: evaluation, presentation, interpretation.* Routledge.

Shand, S.J. 1928. The geology of Pilansberg (Pilaan's Berg) in the Western Transvaal: a study of alkaline rocks and ring-intrusions. *South African Journal of Geology*, **31**(Transactions 1928), 97–156.

Shand, S.J. 1943. *Eruptive rocks: their genesis, composition, and classification, with a chapter on meteorites*. J. Wiley & sons, Incorporated.

Shannon, R.D. 1976. Revised effective ionic radii and systematic studies of interatomic distances in halides and chalcogenides. *Acta crystallographica section A: crystal physics, diffraction, theoretical and general crystallography*, **32**(5), 751–767.

Sørensen, H. 1960. On the agpaitic rocks. *International Geologic Congress. Report of the Twenty-First Session Norden, **13**, 319-327.*

Sørensen, H. 1992. Agpaitic nepheline syenites: a potential source of rare elements. *Applied Geochemistry*, **7**(5), 417–427.

Sørensen, H. 1997. The agpaitic rocks-an overview. *Mineralogical Magazine*, **61**(407), 485–498.

Sørensen, H., Bohse, H., & Bailey, J.C. 2006. The origin and mode of emplacement of lujavrites in the Ilímaussaq alkaline complex, South Greenland. *Lithos*, **91**(1-4), 286–300.

Thomas, R. 2001. A beginner's guide to ICP-MS. *Spectroscopy*, **16**(4), 38–42.

Upton, B.G.J. 2013. Tectono-magmatic evolution of the younger Gardar southern rift, South Greenland. *Geological Survey of Denmark and Greenland Bulletin*, **29**(2013).

Ussing, N.V. 1912. Geology of the country around Julianehaab, Greenland. *Meddelelser om Grønland, **38**, 1-426.*

Verwoerd, J.W. 2006. *The Geology of South Africa*. Pretoria : Council for Geoscience; Johannesburg : Geological Society of South Africa and Council for Geoscience, 2006. Chap. The Pilanesberg Alkaline Province, pages 381–394.

White, W.M. 2013. *Geochemistry*. Whiley-Blackwell. Chap. Trace elements in igneous processes, pages 268–318.

Wolley, A.R. 2002. Alkaline Rocks and Carbonatites of the World. Part 3: Africa. London, Bath: Geological Society of London. *Geological Magazine*, **139**(3), 365–372.

Zeh, A., Ovtcharova, M., Wilson, A.H., & Schaltegger, U.r. 2015. The Bushveld Complex was emplaced and cooled in less than one million years–results of zirconology, and geotectonic implications. *Earth and Planetary Science Letters*, **418**, 103–114.

Web references

https://www.mindat.org/ (last accessed May 2019)

https://www.geoscience.org.za/cgs/(last accessed May 2019)

http://www.earth.google.com/

Appendix A: EDS spectra

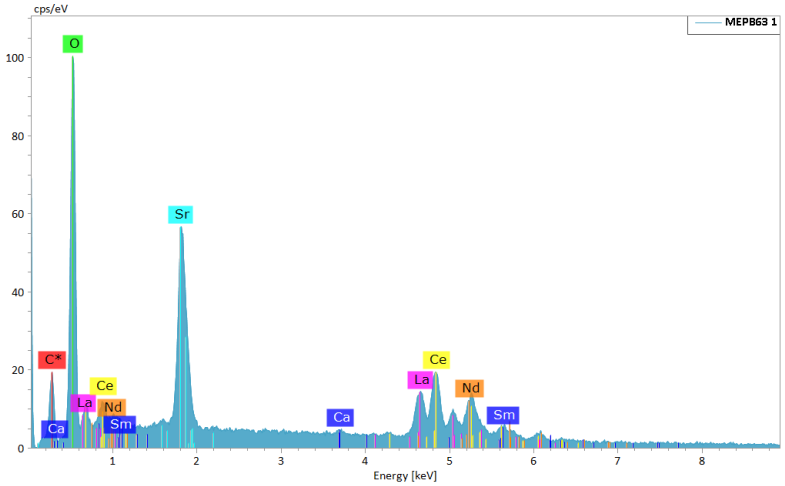

Figure A.1: *EDS spectra identified as ancylite-(Ce)*

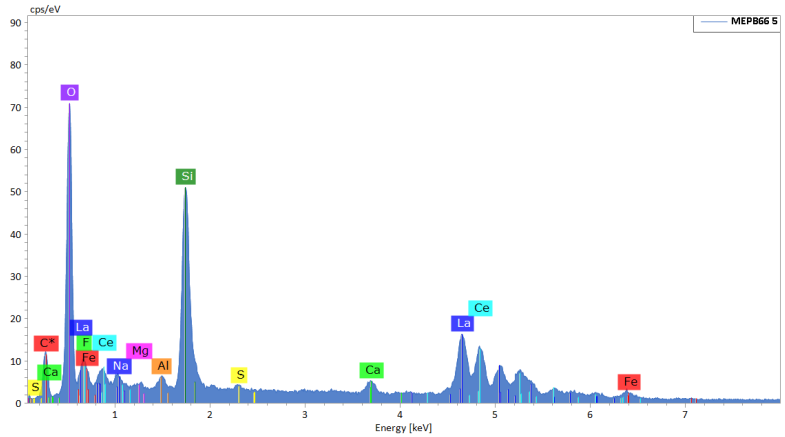

Figure A.2: *EDS spectra identified as britholite*

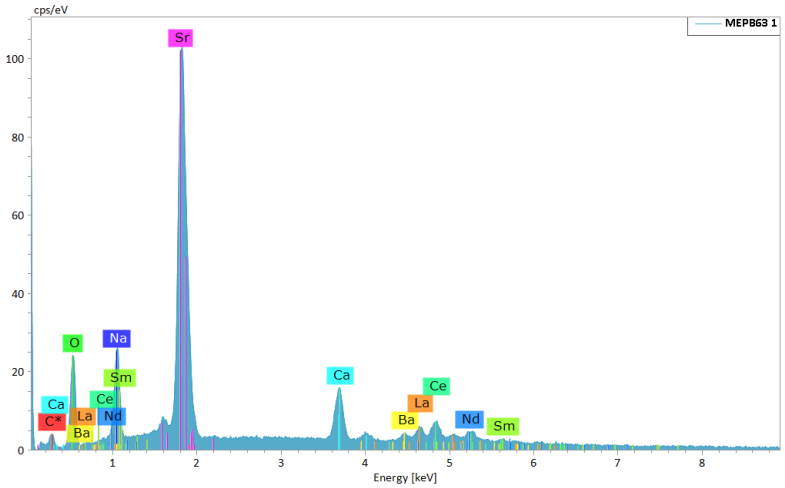

Figure A.3: *EDS spectra identified possibly as burbankite group mineral*

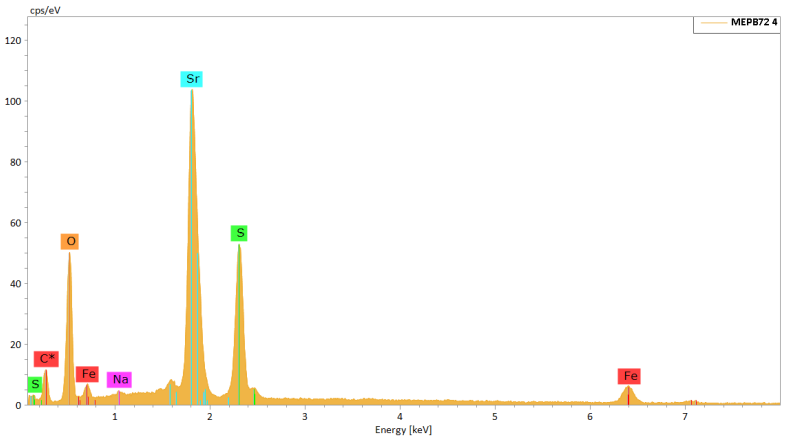

Figure A.4: *EDS spectra identified as celestine*

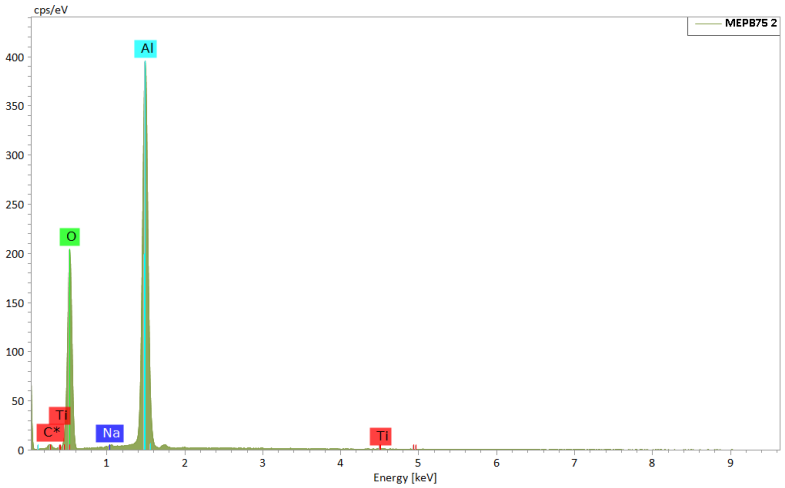

Figure A.5: *EDS spectra identified as gibsitt/bohemitt/diaspor*

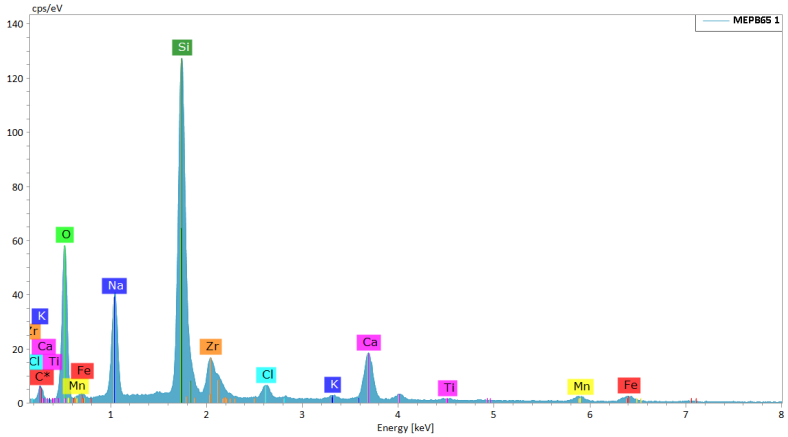

Figure A.6: *EDS spectra identified as eudialyte*

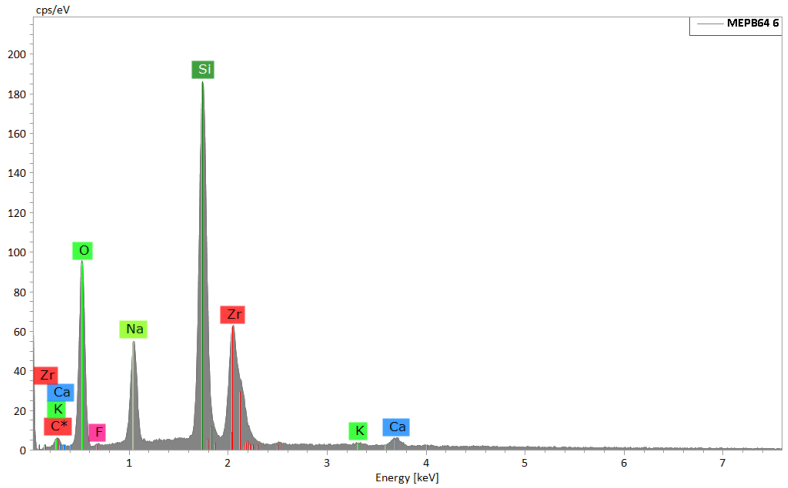

Figure A.7: *EDS spectra identified as hilairite/catapleiite*

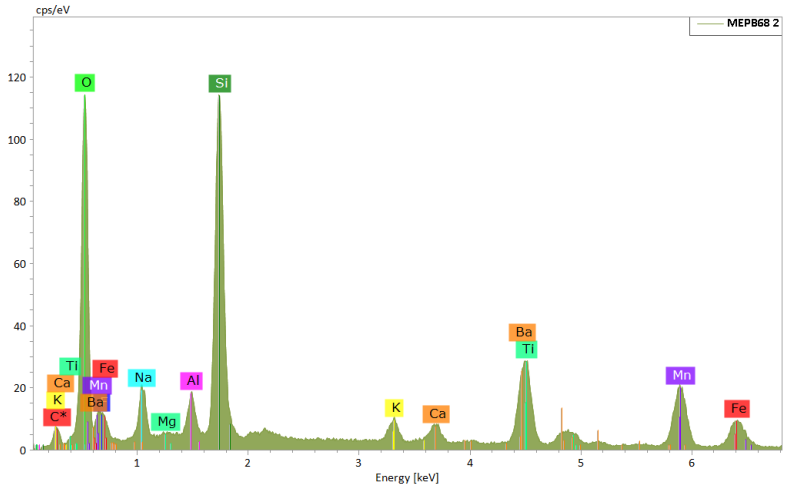

Figure A.8: *EDS spectra identified as possibly jinshajiangite*

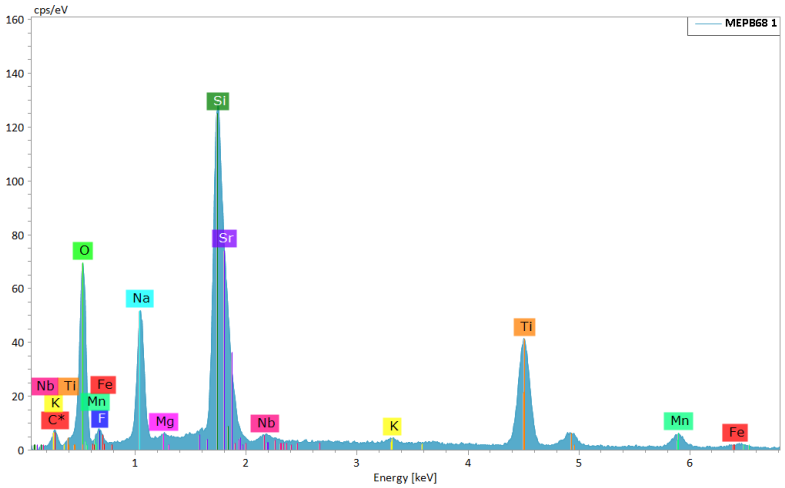

Figure A.9: *EDS spectra identified as lorenzenite*

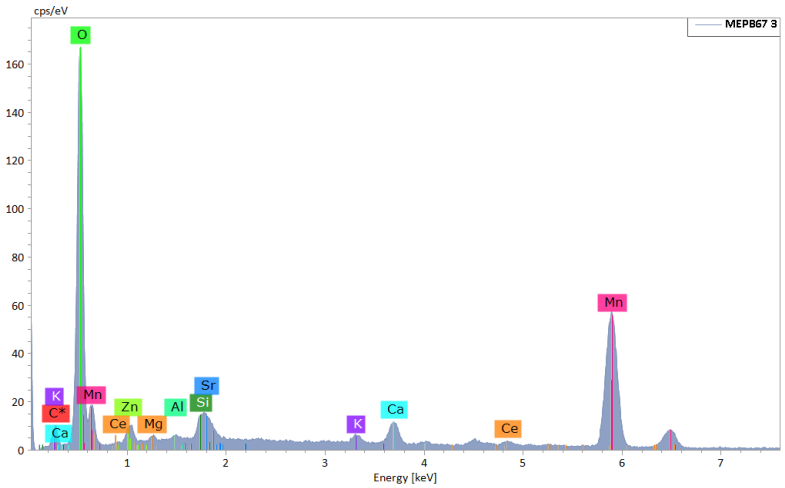

Figure A.10: *EDS spectra of a manganese oxide*

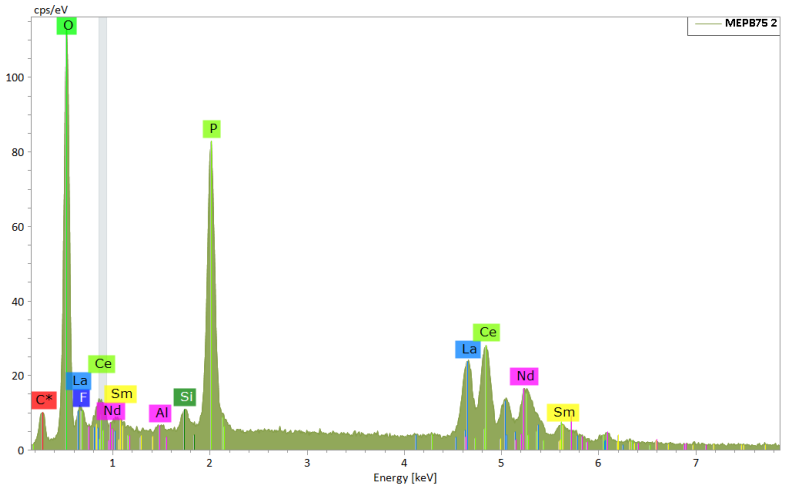

Figure A.11: *EDS spectra identified as monazite*

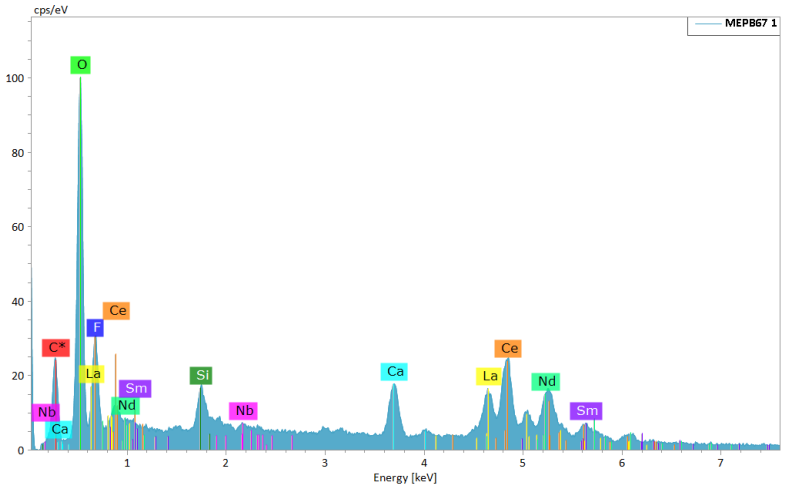

Figure A.12: *EDS spectra identified as parisite-(Ce)*

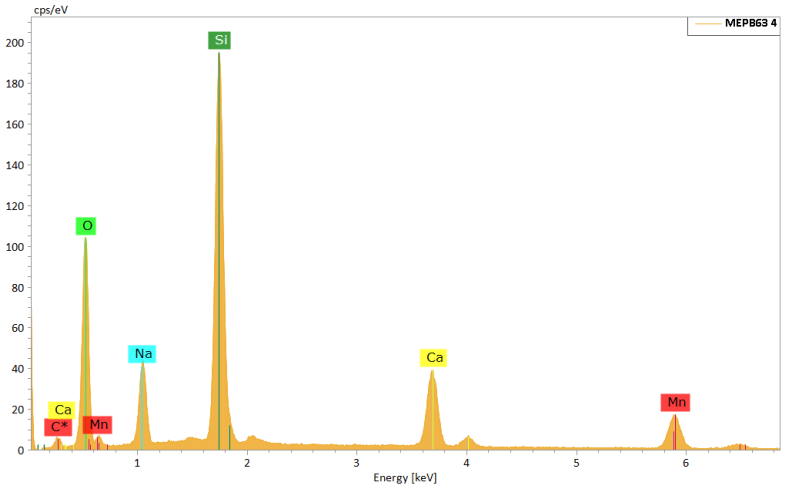

Figure A.13: *EDS spectra identified as pectolite group mineral*

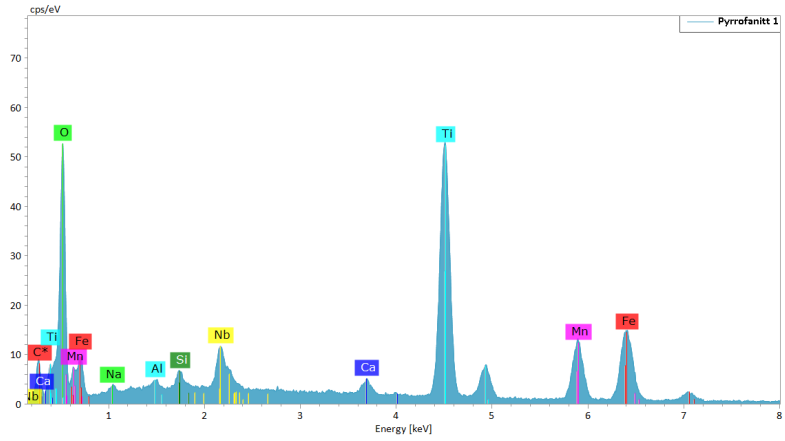

Figure A.14: *EDS spectra identified as phyrophanite*

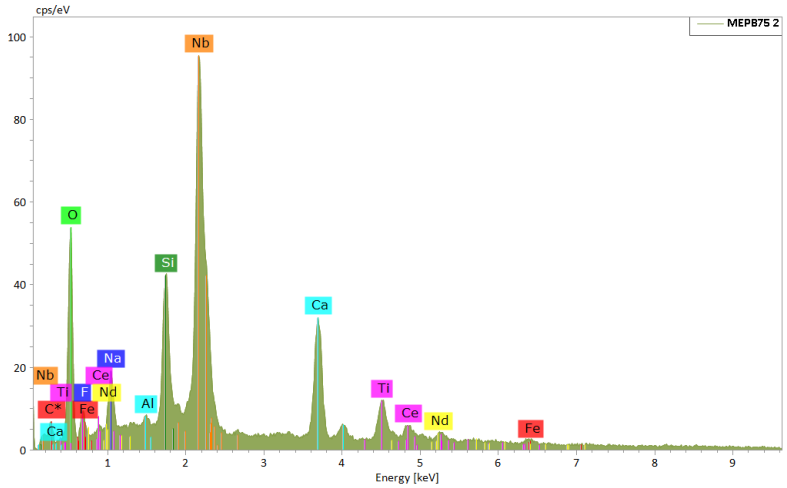

Figure A.15: *EDS spectra identified as a pyrochlor group mineral*

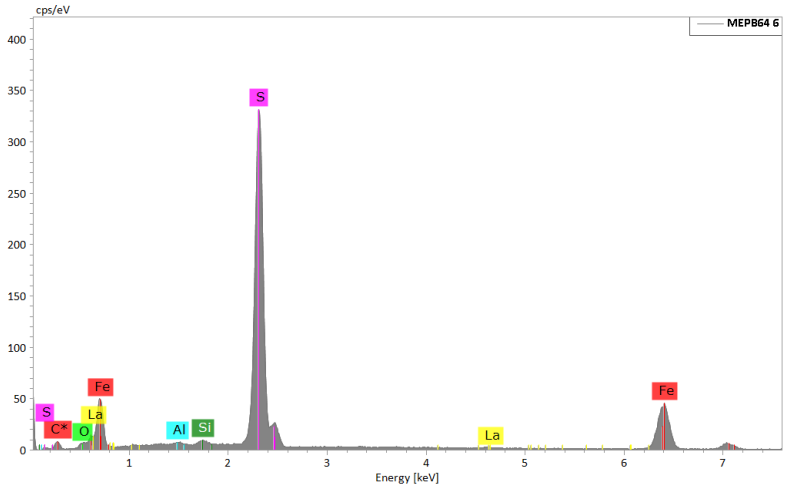

Figure A.16: *EDS spectra identified as pyrrhotite*

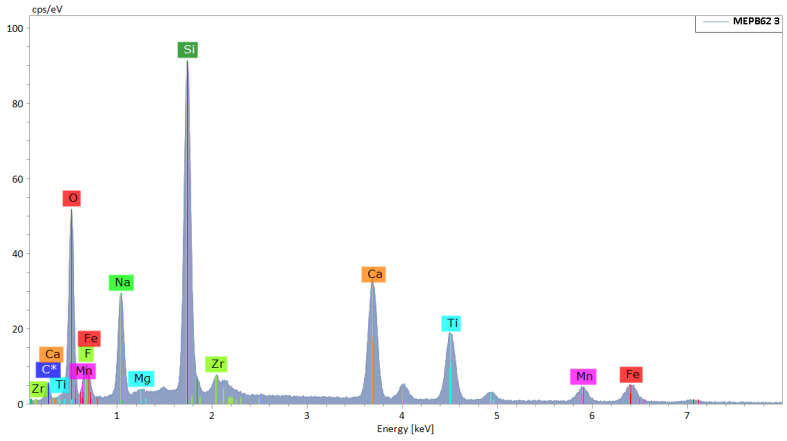

Figure A.17: *EDS spectra identified as rinkite*

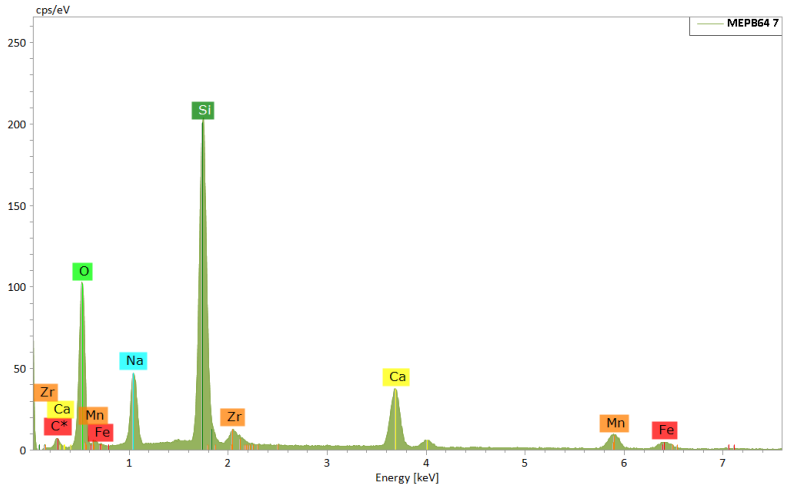

Figure A.18: *EDS spectra identified as possibly rosenbuschite*

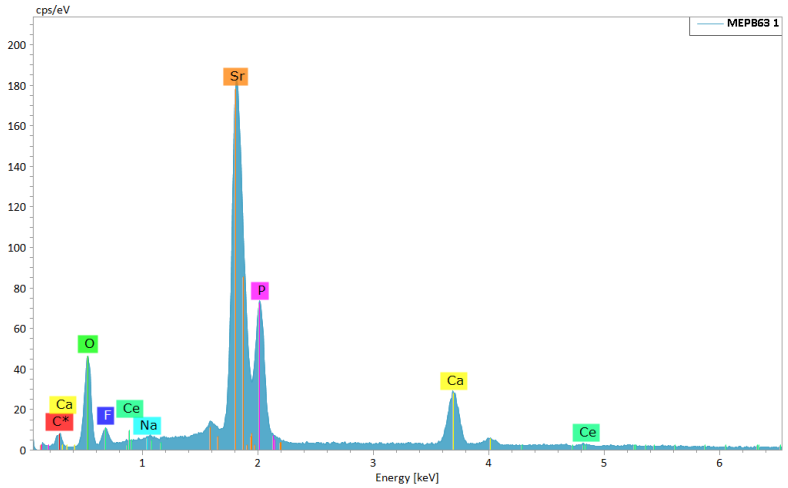

Figure A.19: *EDS spectra identified as strontium apatite*

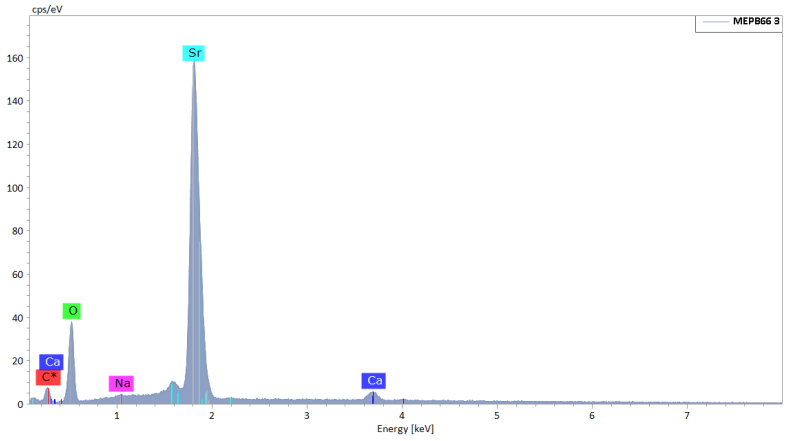

Figure A.20: *EDS spectra identified as strontium carbonate*

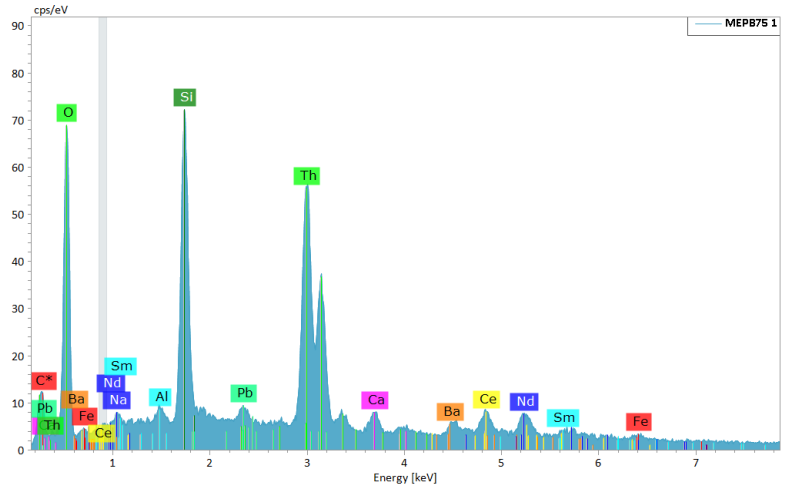

Figure A.21: *EDS spectra identified as thorite*

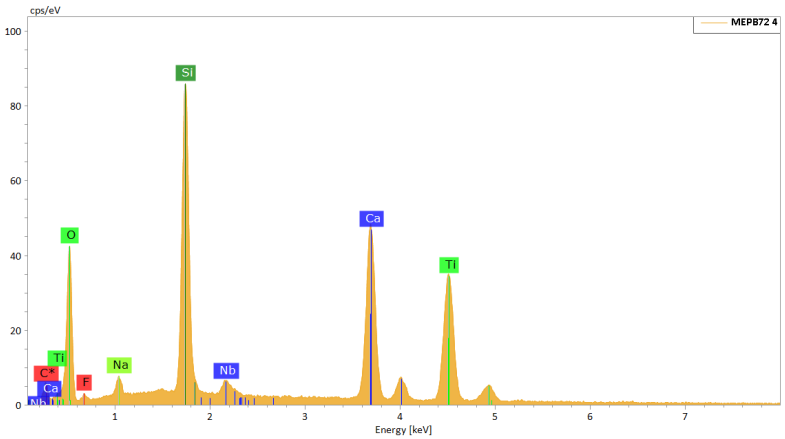

Figure A.22: *EDS spectra identified as titanite*

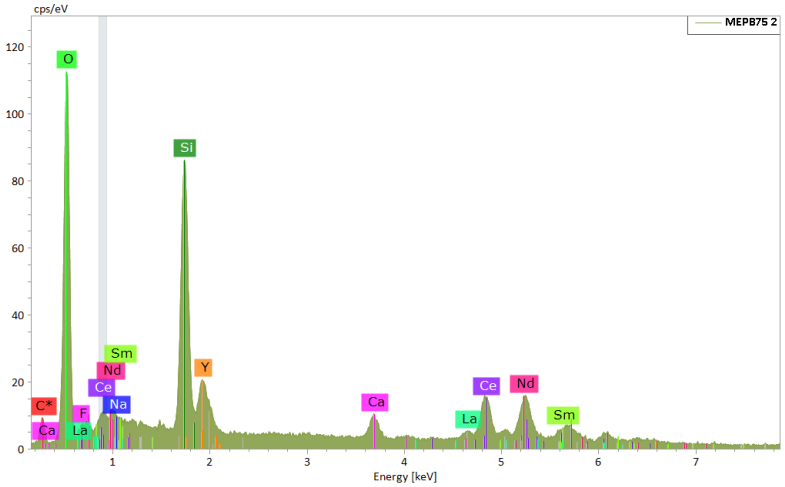

Figure A.23: *EDS spectra identified as tritomite-(Y)*

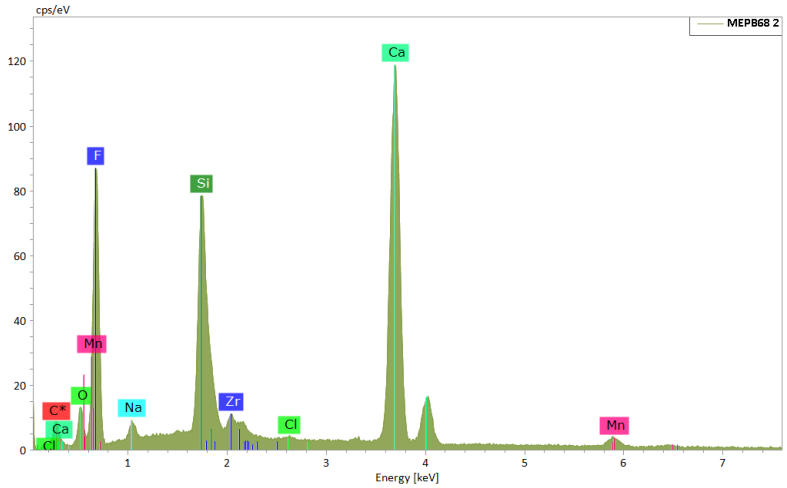

Figure A.24: *EDS spectra identified as a wöhlerite group mineral*

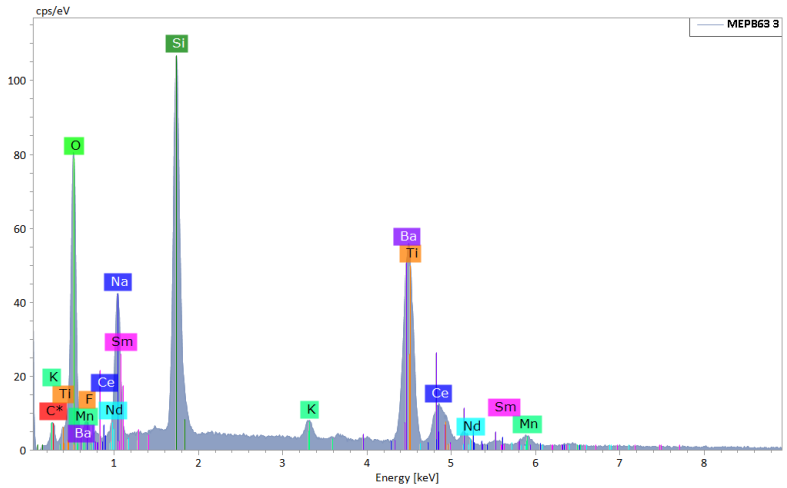

Figure A.25: *EDS spectra of unknown 1*

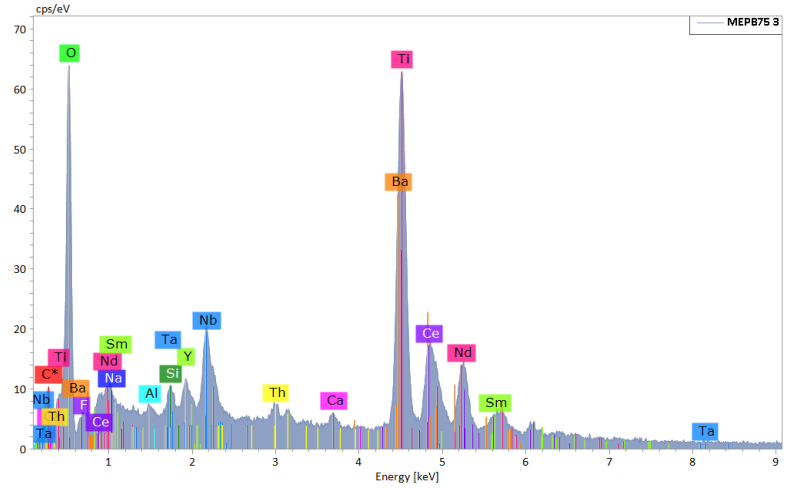

Figure A.26: *EDS spectra of unknown 2*

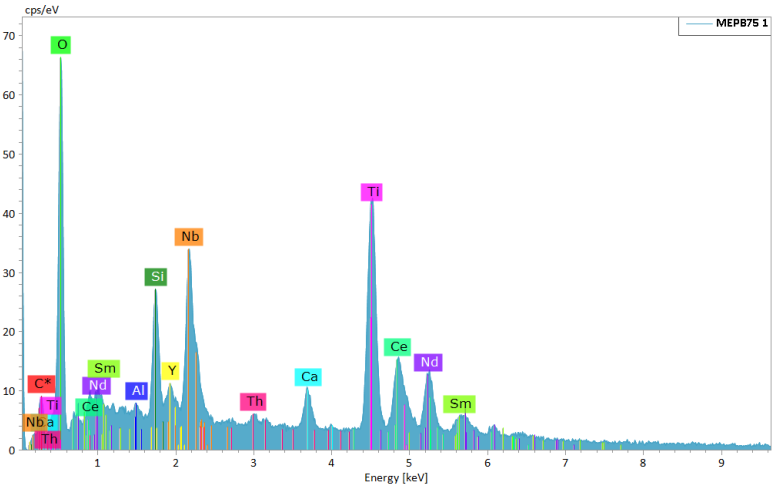

Figure A.27: *EDS spectra of unknown 3*

Appendix B: Tables

Table B.1: *Whole rock XRF analysis data*

Sample	SiO_2	TiO_2	Al_2O_3	Fe_2O_3*	MnO	MgO	CaO	Na_2O	$K2O$	P_2O_5	LOI	Total	(Na+K)/Al
MEPB 61	51.73	0.67	18.28	6.02	0.39	0.58	2.66	9.99	5.88	0.05	2.38	98.81	1.25
MEPB 62	49.29	2.17	18.40	4.22	0.64	0.19	3.19	9.53	6.58	0.58	1.68	96.80	1.24
MEPB 64	51.05	0.92	19.48	3.50	0.51	0.18	2.03	9.02	7.43	0.57	1.99	97.07	1.17
MEPB 65	51.15	0.73	17.16	7.20	0.49	0.60	2.80	9.37	6.19	0.07	1.88	97.92	1.29
MEPB 66	51.71	0.97	13.15	11.33	0.73	1.03	2.96	8.67	4.69	0.23	2.68	98.26	1.47
MEPB 68	50.83	0.93	15.06	7.56	0.80	0.56	2.83	9.67	5.20	0.10	2.63	96.48	1.43
MEPB 69	55.89	0.64	18.84	4.92	0.47	0.29	1.21	10.07	5.25	0.06	0.80	98.44	1.18
MEPB 70	57.69	0.62	17.08	5.25	0.47	0.17	1.53	8.88	5.55	0.34	0.61	98.19	1.21
MEPB 71	55.42	0.91	17.66	6.17	0.48	0.34	1.43	9.84	4.98	-	0.50	97.72	1.22
MEPB 72	55.69	0.51	20.39	4.55	0.44	0.27	0.92	10.92	4.67	0.06	0.61	99.02	1.13
MEPB 73	56.89	0.58	18.98	5.49	0.45	0.17	0.96	10.14	4.50	0.12	0.81	99.08	1.14
MEPB 74	55.56	0.68	18.83	5.27	0.47	0.38	1.26	10.24	5.19	0.06	0.64	98.58	1.19
MEPB 75	56.97	0.61	18.32	4.94	0.44	0.35	1.28	8.89	5.35	0.12	1.22	98.49	1.11
MEPB 76	55.02	0.52	20.63	4.38	0.38	0.23	1.07	10.80	5.19	0.05	0.82	99.10	1.13

Table B.2: *ICPW norm calculations*

	Or	Ab	Ne	Ac	Ns	Di	Wo	Ol	Il	Ap	Sum
MEPB 62	38.89	6.19	28.07	3.24	4.41	6.15	2.07	0.00	4.12	1.37	94.53
MEPB 65	36.58	7.28	25.20	5.53	4.47	11.69	0.00	2.95	1.39	0.17	95.26
MEPB 66	27.72	19.85	11.74	8.68	5.12	11.46	0.00	7.72	1.84	0.54	94.67
MEPB 72	27.60	30.64	26.13	3.47	2.23	3.66	0.00	3.26	0.97	0.14	98.10
MEPB 74	30.67	27.99	21.65	4.05	3.28	5.11	0.00	3.39	1.29	0.14	97.58
MEPB 75	31.62	34.11	16.43	3.79	1.51	4.86	0.00	3.17	1.16	0.28	96.93
MEPB 76	30.67	25.25	28.15	3.36	2.41	4.37	0.00	2.64	0.99	0.12	97.96
MEPB 61	34.75	9.92	27.83	4.60	4.19	11.16	0.00	1.98	1.27	0.12	95.82
MEPB 64	43.91	6.67	28.26	2.69	3.36	5.56	0.00	0.94	1.75	1.35	94.48
MEPB 68	30.73	15.07	18.12	5.79	6.22	11.68	0.00	3.40	1.77	0.24	93.01
MEPB 69	31.03	29.38	20.75	3.76	3.09	4.91	0.00	3.02	1.22	0.14	97.30
MEPB 70	32.80	35.93	11.39	4.02	3.17	4.74	0.00	3.20	1.18	0.81	97.23
MEPB 71	29.43	29.75	18.07	4.72	3.44	6.21	0.00	3.44	1.73	0.00	96.79
MEPB 73	26.59	37.07	19.23	4.20	1.97	3.51	0.00	3.93	1.10	0.28	97.89

Table B.3: *EMP analysis data of clinopyroxene*

Date	02.10.2018	02.10.2018	02.10.2018	02.10.2018	02.10.2018	02.10.2018	02.10.2018	04.10.2018	04.10.2018	04.10.2018
Sample	MEPB61	MEPB61	MEPB61	MEPB61	MEPB61	MEPB61	MEPB61	MEPB62	MEPB62	MEPB62
Point	28/1.	29/1.	30/1.	32/1.	33/1.	36/1.	37/1.	15/1.	16/1.	17/1.
Wt.%										
SiO_2	52.04	51.47	51.84	51.80	51.42	51.74	53.24	51.63	51.23	52.33
TiO_2	0.81	1.19	1.08	0.72	1.18	1.92	2.13	3.38	6.06	5.97
Al_2O_3	0.86	0.84	0.83	0.71	0.88	0.80	1.22	0.72	0.78	0.76
FeO	21.86	22.99	23.28	23.93	23.11	23.84	24.36	23.47	21.56	21.93
MnO	1.11	0.93	0.93	1.74	0.96	0.94	0.68	1.68	2.00	1.86
MgO	3.89	2.85	3.13	2.04	2.87	2.00	1.42	1.26	1.08	1.03
CaO	10.11	8.24	8.53	9.77	8.55	6.43	2.99	3.34	3.66	3.71
Na_2O	7.98	8.93	8.90	7.96	8.73	9.74	12.20	11.63	11.50	11.60
ZrO_2	0.31	0.36	0.42	0.12	0.44	0.21	0.26	0.03	0.02	0.00
Total	98.96	97.87	99.00	98.76	98.17	97.64	98.51	97.12	97.87	99.17
Apfu*										
Si	1.98	1.98	1.97	2.00	1.98	2.00	2.00	1.98	1.97	1.98
Ti	0.02	0.03	0.03	0.02	0.03	0.06	0.06	0.10	0.17	0.17
Al	0.04	0.04	0.04	0.03	0.04	0.04	0.05	0.03	0.04	0.03
Fe^{3+*}	0.53	0.58	0.60	0.52	0.57	0.58	0.70	0.67	0.54	0.51
Fe^{2+*}	0.16	0.16	0.14	0.25	0.17	0.19	0.07	0.08	0.15	0.18
Mn	0.04	0.03	0.03	0.06	0.03	0.03	0.02	0.05	0.06	0.06
Mg	0.22	0.16	0.18	0.12	0.16	0.11	0.08	0.07	0.06	0.06
Ca	0.41	0.34	0.35	0.40	0.35	0.27	0.12	0.14	0.15	0.15
Na	0.59	0.67	0.66	0.60	0.65	0.73	0.89	0.87	0.86	0.85
Zr	0.01	0.01	0.01	0.00	0.01	0.00	0.00	0.00	0.00	0.00
Endmembers										
AlTsch	0.02	0.02	0.01	0.00	0.02	0.00	0.00	0.02	0.00	0.02
Jd	0.00	0.00	0.00	0.03	0.00	0.03	0.05	0.00	0.00	0.00
ZrTiAeg	0.06	0.08	0.08	0.05	0.08	0.12	0.13	0.20	0.35	0.34
Di	0.22	0.16	0.18	0.12	0.16	0.11	0.08	0.07	0.06	0.06
Hd	0.17	0.14	0.13	0.29	0.16	0.16	0.02	0.04	0.04	0.07
Aeg	0.53	0.58	0.58	0.52	0.57	0.58	0.70	0.67	0.50	0.51

*Atoms per formula unit (apfu) calculations based on four cations and six oxygens in formula. Fe^{3+} and Fe^{2+} proportions are calculated values from charge balance.

Table B.3: *(Continued)*

Date	04.10.2018	23.10.2018	23.10.2018	23.10.2018	23.10.2018	23.10.2018	23.10.2018	23.10.2018	23.10.2018	23.10.2018
Sample	MEPB62	MEPB64	MEPB64	MEPB64	MEPB64	MEPB64	MEPB64	MEPB64	MEPB64	MEPB64
Point	18/1.	1/1.	2/1.	3/1.	4/1.	5/1.	6/1.	7/1.	8/1.	9/1.
Wt.%										
SiO_2	51.95	51.84	51.77	51.83	52.03	51.61	52.30	52.59	52.39	51.98
TiO_2	2.03	5.54	5.81	5.30	3.16	4.67	5.68	3.54	5.85	5.54
Al_2O_3	0.76	0.82	0.85	0.63	0.80	0.49	0.77	0.73	0.83	0.81
FeO	25.50	22.64	21.98	22.11	24.66	22.40	22.47	22.96	21.02	22.14
MnO	0.73	1.64	1.51	1.92	1.45	2.27	1.81	2.22	2.47	1.78
MgO	1.36	1.09	1.10	1.09	0.90	1.08	1.09	1.14	1.11	1.13
CaO	4.70	4.14	3.88	4.14	3.62	5.81	4.17	2.96	3.10	4.18
Na_2O	10.86	11.58	11.64	11.34	11.68	10.11	11.35	11.82	11.76	11.61
ZrO_2	0.37	0.02	0.00	0.03	0.00	0.13	0.05	0.08	0.01	0.00
Total	98.22	99.33	98.56	98.37	98.30	98.56	99.67	98.11	98.49	99.13
Apfu*										
Si	1.99	1.96	1.97	1.98	1.98	1.99	1.97	2.00	1.99	1.97
Ti	0.06	0.16	0.17	0.15	0.09	0.14	0.16	0.10	0.17	0.16
Al	0.03	0.04	0.04	0.03	0.04	0.02	0.03	0.03	0.04	0.04
Fe^{3+*}	0.67	0.58	0.55	0.55	0.68	0.48	0.52	0.63	0.51	0.57
Fe^{2+*}	0.15	0.14	0.15	0.16	0.10	0.24	0.19	0.10	0.16	0.13
Mn	0.02	0.05	0.05	0.06	0.05	0.07	0.06	0.07	0.08	0.06
Mg	0.08	0.06	0.06	0.06	0.05	0.06	0.06	0.06	0.06	0.06
Ca	0.19	0.17	0.16	0.17	0.15	0.24	0.17	0.12	0.13	0.17
Na	0.81	0.85	0.86	0.84	0.86	0.75	0.83	0.87	0.87	0.85
Zr	0.01	0.00	0.00	0.00	0.00	0.00	0.00	0.00	0.00	0.00
Endmembers										
AlTsch	0.01	0.00	0.01	0.01	0.02	0.01	0.01	0.00	0.01	0.00
Jd	0.01	0.00	0.00	0.00	0.00	0.00	0.00	0.03	0.02	0.00
ZrTiAeg	0.13	0.32	0.33	0.31	0.18	0.28	0.32	0.21	0.33	0.32
Di	0.08	0.06	0.06	0.06	0.05	0.06	0.06	0.06	0.06	0.06
Hd	0.11	0.03	0.03	0.07	0.06	0.18	0.08	0.07	0.07	0.03
Aeg	0.67	0.53	0.53	0.53	0.68	0.48	0.51	0.63	0.51	0.54

*Atoms per formula unit (apfu) calculations based on four cations and six oxygens in formula. Fe^{3+} and Fe^{2+} proportions are calculated values from charge balance.

Table B.3: *(Continued)*

Date	23.10.2018	23.10.2018	23.10.2018	02.10.2018	02.10.2018	02.10.2018	02.10.2018	02.10.2018	02.10.2018	02.10.2018
Sample	MEPB64	MEPB64	MEPB64	MEPB66	MEPB66	MEPB66	MEPB66	MEPB66	MEPB66	MEPB66
Point	10/1.	11/1.	12/1.	38/1.	40/1.	41/.1	45/1.	46/1.	47/1.	48/1.
Wt.%										
SiO_2	52.08	51.37	51.99	52.09	52.28	51.68	52.03	52.89	52.82	51.82
TiO_2	4.93	5.74	5.81	2.54	3.33	1.81	2.00	2.80	1.84	2.29
Al_2O_3	0.72	0.73	0.85	0.70	0.64	0.75	0.85	1.08	0.82	0.61
FeO	22.66	22.24	22.30	25.03	24.01	24.75	25.02	24.55	25.68	24.65
MnO	1.64	1.70	1.63	1.21	1.54	0.90	0.98	1.17	0.80	1.44
MgO	1.14	1.09	1.06	1.35	1.08	1.75	1.51	1.08	1.10	1.32
CaO	3.93	4.07	3.63	5.47	3.47	5.85	6.00	3.63	1.77	5.61
Na_2O	11.66	11.28	11.64	10.48	11.74	10.31	10.20	11.63	12.56	10.45
ZrO_2	0.04	0.00	0.00	0.13	0.01	0.39	0.31	0.03	0.14	0.18
Total	98.86	98.25	98.82	99.00	98.14	98.19	98.92	98.83	97.52	98.33
Apfu*										
Si	1.97	1.97	1.97	1.98	1.99	1.98	1.98	2.00	2.01	1.98
Ti	0.14	0.17	0.17	0.07	0.10	0.05	0.06	0.08	0.05	0.07
Al	0.03	0.03	0.04	0.03	0.03	0.03	0.04	0.05	0.04	0.03
Fe^{3+*}	0.59	0.54	0.54	0.62	0.66	0.65	0.62	0.65	0.76	0.64
Fe^{2+*}	0.12	0.17	0.17	0.17	0.10	0.14	0.18	0.13	0.05	0.15
Mn	0.05	0.06	0.05	0.04	0.05	0.03	0.03	0.04	0.03	0.05
Mg	0.06	0.06	0.06	0.08	0.06	0.10	0.09	0.06	0.06	0.08
Ca	0.16	0.17	0.15	0.22	0.14	0.24	0.25	0.15	0.07	0.23
Na	0.86	0.84	0.86	0.77	0.87	0.77	0.75	0.85	0.93	0.78
Zr	0.00	0.00	0.00	0.00	0.00	0.01	0.01	0.00	0.00	0.00
Endmembers										
AlTsch	0.01	0.00	0.01	0.02	0.01	0.01	0.02	0.00	0.00	0.01
Jd	0.00	0.00	0.00	0.00	0.01	0.00	0.01	0.05	0.04	0.00
ZrTiAeg	0.28	0.33	0.33	0.15	0.19	0.12	0.13	0.16	0.11	0.14
Di	0.06	0.06	0.06	0.08	0.06	0.10	0.09	0.06	0.06	0.08
Hd	0.04	0.06	0.05	0.14	0.05	0.11	0.14	0.09	0.02	0.13
Aeg	0.57	0.51	0.52	0.62	0.66	0.65	0.62	0.65	0.76	0.64

*Atoms per formula unit (apfu) calculations based on four cations and six oxygens in formula. Fe^{3+} and Fe^{2+} proportions are calculated values from charge balance.

Table B.3: *(Continued)*

Date	02.10.2018	02.10.2018	04.10.2018	04.10.2018	04.10.2018	04.10.2018	04.10.2018	04.10.2018	04.10.2018	04.10.2018
Sample	MEPB66	MEPB66	MEPB67	MEPB67	MEPB67	MEPB67	MEPB67	MEPB67	MEPB67	MEPB67
Point	49/1.	50/1.	1/1.	1/2.	1/3.	5/1.	6/1.	7/1.	8/1.	9/1.
Wt.%										
SiO_2	52.27	51.46	50.63	51.27	52.06	50.91	52.05	51.97	50.82	50.67
TiO_2	3.52	1.59	2.22	1.56	0.69	1.91	2.09	2.64	1.21	1.05
Al_2O_3	0.64	0.75	0.63	0.86	1.59	0.74	0.75	0.61	0.87	0.84
FeO	24.35	24.51	23.57	24.80	26.93	25.27	26.00	24.07	24.04	23.93
MnO	1.29	0.91	1.82	0.74	0.28	1.15	0.83	1.46	0.97	0.93
MgO	1.08	1.88	1.41	1.74	0.66	1.26	1.13	1.38	2.44	2.73
CaO	4.14	6.16	7.01	5.65	1.23	6.37	2.28	3.14	7.75	8.61
Na_2O	11.42	10.37	9.51	10.27	12.81	9.98	12.43	11.98	9.01	8.81
ZrO_2	0.00	0.59	0.27	0.53	0.15	0.38	0.05	0.31	0.47	0.39
Total	98.73	98.24	97.02	97.42	96.38	97.97	97.61	97.62	97.60	97.99
Apfu*										
Si	1.99	1.97	1.98	1.98	1.99	1.97	1.98	1.98	1.97	1.95
Ti	0.10	0.05	0.07	0.05	0.02	0.06	0.06	0.08	0.04	0.03
Al	0.03	0.03	0.03	0.04	0.07	0.03	0.03	0.03	0.04	0.04
Fe^{3+*}	0.64	0.69	0.60	0.66	0.85	0.66	0.80	0.73	0.61	0.64
Fe^{2+*}	0.13	0.10	0.17	0.14	0.02	0.16	0.02	0.04	0.16	0.13
Mn	0.04	0.03	0.06	0.02	0.01	0.04	0.03	0.05	0.03	0.03
Mg	0.06	0.11	0.08	0.10	0.04	0.07	0.06	0.08	0.14	0.16
Ca	0.17	0.25	0.29	0.23	0.05	0.26	0.09	0.13	0.32	0.36
Na	0.84	0.77	0.72	0.77	0.95	0.75	0.92	0.89	0.68	0.66
Zr	0.00	0.01	0.01	0.01	0.00	0.01	0.00	0.01	0.01	0.01
Endmembers										
AlTsch	0.01	0.00	0.01	0.02	0.01	0.00	0.01	0.01	0.01	0.00
Jd	0.00	0.00	0.00	0.00	0.06	0.00	0.00	0.00	0.00	0.00
ZrTiAeg	0.20	0.11	0.14	0.11	0.05	0.13	0.12	0.16	0.09	0.08
Di	0.06	0.11	0.08	0.10	0.04	0.07	0.06	0.08	0.14	0.16
Hd	0.07	0.07	0.16	0.11	0.00	0.14	0.00	0.00	0.15	0.12
Aeg	0.64	0.66	0.58	0.66	0.85	0.62	0.79	0.72	0.59	0.58

*Atoms per formula unit (apfu) calculations based on four cations and six oxygens in formula. Fe^{3+} and Fe^{2+} proportions are calculated values from charge balance.

Table B.3: *(Continued)*

Date	04.10.2018	04.10.2018	04.10.2018	04.10.2018	04.10.2018	04.10.2018	04.10.2018	04.10.2018	04.10.2018	04.10.2018
Sample	MEPB67	MEPB67	MEPB67	MEPB67	MEPB67	MEPB68	MEPB68	MEPB68	MEPB68	MEPB68
Point	10/1.	11/1.	12/1.	13/1.	14/1.	21/1.	22/1.	25/1.	26/1.	27/1.
Wt.%										
SiO_2	52.07	51.12	52.34	52.09	52.77	51.00	50.92	51.14	51.78	51.09
TiO_2	2.33	1.64	2.55	1.72	2.13	0.97	1.12	1.43	2.57	1.27
Al_2O_3	0.72	0.82	0.81	0.73	0.84	0.81	0.77	0.80	0.72	0.82
FeO	24.85	26.16	24.63	25.24	24.97	23.27	24.25	24.88	24.39	24.06
MnO	1.07	0.69	1.06	0.78	1.00	0.98	0.83	0.82	1.52	0.85
MgO	1.34	1.25	1.20	1.45	1.24	2.83	2.43	2.23	1.41	2.63
CaO	2.80	4.51	2.90	4.99	2.68	8.68	7.66	6.25	4.13	7.41
Na_2O	11.93	10.99	12.03	10.86	12.33	8.61	9.39	9.93	11.15	9.39
ZrO_2	0.25	0.47	0.17	0.65	0.17	0.43	0.43	0.37	0.00	0.45
Total	97.36	97.65	97.70	98.49	98.12	97.60	97.83	97.84	97.69	97.98
Apfu*										
Si	1.99	1.97	1.99	1.99	2.00	1.97	1.96	1.96	1.98	1.96
Ti	0.07	0.05	0.07	0.05	0.06	0.03	0.03	0.04	0.07	0.04
Al	0.03	0.04	0.04	0.03	0.04	0.04	0.03	0.04	0.03	0.04
Fe^{3+*}	0.73	0.74	0.71	0.67	0.75	0.59	0.66	0.68	0.68	0.65
Fe^{2+*}	0.07	0.10	0.07	0.13	0.04	0.16	0.12	0.12	0.10	0.13
Mn	0.03	0.02	0.03	0.03	0.03	0.03	0.03	0.03	0.05	0.03
Mg	0.08	0.07	0.07	0.08	0.07	0.16	0.14	0.13	0.08	0.15
Ca	0.11	0.19	0.12	0.20	0.11	0.36	0.32	0.26	0.17	0.30
Na	0.88	0.82	0.89	0.80	0.90	0.65	0.70	0.74	0.83	0.70
Zr	0.00	0.01	0.00	0.01	0.00	0.01	0.01	0.01	0.00	0.01
Endmembers										
AlTsch	0.01	0.00	0.01	0.01	0.00	0.01	0.00	0.00	0.02	0.00
Jd	0.01	0.00	0.02	0.01	0.03	0.00	0.00	0.00	0.00	0.00
ZrTiAeg	0.14	0.11	0.15	0.12	0.13	0.07	0.08	0.10	0.15	0.09
Di	0.08	0.07	0.07	0.08	0.07	0.16	0.14	0.13	0.08	0.15
Hd	0.03	0.07	0.03	0.09	0.01	0.16	0.10	0.10	0.08	0.11
Aeg	0.73	0.71	0.71	0.67	0.75	0.57	0.62	0.64	0.68	0.61

*Atoms per formula unit (apfu) calculations based on four cations and six oxygens in formula. Fe^{3+} and Fe^{2+} proportions are calculated values from charge balance.

Table B.3: *(Continued)*

Date	04.10.2018	04.10.2018	04.10.2018	04.10.2018	06.09.2018	06.09.2018	06.09.2018	06.09.2018	06.09.2018	06.09.2018
Sample	MEPB68	MEPB68	MEPB68	MEPB68	MEPB69	MEPB69	MEPB69	MEPB69	MEPB69	MEPB69
Point	29/1.	32/1.	33/1.	34/1.	4/1.	5/1.	6/1.	7/1.	8/1.	14/1.
Wt.%										
SiO_2	52.59	52.73	51.26	52.36	52.40	51.79	51.95	51.69	52.16	52.25
TiO_2	2.67	3.12	1.04	1.95	3.50	1.35	2.98	5.61	2.73	3.15
Al_2O_3	1.05	0.66	0.83	0.69	0.57	1.10	0.63	0.69	1.83	1.10
FeO	23.71	23.68	23.47	23.35	25.34	27.05	25.71	22.93	25.11	24.42
MnO	1.35	1.54	0.94	1.67	1.70	1.00	1.58	1.97	1.12	1.59
MgO	1.56	1.38	2.79	1.96	0.51	0.53	0.56	0.49	0.29	0.62
CaO	2.78	3.74	8.62	4.42	2.68	2.24	2.83	2.15	1.94	2.27
Na_2O	12.11	11.67	9.04	11.22	11.98	12.26	12.06	12.51	12.34	12.10
ZrO_2	0.19	0.01	0.46	0.32	0.12	0.07	0.07	0.11	0.00	0.08
Total	98.02	98.55	98.45	97.96	98.82	97.40	98.35	98.16	97.52	97.56
Apfu*										
Si	1.99	2.00	1.96	1.99	1.99	1.98	1.98	1.97	1.99	2.00
Ti	0.08	0.09	0.03	0.06	0.10	0.04	0.09	0.16	0.08	0.09
Al	0.05	0.03	0.04	0.03	0.03	0.05	0.03	0.03	0.08	0.05
Fe^{3+*}	0.70	0.66	0.64	0.69	0.67	0.82	0.73	0.63	0.69	0.67
Fe^{2+*}	0.05	0.09	0.12	0.05	0.14	0.05	0.09	0.10	0.11	0.12
Mn	0.04	0.05	0.03	0.05	0.05	0.03	0.05	0.06	0.04	0.05
Mg	0.09	0.08	0.16	0.11	0.03	0.03	0.03	0.03	0.02	0.04
Ca	0.11	0.15	0.35	0.18	0.11	0.09	0.12	0.09	0.08	0.09
Na	0.89	0.86	0.67	0.83	0.88	0.91	0.89	0.92	0.91	0.90
Zr	0.00	0.00	0.01	0.01	0.00	0.00	0.00	0.00	0.00	0.00
Endmembers										
AlTsch	0.01	0.00	0.00	0.01	0.01	0.02	0.01	0.00	0.01	0.00
Jd	0.03	0.02	0.00	0.01	0.01	0.01	0.00	0.00	0.07	0.05
ZrTiAeg	0.16	0.18	0.08	0.12	0.20	0.08	0.17	0.33	0.16	0.18
Di	0.09	0.08	0.16	0.11	0.03	0.03	0.03	0.03	0.02	0.04
Hd	0.01	0.05	0.11	0.05	0.09	0.04	0.05	0.01	0.07	0.08
Aeg	0.70	0.66	0.59	0.69	0.67	0.82	0.72	0.60	0.69	0.67

*Atoms per formula unit (apfu) calculations based on four cations and six oxygens in formula. Fe^{3+} and Fe^{2+} proportions are calculated values from charge balance.

Table B.3: *(Continued)*

Date	06.09.2018	06.09.2018	06.09.2018	06.09.2018	06.09.2018	06.09.2018	23.10.2018	23.10.2018	23.10.2018	23.10.2018
Sample	MEPB69	MEPB69	MEPB69	MEPB69	MEPB69	MEPB69	MEPB70	MEPB70	MEPB70	MEPB70
Point	15/1.	16/1.	17/1.	18/1.	19/1.	20/1.	25/1.	26/1.	27/1.	28/1.
Wt.%										
SiO_2	51.65	51.95	51.91	51.39	51.24	51.70	52.54	52.17	52.15	51.81
TiO_2	0.91	3.89	2.10	1.42	3.20	4.44	4.55	6.63	3.01	0.91
Al_2O_3	1.42	0.90	0.71	1.10	0.94	1.04	0.51	0.72	1.04	1.04
FeO	24.63	25.09	26.75	27.07	25.44	24.12	24.91	23.58	25.56	27.58
MnO	1.37	1.36	0.89	0.70	0.73	1.32	1.45	1.22	1.27	0.52
MgO	1.03	0.54	0.47	0.51	0.40	0.50	0.09	0.13	0.16	0.31
CaO	3.65	3.19	2.59	2.10	2.96	3.00	0.16	0.36	2.84	1.51
Na_2O	11.24	11.83	11.88	12.36	11.73	11.91	13.52	13.63	11.90	12.85
ZrO_2	0.93	0.07	0.46	0.34	1.17	0.09	0.01	0.00	0.00	0.47
Total	96.87	98.82	97.74	96.99	97.83	98.07	97.72	98.41	97.87	97.00
Apfu*										
Si	2.00	1.97	1.99	1.97	1.98	1.98	2.00	1.97	2.00	1.98
Ti	0.03	0.11	0.06	0.04	0.09	0.13	0.13	0.19	0.09	0.03
Al	0.06	0.04	0.03	0.05	0.04	0.05	0.02	0.03	0.05	0.05
Fe^{3+*}	0.70	0.66	0.73	0.83	0.65	0.62	0.72	0.64	0.67	0.87
Fe^{2+*}	0.10	0.14	0.13	0.04	0.17	0.15	0.08	0.10	0.15	0.01
Mn	0.04	0.04	0.03	0.02	0.02	0.04	0.05	0.04	0.04	0.02
Mg	0.06	0.03	0.03	0.03	0.02	0.03	0.01	0.01	0.01	0.02
Ca	0.15	0.13	0.11	0.09	0.12	0.12	0.01	0.01	0.12	0.06
Na	0.84	0.87	0.88	0.92	0.88	0.88	1.00	1.00	0.88	0.95
Zr	0.02	0.00	0.01	0.01	0.02	0.00	0.00	0.00	0.00	0.01
Endmembers										
AlTsch	0.00	0.01	0.01	0.02	0.02	0.02	0.00	0.01	0.00	0.02
Jd	0.06	0.00	0.02	0.00	0.00	0.00	0.02	0.00	0.04	0.02
ZrTiAeg	0.09	0.22	0.14	0.09	0.23	0.26	0.26	0.38	0.17	0.07
Di	0.06	0.03	0.03	0.03	0.02	0.03	0.01	0.01	0.01	0.02
Hd	0.10	0.07	0.09	0.02	0.08	0.06	0.00	0.00	0.10	0.00
Aeg	0.70	0.65	0.73	0.83	0.65	0.62	0.72	0.62	0.67	0.87

*Atoms per formula unit (apfu) calculations based on four cations and six oxygens in formula. Fe^{3+} and Fe^{2+} proportions are calculated values from charge balance.

Table B.3: *(Continued)*

Date	23.10.2018	23.10.2018	23.10.2018	23.10.2018	23.10.2018	23.10.2018	23.10.2018	07.09.2018	07.09.2018	07.09.2018
Sample	MEPB70	MEPB70	MEPB70	MEPB70	MEPB70	MEPB70	MEPB70	MEPB71	MEPB71	MEPB71
Point	29/1.	30/1.	31/1.	32/1.	33/1.	34/1.	35/1.	31/1.	32/1.	33/1.
Wt.%										
SiO_2	51.73	52.38	52.12	52.09	51.76	51.86	52.14	51.51	52.02	51.95
TiO_2	1.61	1.02	0.83	6.12	1.23	0.84	0.87	2.82	4.78	2.08
Al_2O_3	0.78	1.00	0.96	0.81	0.96	0.97	1.03	0.49	1.03	0.67
FeO	26.23	27.48	27.46	23.50	26.69	28.17	28.49	25.16	24.10	26.51
MnO	0.61	0.49	0.60	1.30	0.77	0.63	0.52	0.90	0.86	1.21
MgO	0.45	0.39	0.38	0.18	0.43	0.39	0.29	0.30	0.31	0.33
CaO	2.57	2.17	2.17	0.47	2.94	2.69	1.28	2.36	2.29	3.56
Na_2O	12.03	12.34	12.17	13.49	11.73	12.31	12.82	12.08	12.21	11.68
ZrO_2	1.84	0.41	0.37	0.00	0.34	0.30	0.14	2.76	0.97	0.76
Total	97.84	97.68	97.07	97.95	96.83	98.17	97.58	98.36	98.56	98.78
Apfu*										
Si	1.99	2.00	2.00	1.98	2.00	1.97	1.99	1.99	1.99	1.98
Ti	0.05	0.03	0.02	0.17	0.04	0.02	0.02	0.08	0.14	0.06
Al	0.04	0.05	0.04	0.04	0.04	0.04	0.05	0.02	0.05	0.03
Fe^{3+*}	0.72	0.79	0.79	0.65	0.75	0.86	0.87	0.64	0.57	0.72
Fe^{2+*}	0.12	0.08	0.09	0.10	0.11	0.03	0.03	0.17	0.19	0.12
Mn	0.02	0.02	0.02	0.04	0.03	0.02	0.02	0.03	0.03	0.04
Mg	0.03	0.02	0.02	0.01	0.02	0.02	0.02	0.02	0.02	0.02
Ca	0.11	0.09	0.09	0.02	0.12	0.11	0.05	0.10	0.09	0.15
Na	0.90	0.91	0.91	0.99	0.88	0.91	0.95	0.90	0.90	0.86
Zr	0.03	0.01	0.01	0.00	0.01	0.01	0.00	0.05	0.02	0.01
Endmembers										
AlTsch	0.01	0.00	0.00	0.01	0.00	0.02	0.01	0.01	0.01	0.01
Jd	0.02	0.05	0.04	0.00	0.04	0.00	0.02	0.00	0.02	0.00
ZrTiAeg	0.16	0.07	0.06	0.35	0.08	0.06	0.06	0.27	0.31	0.15
Di	0.03	0.02	0.02	0.01	0.02	0.02	0.02	0.02	0.02	0.02
Hd	0.06	0.06	0.08	0.00	0.10	0.03	0.02	0.07	0.07	0.09
Aeg	0.72	0.79	0.79	0.64	0.75	0.85	0.87	0.64	0.57	0.72

*Atoms per formula unit (apfu) calculations based on four cations and six oxygens in formula. Fe^{3+} and Fe^{2+} proportions are calculated values from charge balance.

Table B.3: *(Continued)*

Date	07.09.2018	07.09.2018	07.09.2018	07.09.2018	07.09.2018	07.09.2018	07.09.2018	07.09.2018	07.09.2018	07.09.2018
Sample	MEPB71	MEPB71	MEPB71	MEPB71	MEPB71	MEPB72	MEPB72	MEPB72	MEPB72	MEPB72
Point	34/1.	35/1.	36/1.	37/1.	38/1.	8/1.	9/1.	30/1.	18/1.	20/1.
Wt.%										
SiO_2	51.96	51.68	51.43	51.80	51.69	51.43	51.39	52.32	52.39	52.14
TiO_2	1.30	3.46	2.52	3.70	2.35	3.79	2.72	3.88	0.44	1.16
Al_2O_3	0.83	1.08	0.54	1.10	0.72	0.99	0.65	0.76	1.24	1.07
FeO	26.76	24.80	25.71	25.27	26.27	24.08	24.44	24.58	26.53	27.21
MnO	1.08	1.36	2.21	1.18	1.69	1.51	2.24	1.49	1.68	0.62
MgO	0.65	0.30	0.25	0.28	0.16	0.78	0.72	0.76	0.72	0.54
CaO	3.37	3.70	5.35	3.14	4.15	3.89	5.79	3.39	4.42	2.53
Na_2O	11.67	11.19	10.43	11.89	11.38	10.97	10.11	11.69	11.05	12.07
ZrO_2	0.41	0.63	0.15	0.14	0.00	0.12	0.56	0.07	0.19	0.38
Total	98.06	98.21	98.59	98.50	98.42	97.59	98.62	98.95	98.66	97.75
Apfu*										
Si	1.99	1.99	1.98	1.97	1.98	1.99	1.98	1.99	1.99	1.99
Ti	0.04	0.10	0.07	0.11	0.07	0.11	0.08	0.11	0.01	0.03
Al	0.04	0.05	0.02	0.05	0.03	0.05	0.03	0.03	0.06	0.05
Fe^{3+*}	0.76	0.58	0.64	0.66	0.72	0.58	0.58	0.63	0.74	0.78
Fe^{2+*}	0.09	0.22	0.19	0.14	0.12	0.20	0.21	0.15	0.10	0.09
Mn	0.03	0.04	0.07	0.04	0.05	0.05	0.07	0.05	0.05	0.02
Mg	0.04	0.02	0.01	0.02	0.01	0.04	0.04	0.04	0.04	0.03
Ca	0.14	0.15	0.22	0.13	0.17	0.16	0.24	0.14	0.18	0.10
Na	0.87	0.84	0.78	0.88	0.84	0.82	0.76	0.86	0.82	0.89
Zr	0.01	0.01	0.00	0.00	0.00	0.00	0.01	0.00	0.00	0.01
Endmembers										
AlTsch	0.01	0.01	0.01	0.02	0.01	0.01	0.01	0.01	0.01	0.01
Jd	0.01	0.03	0.00	0.00	0.00	0.02	0.00	0.00	0.04	0.03
ZrTiAeg	0.09	0.22	0.15	0.22	0.14	0.22	0.18	0.22	0.03	0.08
Di	0.04	0.02	0.01	0.02	0.01	0.04	0.04	0.04	0.04	0.03
Hd	0.08	0.15	0.19	0.07	0.11	0.14	0.19	0.08	0.14	0.07
Aeg	0.76	0.58	0.63	0.66	0.71	0.58	0.58	0.63	0.74	0.78

*Atoms per formula unit (apfu) calculations based on four cations and six oxygens in formula. Fe^{3+} and Fe^{2+} proportions are calculated values from charge balance.

Table B.3: *(Continued)*

Date	07.09.2018	07.09.2018	07.09.2018	07.09.2018	07.09.2018	07.09.2018	07.09.2018	07.09.2018	23.10.2018	23.10.2018
Sample	MEPB72	MEPB72	MEPB72	MEPB72	MEPB72	MEPB72	MEPB72	MEPB72	MEPB73	MEPB73
Point	21/1.	22/1.	23/1.	24/1.	25/1.	27/1.	28/1.	29/1.	36/1.	37/1.
Wt.%										
SiO_2	52.36	51.88	51.71	50.42	51.56	51.74	51.69	51.34	52.33	51.94
TiO_2	3.02	3.23	2.31	1.21	3.55	3.14	1.11	2.24	3.31	1.29
Al_2O_3	0.77	1.15	0.73	0.54	1.05	0.80	0.98	0.53	1.02	0.78
FeO	25.20	25.34	27.29	25.84	25.83	24.74	26.44	24.05	25.57	26.36
MnO	1.23	0.97	0.91	0.92	0.59	1.48	0.92	1.95	0.57	0.97
MgO	0.80	0.65	0.34	0.42	0.40	0.86	0.64	0.85	0.34	0.38
CaO	2.49	3.34	3.37	3.74	2.41	4.07	2.77	5.91	1.75	1.53
Na_2O	12.00	11.50	11.65	10.71	12.14	11.10	11.99	9.98	12.59	12.58
ZrO_2	0.19	0.30	0.02	3.58	0.27	0.12	0.16	1.01	0.56	1.10
Total	98.04	98.37	98.34	97.39	97.74	98.05	96.74	97.84	98.06	96.96
Apfu*										
Si	2.00	1.98	1.98	1.99	1.98	1.99	1.99	2.00	1.99	2.00
Ti	0.09	0.09	0.07	0.04	0.10	0.09	0.03	0.07	0.09	0.04
Al	0.03	0.05	0.03	0.03	0.05	0.04	0.04	0.02	0.05	0.04
Fe^{3+*}	0.68	0.64	0.74	0.61	0.69	0.63	0.80	0.57	0.69	0.79
Fe^{2+*}	0.13	0.17	0.13	0.24	0.14	0.16	0.05	0.22	0.13	0.06
Mn	0.04	0.03	0.03	0.03	0.02	0.05	0.03	0.06	0.02	0.03
Mg	0.05	0.04	0.02	0.02	0.02	0.05	0.04	0.05	0.02	0.02
Ca	0.10	0.14	0.14	0.16	0.10	0.17	0.11	0.25	0.07	0.06
Na	0.89	0.85	0.86	0.82	0.90	0.83	0.90	0.75	0.93	0.94
Zr	0.00	0.01	0.00	0.07	0.01	0.00	0.00	0.02	0.01	0.02
Endmembers										
AlTsch	0.00	0.02	0.01	0.01	0.02	0.01	0.01	0.00	0.01	0.00
Jd	0.03	0.02	0.00	0.00	0.00	0.01	0.03	0.02	0.03	0.04
ZrTiAeg	0.18	0.20	0.13	0.21	0.21	0.19	0.07	0.17	0.21	0.12
Di	0.05	0.04	0.02	0.02	0.02	0.05	0.04	0.05	0.02	0.02
Hd	0.08	0.10	0.09	0.17	0.05	0.12	0.05	0.20	0.04	0.04
Aeg	0.68	0.64	0.73	0.61	0.69	0.63	0.80	0.57	0.69	0.79

*Atoms per formula unit (apfu) calculations based on four cations and six oxygens in formula. Fe^{3+} and Fe^{2+} proportions are calculated values from charge balance.

Table B.3: *(Continued)*

Date	23.10.2018	23.10.2018	23.10.2018	23.10.2018	23.10.2018	23.10.2018	23.10.2018	23.10.2018	23.10.2018	23.10.2018
Sample	MEPB73	MEPB73	MEPB73	MEPB73	MEPB74	MEPB74	MEPB74	MEPB74	MEPB74	MEPB74
Point	38/1.	39/1.	42/1.	43/1.	13/1.	14/1.	15/1.	16/1.	17/1.	18/1.
Wt.%										
SiO_2	51.79	52.39	52.34	52.06	51.79	51.58	51.09	51.71	51.92	50.70
TiO_2	1.76	0.41	4.74	2.76	2.71	2.91	2.73	1.35	1.63	1.07
Al_2O_3	0.79	1.07	0.76	0.58	0.96	1.07	0.90	0.79	0.70	0.48
FeO	27.04	28.33	24.30	26.19	26.03	25.68	25.38	25.28	26.77	26.29
MnO	0.57	0.81	1.57	1.41	0.63	0.60	1.00	2.31	0.60	0.76
MgO	0.40	0.28	0.21	0.39	0.36	0.37	0.54	0.94	0.34	0.33
CaO	1.67	1.66	0.21	0.50	2.59	2.48	3.34	4.15	2.16	3.38
Na_2O	12.50	12.56	13.58	13.09	12.08	12.21	11.76	11.12	12.17	11.54
ZrO_2	1.24	0.39	0.00	0.07	0.94	0.98	0.97	0.09	0.70	2.93
Total	97.77	97.87	97.70	97.06	98.12	97.86	97.72	97.71	96.96	97.46
Apfu*										
Si	1.98	1.99	1.99	1.99	1.98	1.98	1.97	1.98	2.00	1.98
Ti	0.05	0.01	0.14	0.08	0.08	0.08	0.08	0.04	0.05	0.03
Al	0.04	0.05	0.03	0.03	0.04	0.05	0.04	0.04	0.03	0.02
Fe^{3+*}	0.78	0.85	0.72	0.80	0.70	0.70	0.71	0.74	0.75	0.72
Fe^{2+*}	0.09	0.05	0.05	0.04	0.14	0.12	0.11	0.07	0.11	0.13
Mn	0.02	0.03	0.05	0.05	0.02	0.02	0.03	0.08	0.02	0.03
Mg	0.02	0.02	0.01	0.02	0.02	0.02	0.03	0.05	0.02	0.02
Ca	0.07	0.07	0.01	0.02	0.11	0.10	0.14	0.17	0.09	0.14
Na	0.93	0.93	1.00	0.97	0.90	0.91	0.88	0.83	0.91	0.87
Zr	0.02	0.01	0.00	0.00	0.02	0.02	0.02	0.00	0.01	0.06
Endmembers										
AlTsch	0.02	0.01	0.01	0.01	0.02	0.02	0.01	0.02	0.00	0.00
Jd	0.01	0.04	0.01	0.01	0.01	0.00	0.00	0.01	0.03	0.00
ZrTiAeg	0.15	0.04	0.27	0.16	0.19	0.20	0.19	0.08	0.12	0.17
Di	0.02	0.02	0.01	0.02	0.02	0.02	0.03	0.05	0.02	0.02
Hd	0.04	0.06	0.00	0.01	0.06	0.04	0.04	0.11	0.07	0.07
Aeg	0.78	0.85	0.72	0.80	0.70	0.70	0.68	0.74	0.75	0.70

*Atoms per formula unit (apfu) calculations based on four cations and six oxygens in formula. Fe^{3+} and Fe^{2+} proportions are calculated values from charge balance.

Table B.3: *(Continued)*

Date	23.10.2018	23.10.2018	23.10.2018	02.10.2018	02.10.2018	02.10.2018	02.10.2018	02.10.2018	02.10.2018	02.10.2018
Sample	MEPB74	MEPB74	MEPB74	MEPB75	MEPB75	MEPB75	MEPB75	MEPB75	MEPB75	MEPB75
Point	19/1.	23/1.	24/1.	7/2.	8/2.	9/2.	10/2.	11/2.	12/2.	19/1.
Wt.%										
SiO_2	52.06	52.06	52.16	52.24	52.68	51.98	52.76	52.10	52.07	52.40
TiO_2	1.05	1.31	2.28	0.42	3.83	3.74	1.25	1.13	0.90	1.05
Al_2O_3	0.63	1.08	0.74	0.90	1.05	0.96	0.93	0.97	1.02	1.10
FeO	26.84	26.61	26.11	28.08	24.66	25.64	27.50	27.63	28.17	27.85
MnO	0.92	0.72	0.82	0.64	1.10	0.65	0.41	0.41	0.37	0.34
MgO	0.75	0.67	0.45	0.55	0.54	0.34	0.45	0.39	0.35	0.35
CaO	3.05	2.61	2.53	3.30	2.93	2.22	1.91	1.70	1.76	1.70
Na_2O	11.73	11.98	12.01	11.84	12.15	12.12	12.42	12.55	12.35	12.77
ZrO_2	0.00	0.29	0.55	0.62	0.00	0.36	0.96	0.79	0.40	0.58
Total	97.01	97.35	97.65	98.61	98.98	98.05	98.59	97.68	97.35	98.13
Apfu*										
Si	2.00	2.00	2.00	1.99	1.99	1.99	2.00	1.99	2.00	1.99
Ti	0.03	0.04	0.07	0.01	0.11	0.11	0.04	0.03	0.03	0.03
Al	0.03	0.05	0.03	0.04	0.05	0.04	0.04	0.04	0.05	0.05
Fe^{3+*}	0.78	0.76	0.70	0.81	0.64	0.65	0.76	0.81	0.81	0.83
Fe^{2+*}	0.08	0.09	0.13	0.08	0.13	0.17	0.11	0.07	0.09	0.05
Mn	0.03	0.02	0.03	0.02	0.04	0.02	0.01	0.01	0.01	0.01
Mg	0.04	0.04	0.03	0.03	0.03	0.02	0.03	0.02	0.02	0.02
Ca	0.13	0.11	0.10	0.13	0.12	0.09	0.08	0.07	0.07	0.07
Na	0.88	0.89	0.89	0.87	0.89	0.90	0.91	0.93	0.92	0.94
Zr	0.00	0.01	0.01	0.01	0.00	0.01	0.02	0.01	0.01	0.01
Endmembers										
AlTsch	0.00	0.00	0.00	0.01	0.01	0.01	0.00	0.01	0.00	0.01
Jd	0.03	0.04	0.03	0.01	0.03	0.02	0.04	0.03	0.04	0.02
ZrTiAeg	0.06	0.09	0.15	0.05	0.22	0.23	0.11	0.09	0.07	0.08
Di	0.04	0.04	0.03	0.03	0.03	0.02	0.03	0.02	0.02	0.02
Hd	0.08	0.07	0.08	0.07	0.06	0.08	0.07	0.04	0.07	0.02
Aeg	0.78	0.76	0.70	0.81	0.64	0.65	0.76	0.81	0.81	0.83

*Atoms per formula unit (apfu) calculations based on four cations and six oxygens in formula. Fe^{3+} and Fe^{2+} proportions are calculated values from charge balance.

Table B.3: *(Continued)*

Date	02.10.2018	02.10.2018	02.10.2018	02.10.2018	02.10.2018
Sample	MEPB75	MEPB75	MEPB75	MEPB75	MEPB75
Point	20/1.	21/1.	22/1.	23/1.	24/1.
Wt.%					
SiO_2	52.21	52.29	52.20	52.10	52.20
TiO_2	1.78	3.13	1.50	1.00	0.90
Al_2O_3	1.66	0.79	1.00	1.10	1.00
FeO	27.29	25.43	27.60	28.20	27.90
MnO	0.34	1.39	0.40	0.40	0.30
MgO	0.24	0.46	0.40	0.40	0.30
CaO	1.39	2.49	2.10	1.80	1.80
Na_2O	13.21	12.41	12.30	12.40	12.30
ZrO_2	0.11	0.17	0.50	0.50	0.50
Total	98.21	98.56	98.00	97.90	97.20
Apfu*					
Si	1.97	1.98	1.99	1.99	2.01
Ti	0.05	0.09	0.04	0.03	0.03
Al	0.07	0.04	0.04	0.05	0.05
Fe^{3+*}	0.85	0.73	0.78	0.82	0.79
Fe^{2+*}	0.01	0.08	0.10	0.08	0.11
Mn	0.01	0.04	0.01	0.01	0.01
Mg	0.01	0.03	0.02	0.02	0.02
Ca	0.06	0.10	0.09	0.07	0.07
Na	0.97	0.91	0.91	0.92	0.92
Zr	0.00	0.00	0.01	0.01	0.01
Endmembers					
AlTsch	0.03	0.02	0.01	0.01	0.00
Jd	0.01	0.00	0.03	0.02	0.05
ZrTiAeg	0.10	0.18	0.10	0.08	0.07
Di	0.01	0.03	0.02	0.02	0.02
Hd	0.00	0.03	0.06	0.06	0.08
Aeg	0.85	0.73	0.78	0.82	0.79

*Atoms per formula unit (apfu) calculations
based on four cations and six oxygens in formula.
Fe^{3+} and Fe^{2+} proportions
are calculated values from charge balance.

Table B.4: *EMP analysis of amphibole*

Date	02.10.2018	02.10.2018	02.10.2018	02.10.2018	02.10.2018	02.10.2018	02.10.2018	04.10.2018	04.10.2018	04.10.2018	04.10.2018	07.10.2018	07.10.2018	07.10.2018	07.10.2018	07.10.2018
Point	34/1.	35/1.	42/1	43/1.	44/1.	51/1.	52/1.	4/1.	28/1.	30/1.	31/1.	19/1.	40/1.	41/1.	21/1.	22/1.
Sample	MEPB61	MEPB61	MEPB66	MEPB66	MEPB66	MEPB66	MEPB66	MEPB67	MEPB68	MEPB68	MEPB68	MEPB72	MEPB73	MEPB73	MEPB74	MEPB74
SiO_2	52.45	54.93	54.71	52.68	52.96	52.36	52.55	53.81	53.31	53.93	54.14	49.58	47.59	48.02	50.17	49.98
Al_2O_3	0.98	0.80	0.56	0.66	0.70	0.52	1.35	0.95	0.58	0.67	0.77	2.40	3.02	2.92	1.88	2.25
TiO_2	1.33	0.85	0.56	1.11	1.20	0.80	1.03	0.20	0.81	0.74	0.90	1.82	2.00	1.94	1.23	1.81
ZrO_2	0.07	0.02	-	0.01	0.00	0.05	0.08	0.01	0.05	-	-	0.08	0.27	0.28	0.18	0.15
FeO	18.43	16.29	16.64	18.84	18.12	19.25	17.66	16.18	17.05	17.70	17.42	24.28	25.70	25.44	22.91	23.05
MnO	3.00	2.80	2.99	4.18	3.73	4.09	2.79	1.47	3.53	3.53	3.15	2.95	3.14	2.74	3.05	2.88
MgO	8.45	8.83	9.31	7.16	7.66	7.56	8.30	9.84	8.91	7.62	7.68	4.26	2.98	3.28	5.36	4.64
CaO	2.56	1.18	0.41	1.28	0.76	1.34	1.75	0.48	1.36	0.66	0.43	0.99	1.14	1.26	1.20	1.00
Na_2O	7.56	9.02	8.43	7.85	7.94	7.95	7.79	7.91	8.39	8.92	8.99	8.53	8.37	8.26	8.54	8.81
K_2O	2.03	1.72	3.08	2.90	3.23	2.75	2.93	4.05	2.33	2.28	2.18	1.88	1.81	1.76	1.89	1.93
total	96.86	96.46	96.66	96.68	96.29	96.68	96.23	94.89	96.32	96.06	95.64	96.74	96.00	95.89	96.42	96.51
Apfu*																
Si	8.06	8.38	8.29	8.16	8.20	8.09	8.16	8.33	8.17	8.34	8.38	7.90	7.77	7.82	7.95	7.98
Al	0.09	0.07	0.05	0.06	0.06	0.05	0.12	0.09	0.05	0.06	0.07	0.23	0.29	0.28	0.18	0.21
Ti	0.15	0.10	0.06	0.13	0.14	0.09	0.12	0.02	0.09	0.09	0.10	0.22	0.25	0.24	0.15	0.22
Zr	0.01	0.00	0.00	0.00	0.00	0.00	0.01	0.00	0.00	0.00	0.00	0.01	0.02	0.02	0.01	0.01
Fe	2.37	2.08	2.11	2.44	2.34	2.49	2.29	2.10	2.19	2.29	2.26	3.24	3.51	3.46	3.04	3.08
Mn	0.39	0.36	0.38	0.55	0.49	0.54	0.37	0.19	0.46	0.46	0.41	0.40	0.43	0.38	0.41	0.39
Mg	1.94	2.01	2.10	1.65	1.77	1.74	1.92	2.27	2.04	1.76	1.77	1.01	0.73	0.80	1.27	1.10
Ca	0.42	0.19	0.07	0.21	0.13	0.22	0.29	0.08	0.22	0.11	0.07	0.17	0.20	0.22	0.20	0.17
Na	1.13	1.33	1.24	1.18	1.19	1.19	1.17	1.19	1.25	1.34	1.35	1.32	1.33	1.30	1.31	1.36
K	0.20	0.17	0.30	0.29	0.32	0.27	0.29	0.40	0.23	0.22	0.22	0.19	0.19	0.18	0.19	0.20
$Fe_{tot}/(Fe_{tot}+Mg)$	0.55	0.51	0.50	0.60	0.57	0.59	0.54	0.48	0.52	0.57	0.56	0.76	0.83	0.81	0.71	0.74

(-) not detected
*Atoms per formula unit (apfu) calculations based on 24 anions.

Table B.5: *BCR-2G data for Q-LA-ICP-MS analysis with 1σ error*

BCR-2G	La (μg/g)	1σ	Ce (μg/g)	1σ	Pr (μg/g)	1σ	Nd (μg/g)	1σ	Sm (μg/g)	1σ	Eu (μg/g)	1σ	Gd (μg/g)	1σ	Tb (μg/g)	1σ	Dy (μg/g)	1σ	Ho (μg/g)	1σ	Er (μg/g)	1σ	Tm (μg/g)	1σ	Yb (μg/g)	1σ	Lu (μg/g)	1σ
Georem*	24.7	0.3	53.3	0.5	6.7	0.4	28.9	0.3	6.59	0.07	1.97	0.02	6.71	0.07	1.02	0.08	6.44	0.06	1.27	0.08	3.7	0.04	0.51	0.04	3.39	0.03	0.503	0.005
01.11.18-01	27.9	1.6	55.2	2.6	7.3	0.4	30.7	1.5	7.3	0.4	2.1	0.1	7.3	0.4	1.1	0.1	7.0	0.5	1.4	0.1	3.9	0.3	0.6	0.0	3.6	0.3	0.5	0.0
01.11.18-02	28.2	1.6	56.2	2.7	7.4	0.4	31.5	1.6	7.3	0.4	2.2	0.1	7.3	0.4	1.1	0.1	7.0	0.5	1.4	0.1	4.0	0.3	0.6	0.0	3.6	0.3	0.5	0.0
01.11.18-03	28.7	2.6	58.0	4.2	7.6	0.6	32.1	2.6	7.3	0.6	2.2	0.2	7.8	0.6	1.1	0.1	7.2	0.8	1.5	0.2	4.2	0.5	0.6	0.1	3.8	0.5	0.6	0.1
01.11.18-04	28.7	2.7	58.1	4.3	7.5	0.6	32.1	2.6	7.5	0.6	2.2	0.2	7.6	0.6	1.2	0.1	7.5	0.9	1.5	0.2	4.2	0.5	0.6	0.1	3.8	0.5	0.6	0.1
01.11.18-05	27.0	1.3	53.7	2.5	7.0	0.4	29.8	1.4	6.9	0.4	2.0	0.1	7.1	0.3	1.0	0.0	6.6	0.3	1.3	0.1	3.7	0.2	0.5	0.0	3.5	0.1	0.5	0.0
01.11.18-06	27.3	1.3	54.3	2.6	7.1	0.4	29.9	1.4	7.1	0.4	2.0	0.1	6.9	0.3	1.0	0.0	6.7	0.3	1.3	0.1	3.8	0.2	0.5	0.0	3.5	0.1	0.5	0.0
01.11.18-07	24.8	1.4	52.4	3.0	6.6	0.4	27.1	1.6	6.1	0.4	1.8	0.1	6.4	0.3	0.9	0.1	6.0	0.3	1.2	0.1	3.4	0.2	0.5	0.0	3.1	0.1	0.5	0.0
02.11.18-01	25.3	1.2	53.8	2.1	6.9	0.3	29.3	1.7	6.7	0.4	2.0	0.1	6.7	0.4	1.0	0.1	6.2	0.4	1.3	0.1	3.5	0.2	0.5	0.0	3.5	0.3	0.5	0.0
02.11.18-02	25.5	1.2	54.0	2.1	6.9	0.4	29.4	1.7	6.7	0.4	2.0	0.1	6.8	0.4	1.0	0.1	6.3	0.4	1.3	0.1	3.6	0.2	0.5	0.0	3.5	0.3	0.5	0.0
02.11.18-03	26.0	1.2	53.7	2.1	6.9	0.4	29.0	1.7	6.8	0.5	1.9	0.1	6.7	0.4	1.0	0.1	6.2	0.4	1.3	0.1	3.7	0.2	0.5	0.0	3.2	0.3	0.5	0.1
02.11.18-04	28.9	2.7	56.5	3.6	7.4	0.7	32.6	4.0	7.3	1.0	2.1	0.3	7.7	1.0	1.2	0.1	7.4	1.0	1.5	0.2	4.3	0.6	0.6	0.1	3.7	0.8	0.6	0.1
05.11.18-01	28.8	1.3	56.4	2.8	7.4	0.4	31.5	1.8	7.4	0.4	2.2	0.1	7.4	0.5	1.1	0.1	7.3	0.4	1.5	0.1	4.3	0.3	0.6	0.0	3.6	0.2	0.6	0.0
05.11.18-02	27.4	1.5	53.8	3.2	7.0	0.4	29.9	2.2	7.0	0.4	2.0	0.2	7.2	0.6	1.1	0.1	7.0	0.5	1.4	0.1	4.0	0.3	0.6	0.0	3.5	0.3	0.5	0.0
05.11.18-03	27.6	1.5	54.3	3.3	7.1	0.4	30.1	2.2	7.0	0.4	2.1	0.2	7.3	0.6	1.1	0.1	7.0	0.5	1.5	0.1	4.0	0.3	0.6	0.0	3.6	0.3	0.6	0.0
05.11.18-04	27.9	2.1	54.3	4.4	7.2	0.6	30.5	3.1	7.2	0.6	2.0	0.2	7.3	0.8	1.1	0.1	7.1	0.7	1.5	0.2	4.2	0.4	0.6	0.1	3.8	0.5	0.5	0.1
05.11.18-05	28.3	2.1	55.2	4.6	7.3	0.6	30.8	3.2	7.4	0.6	2.2	0.2	7.4	0.8	1.1	0.1	7.1	0.7	1.5	0.2	4.3	0.4	0.6	0.1	4.0	0.5	0.6	0.1
26.11.18-01	26.5	1.2	53.5	2.5	7.0	0.3	28.2	1.3	6.6	0.3	2.0	0.1	6.5	0.4	1.0	0.1	6.3	0.3	1.3	0.1	3.7	0.2	0.5	0.0	3.4	0.2	0.5	0.0
26.11.18-02	26.3	1.2	53.4	2.6	7.0	0.3	28.0	1.3	6.7	0.3	2.0	0.1	6.6	0.4	1.0	0.1	6.3	0.3	1.3	0.1	3.8	0.2	0.5	0.0	3.3	0.2	0.5	0.0
26.11.18-03	26.4	1.2	53.3	2.6	7.0	0.3	28.6	1.4	6.7	0.3	2.0	0.1	6.6	0.4	1.0	0.1	6.4	0.4	1.3	0.1	3.7	0.2	0.5	0.0	3.4	0.2	0.5	0.0
26.11.18-04	27.7	1.8	54.9	3.8	7.3	0.4	30.3	2.0	7.2	0.5	2.1	0.2	7.2	0.6	1.1	0.1	6.8	0.5	1.4	0.1	4.1	0.3	0.5	0.0	3.6	0.3	0.6	0.0
26.11.18-05	27.6	1.8	54.6	3.9	7.2	0.4	30.6	2.1	7.3	0.5	2.1	0.2	7.3	0.6	1.1	0.1	6.8	0.6	1.4	0.1	4.1	0.3	0.6	0.0	3.6	0.3	0.6	0.0
26.11.18-06	27.1	2.5	54.5	5.2	7.3	0.5	30.8	2.9	7.3	0.7	2.2	0.2	7.5	0.9	1.1	0.1	6.8	0.8	1.4	0.1	4.0	0.4	0.6	0.1	3.7	0.4	0.6	0.1
26.11.18-07	28.1	2.6	55.8	5.5	7.4	0.5	31.5	3.0	7.4	0.7	2.2	0.2	7.8	1.0	1.1	0.1	7.0	0.8	1.5	0.1	4.2	0.5	0.6	0.1	3.6	0.4	0.6	0.1
26.11.18-08	29.1	1.1	58.2	2.7	7.7	0.3	32.2	1.2	7.4	0.3	2.2	0.1	7.5	0.3	1.2	0.0	7.1	0.3	1.4	0.1	4.2	0.2	0.6	0.0	3.7	0.2	0.6	0.0
27.11.18-01	27.2	0.9	55.5	1.8	7.1	0.3	29.7	1.1	6.9	0.3	2.1	0.1	7.0	0.3	1.1	0.0	6.8	0.3	1.4	0.1	3.9	0.2	0.5	0.0	3.5	0.2	0.5	0.0
26.11.18-02	27.3	0.9	55.2	1.8	7.1	0.3	30.0	1.1	6.8	0.3	2.0	0.1	7.0	0.3	1.1	0.0	6.8	0.3	1.4	0.1	4.0	0.2	0.5	0.0	3.5	0.2	0.5	0.0
26.11.18-03	28.6	1.1	57.6	2.1	7.5	0.4	32.3	1.6	7.7	0.3	2.2	0.1	7.8	0.5	1.2	0.1	7.3	0.4	1.5	0.1	4.2	0.2	0.6	0.0	4.0	0.2	0.6	0.0
26.11.18-04	29.1	1.1	58.2	2.1	7.6	0.4	32.6	1.6	7.8	0.4	2.2	0.1	8.0	0.5	1.2	0.1	7.4	0.4	1.5	0.1	4.3	0.2	0.6	0.0	3.9	0.2	0.6	0.0

*Georem data from Jochum *et al.* (2005)

Table B.6: *Analyses results from QLA-ICP-MS of sodic pyroxenes. Values given in ppm.*

Analysis	La	Ce	Pr	Nd	Sm	Eu	Gd	Tb	Dy	Ho	Er	Tm	Yb	Lu
MEPB61-01.01	81.74	190.96	25.76	102.68	19.81	5.66	15.88	2.19	12.53	2.28	6.19	0.86	5.63	0.87
MEPB61-01.02	5.80	13.42	1.81	6.66	1.05	0.32	0.79	0.16	1.07	0.26	0.91	0.17	1.39	0.23
MEPB61-02.01	38.66	80.28	10.22	40.07	7.90	1.92	5.07	0.62	3.33	0.55	1.47	0.22	1.47	0.24
MEPB61-02.02	63.06	140.40	18.54	72.51	14.58	3.99	9.96	1.41	7.42	1.24	3.04	0.48	3.38	0.51
MEPB61-03.01	27.98	72.14	8.00	29.07	3.48	0.75	1.64	0.16	0.74	0.14	0.40	0.06	0.59	0.13
MEPB61-04.01	356.61	870.46	116.66	460.76	85.79	24.78	67.97	9.41	52.91	9.84	25.71	3.44	21.87	3.08
MEPB61-05.01	250.77	493.12	63.07	256.69	64.05	17.62	55.04	8.20	49.96	9.79	26.58	3.81	24.35	3.51
MEPB61-06.01	470.76	744.20	140.72	554.06	108.43	31.66	89.86	13.18	76.31	14.24	39.39	5.46	35.07	4.86
MEPB61-06.02	55.76	115.33	13.82	55.50	10.07	3.18	8.39	1.31	8.64	1.59	4.74	0.69	5.10	0.82
MEPB61-06.02	55.92	115.72	13.86	55.71	10.11	3.19	8.42	1.31	8.68	1.60	4.76	0.69	5.13	0.83
MEPB61-07.01	2.03	4.11	0.56	2.43	0.50	0.13	0.59	0.04	0.33	0.05	0.17	0.05	0.45	0.11
MEPB61-07.03	106.31	194.74	24.08	89.94	16.84	4.99	14.65	2.14	12.45	2.30	6.31	0.87	5.65	0.79
MEPB61-07.05	98.67	203.98	26.54	109.41	26.39	8.21	26.92	4.36	26.88	5.26	14.72	2.07	13.27	1.92
MEPB62-01.01	13.14	32.28	4.17	14.65	1.74	0.36	0.93	0.08	0.40	0.07	0.27	0.05	0.55	0.15
MEPB62-01.02	13.89	33.29	4.27	14.66	1.74	0.40	0.81	0.09	0.39	0.06	0.22	0.05	0.48	0.11
MEPB62-01.03	3.78	4.32	0.38	1.22	0.25	0.06	0.29	0.04	0.36	0.09	0.39	0.12	1.35	0.38
MEPB62-01.04	4.28	5.44	0.59	2.03	0.50	0.18	0.53	0.10	0.66	0.15	0.58	0.15	2.00	0.57
MEPB62-01.05	0.91	1.27	0.14	0.47	0.08	0.03	0.12	0.01	0.06	0.02	0.12	0.05	0.86	0.28
MEPB62-01.06	14.87	35.08	4.41	15.07	1.77	0.43	0.96	0.09	0.44	0.08	0.27	0.07	0.57	0.12
MEPB62-01.07	12.94	31.11	4.00	14.04	1.62	0.40	0.85	0.08	0.37	0.06	0.22	0.05	0.50	0.12

Table B.6 (continued)

Analysis	La	Ce	Pr	Nd	Sm	Eu	Gd	Tb	Dy	Ho	Er	Tm	Yb	Lu
MEPB62-01.08	20.02	46.49	5.82	19.72	2.33	0.51	1.22	0.12	0.51	0.09	0.29	0.06	0.61	0.14
MEPB62-01.09	15.99	38.70	4.98	17.64	2.20	0.55	1.15	0.11	0.47	0.09	0.26	0.06	0.56	0.13
MEPB62-01.10	19.97	45.99	5.73	19.17	2.26	0.52	1.12	0.12	0.54	0.09	0.29	0.06	0.58	0.13
MEPB62-01.11	5.37	9.53	1.01	3.03	0.38	0.10	0.27	0.03	0.21	0.03	0.19	0.04	0.54	0.15
MEPB62-01.12	14.38	34.31	4.42	14.92	1.84	0.42	0.93	0.08	0.41	0.07	0.23	0.05	0.46	0.11
MEPB62-01.13	11.87	27.43	3.48	11.63	1.51	0.36	0.71	0.08	0.38	0.08	0.23	0.06	0.47	0.11
MEPB62-08.01	2.15	2.94	0.26	0.85	0.13	0.04	0.11	0.02	0.11	0.04	0.31	0.12	1.80	0.50
MEPB62-08.02	0.47	0.65	0.07	0.27	0.04	0.02	-	0.01	0.05	0.02	0.22	0.08	1.57	0.48
MEPB62-09.01	13.39	32.67	4.19	14.44	1.86	0.41	0.98	0.10	0.44	0.08	0.29	0.06	0.63	0.15
MEPB62-09.02	14.38	34.69	4.40	14.90	1.80	0.42	0.94	0.10	0.40	0.06	0.23	0.05	0.49	0.12
MEPB64-01.01	3.49	6.14	0.42	1.16	0.13	0.04	0.11	0.02	0.13	0.03	0.14	0.05	0.68	0.20
MEPB64-01.02	5.38	8.08	0.94	2.47	0.44	0.17	0.45	0.08	0.53	0.13	0.43	0.09	1.08	0.27
MEPB64-01.03	7.72	6.29	0.45	1.14	0.15	0.04	-	0.03	0.11	0.03	0.18	0.06	0.74	0.22
MEPB64-02.01	1.78	2.50	0.22	0.62	0.08	-	-	0.01	0.07	0.03	0.24	0.10	1.44	0.39
MEPB64-02.02	13.02	12.85	0.91	2.17	0.30	0.05	0.23	0.02	0.16	0.05	0.18	0.06	0.94	0.30
MEPB64-02.03	13.46	12.65	0.97	2.97	0.45	0.13	0.35	0.04	0.20	0.04	0.14	0.04	0.51	0.15
MEPB64-02.04	4.22	4.46	0.38	2.05	0.13	0.04	0.09	0.01	0.10	0.02	0.17	0.06	0.79	0.26
MEPB66-01.01	10.47	27.70	3.67	12.95	1.65	0.39	0.84	0.08	0.40	0.06	0.22	0.05	0.49	0.11
MEPB66-01.02	17.80	40.66	4.88	16.22	1.96	0.48	1.00	0.10	0.51	0.09	0.31	0.06	0.70	0.18
MEPB66-01.03	7.16	16.03	1.91	6.36	0.78	0.17	0.41	0.03	0.22	0.04	0.11	0.03	0.29	0.08
MEPB66-02.01	8.43	19.60	2.44	7.95	1.05	0.26	0.51	0.06	0.29	0.04	0.17	0.04	0.44	0.08

Table B.6 (continued)

Analysis	La	Ce	Pr	Nd	Sm	Eu	Gd	Tb	Dy	Ho	Er	Tm	Yb	Lu
MEPB66-02.02	5.89	13.28	1.56	4.71	0.60	0.13	0.28	0.03	0.13	0.02	0.11	0.03	0.28	0.06
MEPB66-02.03	5.89	13.30	1.56	4.71	0.60	0.13	0.28	0.03	0.13	0.02	0.11	0.03	0.28	0.06
MEPB66-03.01	13.63	33.71	4.31	14.60	1.85	0.47	1.05	0.09	0.42	0.09	0.22	0.06	0.54	0.13
MEPB66-03.02	5.66	12.57	1.46	4.45	0.47	0.17	0.24	0.03	0.15	0.02	0.12	0.02	0.34	0.07
MEPB66-03.03	11.14	25.76	3.21	10.56	1.30	0.31	0.66	0.07	0.29	0.05	0.14	0.03	0.39	0.09
MEPB66-03.05	13.32	30.47	3.99	13.59	1.96	0.48	1.11	0.14	0.83	0.17	0.55	0.10	0.77	0.15
MEPB67-01.01	11.85	29.48	4.13	15.15	1.95	0.46	0.99	0.11	0.53	0.08	0.25	0.05	0.66	0.15
MEPB67-01.02	11.58	29.04	4.06	15.38	2.09	0.48	1.07	0.12	0.49	0.09	0.31	0.06	0.65	0.17
MEPB67-01.03	7.62	19.96	2.55	8.92	1.36	0.38	0.81	0.13	0.75	0.15	0.44	0.06	0.72	0.17
MEPB67-02.01	9.75	24.25	3.37	12.44	1.71	0.37	0.82	0.09	0.43	0.07	0.25	0.05	0.55	0.13
MEPB67-02.02	8.65	21.01	2.93	10.43	1.42	0.28	0.54	0.05	0.25	0.06	0.12	0.04	0.31	0.08
MEPB67-04.01	15.29	23.56	3.07	10.77	1.31	0.35	0.81	0.08	0.42	0.07	0.28	0.05	0.49	0.13
MEPB67-04.02	9.90	22.88	3.30	12.38	1.73	0.31	0.91	0.10	0.40	0.08	0.29	0.07	0.60	0.13
MEPB68-01.01	10.02	24.32	3.28	11.82	1.41	0.39	0.78	0.10	0.40	0.06	0.22	0.05	0.50	0.13
MEPB68-01.02	28.44	68.76	9.50	36.66	6.99	1.68	4.95	0.60	3.07	0.47	1.21	0.16	1.18	0.21
MEPB68-01.03	40.60	69.00	8.13	29.32	3.78	1.11	2.60	0.34	1.98	0.37	1.10	0.18	1.22	0.25
MEPB68-02.01	6.15	14.16	1.85	6.59	1.01	0.24	0.60	0.08	0.49	0.09	0.37	0.07	0.80	0.21
MEPB68-02.02	8.65	20.70	2.64	9.28	1.37	0.27	0.64	0.07	0.44	0.08	0.28	0.07	0.70	0.15
MEPB68-02.03	6.74	16.02	2.16	7.89	1.21	0.31	0.80	0.08	0.47	0.09	0.34	0.08	1.05	0.29
MEPB68-03.01	13.38	32.79	4.43	16.33	2.12	0.44	1.07	0.11	0.56	0.09	0.31	0.08	0.81	0.16
MEPB68-03.02	5.81	12.57	1.53	5.19	0.74	0.18	0.56	0.06	0.36	0.06	0.24	0.07	0.84	0.21

Table B.6 (continued)

Analysis	La	Ce	Pr	Nd	Sm	Eu	Gd	Tb	Dy	Ho	Er	Tm	Yb	Lu
MEPB68-03.03	7.54	18.05	2.41	9.30	1.32	0.30	0.94	0.10	0.59	0.10	0.40	0.10	1.02	0.28
MEPB69-01.01	8.16	17.70	2.14	8.07	1.57	0.41	1.40	0.30	2.29	0.59	2.39	0.49	4.58	0.92
MEPB69-01.02	3.55	5.49	0.58	1.83	0.25	0.04	0.18	0.02	0.15	0.04	0.27	0.10	1.46	0.36
MEPB69-02.01	2.54	4.09	0.41	1.13	0.15	0.05	0.16	0.01	0.09	0.03	0.27	0.10	1.68	0.44
MEPB69-02.02	1.68	2.97	0.30	0.91	0.14	-	-	0.01	0.11	0.03	0.31	0.14	2.24	0.71
MEPB69-03.01	6.89	13.41	1.73	6.08	0.93	0.22	0.70	0.08	0.50	0.13	0.75	0.24	3.00	0.78
MEPB69-03.02	1.30	3.57	0.50	1.84	0.28	0.08	0.23	0.03	0.17	0.03	0.17	0.06	0.93	0.29
MEPB69-04.01	3.77	6.49	0.84	3.30	0.67	0.21	0.61	0.10	0.72	0.19	0.90	0.20	1.82	0.27
MEPB69-04.02	1.39	3.43	0.48	1.87	0.32	0.07	0.13	0.03	0.13	0.04	0.19	0.07	1.10	0.32
MEPB69-05.02	1.67	4.11	0.58	2.12	0.32	0.05	0.21	0.02	0.15	0.04	0.14	0.05	0.78	0.21
MEPB69-05.03	1.01	2.85	0.41	1.54	0.25	0.05	0.15	0.02	0.10	0.02	0.12	0.03	0.57	0.17
MEPB69-05.04	5.38	10.10	1.01	2.60	0.32	0.10	0.21	0.04	0.33	0.12	0.88	0.36	4.99	1.48
MEPB70-01.01	12.29	16.36	3.67	8.46	2.47	0.68	1.77	0.22	1.14	0.27	1.39	0.59	9.06	2.74
MEPB70-01.02	23.66	39.80	12.17	40.09	20.63	5.60	14.44	1.81	6.99	1.19	3.87	1.02	11.11	2.95
MEPB70-01.03	18.25	36.49	8.88	24.10	5.92	1.48	3.53	0.48	2.21	0.48	2.04	0.63	8.89	2.72
MEPB70-02.01	18.31	47.01	8.70	23.35	4.87	1.11	3.36	0.44	2.43	0.65	3.24	1.08	15.28	4.44
MEPB70-02.02	13.13	30.73	7.01	20.83	4.23	1.01	2.56	0.33	1.60	0.32	1.40	0.43	5.47	1.73
MEPB70-02.03	16.53	29.97	6.28	17.85	3.81	0.87	2.51	0.26	1.23	0.23	1.31	0.33	5.17	1.61
MEPB70-03.02	67.14	93.61	15.99	46.50	9.40	2.31	6.46	0.88	3.94	0.68	2.32	0.52	5.51	1.21
MEPB70-03.03	12.26	27.23	5.21	15.56	3.20	0.77	1.89	0.22	1.50	0.26	1.10	0.39	5.55	1.67
MEPB71-01.02	21.51	28.86	2.79	8.96	1.08	0.30	0.96	0.15	0.99	0.22	0.83	0.17	1.86	0.46

Table B.6 (continued)

Analysis	La	Ce	Pr	Nd	Sm	Eu	Gd	Tb	Dy	Ho	Er	Tm	Yb	Lu
MEPB71-02.01	20.28	35.48	4.22	14.75	2.31	0.51	1.48	0.19	0.93	0.20	1.02	0.36	5.17	1.47
MEPB71-02.02	8.02	16.73	2.12	7.60	1.14	0.22	0.89	0.10	0.71	0.19	1.08	0.33	4.90	1.40
MEPB71-02.03	19.03	42.84	6.04	23.24	4.18	0.87	2.09	0.25	1.17	0.20	0.74	0.19	2.32	0.69
MEPB71-03.02	107.96	180.73	18.23	52.32	3.93	0.67	1.87	0.22	1.32	0.30	1.21	0.28	2.90	0.71
MEPB71-03.03	8.21	15.23	1.89	6.59	0.97	0.24	0.54	0.09	0.49	0.15	0.84	0.27	3.52	0.87
MEPB72-01.01	26.28	32.82	3.66	8.97	1.52	0.20	0.93	0.16	0.94	0.17	0.70	0.23	3.24	1.09
MEPB72-01.02	30.14	55.43	7.63	23.19	4.75	0.97	3.30	0.57	2.95	0.53	1.60	0.45	4.97	1.36
MEPB72-01.03	20.23	46.36	6.78	21.38	4.20	1.27	3.67	0.58	3.08	0.58	2.03	0.49	5.93	1.57
MEPB72-02.01	13.02	23.36	3.17	8.35	1.14	0.23	0.69	0.09	0.71	0.23	1.50	0.49	6.85	1.62
MEPB72-02.03	219.17	365.70	44.60	129.59	19.49	5.31	13.45	1.69	8.14	1.33	3.71	0.77	8.01	1.94
MEPB72-03.01	9.05	12.16	1.31	3.01	0.45	-	-	0.04	0.25	0.09	0.52	0.18	3.03	0.78
MEPB72-03.02	23.37	46.61	6.84	20.29	2.88	0.61	1.86	0.29	1.76	0.53	3.27	1.09	14.66	3.83
MEPB72-03.03	10.67	17.93	2.11	5.23	0.86	0.24	0.42	0.06	0.46	0.12	0.83	0.33	4.86	1.35
MEPB72-04.01	272.36	466.69	52.12	147.83	17.51	5.39	10.47	1.12	5.23	0.83	2.08	0.43	3.70	0.85
MEPB72-04.02	2.98	4.10	0.41	1.06	0.15	-	-	0.02	0.12	0.04	0.30	0.11	1.85	0.59
MEPB72-04.03	259.76	475.18	50.73	151.37	21.31	4.01	14.67	1.88	9.69	1.59	4.06	0.57	4.52	0.81
MEPB72-05.01	28.68	29.97	2.30	5.60	0.73	0.17	0.50	0.08	0.46	0.09	0.30	0.08	1.07	0.31
MEPB72-05.02	28.84	51.14	4.02	11.30	1.81	0.43	1.50	0.24	1.47	0.28	0.89	0.16	1.62	0.39
MEPB72-05.03	6.03	12.42	1.23	3.98	0.81	0.20	0.70	0.11	0.62	0.11	0.43	0.11	1.33	0.42
MEPB73-01.01	6.43	13.64	1.86	6.21	0.77	0.17	0.43	0.06	0.22	0.08	0.62	0.25	4.24	1.31
MEPB73-01.02	18.58	34.55	4.34	13.55	1.81	0.35	0.99	0.12	0.78	0.18	1.06	0.35	5.19	1.40

Table B.6 (continued)

Analysis	La	Ce	Pr	Nd	Sm	Eu	Gd	Tb	Dy	Ho	Er	Tm	Yb	Lu
MEPB73-01.03	9.09	27.33	3.35	12.30	1.99	0.45	1.40	0.21	1.39	0.29	1.46	0.55	8.20	2.48
MEPB73-02.01	6.83	19.67	1.33	4.54	0.80	0.17	0.40	0.09	0.50	0.10	0.44	0.15	2.02	0.55
MEPB73-02.02	28.32	87.91	4.54	15.19	3.02	0.73	2.55	0.38	1.88	0.33	1.05	0.24	2.48	0.57
MEPB73-02.03	19.28	78.46	3.63	12.21	2.05	0.45	1.67	0.21	1.25	0.21	0.86	0.23	2.73	0.63
MEPB74-01.03	21.49	45.46	5.28	16.93	2.43	0.46	1.31	0.17	0.72	0.14	0.44	0.11	1.36	0.40
MEPB74-02.01	10.89	19.74	2.17	7.02	0.93	0.17	0.65	0.11	0.72	0.21	1.13	0.41	5.68	1.56
MEPB74-02.02	6.59	12.27	1.35	3.72	0.50	0.17	0.28	0.06	0.36	0.12	0.90	0.39	6.96	2.21
MEPB74-03.01	5.80	9.95	0.96	2.45	0.27	0.09	0.43	0.07	0.57	0.16	1.00	0.36	5.35	1.50
MEPB74-03.02	6.32	16.21	2.22	7.74	1.12	0.23	0.74	0.09	0.63	0.18	1.18	0.42	5.12	1.31
MEPB74-03.03	14.51	31.93	3.69	10.61	1.43	0.30	0.85	0.14	0.93	0.23	1.46	0.44	6.12	1.70
MEPB75-01.01	3.15	10.76	1.78	6.95	1.20	0.25	0.68	0.09	0.53	0.10	0.47	0.13	1.80	0.48
MEPB75-01.02	3.46	10.41	1.59	5.80	0.97	0.24	0.59	0.07	0.43	0.10	0.43	0.13	1.74	0.49
MEPB75-01.03	7.51	15.24	2.07	7.65	1.35	0.27	0.79	0.11	0.53	0.11	0.45	0.11	1.47	0.39
MEPB75-02.02	4.87	10.86	1.43	5.31	0.99	0.26	0.70	0.12	0.69	0.15	0.69	0.23	3.85	1.14
MEPB75-03.01	2.46	3.92	0.41	1.11	0.22	0.05	0.14	0.02	0.12	0.03	0.19	0.07	0.96	0.24
MEPB75-03.02	32.39	52.47	4.88	14.50	2.19	0.56	2.12	0.41	3.41	0.95	3.67	0.74	6.49	1.31
MEPB75-03.03	17.57	24.65	3.03	10.14	1.99	0.47	1.49	0.23	1.26	0.22	0.83	0.22	3.19	0.74
MEPB75-04.01	4.24	8.42	1.08	3.61	0.66	0.20	0.29	0.07	0.49	0.08	0.35	0.10	1.41	0.41
MEPB75-04.02	5.24	12.67	1.71	6.40	1.17	0.30	0.96	0.17	0.95	0.19	0.84	0.23	3.70	1.07
MEPB75-05.01	4.04	11.50	1.66	6.20	1.06	0.26	0.61	0.08	0.49	0.11	0.46	0.12	1.82	0.48
MEPB75-05.02	2.87	4.92	0.50	1.57	0.23	0.05	-	0.02	0.17	0.05	0.25	0.08	1.11	0.31

Table B.6 (continued)

Analysis	La	Ce	Pr	Nd	Sm	Eu	Gd	Tb	Dy	Ho	Er	Tm	Yb	Lu
MEPB75-05.03	6.61	13.38	1.66	5.73	1.07	0.30	0.91	0.15	1.11	0.26	1.03	0.28	3.66	0.95
MEPB75-06.01	6.71	12.15	1.38	4.45	0.64	0.13	0.38	0.05	0.30	0.05	0.24	0.09	1.04	0.28
MEPB76-01.01	2.68	7.35	1.10	3.97	0.70	0.12	0.40	0.04	0.21	0.04	0.19	0.06	0.79	0.25
MEPB76-01.02	5.21	9.07	0.95	2.80	0.35	0.09	0.15	0.04	0.28	0.08	0.46	0.18	2.44	0.65
MEPB76-02.03	16.11	40.31	5.63	22.52	5.17	1.33	5.43	1.00	7.29	1.70	5.93	0.97	7.98	1.31
MEPB76-03.01	12.92	23.82	2.45	6.47	0.80	0.16	0.41	0.08	0.40	0.09	0.57	0.15	2.31	0.64
MEPB76-03.02	32.27	99.04	12.36	41.01	6.93	1.78	5.26	0.83	5.58	1.24	3.80	0.65	4.73	0.82
MEPB76-03.03	8.95	22.82	2.99	10.31	1.83	0.37	1.13	0.14	0.79	0.14	0.52	0.12	1.44	0.39
MEPB76-04.01	7.43	15.86	2.63	11.52	3.50	1.04	2.90	0.39	2.08	0.36	1.01	0.12	0.93	0.17
MEPB76-04.02	6.62	17.09	2.40	8.36	1.24	0.29	0.72	0.09	0.51	0.16	0.95	0.30	4.45	1.18
MEPB76-04.03	4.07	9.12	1.47	6.13	1.16	0.27	0.64	0.08	0.40	0.09	0.37	0.12	1.24	0.23
MEPB76-04.04	2.23	6.67	1.07	4.04	0.80	0.19	0.40	0.05	0.21	0.05	0.27	0.08	1.15	0.32

(-) not detected.

Table B.7: *Analyses results from QLA-ICP-MS of amphibole. Values given in ppm.*

Analysis	La	Ce	Pr	Nd	Sm	Eu	Gd	Tb	Dy	Ho	Er	Tm	Yb	Lu
MEPB68-01.01	3.53	6.46	0.67	1.99	0.25	0.08	0.18	0.03	0.18	0.04	0.25	0.07	0.75	0.17
MEPB68-01.02	3.29	6.11	0.61	1.84	0.13	0.02	0.08	0.02	0.11	0.02	0.19	0.05	0.66	0.14
MEPB68-01.03	17.64	37.62	6.55	21.78	2.69	0.73	1.64	0.19	0.98	0.20	0.62	0.09	0.46	0.08
MEPB68-01.04	4.23	7.49	0.78	2.07	0.26	0.06	0.23	0.02	0.14	0.04	0.21	0.05	0.75	0.17
MEPB68-01.06	5.90	7.37	0.59	1.55	0.18	0.07	0.16	0.01	0.09	0.02	0.08	0.02	0.39	0.09
MEPB69-01.01	2.35	4.37	0.49	1.39	0.18	0.05	0.19	0.01	0.07	0.02	0.17	0.06	0.83	0.26
MEPB69-01.03	4.70	9.30	1.05	3.20	0.33	0.08	0.20	0.04	0.17	0.04	0.27	0.08	1.15	0.33
MEPB69-01.05	7.41	14.54	1.84	6.13	1.11	0.24	1.01	0.17	1.25	0.33	1.15	0.26	2.55	0.57
MEPB69-01.06	63.52	80.65	7.19	20.41	1.78	0.34	1.05	0.10	0.44	0.08	0.31	0.07	0.99	0.29
MEPB69-01.07	3.72	7.79	0.98	3.16	0.44	0.12	0.28	0.05	0.33	0.07	0.34	0.10	1.20	0.33
MEPB69-01.08	4.49	9.52	1.20	3.81	0.53	0.12	0.35	0.03	0.19	0.04	0.24	0.10	1.25	0.35
MEPB71-01.01	21.00	45.43	5.43	17.60	2.08	0.39	1.02	0.12	0.68	0.13	0.60	0.19	2.51	0.73
MEPB71-01.02	11.24	25.23	2.98	9.58	1.15	0.22	0.61	0.06	0.37	0.10	0.51	0.14	1.93	0.51
MEPB71-01.03	10.10	22.21	2.69	8.89	0.98	0.22	0.54	0.07	0.37	0.09	0.46	0.13	1.73	0.46
MEPB71-01.04	11.41	23.51	2.72	8.53	1.14	0.23	0.68	0.10	0.67	0.18	0.83	0.21	2.30	0.56
MEPB71-01.05	26.96	50.95	6.18	21.10	2.88	0.96	2.03	0.31	1.77	0.40	1.35	0.27	2.66	0.68
MEPB71-01.07	12.37	25.71	3.12	10.08	1.15	0.23	0.54	0.06	0.40	0.09	0.49	0.14	1.80	0.51
MEPB71-01.09	12.12	26.76	3.20	10.30	1.21	0.24	0.65	0.08	0.43	0.10	0.50	0.15	1.97	0.50
MEPB71-01.10	5.64	11.67	1.38	4.42	0.55	0.09	0.29	0.05	0.28	0.08	0.40	0.11	1.65	0.46
MEPB71-01.11	9.76	20.21	2.34	7.32	0.96	0.20	0.47	0.07	0.46	0.11	0.48	0.15	1.97	0.50

Table B.7 (continued)

Analysis	La	Ce	Pr	Nd	Sm	Eu	Gd	Tb	Dy	Ho	Er	Tm	Yb	Lu
MEPB72-01.01	34.25	72.28	8.19	24.71	2.75	0.60	1.47	0.20	1.16	0.31	1.46	0.40	4.83	1.23
MEPB72-01.02	47.91	93.24	10.05	28.85	3.17	0.59	1.71	0.22	1.40	0.35	1.71	0.47	5.32	1.29
MEPB72-01.03	8.74	16.62	1.78	4.97	0.60	0.07	0.32	0.04	0.18	0.04	0.23	0.08	1.08	0.33
MEPB72-01.04	38.07	52.01	5.94	17.23	1.28	0.20	0.48	0.05	0.21	0.04	0.24	0.07	0.97	0.28
MEPB72-01.05	3.28	7.72	1.07	4.90	1.45	0.41	1.17	0.14	0.68	0.15	0.72	0.21	2.41	0.57
MEPB72-01.06	215.14	257.90	26.62	74.43	7.14	2.13	3.79	0.30	1.22	0.18	0.56	0.13	1.29	0.38
MEPB72-01.07	21.16	44.00	5.07	15.44	1.74	0.36	0.95	0.11	0.79	0.22	1.17	0.32	3.93	1.00
MEPB73-01.01	14.04	30.30	3.71	12.07	1.64	0.31	0.87	0.09	0.48	0.10	0.49	0.14	1.86	0.54
MEPB73-01.02	20.78	44.52	5.34	17.39	2.27	0.43	1.13	0.13	0.67	0.16	0.68	0.18	2.19	0.60
MEPB73-01.03	19.35	41.58	5.11	16.48	2.14	0.42	1.22	0.13	0.61	0.13	0.56	0.15	1.92	0.50
MEPB73-01.04	20.94	50.42	6.91	24.04	3.71	0.74	1.97	0.20	1.03	0.19	0.84	0.22	2.65	0.64
MEPB73-01.05	18.92	39.73	4.87	15.62	1.95	0.39	1.16	0.11	0.62	0.15	0.83	0.23	3.21	0.91
MEPB73-01.06	26.17	64.02	7.79	27.12	4.09	0.87	2.38	0.28	1.39	0.30	1.18	0.31	3.67	0.92
MEPB73-01.07	28.18	63.17	8.12	26.07	3.56	0.75	1.91	0.20	0.99	0.25	1.25	0.40	5.20	1.38
MEPB74-01.03	5.68	10.89	1.20	3.29	0.36	0.08	0.39	0.03	0.17	0.03	0.20	0.07	0.93	0.25
MEPB74-01.06	4.20	8.47	1.01	3.25	0.39	0.12	-	0.02	0.13	0.03	0.18	0.06	0.86	0.28
MEPB74-01.08	4.51	8.58	0.96	2.83	0.32	0.07	-	0.02	0.09	0.02	0.18	0.07	1.03	0.27
MEPB74-01.09	12.54	19.28	1.95	5.95	0.61	0.10	0.40	0.03	0.29	0.04	0.22	0.06	1.01	0.29
MEPB75-01.01	10.24	24.99	3.07	9.70	1.16	-	0.86	0.08	0.32	0.11	0.68	0.20	2.15	0.55
MEPB75-01.02	12.50	30.42	3.80	11.72	1.54	0.29	0.90	0.09	0.47	0.13	0.81	0.22	2.57	0.62
MEPB75-01.03	11.66	28.18	3.42	10.54	1.35	0.27	0.79	0.07	0.51	0.14	0.80	0.22	2.63	0.65

Table B.7 (continued)

Analysis	La	Ce	Pr	Nd	Sm	Eu	Gd	Tb	Dy	Ho	Er	Tm	Yb	Lu
MEPB75-01.04	14.84	35.43	4.43	13.89	1.70	0.36	1.01	0.11	0.72	0.13	0.81	0.20	2.38	0.56
MEPB76-01.01	7.00	16.11	1.97	6.36	0.72	0.16	0.48	0.05	0.25	0.06	0.33	0.09	1.19	0.31
MEPB76-01.03	10.42	19.80	2.29	7.35	0.96	0.21	0.57	0.09	0.39	0.08	0.34	0.09	1.09	0.32

(-) not detected.

Table B.8: *Calculated average REE distributions for each group and for each type of pyroxene and amphibole. Values given in ppm.*

	La	Ce	Pr	Nd	Sm	Eu	Gd	Tb	Dy	Ho	Er	Tm	Yb	Lu
Gr 1: cpx-II	132.17	263.89	37.97	150.54	30.46	8.80	25.29	3.69	21.71	4.08	11.17	1.57	10.23	1.48
Gr 1: cpx-III	27.98	72.14	8.00	29.07	3.48	0.75	1.64	0.16	0.74	0.14	0.40	0.06	0.59	0.13
Gr 2 : cpx-III	5.46	6.37	0.55	1.68	0.25	0.08	0.25	0.03	0.22	0.06	0.26	0.08	1.06	0.31
Gr 2: cpx-I	14.99	35.64	4.53	15.53	1.88	0.43	0.96	0.09	0.43	0.08	0.25	0.05	0.54	0.12
Gr 3: cpx-II	12.36	25.95	3.30	11.97	1.62	0.40	1.00	0.12	0.66	0.12	0.41	0.09	0.87	0.21
Gr 4: cpx-II	10.37	24.13	3.12	10.77	1.41	0.33	0.74	0.08	0.39	0.07	0.24	0.05	0.51	0.12
Gr 5: cpx-II	16.77	32.97	5.84	17.52	4.40	1.09	2.87	0.36	1.71	0.35	1.51	0.46	6.14	1.77
Gr 6: cpx-II	34.41	65.00	7.01	20.80	3.36	0.83	2.40	0.34	1.85	0.35	1.41	0.40	5.08	1.35
Gr 6: cpx-III	6.02	8.13	0.86	2.04	0.30	-	-	0.03	0.18	0.06	0.41	0.14	2.44	0.69
Gr 7: cpx-II	6.94	14.12	1.73	5.84	0.98	0.23	0.67	0.10	0.62	0.14	0.68	0.20	2.66	0.71
Gr 7: cpx-III	2.67	4.42	0.46	1.34	0.23	0.05		0.02	0.14	0.04	0.22	0.07	1.04	0.28
Gr 3: m-arf	6.92	13.01	1.84	5.85	0.70	0.23	0.55	0.05	0.30	0.06	0.27	0.06	0.60	0.13
Gr 5: arf	13.40	27.96	3.34	10.87	1.34	0.31	0.76	0.10	0.60	0.14	0.62	0.17	2.06	0.55
Gr 6: arf	23.21	47.66	5.69	18.07	2.33	0.47	1.29	0.15	0.79	0.18	0.87	0.24	3.02	0.78
Gr 7: arf	8.40	18.00	2.16	6.77	0.86	0.16	0.62	0.06	0.39	0.09	0.48	0.13	1.60	0.41

Table B.9: *Calculated average REE distributions of aegirines in the Green Foyaite, and the average pyroxene and amphibole of the White Foyaite from Giles (2018). Values given in ppm.*

	La	Ce	Pr	Nd	Sm	Eu	Gd	Tb	Dy	Ho	Er	Tm	Yb	Lu
MEPB61 (cpx-II)	132.2	263.9	38.0	150.5	30.5	8.8	25.3	3.7	21.7	4.1	11.2	1.6	10.2	1.5
MEPB62(cpx-I)	15.0	35.6	4.5	15.5	1.9	0.4	1.0	0.1	0.4	0.1	0.3	0.1	0.5	0.1
Average cpx-III	4.9	5.8	0.5	1.6	0.2	0.1	0.3	0.0	0.2	0.1	0.3	0.1	1.1	0.3
Average cpx-II (foliated)	11.7	26.3	3.4	12.3	1.7	0.4	1.0	0.1	0.6	0.1	0.3	0.1	0.6	0.2
Average cpx-II (un-foliated)	21.4	40.2	5.4	17.8	3.0	0.8	2.3	0.3	1.6	0.3	1.3	0.3	3.7	1.0
Average aegrine (Giles (2018))	5.8	13.7	1.7	5.8	0.9	0.2	0.6	0.1	0.5	0.1	0.5	0.2	2.1	0.6
Average arf	20.9	39.8	4.6	14.4	1.9	0.4	1.4	0.2	1.0	0.2	0.9	0.2	2.3	0.6
Average blue amph (Giles (2018))	23.0	47.8	6.3	20.9	2.9	0.6	1.7	0.2	1.0	0.2	0.8	0.2	2.1	0.5
MEPB42 (Giles (2018)	31.72	109.36	20.98	92.78	20.3	6.92	21.68	1.9	10.24	1.61	4.81	0.97	8.67	1.04

Table B.10: *Calculated average primary (cpx-I and II) and secondary (cpx-III) pyroxenes, with their calculated K_D values based on Beard (2018) spreadsheet, and the calculated liquid REE-concentrations. Values in ppm.*

	La	Ce	Pr	Nd	Sm	Eu	Gd	Tb	Dy	Ho	Er	Tm	Yb	Lu
Gr2 : cpx-III	5.5	6.4	0.6	1.7	0.3	0.1	0.3	0.0	0.2	0.1	0.3	0.1	1.1	0.3
Gr 2: cpx-I	15.0	35.6	4.5	15.5	1.9	0.4	1.0	0.1	0.4	0.1	0.3	0.1	0.5	0.1
Kd: cpx-I (Gr 2)	1.3	1.5	1.6	1.6	1.3	1.1	0.8	0.7	0.4	0.4	0.3	0.3	0.4	0.3
Kd: cpx-III (Gr 2)	3.4	3.6	3.6	3.5	2.8	2.5	2.1	1.8	1.3	1.2	1.0	0.8	0.7	0.5
CL: Cpx-III	1.6	1.8	0.2	0.5	0.1	0.0	0.1	0.0	0.2	0.0	0.3	0.1	1.6	0.6
CL:Cpx-I	11.5	23.6	2.8	9.8	1.5	0.4	1.1	0.1	1.1	0.2	0.8	0.2	1.5	0.4
Gr 6: cpx-II	34.4	65.0	7.0	20.8	3.4	0.8	2.4	0.3	1.8	0.4	1.4	0.4	5.1	1.4
Gr 6: cpx-III	6.0	8.1	0.9	2.0	0.3	-	-	0.0	0.2	0.1	0.4	0.1	2.4	0.7
Kd: cpx-II (Gr 6)	2.4	2.6	2.7	2.6	2.2	2.0	1.7	1.5	1.1	1.0	0.8	0.7	0.6	0.5
Kd: cpx-III (Gr 6)	2.0	2.1	2.1	2.0	1.6	1.4	1.2	1.0	0.7	0.7	0.5	0.4	0.3	0.3
CL: cpx-II (Gr 6)	14.4	25.1	2.6	8.0	1.5	0.4	1.4	0.2	1.7	0.3	1.7	0.6	8.9	2.8
CL: cpx-III (Gr 6)	3.1	3.9	0.4	1.0	0.2	0.0	0.0	0.0	0.3	0.1	0.8	0.3	7.1	2.4
Gr 7: cpx-II	17.6	24.7	3.0	10.1	2.0	0.5	1.5	0.2	1.3	0.2	0.8	0.2	3.2	0.7
Gr 7: cpx-III	2.7	4.4	0.5	1.3	0.2	0.0	0.0	0.0	0.1	0.0	0.2	0.1	1.0	0.3
Kd: cpx-II (Gr 7)	2.4	2.6	2.7	2.6	2.2	2.0	1.7	1.5	1.1	1.0	0.8	0.7	0.6	0.5
Kd: cpx-III (Gr 7)	2.0	2.1	2.1	2.0	1.6	1.4	1.2	1.0	0.7	0.7	0.5	0.4	0.3	0.3
CL: cpx-II (Gr 7)	7.3	9.5	1.1	3.9	0.9	0.2	0.9	0.2	1.2	0.2	1.0	0.3	5.6	1.5
CL: cpx-III (Gr 7)	1.4	2.1	0.2	0.7	0.1	0.0	0.0	0.0	0.2	0.1	0.4	0.2	3.0	1.0
Gr 1: cpx-II	132.2	263.9	38.0	150.5	30.5	8.8	25.3	3.7	21.7	4.1	11.2	1.6	10.2	1.5
Gr 1: cpx-III	28.0	72.1	8.0	29.1	3.5	0.7	1.6	0.2	0.7	0.1	0.4	0.1	0.6	0.1
Kd. Cpx-III (Gr 1)	1.3	1.5	1.6	1.5	1.1	0.9	0.7	0.5	0.3	0.2	0.2	0.2	0.2	0.2
Kd. Cpx-II (Gr 1)	1.0	1.3	1.5	1.6	1.3	1.1	0.9	0.7	0.4	0.4	0.5	0.6	0.6	0.7
CL: cpx-II (Gr 1)	135.6	207.7	25.5	96.2	22.7	7.7	27.6	5.3	53.6	10.8	23.4	2.8	16.0	2.2
CL: cpx-III (Gr 1)	21.7	48.2	5.1	19.3	3.2	0.9	2.5	0.3	2.9	0.6	2.3	0.3	3.3	0.7

Table B.11: *Average analysis of clinopyroxene in MEPB42, with the calculated melt concentrations, the fractionated melt, the consentration in a mineral that crystallized from the fractionated melt and the average cpx in group 6. Values given in ppm.*

	La139	Ce140	Pr141	Nd143	Sm147	Eu151	Gd157	Tb159	Dy163	Ho165	Er166	Tm169	Yb173	Lu175
MEPB42	31.72	109.36	20.98	92.78	20.30	-	-	1.90	10.24	1.61	4.81	0.97	-	1.04
C0 (MEPB42)	11.14	28.46	4.43	17.41	3.81	-	-	0.52	3.48	0.69	2.67	0.69	-	1.20
CL (0.8 frac)	7.38	15.10	1.93	6.63	1.45	-	-	0.29	2.26	0.52	2.23	0.63	-	1.24
Cmin	17.65	39.12	5.14	17.31	3.24	-	-	0.43	2.45	0.53	1.86	0.44	-	0.60
Gr 6: cpx-II	34.41	65.00	7.01	20.80	3.36	0.83	2.40	0.34	1.85	0.35	1.41	0.40	5.08	1.35

Appendix C: Thin section images

MEPB60

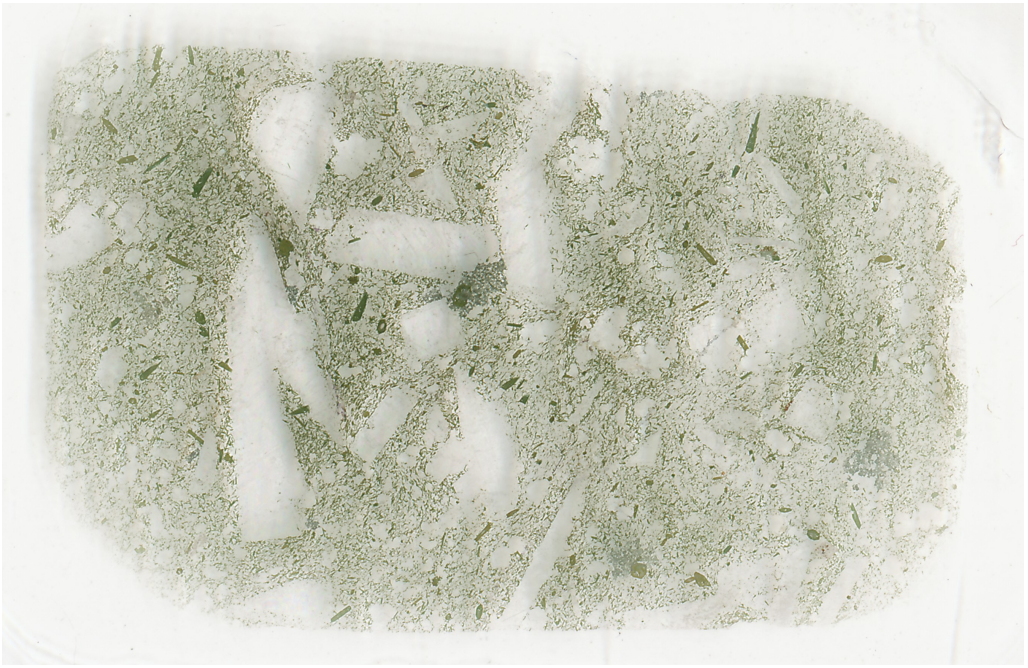

MEPB61

MEPB62

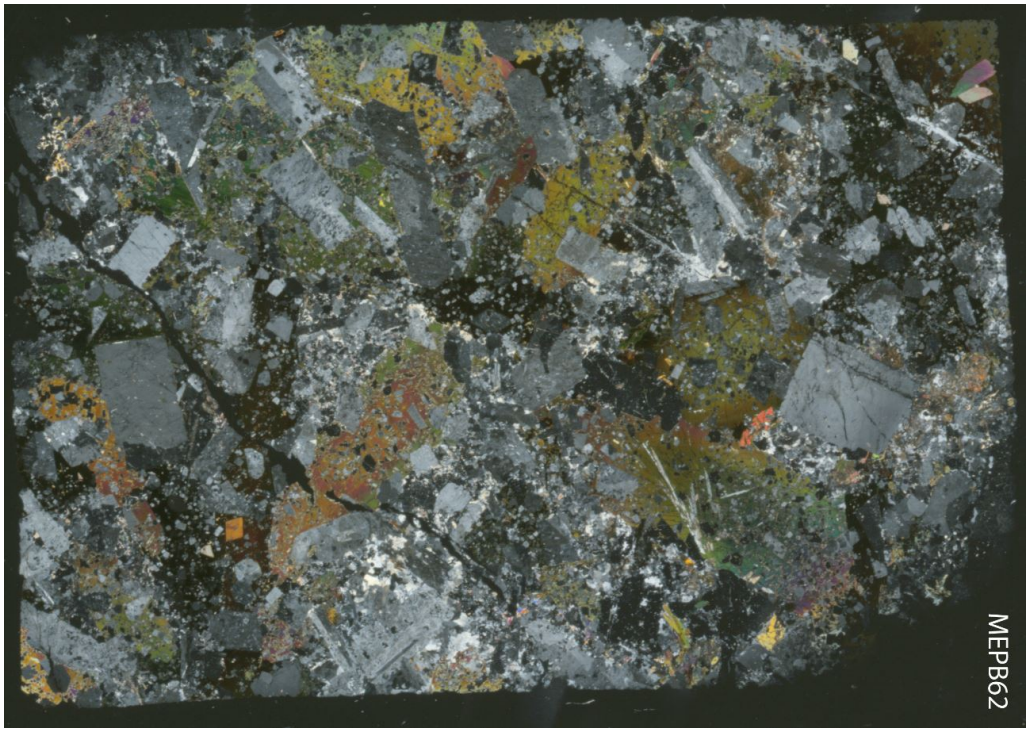

MEPB63

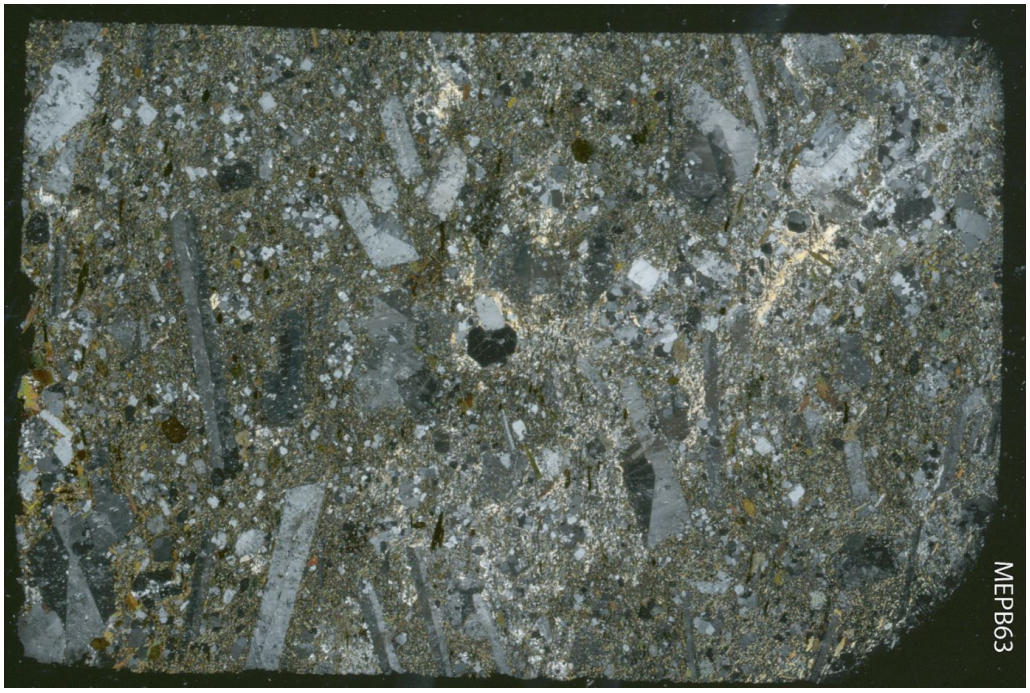

MEPB64

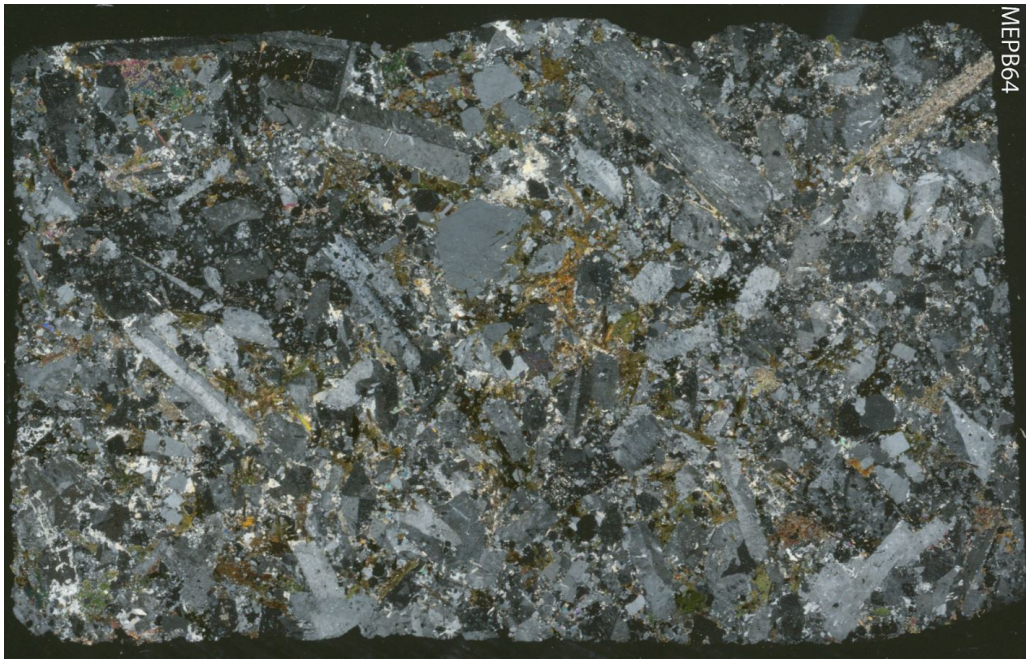

MEPB65

MEPB66

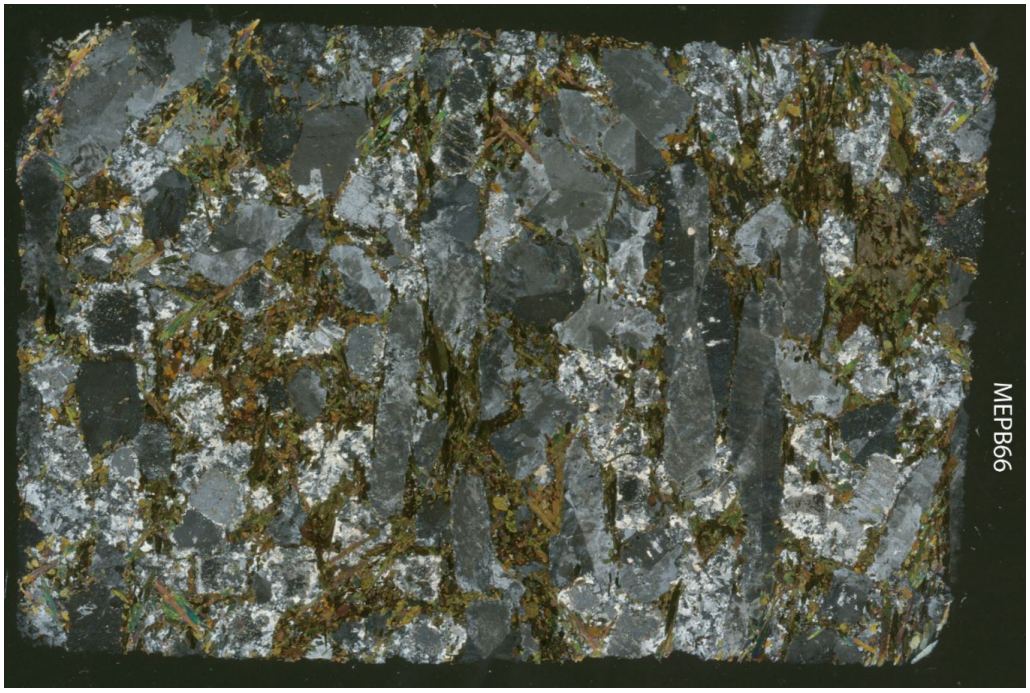

MEPB67

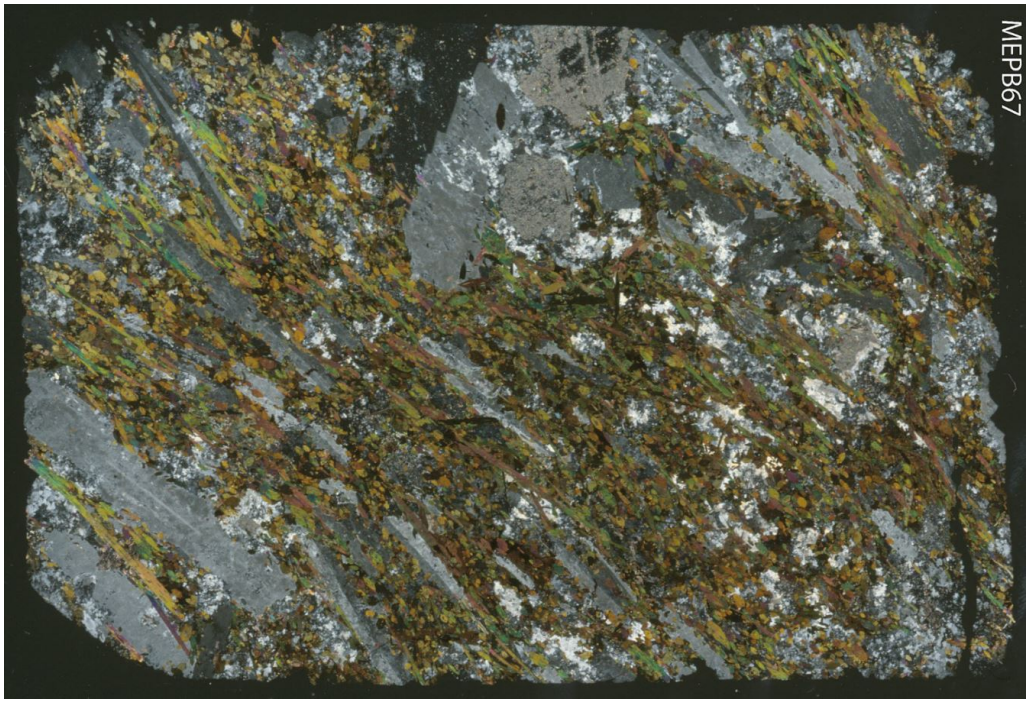

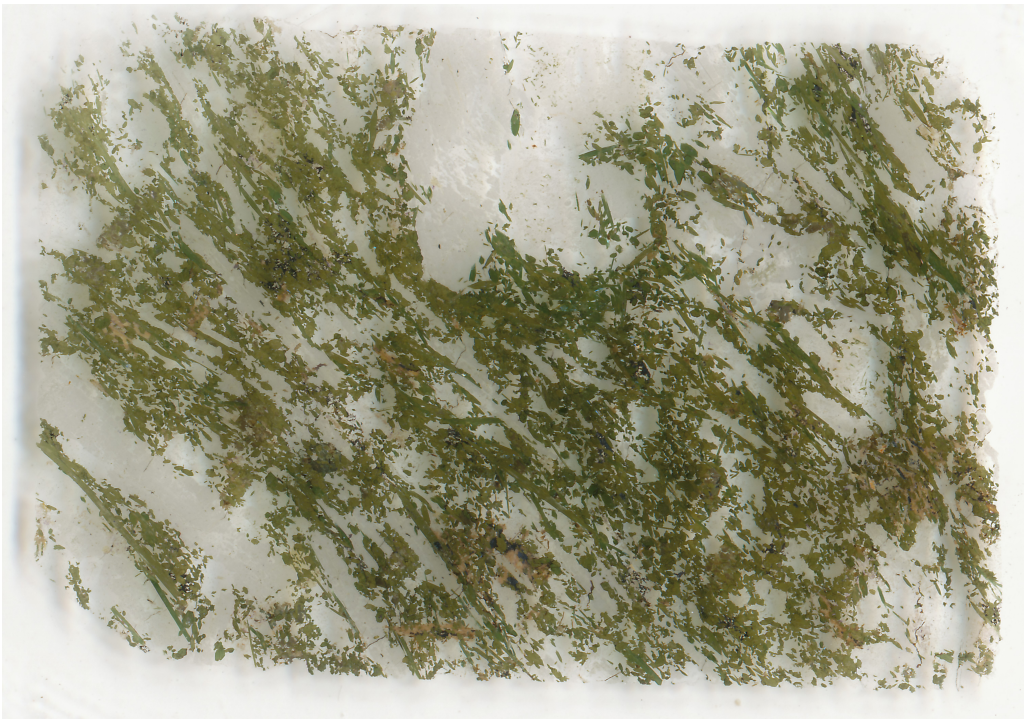

MEPB68

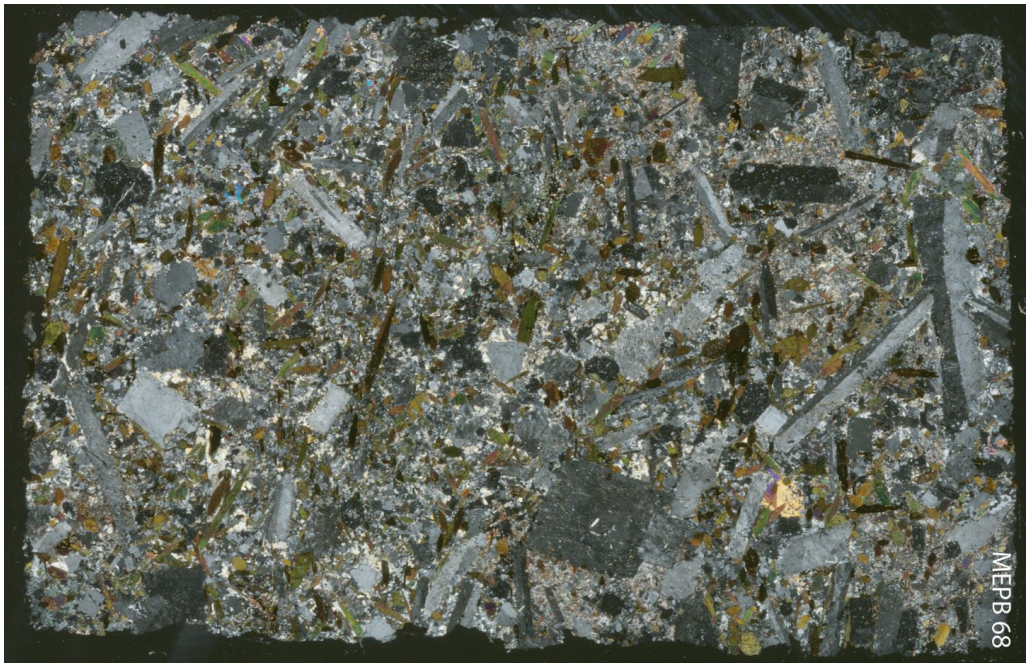

MEPB69

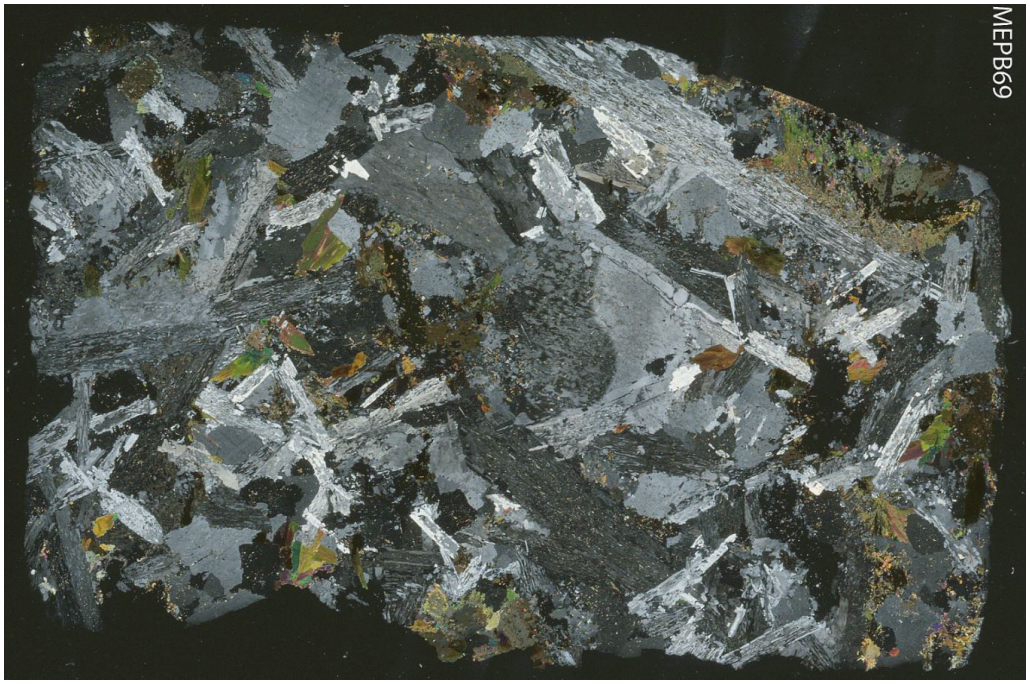

MEPB70

MEPB71

MEPB72

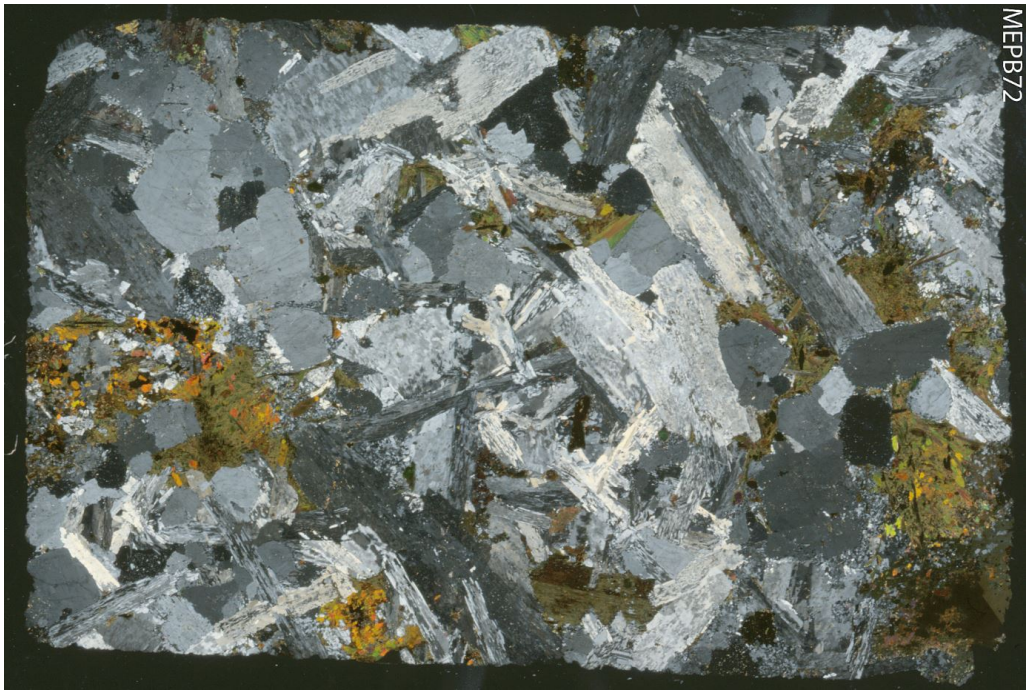

MEPB73

MEPB74

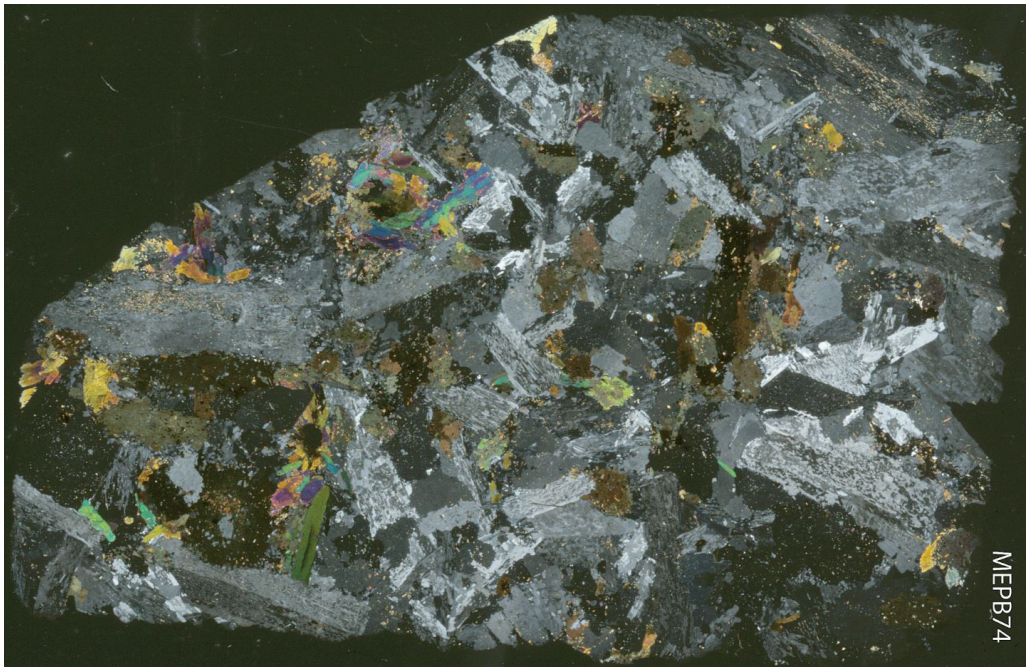

MEPB75

MEPB76

Appendix D: Endmember calculation for Pilanesberg clinopyroxene

Method for enmbember calculations (T.Andersen, pers.comm).

Site allocation and endmember calculation for Pilanesbeg cpx

1. Do a normal structural formula calculation based on 4 cations with all Fe as Fe^{2+}_{tot}. Calculate the sum of cation charge, which should be ≤ 12.00.

2. Estimate Fe^{3+} and Fe^{2+}.
   Fe^{3+} = 12.00 – SumCharge
   Fe^{2+} = Fe^{2+}_{tot} – Fe^{3+}

   If Fe^{2+} <0 there is something seriously wrong with the analysis, and it should be discarded.

3. If Si<2.00, fill the T position with Al^{3+} (and then Fe^{3+} if there is not sufficient Al^{3+}, but that will not apply for these analyses). The remaining Al^{3+} goes to M1.

4. Assign Ti, Zr, Fe^{3+}, Fe^{2+}, Mn, Mg to M1. Na and Ca goes to M2.

   Then comes endmember calculation:

5. Aluminium Tschermak's component: AlTs=min(Al_T, Al_{M1}). In this and other steps, it is convenient to use the "MIN" (minimum) function in Excel.

6. Assign any remaining Al_{M1} to Jd

7. Calculate the "TiZrAeg" ($Na(Ti, Zr)_{0.5}Fe^{2+}_{0.5}Si_2O_6$) component as TiZrAeg= 2(Ti+Zr)

8. Diopside: Di=Mg

9. Add Mn to Fe^{3+} remaining after step 7 and assign to hedenbergite: Hd=(Mn+Fe^{2+})-2TiZrAeg

10. Aegirine: Aeg=min((Na-Jd-TiZrAeg),Fe^{3+})

    To check, see how well the model matches the observed Ca and Na in M2:

    Excess Ca= Ca- AlTs – Hd – Di Excess Na= Na - TiZrAeg – Jd – Aeg

    These excesses should be rather close to zero.